DURABILITY OF TERNARY BINDERS BASED ON PORTLAND CEMENT, CALCIUM ALUMINATE CEMENT AND CALCIUM SULFATE

THÈSE N^{O} 3151 (2005)

PRÉSENTÉE À LA FACULTÉ SCIENCES ET TECHNIQUES DE L'INGÉNIEUR

Institut des matériaux

SECTION DES MATÉRIAUX

ÉCOLE POLYTECHNIQUE FÉDÉRALE DE LAUSANNE

POUR L'OBTENTION DU GRADE DE DOCTEUR ÈS SCIENCES

PAR

Séverine LAMBERET

DEA en Matériaux Polymères et Composites, Université de Lyon, France
et de nationalité française

acceptée sur proposition du jury:

Prof. K. Scrivener, directrice de thèse
Prof. F. Glasser, rapporteur
Dr D. Guinot, rapporteur
Prof. H. Hofmann, rapporteur

Lausanne, EPFL
2005

Acknowledgements

I would like to thank my thesis director Professor Karen Scrivener who introduced me to the delights of the complex field of cement. The success of this PhD work is mainly due to the motivating and stimulating atmosphere she has been able to create around her.
Another particular thought goes to Dr. Emmanuel Gallucci for his guidance and the numerous scientific discussions we had.

This thesis was an industrial project financed by Lafarge Aluminates. Sincere thanks to Dr. Dominique Guinot, Dr. Hervé Fryda and Dr. Loris Amathieu for having closely followed the project and for the fruitful discussions. I also acknowledge all the team of Lafarge Aluminates, especially Christelle Darmochod and Eric Charpentier.

I wish to express my thanks to the thesis defence committee: Professor Frederic Glasser, Professor Heinrich Hofmann and the president of the jury Professor Michel Rappaz .

I also would like to thank the Professor Nick Buenfeld from Imperial College for the opportunity he gave me to do transport properties measurements and Dr. Hélène Zanni and Dr. Fabien Barberon from ESPCI for performing the NMR analysis of my specimens.
I am grateful to Dr. Steve Sclosa and Dr. Jürgen Klein for their help into the collection of the samples stored under outdoor conditions in Japan, Norway and Germany.

I shall not forget my colleagues of the LMC for their friendship and for creating a pleasant work atmosphere that made these three years to pass so fast.
Life has not only consisted of work these last few years. I wish to express my sincerest thanks to all my friends within and outside the EPFL for all the pleasant moments we spent together.

Last but not the least, je remercie mes parents ainsi que mes frères et soeur (Sébastien, Thomas, Julien et Mylène) pour leur soutien et leur amour.

Abstract

The applications of systems based on Portland Cement (PC), Calcium Aluminate Cement (CAC) and Calcium Sulphate (C$) are usually limited to indoor uses in the field of Building Chemistry because no durability data exist on the outdoor uses. These ternary binders have different phase compositions and microstructure than those of the products based purely on Portland cement. Whereas Portland cement is widely studied, there exists very little published data on the performance of these materials over time.

This research work aimed at understanding the development of the microstructure of these ternary systems and identifying the degradation mechanisms under controlled atmosphere and under natural weathering. The influence of the formulation was thoroughly studied with respect to hydration mechanism, porosity and transport properties. SEM (BSE observations and EDS microanalysis) was the main analytical technique to understand the hydration mechanisms and was also coupled with XRD, TGA and ^{27}Al NMR. Porosity was examined by solvent exchange and desorption isotherm. Transport properties were studied through oxygen diffusion, oxygen permeability and water sorption. In parallel, performance of different systems were tested with respect to the storage, carbonation, acid corrosion and external sulphate attack. Alongside with that study, the degradation mechanisms after 3 years of natural weathering were examined.

The microstructural investigations of the cementitious matrix show that the hydration mechanisms of Portland-rich systems depend on the PC/CAC and CAC/C$ ratios but all present a delay of the silicates' hydration. The CAC-C$ rich binders lead to ettringite and AH_3 formation. Despite different hydration mechanisms, Portland and CAC-C$ rich binder at similar porosity have similar transport properties.

A first durability "map" was drawn with the data from accelerated ageing. It was found that binders containing portlandite provide superior resistance to carbonation but were more sensitive to sulphate attack, those with AH_3 perform better in acidic media. The 3 years natural weathering reveals that samples underwent leaching and carbonation and the mechanical strengths remain the same from 1 to 3 years.

Version abrégée

Actuellement, la commercialisation des mélanges ternaires à base de Ciment Portland (PC), de Ciment Alumineux (CAC) et de sulfate de calcium (C$) se limite essentiellement aux applications intérieures car aucune donnée n'existe sur leur durabilité à l'extérieur. Les mécanismes d'hydratation de ces systèmes sont différents de ceux d'un ciment Portland seul. Tandis que ce dernier est très étudié, peu de données existent sur la performance de ces matériaux complexes.

L'objectif de ce travail était de comprendre le développement de la microstructure de ces mélanges et d'identifier les mécanismes de dégradation sous atmosphère contrôlée et en milieu naturel. Les trois axes d'étude de la microstructure ont été les mécanismes d'hydratation, la porosité et les propriétés de transport. Le MEB (observations en électrons rétrodiffusés et microanalyses EDS) a été l'outil principal pour l'étude des mécanismes d'hydratation; la diffraction X, ATG et ^{27}Al RMN ont également été employées. La porosité a été mesurée par échange de solvant et analyse des isothermes de désorption. La durabilité de chaque formulation a été évaluée vis à vis de l'environnement de conservation, de la carbonatation, de l'attaque acide et de l'attaque par les sulfates. En parallèle de ces vieillissements accélérés, nous nous sommes intéressés aux mécanismes de dégradations après 3 ans en milieu naturel.

L'étude microstructurale de la matrice cimentaire a démontré que les mécanismes d'hydratation des systèmes à base de Portland dépendent des rapport PC/CAC et CAC/C$ mais tous présentent un retard de l'hydratation des silicates. La formation d'ettringite et de AH_3 sont les hydrates caractéristiques des mélanges riches en CAC et C$. Malgré des mécanismes d'hydratation différents, les mélanges à base de Portland et ceux à base de CAC et C$ présentent les mêmes propriétés de transport à porosité égale.

Toutes les données ont été rassemblées pour construire une premier «diagramme de durabilité». Des tendances générales sont mises en évidence; par exemple, les mélanges contenant de la portlandite résistent mieux à la carbonatation mais sont plus sensibles à l'attaque des sulfates; ceux avec AH_3 offrent une meilleure résistance à l'attaque acide, ….

La carbonatation et la lixiviation sont les 2 principaux mécanismes de dégradations après 3 ans de conservation en milieu naturel, les résistances mécaniques restant toutefois stables entre 1 et 3 ans.

Glossary

Cementitious notation

$C = CaO$

$A = Al_2O_3$

$F = Fe_2O_3$

$H = H_2O$

$S = SiO_2$

\$ or $\overline{S} = SO_3$

$T = TiO_2$

BSE	Backscattered electron
CAC	Calcium Aluminate Cement
C$Hx or C$	Calcium Sulfate
EDS	Energy dispersive spectroscopy
hcp	Hardened cement paste
IA	Image analysis
ICP	Inductive coupled plasma
MIP	Mercury intrusion porosimetry
NC	Neutralisation capacity
NMR	Nuclear magnetic resonance
PC	Portland Cement
RH	Relative humidity
R_c	Compressive strength
R_f	Flexural strength
SE	Secondary Electron
SEM	Scanning Electron Microscope
TEM	Transmission Electron Microscope
TGA	Thermogravimetric analysis
w/c	water/cement ratio
XRD	X-ray diffraction
XRF	X-ray fluorescence

Table of contents

Chapter 1. Introduction

Nowadays, a wide range of products are available based on Portland Cement (PC), Calcium Aluminate Cement (CAC) and Calcium Sulfate (C$). Their applications are usually limited to indoor uses in the field of Building Chemistry because no durability data exist on the outdoor uses. Two major areas cover most of the known applications as depicted in the triangle of figure1-1. The demand for such products is increasing as the need for rapid return to service is a strong construction trend. The systems in area 1 are mostly used when fast set is required combined with moderate hardening kinetics; main applications are masonry, fixing, small repairs. Compositions in area 1 but richer in CAC and with supplementary calcium sulfate will be characterized by better hardening profile and shrinkage compensation, and they will find applications as fast hardening cement and technical mortars for concrete repair and protection. Systems in area 2, are used in very high demanding mortars where they provide a set of characteristics like very fast hardening kinetics, self drying capacity and size variations control. Most of Self-levelling screeds, high tech tile adhesives and rapid repair mortar are based on this technology.

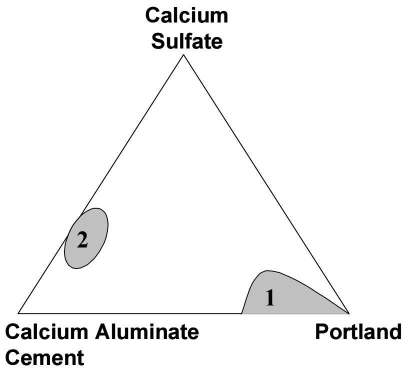

Figure 1- 1: Areas composition for various applications in the CAC-PC-C$ system.

These binders systems have different phase compositions and microstructure than products based purely on Portland cement. Whereas Portland cement is widely studied , there exists very little published data on the performance of these materials over time. It is therefore important to study the durability of these ternary binders with regards to parameters such as the exposure to various environments and potential degradation processes.

The objectives are twofold:

- *Clarify the hydration pattern of these ternary mortars in the long-term*

Ternary blends with Portland cement, calcium aluminate cement and calcium sulfate contain ettringite as a significant or major hydration product. Based purely on this fact, many questions are posed about the durability of these products. Although some instances of poor durability exist, these seem not to be based on the presence of ettringite per se, but more on factors such as porosity or transport properties which are already known to have a major impact on durability. This project should provide a rational basis on which to discuss the role of ettringite in the durability of these materials and to provide insights into how microstructure of these ternary systems evolves in different environments.

- *Identify strengths and weaknesses of the different formulations, as well as important parameters affecting performance*

A long-term goal is to work towards a type of durability “map” for ternary binders. An understanding of which regions on the PC/CAC/C$ diagram provide superior resistance to different exposure conditions, would serve to develop new composite binder products for special applications.

It is only by gaining an understanding of the underlying generic principles of phase composition and microstructure and how these properties change over time and exposure, that the full potential of these ternary binders will be realized.

Thus, the thesis is based on three interrelated approaches which can be illustrate as follows:

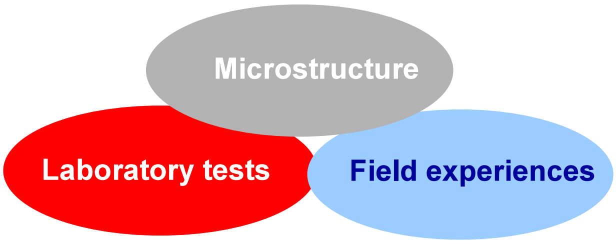

Figure 1- 2: Overview of the research approach

In this framework, the strategy applied for this durability study involved successive steps:

- ☞ Knowledge of the development of the microstructure of the complex cementitious systems:

  - Hydration mechanism in “normal” conditions
  - Porosity and transport properties
- ☞ Understanding the degradation mechanisms in controlled atmosphere via accelerated tests
- ☞ Understanding the behaviour of the different binders in natural weathering

The thesis work was built on these three main axis. However, the very first step of the project begun before the start of the author’s work was the choice of the ternary binders and the accelerated ageing, and the installation of the samples on the natural sites. Chapter 2 gives an overview of this phase and the experimental program for the microstructural investigations. After the explanation of the experimental program, the development of the microstructure was investigated and results are presented in chapters 3 and 4. Chapter 3 describes the hydration mechanisms of the different binders between 28 days, 1 year and 3 years by SEM. Chapter 4 focuses on the physical aspect of the cementitious matrix with the study of porosity assessed by solvent exchange and desorption isotherms and transport properties; the former were studied regarding the degree of water pore filling.

Durability is obviously linked to the environment. Therefore, after the chemistry and physical features of the matrix, the impact of the environment surrounding the sample is studied and results are found in Chapters 5 and 6. Two approaches are done; Chapter 5 is the accelerated ageing including the influence of the storage, carbonation, acid corrosion and sulfate attack. The Chapter 6 was the understanding of the degradation mechanisms under natural weathering by SEM investigations. As the data about ternary binders are limited, the literature survey is reviewed at the beginning of each chapter.

Chapter 7 discusses the results as a whole and Chapter 8 concludes on the main findings in this work and presents suggestions for future work.

Chapter 2. Mix design and experimental techniques

The research program was divided into two phases; phase I conducted by Andrea Boddy in 2000 dealt with the choice of the binders compositions, the choice of the laboratory tests and the natural weathering sites. This phase is described in the first part of this chapter. The thesis was related to the Phase II which included the characterisation of the ternary binders with different tools and the understanding of degradation mechanisms. The second part of the chapter presents briefly the strategy adopted for the microstructural investigations.

2.1 BINDERS COMPOSITION

2.1.1 The choice of the compositions

Two types of ternary systems based on a combination of Portland cement, Calcium Aluminate Cement and Calcium Sulfate, were examined:

- Predominantly CAC + $C\$H_x$ generally as hemihydrate, with minor PC content
- Predominantly PC with minor CAC and calcium sulfate usually as anhydrite

The objective at the start of the project was to study a large number of mortars mixtures including variations of several parameters such as the water/cement ratio, the type of sulfate, the use of slag. The range of mixtures highlighting these variables is shown in the ternary diagram figure 2-1. Earlier internal studies examining this system have identified the ranges where formulations become expansive (figure 2-1, region above the blue line).

Different water/binder ratios were selected, namely 0.25, 0.35, 0.5 to represent a range of porosities. In many applications w/c ratio is much higher due to use of fillers; these were eliminated to keep the basic systems as simple as possible.

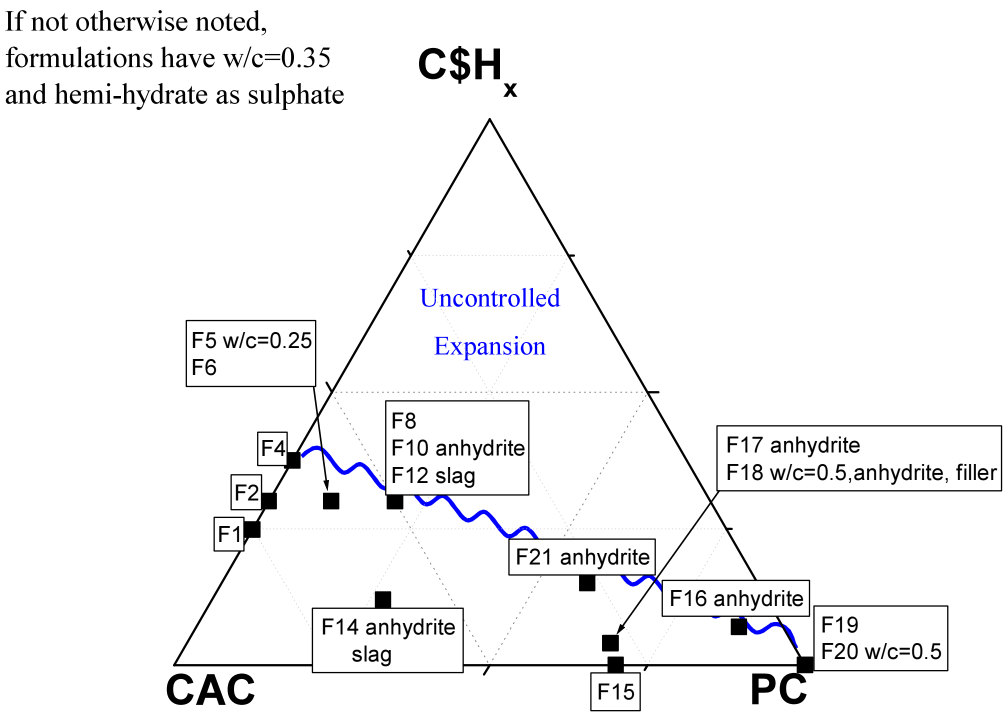

Figure 2- 1: Initial formulations at the project launching (phase I)

The table 2-1 gives the accurate composition of the cement paste. This table also details the admixtures used to control set times to allow mixing and placing, because it is known that addition of CAC accelerates the setting time of Portland cement [1-6].

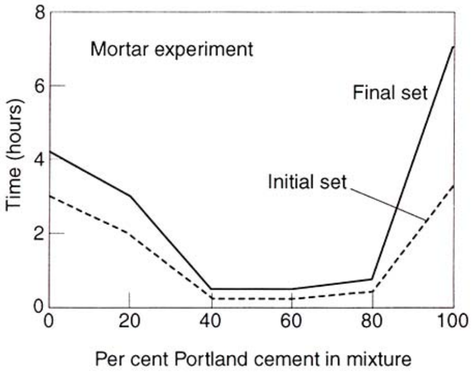

Figure 2- 2:Setting time according to the quantity of CAC added [7]

Previous internal studies allowed the most appropriate retarder / accelerator couples for the different systems to be chosen. Table 2-2 summarizes the effect of the various additives used in the formulations.

Mix *w/c*	**PC**	**C$** *nature*	**CAC** *nature*	**Mineral additive**	**CH**	**Additives**	**Fluidity**	**Workability**	**Notes**
F20 *0.5*	100	—	—	—	—	—	++	+	Noticeable efflorescence Demould after 24h
F19	100	—	—	—	—	—			
F16	85.9	6.9 *ICI*	6.9 *Secar 51®*	—	1	Sodium carbonate Citric acid Optima 100	+	+ +	Substantial efflorescence Yellowish colour
F21	58	27 *ICI*	15 *Secar 51®*	—	—	Sodium carbonate Trisodium citrate	+	+	
F17	66.5	4 *ICI*	28.5 *Secar 51®*	—	1		+	+ +	Substantial efflorescence
F18 *0.5*	45.4	2.7 *ICI*	19.5 *Secar 51®*	31.7 *filler*	0.7		+ +	+ +	
F15	70	—	30 *Secar 51®*	—			+ +	+ +	Little efflorescence
F14	20	8.8 *ICI*	44.8 *Secar 51®*	26.4 *slag*	—	Lithium chloride Ecoflo® Kelcocrete®	+ +	-	Sand Sifraco (<0.4mm)
F12	13.9	20.8 *Prestia*	34.7 *Fondu®*	30.6 *slag*	—	Lithium carbonate Sodium gluconate	- -	- -	
F10	20	30 *ICI*	50 *Fondu®*	—	—		+	+	
F8	20	30 *Prestia*	50 *Fondu®*	—	—		+	+	
F6	9.9	30 *Prestia*	60.1 *Fondu®*	—	—		+	+	
F5 *0.25*	9.9	30 *Prestia*	60.1 *Fondu®*	—	—	Lithium carbonate Sodium gluconate Melflux 100®	-	- -	Yellow colour on surface due to Melflux
F4	—	37.5 *Prestia*	62.5 *Fondu®*	—	—	Lithium carbonate Sodium gluconate	+	+	
F2	—	30 *Prestia*	70 *Fondu®*	—	—		+	+	
F1	—	24.8 *Prestia*	75.2 *Fondu®*	—	—		+	+	

Table 2- 1: Binders composition (wt %). The Portland cement used was CPA Le Havre 52,5. Prestia is hemihydrate and ICI Andricite anhydrite. Optima 100 and Ecoflo® are superplasticisers and Melflux® and Kelcocrete® are fluidifiers.

Accelerators	Retarders
Lithium carbonate	Citric acid
Lithium chloride	Trisodium citrate
Sodium carbonate	Sodium gluconate

Table 2- 2: Effect of various admixtures on setting time

It was obvious that a choice was essential in order to restrict the number of mixtures to be thoroughly studied; the formulations kept for extensive study were those with the water-cement ratio equal to 0.35 as shown by the diagram below.

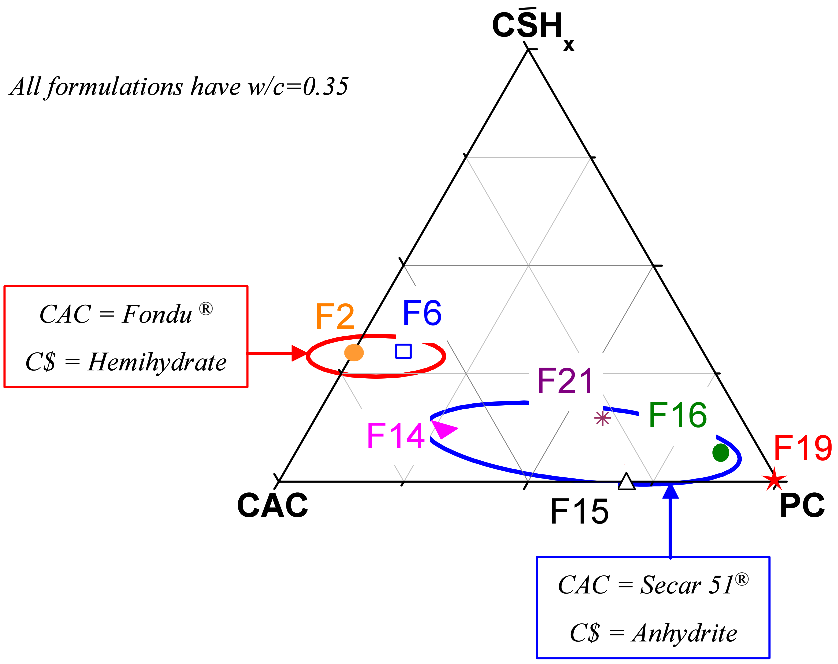

All formulations have w/c=0.35

CAC = Fondu ®
C\$ = Hemihydrate

CAC = Secar 51®
C\$ = Anhydrite

Figure 2- 3: Selected formulations for microstructural study (phase II)

2.1.2 Data on anhydrous cements used

The chemistry and mineralogy of the anhydrous cements were characterized by X ray fluorescence (XRF) and X ray diffraction, the results are summarized in the tables below.

Cement	**CaO**	**SiO_2**	**Al_2O_3**	**Fe_2O_3**	**K_2O**	**Na_2O**	**TiO_2**	**MgO**	**SO_3**
Fondu®	37.44	4.65	39.15	15.50	<0.01	0.08	1.87	0.92	<0.05
Secar 51®	37.48	5.07	52.41	1.12	0.19	0.11	2.51	0.51	<0.05
CPA Le Havre	65.49	20.58	4.92	1.83	0.24	0.14	0.22	1.00	3.76

Table 2- 3: Chemical analyses of cements (wt %) obtained by XRF and ICP (carried out in LCR Lafarge)

Fondu®	CA Main phase	C_2AS gehlenite	$C_{12}A_7$ mayenite	C_2S larnite	C_4AF ferrites	C_3FT	CT	$MgAl_2O_4$ Spinel
Secar 51®	CA Main phase	C_2AS	C_3FT	CT	Spinel			
CPA Le Havre	C_3S 61.7 %	C_2S 12.2%	C_3A 10%	C_4AF 5.6%	MgO	$C\$H_2$	C$	calcite

Table 2- 4: Mineralogical composition of cement (Bogue calculations for CPA Le Havre)

The different calcium sulfates were also analysed, table 2-5.

$C\$H_x$	**CaO**	**SO_3**	**Al_2O_3**	**Fe_2O_3**	**K_2O**	**Na_2O**	**MgO**	**Cl**
Hemi-Hydrate Prestia	41.35	57.15	0.03	0.05	<0.01	<0.01	0.01	<0.01
Anhydrite ICI	38.3	52.10	0.01	0.03	<0.01	<0.01	0.13	<0.01

Table 2- 5: Chemical analyses of calcium sulfate (wt %)

2.2 SAMPLES CASTING

The mortars prisms were cast in 4×4×16 cm^3 moulds with a sand/cement ratio of 4:3 and the amount of siliceous sand divided into 3 granulometries of equal weight: 0-0.315 mm/ 0.315-1 mm/ 1-4 mm except for the formulation F14 which was prepared with a specific siliceous sand whose granulometry did not exceed 0.4 mm and with a sand/cement ratio of 1:1.

The same casting sequence used for casting both at Lafarge LCR and at outside institutes was respected and was as follows:

- 2 × 5 minutes dry materials at high speed
- Add water and 30 seconds on medium speed
- 60 seconds at high speed
- Rest for 90 seconds
- 60 seconds at high speed

The formulation F14 was never mixed in batches greater than 2 kg due to rapid setting. All other formulations were mixed in the quantities necessary to cast the required specimens, which were never greater than 12 kg. After gauging, the mortar specimen were stored at about 100% RH and were demoulded after 4 hours except the plain Portland system which was demoulded after 24h. Up to the test time or exposure time, samples were stored at about 100% RH.

2.2.1 Initial strength properties

An initial mechanical characterization was undertaken to provide a baseline for comparison with the characterization of samples that have undergone natural weathering or laboratory durability test. It should be noted that for all of the data presented in this section, the samples were cured at about 100% RH, 20°C up to the test time. Figures 2-4 and 2-5 present the evolution of flexural and compressive strength respectively; only binders which have been systematically studied are plotted.

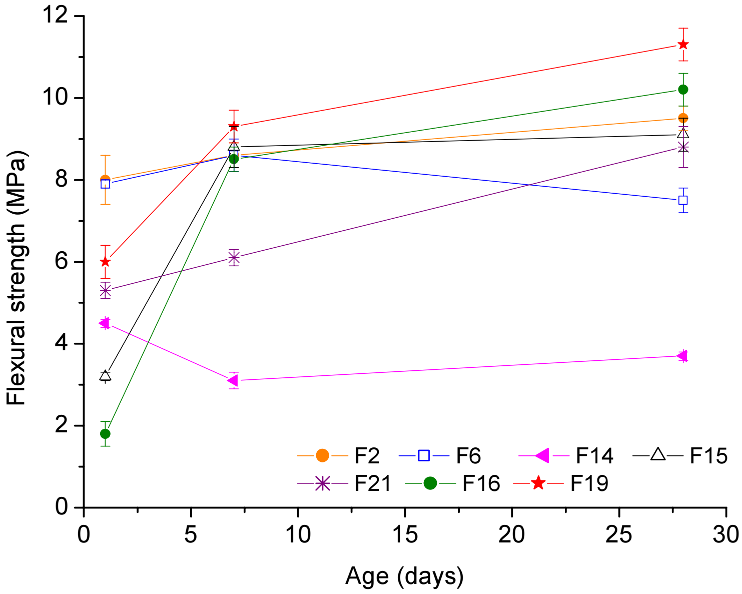

Figure 2- 4: Flexural strength evolution. Cure 100% RH

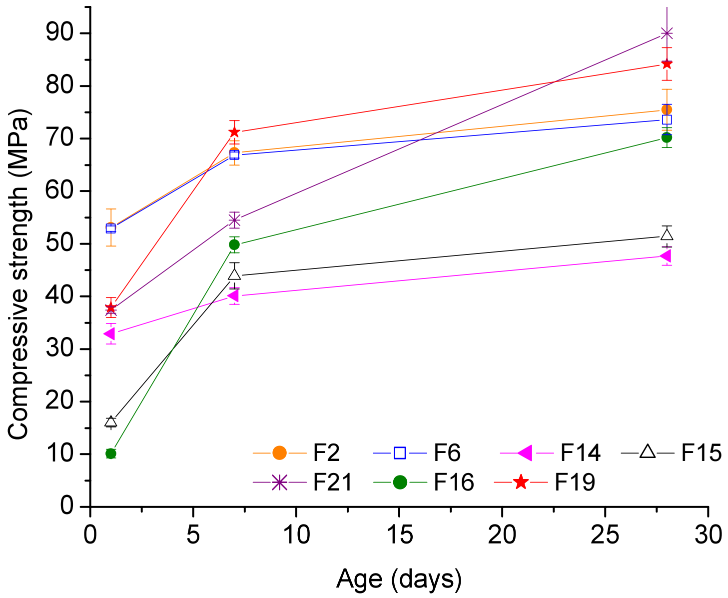

Figure 2- 5: Compressive strength evolution. Cure 100% RH

All of the formulations have acquired at least 45 MPa compressive strength by 28 days. For both compressive and flexural strength results, it was observed that binders with CAC as the major component have higher early strengths with little gain after 7 days, while the mixtures with Portland as the main component have lower early strengths but still have significant strength gain between 7 and 28 days. The mechanical behaviour of F2 and F6 is similar. F16 had the lowest R_c at 1 day but at 28 days, its strength was similar to CAC-C$ rich binders F2 and F6. On the other hand, the binary PC/CAC mix F15 showed poor strength development. The minimum 28-day flexural strength is about 4 MPa; this low value occurred for F14 which contains slag addition and finer sand grains. Otherwise, flexural strengths vary between 7.5 and 11 MPa.

2.3 LABORATORY DURABILITY TESTING

The evaluation of the durability of concrete is a real challenge because potential sources of degradation are numerous. Important degradation mechanisms in concrete structures include the following:

- Alkali-aggregate reactions (chemical effects)

- Sulfate attack (chemical effects)
- Microbiologically induced attack or acid attack (chemical effects)
- Corrosion of reinforcing steel embedded in concrete (chemical effects) due to
    a. carbonation of concrete
    b. chloride induced
- Freeze-thaw damage (physical effects, weathering)
- Abrasion (physical effects).
- Mechanical loads (physical effects).

As the time available to perform the research was limited, one approach is the use of accelerated ageing. Table 2-6 outlines the laboratory testing program. Some of this testing was performed at outside institutes which have a high level of expertise on particular durability issues. A literature survey was carried out before the choice of the test methods [8] and the following section outlines why they were chosen among a large number of accelerated tests.

Test / **Location**	Formulations tested	Curing Regime
Thermal/ Humidity cycling **Lafarge Aluminates**	1, 4, 8, 12, 14, 16, 17, 19, 21	7d, 20°C, 100%RH
Carbonation resistance **Lafarge Aluminates**	1, 4, 8, 12, 16, 17, 19, 21	28d, 20°C, 100%RH
Acid resistance **Lafarge Aluminates**	All except F21	28d, 20°C, 100%RH
Sulfate resistance **University of Berkeley and EPFL**	1, 4, 8, 12, 14, 16, 17, 19, 21	28d, 20°C, 100%RH
Freeze / Thaw **Lafarge Roofing**	All except F21	2 cures: 28d, 20°C, 100% and 65%RH

Table 2- 6: Laboratory testing program

2.3.1 Acid attack

The resistance of concrete to aggressive liquids can be tested in laboratory experiments with different regimes:

- Solution renewal at specific intervals [9-12]
- Solution renewal when the acidity becomes sufficiently weak [13, 14]
- Maintenance of acidity by addition of a more concentrated acid [15-17]
- Continuous flow of acid [12, 18]

Most studies are carried out in static conditions; the renewal of the solution accelerates the degradation but is not necessary representative of the real mode of solicitation. These methods emphasize more the potential of neutralization of the material than the kinetics. Dynamic conditions were thought to better simulate real-life situations, therefore in this context, Lafarge Aluminates developed a drip test method. The set up is described in more detail in Chapter 5.

The main advantages were:

- Control of the drip-by drip flow
- Initially water saturated samples are maintained in a water saturated atmosphere during the test
- Possible quantification of the effluent (consumed H^+ or elements passed in solution)

2.3.2 Sulfate attack test methods

There are several test methods related to sulfate resistance. The first is ASTM C 452 - Test for Potential Expansion of Portland Cement Mortars Exposed to Sulfate. The relevance of this procedure is controversial [19-21]. The other ASTM test method – Length Change of Hydraulic-Cement Mortars Exposed to Sulfate Solution, ASTM C1202, has been known to give results inconsistent with field experience [22]. In addition, both ASTM methods only have the potential to initiate expansion/cracking deterioration and do not allow for evaluation of the resistance to the softening-spalling type of sulfate attack [19, 23]. Other sulfate-resistance test methods exist such as the Le-Chatelier-Anstett-Blondiau, Koch-Steinegger, and Merriman tests which have also been found inadequate [24].

Several researchers agree that a method based on the procedure by Mehta is most likely to result in an acceptable accelerated test consistent with long-term data [22, 25]. When developing this test method, Mehta addressed the limitations/weaknesses observed in existing methods; the end result was a method that would (1) yield reliable and reproducible information within a relatively short period, to be of practical value to both the manufacturer and consumer of a cement, (2) correlate well with field experience…reproduce natural sulfate attack processes on cement paste structure, (3) be applicable to a wide variety of sulfate-resisting cements [19]. A test procedure based on that of Mehta is currently being used at University of Berkeley, California [26]. The method is advantageous in that it incorporates the sound philosophy and procedure of Mehta, and is adapted to address the advancements in knowledge regarding sulfate-resistance testing, as well as mechanisms and prevention of attack.

2.3.3 Freezing and thawing methods

There exists numerous freezing-thawing tests such as the Scandinavian slab test (SS 1372 44, proc 1, method A), the ASTM C666, the German cube test, the CDF (Capillary Suction of De-icing solution and Freeze thaw) and CIF (Capillary Suction, Internal Damage and Freeze thaw) tests [27]. Lafarge Roofing has used 2 types of resistance to freezing and thawing testing: “Heat/Freeze/Thaw test” and “Sekisui test”. These tests are rapid index tests. However they are very useful in that they will provide an overall image of how freezing and thawing resistance varies for different compositions on the CAC/PC/C$ spectrum since a large number of samples can be tested in a relatively short time. Also, Lafarge Roofing has extensive experience in the correlation of results from these tests with field performance.

These accelerated tests predict behaviours which are essential to check under natural weathering. Only one single mechanism of degradation is taken into account in one accelerated test but in real service life, a synergy between deterioration processes may occur, hence the need of natural weathering .

2.4 NATURAL WEATHERING SITES

Table 2-7 outlines the various natural weathering sites on which samples have been placed. The information provided includes the location of these sites, their typical climates and associated durability issues. These sites were chosen in order to expose the formulations to a wide range of climates and possible deterioration mechanisms.

All the sites are managed by Lafarge BRAAS and are typically used for outdoor exposure of roof tile products. The samples were placed with an exposure at a 45° angle; in this arrangement, the top surface of the samples is fully exposed to all climatic conditions. The bottom surface is also open to air and the samples are relatively tightly packed together, thus the side are relatively protected as shown in figure 2-6.

Fifteen $4\times4\times16$ cm^3 prisms of each formulations were placed at each sites. These samples were all cast by Lafarge LCR. A total of 15 prisms per formulation allows 3 samples to be examined at each of the 5 predicted ages of interest, namely 1 ,3, 5 and 10 years and later.

Site Location	Climate *Durability issues*	Average Relative humidity	Temperature (lowest / highest)	Precipitations (lowest / highest)
Bergen **Norway**	Sub-artic *Freeze / Thaw* *Acid rains*	78%	1 / 15°C Feb / July	83 / 236 mm May / Oct
Asahikawa **Japan**	Cold oceanic *Freeze / Thaw, Snow*	76%	-8 /26°C Jan / Aug	52 / 138 mm March / Aug
Heusenstamm **Germany**	Mid-European Freeze / Thaw	Morning: 84% Afternoon: 62%	-2 /25°C Jan / July	38 / 76mm March / August
Lake Wales **Florida**	Sub-tropical *Humidity* *Algae growth*	Morning: 88% Afternoon: 56%	16 / 27°C Jan / July	50 / 190 mm April / July

Table 2- 7: Details of natural weathering sites

Figure 2- 6: Samples exposed in Japan at Asahikawa

2.5 STRATEGY FOR MICROSTRUCTURAL INVESTIGATIONS

Some of the methods available and commonly used for the characterization and quantification of cement microstructure with specific reference to microscopic techniques are discussed by Scrivener [28]. Scanning electron microscopy (SEM), especially backscattered electron (BSE) is universally accepted by the concrete technologists as an investigative tool. In this work, a combination of BSE and independent techniques, namely X ray diffraction (XRD), thermogravimetric analysis (TGA) and Nuclear Magnetic Resonance (NMR), were used to characterize the cementitious matrix.

At dates of 28 days, 1 and 3 years, samples were systematically characterized by BSE, XRD and TGA and NMR for the 28-days old samples. Pore measurements were also performed and more details are given in Chapter 4.

2.5.1 BSE and EDS

Through the combination of the information provided by BSE and Energy Dispersive Spectroscopy (EDS), a detailed quantification of the hydrated cementitious matrix may be achieved. More information about EDS can be found in Appendix A. A Philips Quanta 200 microscope and a PGT energy dispersive x-ray analyser were used. An accelerating voltage of

15 kV was chosen to provide the best compromise between spatial resolution and adequate excitation of the FeKα peak. BSE and EDS analysis require a highly polished surface for optimum imaging and x-ray microanalysis; experimental procedure to obtain a flat polished section is given in Appendix A.

2.5.1.1 BSE imaging

Atomic number is the main factor determining the grey level contrast in BSE images. The higher the average atomic number of a phase, the higher the number of generated BSE, and consequently the brighter the phase will appear on the screen. More information about the calculations of backscatter coefficient are available in Appendix A.

A strong contrast is obtained between anhydrous and hydrates. For the anhydrous phases, the ferrite is the brightest followed by C_3S (alite) and C_3A and C_2S (belite which is often striated due to the cooling of clinker), figure 2-7. Portlandite is the brightest hydrate and the grey level of C-S-H can be affected by its variable composition and especially the Ca/Si ratio (due to carbonation, leaching…). Inner C-S-H, which has formed in the place of the original cement grain, form as a rim around the grains.

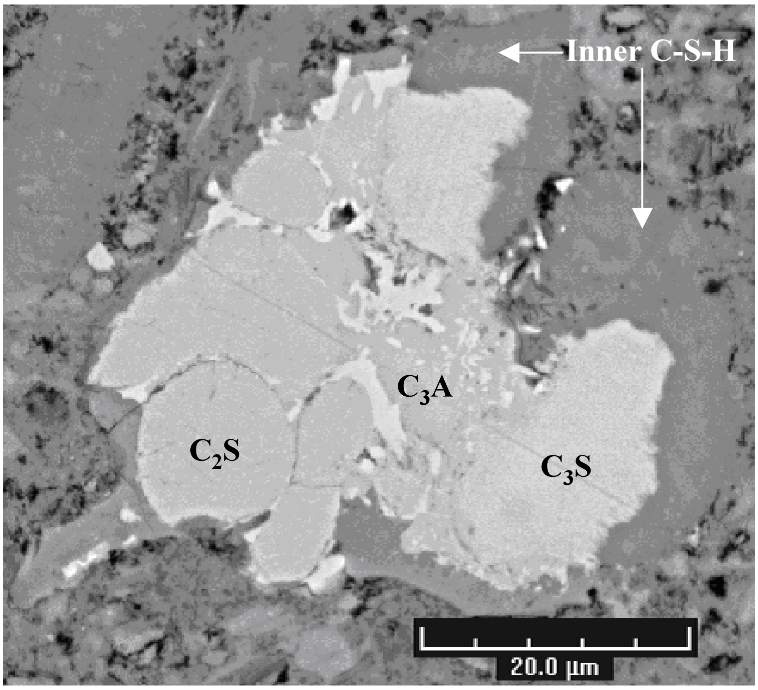

Figure 2- 7: BSE image of a polymineralic grain of Portland

The micrograph below represents an anhydrous grain of Fondu; the brightest phase is ferrite, the darkest one is CA and the intermediate grey level corresponds to gehlenite C_2AS.

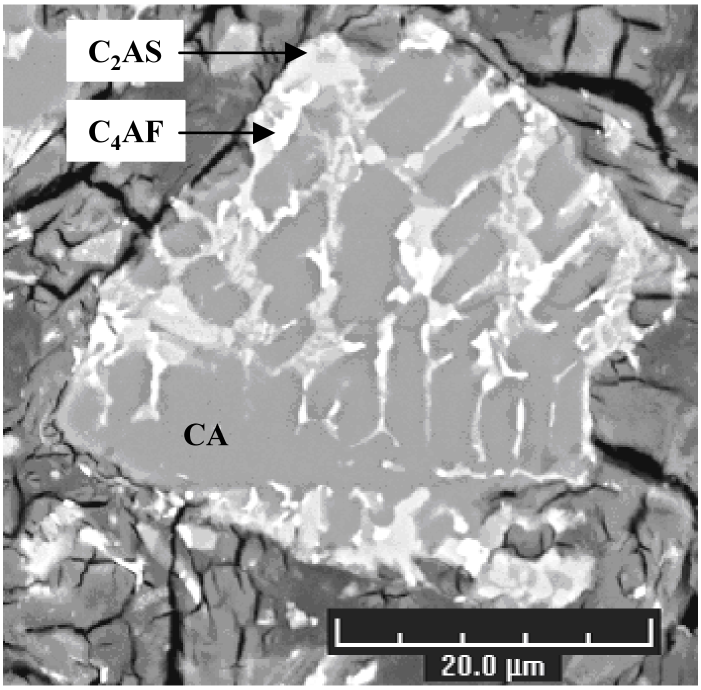

Figure 2- 8: BSE image of anhydrous Fondu grain

Moreover, BSE imaging allows quantification by image analysis (IA) based on grey levels. BSE/IA was used to calculate the degree of reaction; the procedure is described in Appendix A.

2.5.1.2 Interpretation of energy dispersive X-ray microanalysis (EDS analysis)

It is necessary to keep in mind that because the X-ray generation volume is relatively large, ~1 μm^3, EDS analysis of one phase may include contributions from other phases intimately mixed.

The microanalysis results are plotted as atomic ratios and not as absolute contents of elements to eliminate the effects of microporosity and water content of the C-S-H [29, 30]. The atom ratios of most interest are Si/Ca, Al/Ca and S/Ca for Portland-rich systems while it is Ca/Al and S/Al for CAC-rich binders. Different features are highlighted according to the considered atomic ratios:

- Al/Ca against Si/Ca plot: shows the distributions of Ca/Si ratios and Al substitution in the C-S-H.

- S/Ca vs. Al/Ca graph: shows the nature of the hydrated aluminate or sulfoaluminate phases and gives an indication of the closeness of mixing of the phases. In figure 2-9, the blue lines whose slopes are S/Al=3/2 and S/Al=1/2 indicate the composition of an intimate mixtures of C-S-H / ettringite (black squares) and C-S-H / calcium monosulfate (empty squares) respectively. In all the graphs, the end points of ettringite and monosulfate lines are fixed but they originate either from the origin point when there is no clear cluster of C-S-H composition or from a point belonging to the cluster of C-S-H.

- S/Al against Ca/Al: shows clearly when AH_3 has formed

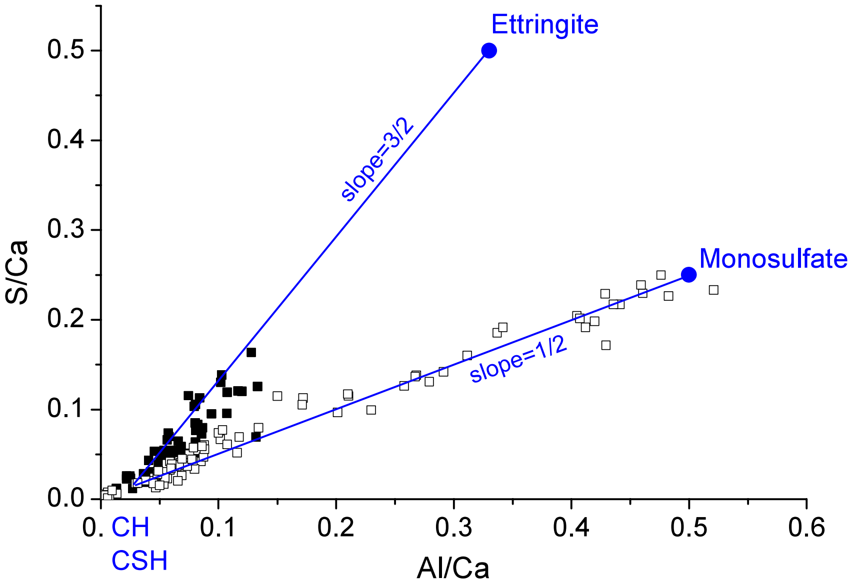

Figure 2- 9: Example of S/Ca vs. Al/Ca plot

2.5.2 ^{27}Al MAS NMR

Kirkpatrick [31] gave an introduction to NMR in cement science. ^{29}Si and ^{27}Al MAS NMR (MAS- Magic Angle Spinning -spinning of the sample about an axis at 54.7° relative to the magnetic field) have proved to be valuable tools for characterisation and quantitative analysis of cement-based materials [32-34].

In this work, ^{27}Al (quadrupole nucleus, I=5/2) was chosen. ^{27}Al MAS NRM is sensitive to the local coordination of the aluminate species. Skibsted's work [35] gave a solid database of ^{27}Al NMR parameters (chemical shifts, quadrupolar coupling constants…) for the main aluminate phases. In the anhydrous phases, aluminium occurs only in tetrahedral sites, whereas in the aluminate hydrates, aluminium occurs only in octahedral sites. Despite a chemical shift of only 1.3 ppm between ettringite and monosulfate, these phases are distinguished in high-resolution ^{27}Al MAS NRM spectra.

In this research, the solid-state ^{27}Al MAS NMR spectra were recorded at the ESPCI (Ecole Supérieure de Physique et Chimie Industrielle) by Dr. F. Barberon with a magnetic field of 11.7 T. Typical acquisition parameters for recording the ^{27}Al spectra were 15 kHz sample spinning speed, 1 µs pulse lengths with a recycle delay of 1 second between scans. ^{27}Al chemical shift are reported in ppm relative to an external reference of $AlCl_3.6H_2O$.

^{27} Al NMR	**Chemical shift (ppm)**
Tetrahedral Al-containing anhydrous	50 to 80
Ettringite	13.4
AH_3	10.4
Monosulfate	10.1
C_4AH_{13}	10.2
C_3AH_6	12.4

Table 2- 8: ^{27}Al chemical shift data of aluminate phases found in cement [35]

As shown in table 2-8, the chemical shift of the different AFm phases is in the same range, therefore it is impossible to separate them in ^{27}Al NMR.

2.5.3 X ray diffraction

X ray diffraction (XRD) is a non-destructive analytical technique for identification and quantitative determination of the various crystalline phases.

The XRD pattern of each crystalline material is unique. The positions of the peaks are determined by the spacing of crystallographic planes according to Bragg's law:

$$n\lambda = 2d\sin\theta \tag{2.1}$$

where n is an integer, λ is the wavelength of the radiation used, d the spacing of the crystal planes and θ the angle of the diffraction peak.

The XRD patterns were recorded for powders crushed to 100 μm and pressed into a sample holder. The phase identification was achieved by comparing the X-ray pattern obtained with an international recognized database (JCPDS) containing reference patterns for more than 70000 phases.

The technique of Rietveld refinement now allows quantification of plain Portland cement paste [36]. There are several difficulties of Rietveld analysis with mortars binders because its accuracy is greatly reduced by substantial dilution of the cement paste due to the presence of a high proportion of sand; consequently its development requires more work, and for this project XRD was used only for qualitative phase identification.

2.6 REFERENCES

1. Mathieu, A. (1988). Le ciment fondu Lafarge en mélange avec les ciments portland. *Ciments, Bétons, Plâtres , Chaux* **771**, 109-113.
2. Gu, P., et al. (1997). Early strength development and hydration of ordinary Portland cement calcium aluminate cement pastes. *Advanced Cement Based Materials* **6**, 53-58.
3. Gu, P., et al. (1994). A Study of the Hydration and Setting Behaviour of OPC-HAC Pastes. *Cement and Concrete Research* **24**, 682-694.
4. Garces, P., et al. (1998). Hydration characteristics of high alumina cement Portland cement mixtures. *Zkg International* **51**, 646-649.
5. Bayoux, J.P., et al. Shotcrete- Understanding of the hydration process of mixes containing CAC and OPC and proposal for a simple rheological characterization. 208-216.
6. Zhang, X., et al. (1997). Study of early hydration of OPC-HAC blends by microwave and calorimetry technique. *Cement and Concrete Research* **27**, 1419-1428.
7. Scrivener , K.L., and Capmas, A. (1998). Calcium Aluminate Cement. In Lea's Chemistry of Cement and Concrete, Volume 13, 4th Edition, P.C. Hewlett, ed. pp. 709-778.
8. Boddy, A. (2001). Durability of ternary binders. *Internal Communication.*
9. Mehta, P.K. (1985). Studies on chemical resistance of low water/cement ratio concretes. *Cement and Concrete Research* **15**, 969-978.
10. De Ceukelaire, L. (1992). The effects of hydrochloric acid on mortar. *Cement and Concrete Research* **22**, 903-914.
11. Bayoux, J.P., Letourneux, J.P., Marcdargent, S. (1990). Acidic corrosion of high alumina cement. In *Calcium Aluminate Cements* (Mangabhai, ed.): London.
12. Espinosa, B., et al. Acid attack of hydraulic cement-bound materials: corrosion kinetics and neutralisation capacity. In *13th Int. corrosion Congress*. pp. 1-10: Melbourne.
13. Chandra, S. (1988). Hydrochloric-Acid Attack on Cement Mortar - an Analytical Study. *Cement and Concrete Research* **18**, 193-203.
14. Attiogbe, E.K., and Rizkalla, S.H. (1988). Response of Concrete to Sulfuric-Acid Attack. *Aci Materials Journal* **85**, 481-488.
15. Pavlik, V. (1994). Corrosion of hardened cement paste by acetic and nitric acids part I: Calculation of corrosion depth. *Cement and Concrete Research* **24**, 551-562.
16. Shi, C., and Stegemann, J.A. (2000). Acid corrosion resistance of different cementing materials. *Cement and Concrete Research* **30**, 803-808.
17. Torii, K., and Kawamura, M. (1994). Effects of fly ash and silica fume on the resistance of mortar to sulfuric acid and sulfate attack. *Cement and Concrete Research* **24**, 361-370.
18. Fattuhi, N.I., and Hughes, B.P. (1988). The Performance of Cement Paste and Concrete Subjected to Sulfuric-Acid Attack. *Cement and Concrete Research* **18**, 545-553.
19. Mehta, P.K., and Gjorv, O.E. (1974). A new test for sulfate resistance of cement. *Journal of Testing and Evaluation* **2**, 510-514.
20. Tumidajski, P.J., and Turc, I. (1995). A rapid test for sulfate ingress into concrete. *Cement & Concrete Research* **25**, 924-928.
21. Depuy, W. (1994). Chemical resistance of concrete, in ASTM STP 169C-Significance of Test and Properties of Concrete and Concrete-Making Materials. 263-281.

22. Plowman, C., and Cabrera, J.G. (1996). The use of fly ash to improve the sulfate resistance of concrete. *Waste Management* **16**, 175-192.
23. Cao, H.T., et al. (1997). The effect of cement composition and pH of environment on sulfate resistance of Portland cements and blended cements. *Cement and Concrete Composites* **19**, 161-171.
24. Lawrence, C.D. (1990). Sulfate attack on concrete. *Magazine of Concrete Research* **42**, 249-264.
25. Reardon, E.J. (1990). An Ion Interaction-Model for the Determination of Chemical-Equilibria in Cement Water-Systems. *Cement and Concrete Research* **20**, 175-192.
26. Kurtis, K.E., et al. (2001). Accelerated test for measuring sulfate resistance of calcium sulfoaluminate, calcium aluminate, and portland cements. *Journal of Materials in Civil Engineering* **13**, 216-221.
27. Setzer, M.J., et al. (1997). Rilem recommendation for test method for the freeze-thaw resistance of concrete- Tests with sodium chloride solution (CDF). *Concrete precasting plant and technology* **4**, 100-106.
28. Scrivener, K.L. (1997). Microscopy methods in cement and concrete science. *World Cement Research and Development*, 92-112.
29. Harrisson, A.M., and Taylor, H.F.W. (1987). X-ray microanalysis of microporous materials. *Journal of materials scinece letters* **6**, 1339-1340.
30. Kjellsen, K.O., and Atlassi, E.H. (1998). X-ray microanalysis of hydrated cement: Is the analysis total related to porosity? *Cement and Concrete Research* **28**, 161-165.
31. Kirkpatrick, R.J., and Cong, X. (1994). An introduction to ^{27}Al and ^{29}Si NMR spectroscopy of cement and concretes. In Application of NMR spectroscopy to cement science, P. Colombet, Grimmer, A.R, ed. pp. 55-75.
32. Zanni, H. (1995). La RMN: une technique pour l'étude des ciments. *Bulletin des Laboratoires des Ponts et Chaussées* **195**, 61-72.
33. Skibsted, J., and Jakobsen, H.J. Characterization of the calcium silicate and aluminate phases in anhydrous and hydrated OPC by ^{27}Al ans ^{29} Si MAS NMR spectroscopy. In Resonance Spectroscopy of cement based materials, H. Zanni, Sozzani, P., Colombet, P., ed.
34. Faucon, P., et al. (1998). Characterization of calcium aluminate hydrates and related hydrates of cement pastes by ^{27}Al MQ-MAS NMR. *Inorganic chemistry* **37**, 3726-3733.
35. Skibsted, J., et al. (1993). Characterization of Calcium Aluminate Phases in Cements by ^{27}Al MAS NMR Spectroscopy. *Inorganic Chemistry* **32**, 1013-1027.
36. Scrivener, K.L., et al. (2004). Quantitative study of Portland cement hydration by X-ray diffraction/Rietveld analysis and independent methods. *Cement and Concrete Research* **34**, 1541-1547.

Chapter 3. Microstructure development

This chapter deals with the hydration of CAC/ PC/ C$ binders which is very different from that of either of the individual cements. The way in which the addition of a component in the system influences the hydration pattern is presented; after a brief presentation of the main hydrates found in cementitious systems, the simplest system, i.e. plain Portland, is presented. More complicated systems are dealt with afterwards. Portland-rich systems are described first and then aluminous-rich binders. Attention is directed toward the chemistry of cement hydration with observations of the development of microstructure in the bulk between 28 days, 1 year and 3 years using XRD, TGA, NMR and SEM techniques.

3.1 DESCRIPTION OF HYDRATED PHASES

Throughout the following paragraphs, we refer to various hydrates, for a better understanding, some of their characteristics are reviewed in the table below.

AFt (Al_2O_3-Fe_2O_3-tri) and AFm (Al_2O_3-Fe_2O_3-mono) phases have the general formula $C_3(A,F).3CX_n.yH_2O$ and $C_3(A,F).CX_n.yH_2O$ respectively where several different anions can serve as X but the most important in cement hydration are SO_4^{2-} (n=1), OH^- (n=2) and CO_3^{2-} (n=3).

Hydrates	Density ($g.cm^{-3}$)	Water (wt%)	Typical morphology
CH portlandite	2.22	24	Hexagonal slabs
C-S-H	1.2 – 2.3[1]	32 for Ca/Si=1.7	Various
AFt : Ettringite $C_3A.3C\$.H_{32}$	1.775	46	Hexagonal crystals, needles
AFm: $C_3A.C\$.H_{12}$	2.0	35	Thin hexagonal plates
C_4AH_{13}	2.05	42	
C_2ASH_8	1.94	53	

$C_4A\bar{C}H_{11}$	2.17	34	
C_2AH_8	1.95	42	
Hydrogarnet: C_3AH_6	2.52	29	Small equiaxed crystals
AH_3	2.4 (gibbsite)	35	More or less crystalline

Table 3- 1: Short summary of the main hydrates in hardened cement paste

3.1.1 Calcium silicate hydrate C-S-H

3.1.1.1 Structural models

The current general view is that C-S-H has a disordered layer structure in which individual layers are formed from calcium ions to which are attached silicates ions and hydroxyl groups, together with interlayer of calcium ions and water molecules. Many models have been proposed over the years to explain the extensive range of experimental data reported for CSH in Portland cement. It has been described as tobermorite with many imperfections and irregularities such that it becomes nearly amorphous, possibly intermixed at a very fine scale with a similar version of jennite.

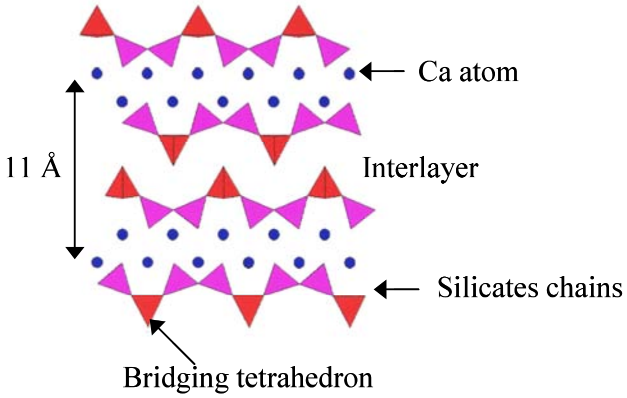

Figure 3- 1: Structure of Tobermorite

Taylor [2] proposed a mixed tobermorite-jennite model which takes into account of local variability in composition and structure.

Richardson and Groves [3] proposed a generalized model for the C-S-H formed in C_3S and C_2S pastes. They expressed the formula as

$$Ca_xH_{(6n-2x)}Si_{(3n-1)}O_{(9n-2)}.zCa(OH)_2.mH_2O$$

The model was extended to cement pastes by allowing the possibility of various ionic substitution [4].

Gauffinet et al. [5] observed the growth of C-S-H by Atomic Force Microscopy and C-S-H morphology has been identified as assembly of oriented nanoparticles with $60 \times 30 \times 5$ nm^3 characteristic dimensions. Very recently, taking into account the structure and the morphological properties of C-S-H described above, a surface reaction thermodynamic model has been proposed by Nonat [6].

A model based of two types of C-S-H at the mesolevel was proposed by Jennings [7]. The model is basically units that pack to form globules, which in turn pack together to form low density and high density C-S-H structure. These units pack together to form the microstructure of C-S-H.

3.1.1.2 Ca/Si ratio of C-S-H

C-S-H in ordinary Portland cement paste has a wide compositional range with Ca/Si ratio between 0.8 and about 2 [8]; TEM study [1] illustrates the extent of compositional variation possible for C-S-H present in neat Portland cement pastes: from a Ca/Si ratio of ~1.2 to ~2.3 with a mean of 1.7-1.8 [9]. Distributions vary with age: C-S-H present in young pastes displays a bimodal Ca/Si ratio distribution which becomes unimodal with age [10]. However, local variability may occur; this variation may be explained by the incorporation of other phases or minor elements into the C-S-H.

3.1.1.3 Interactions with aluminium and sulfates ions

The main substituent in C-S-H is aluminium. ^{27}Al and ^{29}Si NMR data indicated that the substitution of Al^{3+} for Si^{4+} is essentially limited to the silicon sites of bridging tetrahedral [1, 4, 10-12]. Experimentally the maximum substitution level is about 0.26 [12] whilst one might expect a maximum theoretical level of 0.33.

Odler [13] postulated that sulfate ions were only adsorbed on the C-S-H surface rather than substituted for silicon as it was thought. This adsorption was confirmed by Courault [14] and was found to be reversible [15].

3.1.2 AFt phases

The general constitutional formula is $\left[Ca_3\left(Al,Fe\right)\left(OH\right)_6.12H_2O\right]_2.X_3.yH_2O$ where X represents one formula unit of a doubly charged anion.

Ettringite $\left[Ca_3Al\left(OH\right)_6.12H_2O\right]_2.\left(SO_4\right)_3.4H_2O$ or $C_3A.3C\overline{S}.H_{32}$ is the most important AFt phases and its formation is described by the following equation [16]:

$$6\mathrm{Ca}^{2+}+2\mathrm{Al(OH)}_4^-+4\mathrm{OH}^-+3\mathrm{SO}_4^{2-}+26\mathrm{H}_2\mathrm{O}\rightarrow\mathrm{Ca}_6[\mathrm{Al(OH)}_6]_2.3\mathrm{SO}_4.26\mathrm{H}_2\mathrm{O} \qquad (3.1)$$

The solubility product of ettringite is low (K_{ett}= 4.9×10^{-44}). The nucleation rate and crystals growth depend on several parameters especially the supersaturation coefficient β. The latter is connected to the ions activities and K_{ett} by the following relationship:

$$\beta=(a_{Ca^{2+}})^6*(a_{Al(OH)_4^-})^2*(a_{SO_4^{2-}})^3*(a_{OH^-})^4/K_{ett} \qquad (3.2)$$

Precipitation can occur if $\beta>1$, indicating that the nucleation essentially depends strongly on calcium concentration in solution and the pH.
Ettringite, as hexagonal prismatic or acicular crystals, consist of four positively charged columns running parallel to the prism axis (c) between which occur channels. The anion SO_4^{2-} and water are present in the intervening channels with the $\left[\left(SO_4\right)_3.2H_2O\right]^{6-}$ composition (figure 3-2). Each column with an empirical formula $\left[Ca_3Al\left(OH\right)_6.12H_2O\right]^{3+}$ is a chain of alternating polyhedra , one of aluminium and three of calcium. A calcium atom is coordinated with four H_2O molecules and four OH^- whereas the aluminium atom is linked with six hydroxyl groups [17].

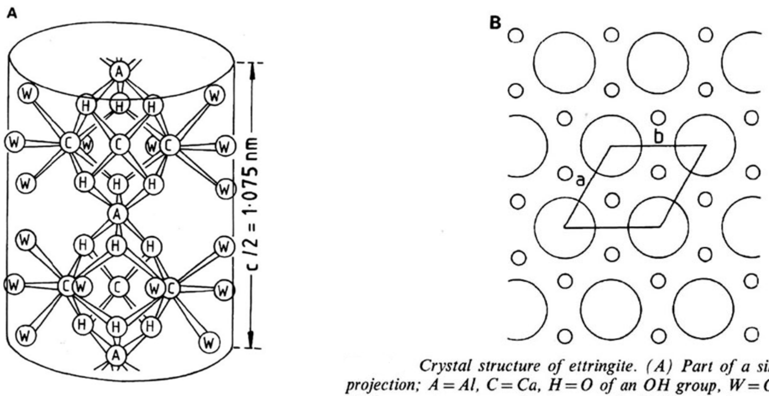

Crystal structure of ettringite. (A) Part of a single column in $(11\bar{2}0)$ projection; A = Al, C = Ca, H = O of an OH group, W = O of an H_2O molecule. Hydrogen atoms are omitted, as are the H_2O molecules attached to those calcium atoms lying in the central vertical line of the figure. (B) Projection on the ab-plane, showing columns (large circles) and channels (small circles); the unit cell, with a = 1·123 nm, is outlined.

Figure 3- 2: Crystal structure of ettringite [17]

3.1.2.1 Stability of ettringite

Its structure is well known and its stability in the CaO-Al_2O_3-SO_3-H_2O system is relatively well established up to its decomposition point at 114°C [18, 19]. The stability of ettringite has been the subject of numerous studies which reveal the importance of water molecules because of the high water content of the solid. Ettringite can undergo dehydration; recently, Zhou and Glasser [20, 21] described the decomposition of ettringite over a range of temperatures and pressures and identified different stages; in the first stage, zeolitic water was lost, the water content decreasing form 32 H_2O to 30 H_2O per formula unit. Then water molecules progressively get removed with loss of crystallinity to a final amorphous state containing 11-13 H_2O [20]. However, it is a reversible dehydration process and crystallinity can be restored on hydration. For example, at about 50%RH, 20°C, ettringite remains stable up to 90 days and then loses progressively water molecules up to a final state with 13 H_2O, figure 3-3 [21].

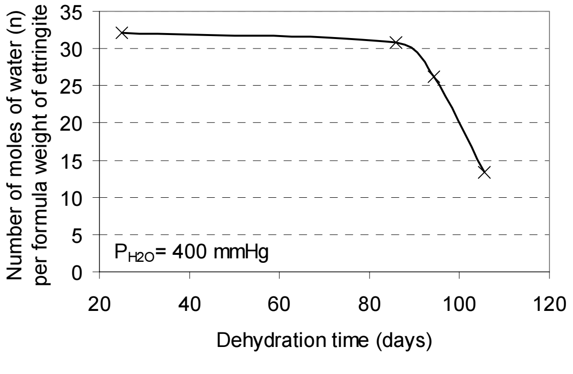

Figure 3- 3: Ettringite decomposition [21]

Ettringite also undergoes dehydration under vacuum which lead to lattice shrinkage, mainly in the *ab* plane giving a product with a=0.840 nm and c=1.020 nm. [22-24]
Between 25°C and 85°C, the range of aqueous pH's at which ettringite is stable does not vary significantly [25]:

- 25°C: $10.43<pH<12.52$
- 50°C: $10.52<pH<12.41$
- 85°C: $10.87<pH<12.25$

However, ettringite can also exist at pH values<10.5 but only in association with gypsum and Al-hydroxide [26].

3.1.2.2 Carbonate ettringite

A carbonate analogue of ettringite, $C_3A.3C\overline{C}.H_{32}$ with a similar crystalline structure is well established and the cell parameters differ sufficiently to permit distinction by XRD. Carbonate can in part replace sulfate in ettringite giving rise to a solid solution, $Ca_6Al_2[(SO_4)_{1-x}(CO_3)_x]_3(OH)_{12}.26H_2O$. Glasser [18] proposed a generalised stability diagram for ettringite-structured phases at or below 20°C, figure 3-4. Pöllmann et al.[27] showed that up to two-thirds of the SO_4^{2-} can be replaced by CO_3^{2-} and with increasing incorporation of CO_3^{2-} in the crystal lattice of sulfate ettringite, the lattice parameter c decreases (shift to higher 2θ).

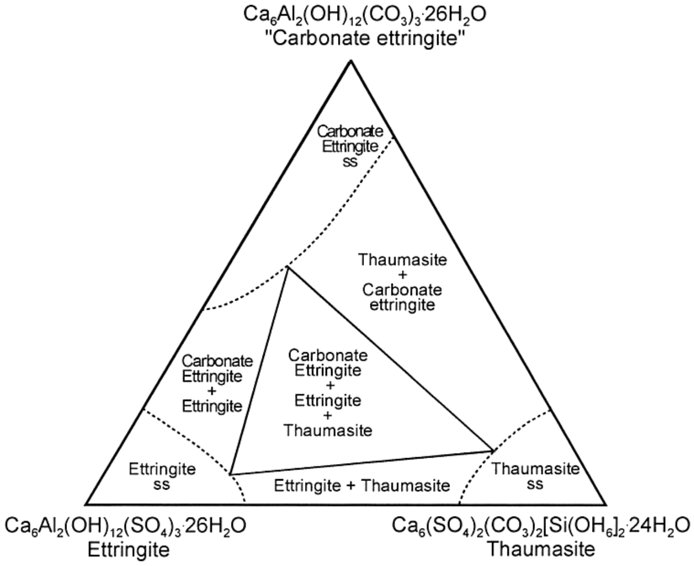

Figure 3- 4 :Generalised stability diagram for ettringite-structured phases at or below 20°C. Solid solution between ettringite and "carbonate ettringite" and between ettringite and thaumasite are known to be incomplete. Boundaries are schematic.

3.1.2.3 Fe substitution in ettringite

An analogue of ettringite with Fe^{3+} in place of Al^{3+} exists; solid solution in the Fe^{3+} - Al^{3+} series is almost continuous, there is probably a small gap at 70-80 mole % Fe^{3+} [28]. However, at high pH, Fe mobility is low which will limit actual substitution. The Fe^{3+} phase has a=1.1182nm, c=2.2008 [17] which is sufficient to be distinguished from ettringite (a=1.123nm, c=2.150nm) by XRD (shift to smaller 2θ).

3.1.3 AFm phases

The general constitutional formula is $\left[Ca_2\left(Al,Fe\right)\left(OH\right)_6\right].X.yH_2O$ where X denotes a singly charged anion or half of a doubly charged anion. Many different anions can serve as X and the most important are OH^-, SO_4^{2-} and CO_3^{2-}.

AFm phases have a layer structure derived from that of CH by the replacement of one Ca^{2+} ion in three by Al^{3+} or Fe^{3+}. This principal layer alternates with interlayer space containing anions, which balance the charge and water molecule.

The table below summarizes the main AFm phases found in cementitious materials

Formula	**Compound name**	**Interlayer anions**
$C_4A\overline{S}H_{12}$	Monosulfoaluminate	Sulfate
C_4AH_{13}	---	Hydroxyl group
$C_4A\overline{C}H_{11}$	Monocarboaluminate	Carbonate
$C_4A\overline{C}_{0.5}H_{12}$	Hemicarboaluminate	Carbonate and hydroxyl group
C_2AH_8	---	Aluminate
C_2ASH_8	Strätlingite	Aluminosilicate

Table 3- 2: Different AFm phases

Anion exchange in AFm takes place easily and consequently many solid solutions exist [29].

Calcium monosulfoaluminate is the best known hydrate in Portland hydration; its formation and supersaturation coefficient are given below:

$$4\mathrm{Ca}^{2+} + 2\mathrm{Al(OH)}_4^- + 4\mathrm{OH}^- + \mathrm{SO}_4^{2-} + 6\mathrm{H}_2\mathrm{O} \rightarrow \mathrm{Ca}_4[\mathrm{Al(OH)}_6]_2.\mathrm{SO}_4.6\mathrm{H}_2\mathrm{O} \qquad (3.3)$$

$$\beta = (a_{Ca^{2+}})^4 * (a_{Al(OH)_4^-})^2 * (a_{SO_4^{2-}}) * (a_{OH^-})^4 / K_{monosulfo} \qquad (3.4)$$

with $K_{monosulfate}$=2.9×10^{-30}; the nucleation depends mainly on the pH and the calcium ions concentration.

Damidot and Glasser [19, 25] defined the stability of hydrates in the CaO-Al_2O_3-$CaSO_4$-H_2O systems at 25, 50, 85°C by thermodynamic calculations. At 25°C, monosulfate in cement is always metastable with respect to C_3AH_6 or to ettringite (figure 3-5) but at temperature above 45°C, monosulfate becomes increasingly stable at the expense of ettringite (figure 3-6).

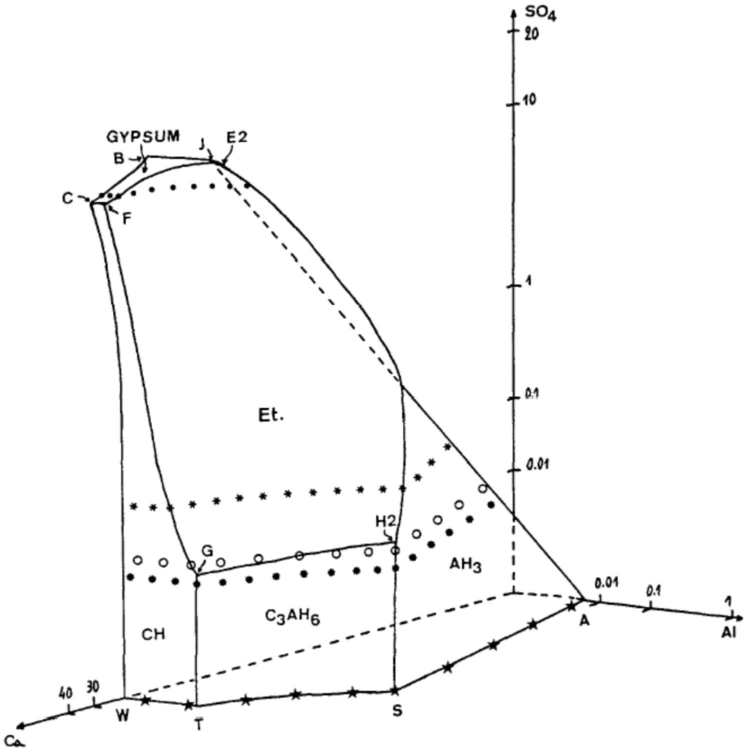

Figure 3- 5: Three dimensional representation of the CaO-Al_2O_3-$CaSO_4$-H_2O systems at 25°C [19]

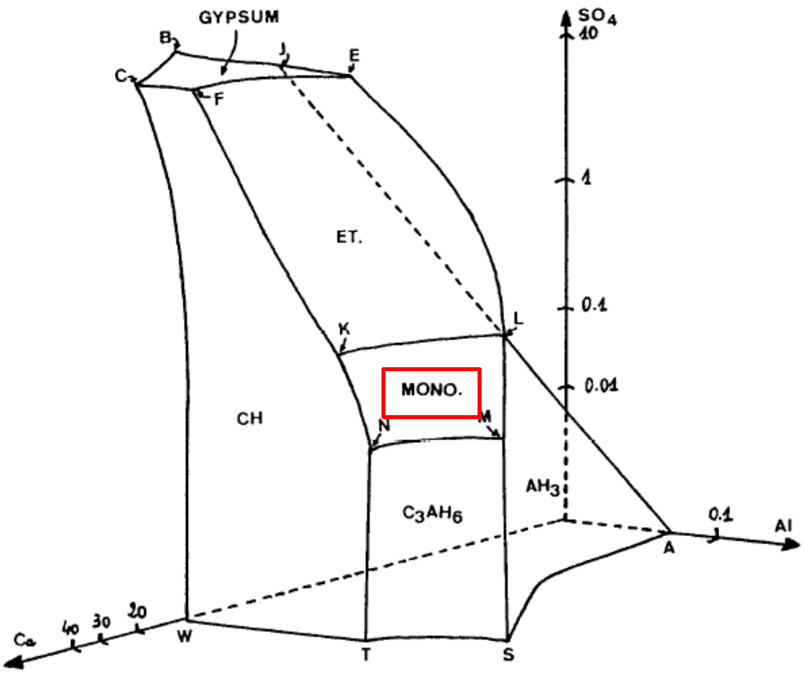

Figure 3- 6: Three dimensional representation of the CaO-Al_2O_3-$CaSO_4$-H_2O *systems at 85°C [25]*

3.1.4 Hydrogarnet phases

These phases have structures related to that of garnet containing hydroxyl in its structure in place of some silica and its formula is $C_3AS_xH_{6-2x}$. Complete replacement of Si^{4+} by $4H^+$ in garnet gives C_3AH_6 and solid solutions exist within a compositional region bounded by C_3AH_6, C_3FH_6, C_3AS_3 and C_3AF_3 [30]. Hydrogarnet phases crystallize in various cubic forms.

The stability of hydrogarnet has been investigated by thermodynamic calculations by Damidot and Glasser [31]. They distinguished three series of hydrogarnet:

- C_3AH_6: no Si
- HG Si Low: $C_3AS_xH_{6-2x}$ with $0.2<x<0.4$
- HG Si High: $C_3AS_xH_{6-2x}$ with $0.6<x<1$

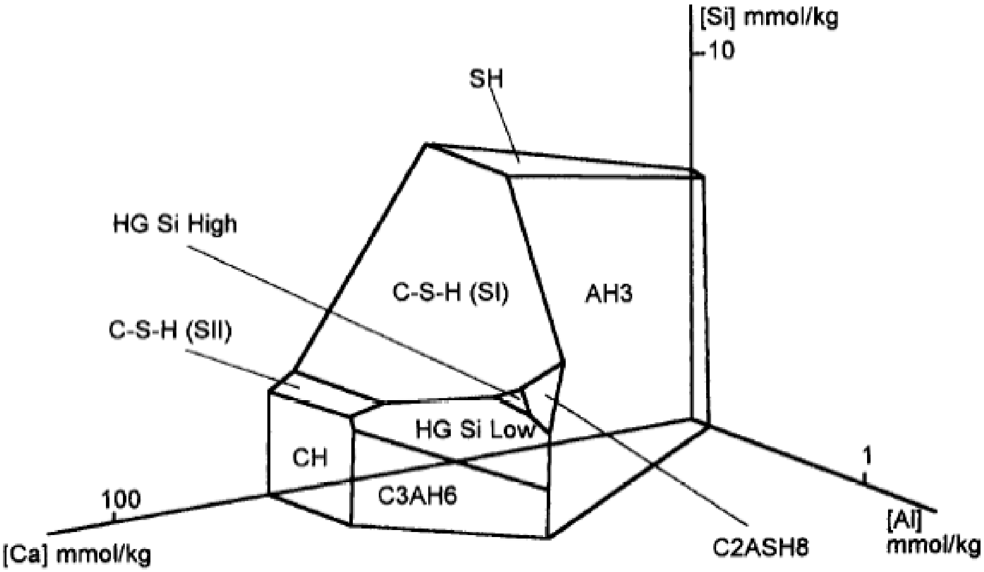

Figure 3- 7: Phase diagram of the CaO-Al_2O_3-SiO_2-H_2O system at 25°C (HG= hydrogarnet) [31].

As the content of Si in hydrogarnet increases, the cell parameter *a* decreases which can be detected by XRD, figure 3-8.

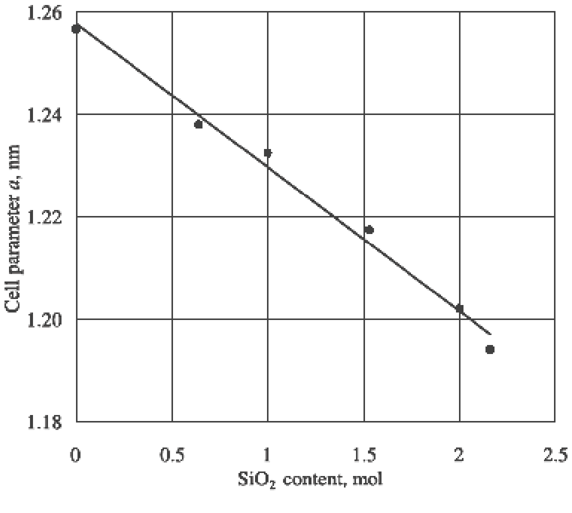

Figure 3- 8 :The lattice parameter of hydrogarnet ($C_3AS_xH_{6-2x}$) versus SiO_2 content [32]

3.2 PORTLAND AS THE MAJOR COMPONENT

3.2.1 Portland hydration

3.2.1.1 Literature survey [30, 33, 34]

The hydration of pure Portland cement is already a complex process because of the presence of different phases: calcium silicates (C_3S, C_2S), calcium aluminate (C_3A) and ferrites (C_4AF). Some gypsum is added to the clinker to avoid flash set. The mechanism leading to the stiffening of the cement paste if no calcium sulfate is available is still not clearly understood. Generally it is accepted that C_3A reacts immediately with the water to form C_4AH_{13} and C_2AH_8 (AFm phases).

In presence of gypsum, C_3A reacts with the available sulfate to form ettringite:

$$C_3A + 3C\overline{S}H_2 + 26H \rightarrow C_3A.3C\overline{S}.H_{32} \quad (3.5)$$

When there is no sulfate left, it reacts further with ettringite to form calcium monosulfate.

$$2C_3A + C_3A.3C\overline{S}.H_{32} + 4H \rightarrow 3C_3A.C\overline{S}.H_{12} \quad (3.6)$$

Instead of gypsum, other forms of calcium sulfate can be used: hemihydrate $CaSO_4,1/2H_2O$ or anhydrite $CaSO_4$. The nature of the sulfate is a key parameter due to their relative dissolution rates (dissolution rate: hemihydrate > gypsum > anhydrite). The hydrates formed at very early age will depend on the ionic concentration in the interstitial solution, as described by equations (3.2) and (3.4).

In parallel, the basic reaction for tricalcium silicates is:

$$C_3S + (3 - x + y)H \rightarrow C_xSH_y + (3 - x)CH \quad (3.7)$$

where x= Ca/Si and y=H_2O/Si.

Two categories of C-S-H are defined as inner hydration product, formed within the boundaries of the original C_3S grain, and outer hydration product forming in the initially water-filled space.

The hydration of C_2S leads to the same products but the hydration rate is slower.

Scrivener has proposed an overview of a Portland hydration as shown below:

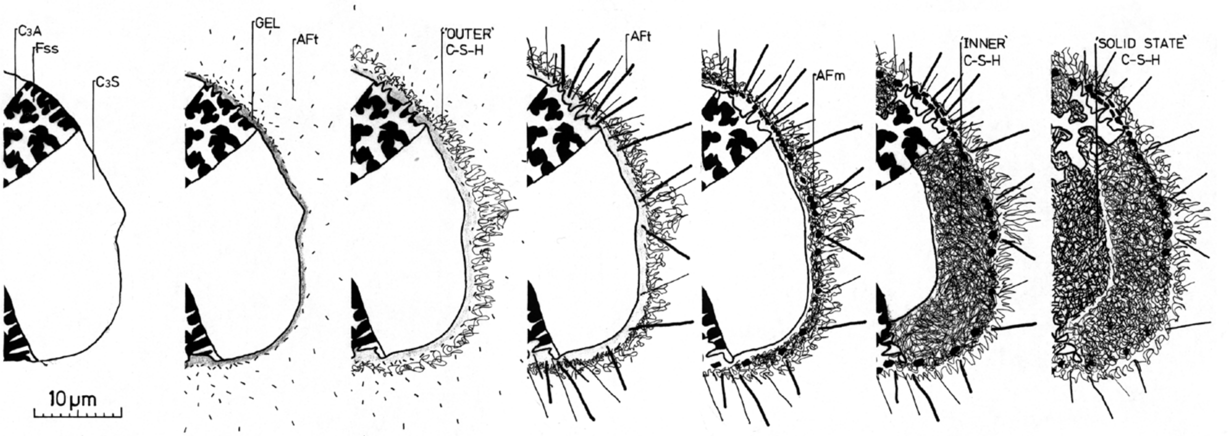

a) Unhydrated
Section of poly-mineralic grain. (scale of interstitial phase is slightly exaggerated)

b) ~10min
Some C_3A (&/or Fss) reacts with calcium sulphate in solution. Amorphous, aluminate rich gel forms on the surface and short AFt rods nucleate at edge of gel and in solution.

c) ~10hrs
Reaction of C_3S to produce 'outer' product C-S-H on AFt rod network leaving ~1µm between grain surface and hydrated shell.

d) ~18hrs
Secondary hydration of C_3A (&/or Fss) producing long rods of AFt. C-S-H 'inner' product starts to form on inside of shell from continuing hydration of C_3S.

e) 1-3days
C_3A reacts with any AFt inside shell forming hexagonal plates of AFm. Continuing formation of 'inner' product reduces separation of anhydrous grain and hydrated shell.

f) ~14days
Sufficient 'inner' C-S-H has formed to fill in the space between grain and shell. The 'outer' C-S-H has become more fibrous.

g) ~ years
The remaining anhydrous material reacts by a slow solid state mechanism, to form additional 'inner' product C-S-H. The ferrite phase appears to remain unreacted.

Figure 3- 9: Portland cement hydration [34]

The Portland hydration mechanism leads to several hydrates and the graph below summarizes the volumetric percentage of latter in the cementitious matrix for a w/c of 0.5.

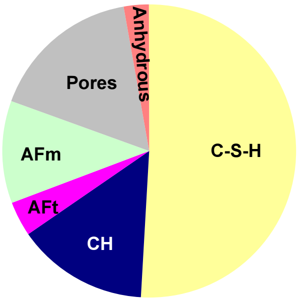

Figure 3- 10: Volumetric % of the different phases in a 14 month old Portland cement, w/c=0.5 [30]

It is worth pointing out that the hydration of a Portland cement is a dynamic system; in other words, the calcium silicates and calcium aluminates mechanisms are not independent but are subjected to interactions.

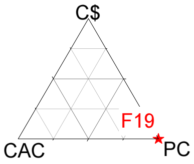

3.2.1.2 Microstructure development of plain Portland F19

This section discusses the microstructure development of the plain Portland mix, F19.

As the microstructure does not change significantly over time, only the microstructure of the 3 year old samples is shown. At 28 days, lots of anhydrous clinker remain as confirmed by the hydration degree (see 3.2.1.4). With time, the microstructure shows a depletion of anhydrous and the smallest alite grains entirely react. The hydrated layer around the belite grain is thinner than for C_3S, indicating that the hydration is slower. Large masses of portlandite are distributed in the cementitious matrix as shown on figure 3-11; CH precipitates in the initially water filled space.

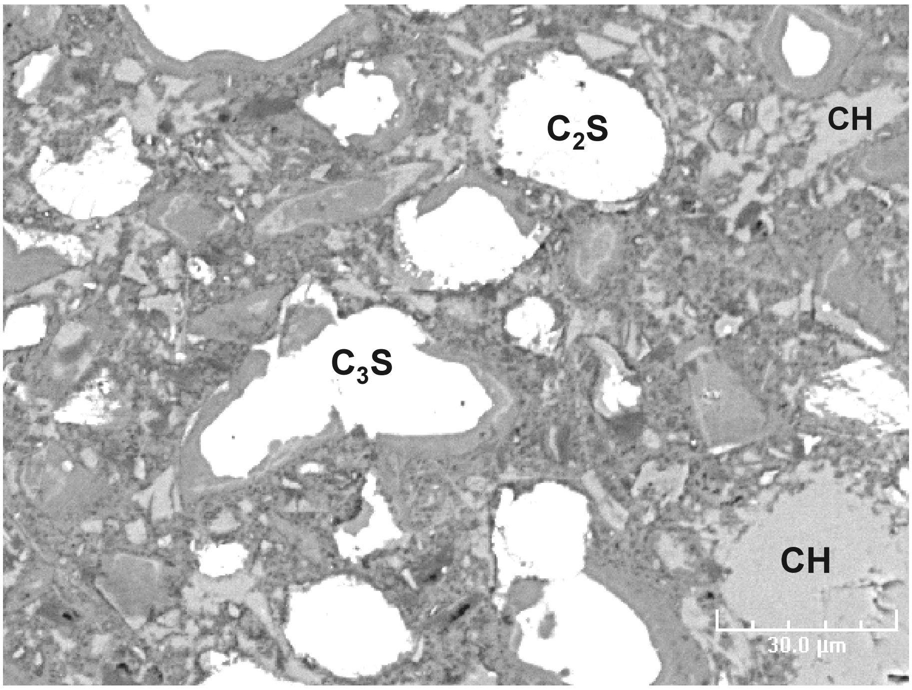

Figure 3- 11: BSE image of the bulk of F19 (Portland) - 3 years- The bright area corresponds to unreacted clinker grains, the lighter grey is portlandite whereas the darker is outer products and the porosity appears black.

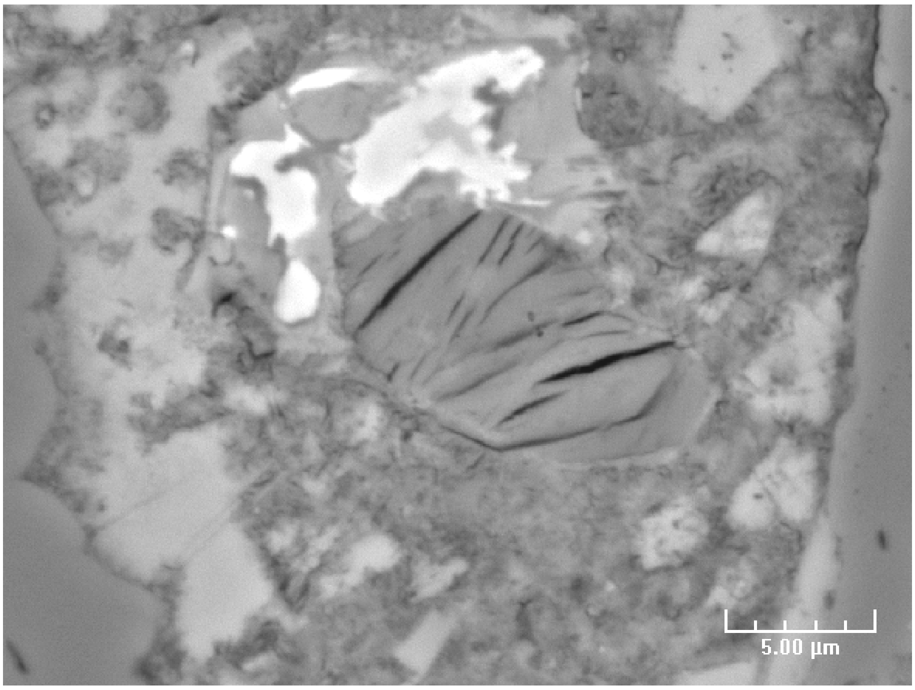

Figure 3- 12: High magnification BSE picture of F19. Monosulfate plate in the centre

3.2.1.3 EDS microanalysis

EDS microanalysis of the 28 day, 1 and 3 year old mortar were carried out to identify hydrates in the outer products. Results are shown in figures 3-13 and 3-14. It is worth pointing out that the spot analysis have not been chosen randomly; we avoided portlandite and monosulfate plates, so they are underestimated.

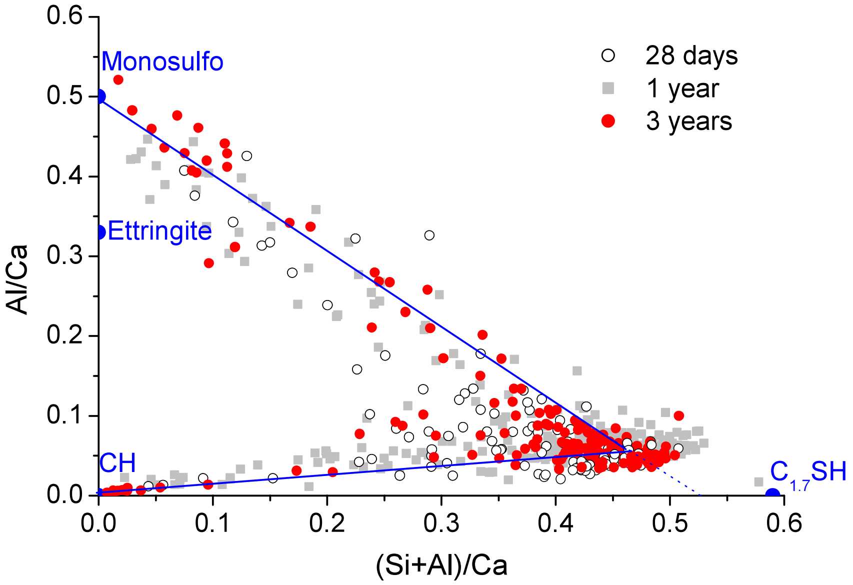

Figure 3- 13: Al/Ca atom ratio vs. (Si+Al)/Ca atom ratio. Evolution of the composition of the cementitious matrix between 28 days, 1 and 3 years of F19.

Plot of S/Ca vs. Al/Ca are useful for determining hydrates containing sulfate .

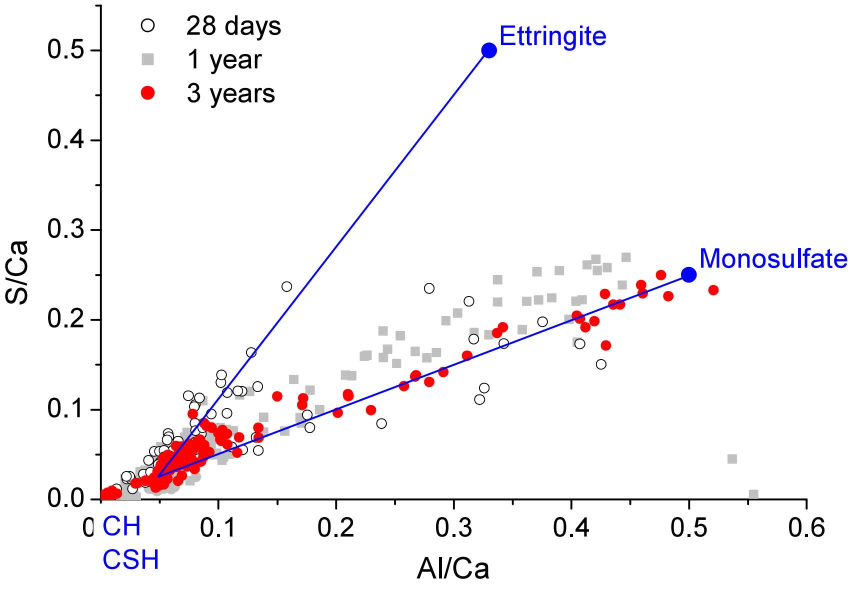

Figure 3- 14: S/Ca atom ratio vs. Al/Ca atom ratio. Evolution of the composition of the cementitious matrix between 28 days, 1 and 3 years

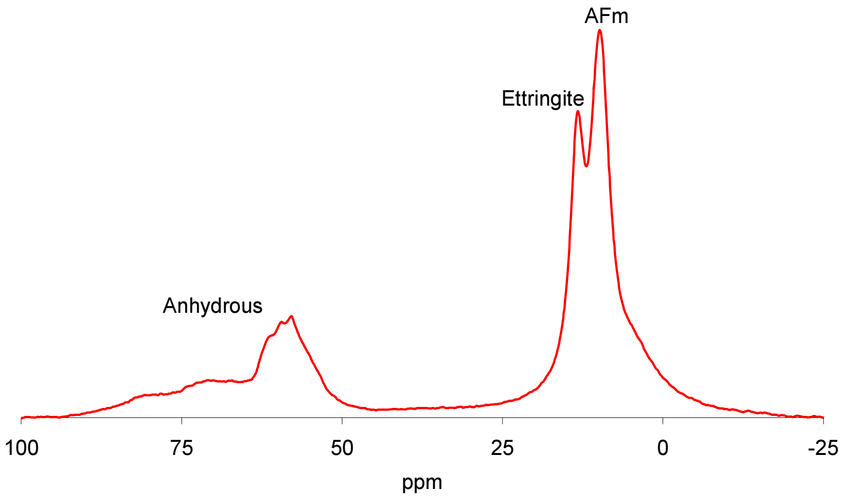

Figure 3- 15: ^{27}Al MAS NMR spectrum of the 28-days old Portland mortar.

Microanalysis in graph 3-13 points lying close to a straight line that passes through the C-S-H and CH composition mean that in addition to masses, microcrystalline CH is intermixed within outer C-S-H.

The graph 3-14 suggests that at 28 days, ettringite is embedded with C-S-H at a submicrometer level (the points follow the line S/Al=3/2 but are close to the C-S-H points) as previously reported by Scrivener [34]. Monosulfate has also been identified, meaning that some ettringite has already partially reacted with residual aluminate; this reaction is clear at 1 and 3 years. In contrast to ettringite crystals which are small and scattered in the C-S-H, some monosulfate plates are easily identifiable in the matrix (figure 3-12). The ^{27}Al MAS NMR analyses, figure 3-15, confirm the presence of ettringite and AFm phase which corresponds to monosulfate.

EDS microanalysis show that the composition of the C-S-H remains essentially constant as hydration proceeds; Richardson has already observed this characteristics by TEM in hardened Portland cement paste [9]. The Ca/Si ratios range from 2 to 2.2 which is higher than the Ca/Si ratio normally reported for cement paste, i.e. about 1.7. This could be explained by the extra calcium contained in portlandite, ettringite or monosulfate intermixed with the C-S-H. An other explanation could be the Al^{3+} substitution for Si^{4+} in the C-S-H, lowering the Si/Ca ratio. By extrapolation at Al content = 0 in graph 3-13, the mean average Ca/Si ratio is 1.9 which is closer the theoretical value.

Calcium contributions of phases intimately mix with C-S-H is consistent with Richardson's TEM study [1] which confirms a Ca/Si ratio of about 1.75. As TEM resolution is higher than that of SEM, C-S-H free of admixture with other phases can be analysed. Famy [15] also confirmed that EDS microanalysis in a TEM reflect the composition of "pure C-S-H" by comparing the Ca/Si ratio obtained by in a TEM (Ca/Si~1.9) and in a SEM (Ca/Si~2.4) for 1 day old specimens.

3.2.1.4 Hydration degree and Inner C-S-H layer

A common parameter to describe the progress of the hydration reaction is the degree of hydration ($\alpha = \frac{V^{0}_{anhydrous} - V^{t}_{anhydrous}}{V^{0}_{anhydrous}}$). The latter was measured by image analysis as described in appendix A.

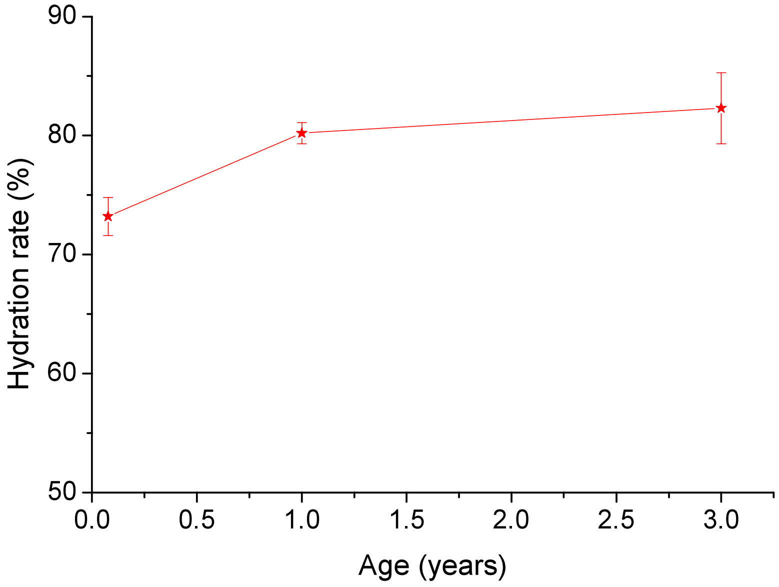

Figure 3- 16: Evolution of the degree of hydration of F19

At 28 days, more than 70% of anhydrous has been hydrated, then the hydration progresses slowly to reach 82% after 3 years.

In this chapter, we only study the interior sections (bulk) of the samples which have been exposed at different sites. In order to check the influence of the exposure place on the bulk hydration, the hydration rates have been determined for F19 and F16 exposed for one year in Japan, Florida and Germany, graph 3-17. 1-year old samples from Norway were not available.

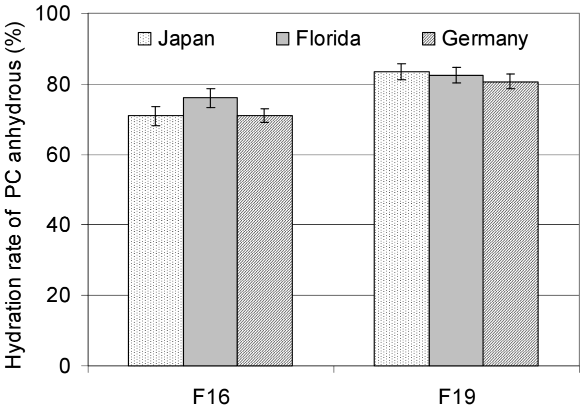

Figure 3- 17: Comparison of the 1- year hydration degree according to the exposure site

Small differences exist but within the experimental error. It is assumed that the rate of hydration for the interior of the sample is not affected by the exposure sites.

The thickness of the inner C-S-H is another aspect with which the evolution of hydration can be studied.

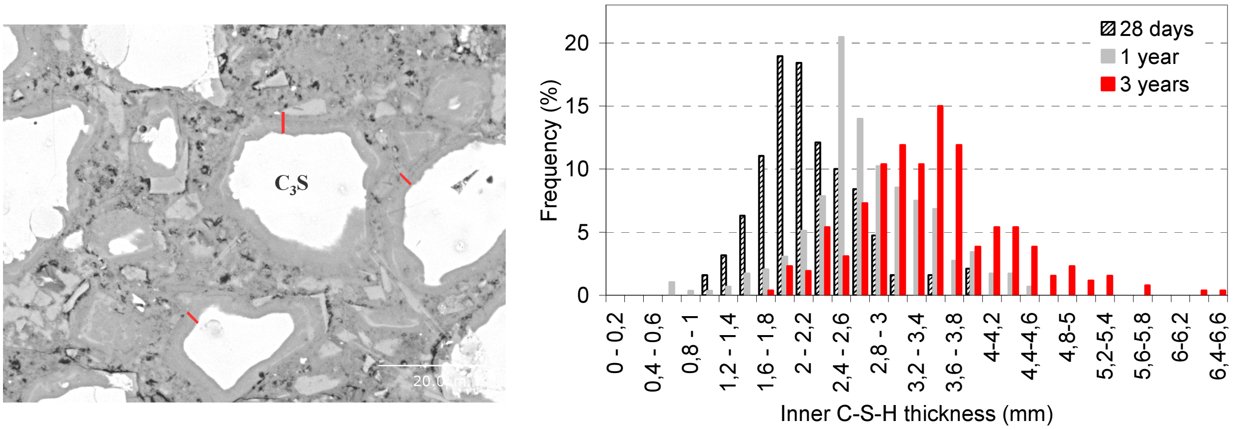

Figure 3- 18: Distribution of the inner C-S-H layers at 28 days, 1 and 3 years of plain Portland mix

It is important to notice that the thickness of inner C-S-H layer will be overestimated because the section through cement grains will generally not be equatorial, figure 3-19.

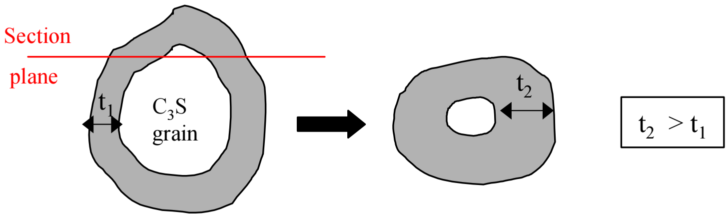

Figure 3- 19: Scheme of cut section in BSE images

The C-S-H layers were measured around the C_3S; it should be noted that the distributions vary with age. The inner C-S-H grows inward into the grain.

In conclusion, the identified hydrates and the microstructure exhibit typical features found in a Portland mortar. These data serve as a reference for the other formulations

3.2.2 Addition of Calcium Aluminate Cement (CAC) on Portland cement (PC)

3.2.2.1 Literature survey

As already mentioned in Chapter 2, the addition of CAC accelerates the setting time of Portland cement. Amathieu et al. [35] propose a mechanism of production of rapid set in PC/CAC binders. When CAC is added, the CA phase reacts with the available sulfate ions to form ettringite in the bulk of the paste rather than at the surface of C_3A grain. When sufficient CAC is added, a flash set is obtained and but it is not known if this is exclusively linked to the ettringite formation or if it results also from the C_4AH_{13} formation from C_3A whose hydration is now unblocked [36]. The amount of CAC needed to produce rapid setting depends on the nature of calcium sulfate in the Portland cement, being higher when calcium sulfate is present as gypsum or hemihydrate and lower when anhydrite is present [35, 36].

Thus, ettringite is the prime cause of setting but may not be the sole cause; there could also be contributions from simultaneous early formation of calcium aluminate phases [37].

Most studies have been focussed on the early hydration and techniques such as microwave, calorimetry and impedance measurement techniques have been used [38-42]. These reveal the complexity of the hydration mechanism. For instance, a simple complementary addition of CAC and/ or C$ can drastically modify the hydration pattern. However, authors [35, 36, 42] agree that the early hydration is dominated by the formation of ettringite, equations (3.8) and (3.9), and Gu [39, 40] confirmed the presence of ettringite needles at early ages by SEM.

$$CA + 3C\overline{S}H_x + 2C + (32-3x)H \rightarrow C_3A.3C\overline{S}.H_{32} \tag{3.8}$$

$$C_3A + 3C\overline{S}H_x + (32-3x)H \rightarrow C_3A.3C\overline{S}.H_{32} \tag{3.9}$$

The early strength is attributed to these reactions [42].

Several authors have identified the hydrates in different systems at early age as summarised here. The hydration of the pastes containing 10% CAC is expected to be similar to that of the pure PC [38, 39]. This behaviour becomes more complex when the CAC content falls within the range 15-30%. If more CAC is added, C_4AH_{13} is reported to form after the appearance of ettringite [35, 36, 43].

However, authors agree that there is a delay of Portland hydration because of the poisoning of calcium silicates reactions [35, 42]. This delay may result in poor strength but the strength development may be enhanced through addition of calcium sulfate which increases the potential amount of ettringite formation or addition of other additives.

3.2.3 Ternary binder PC/CAC/C$ (F16)

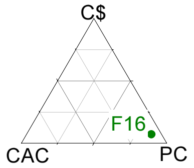

The following image shows the microstructure of F16.

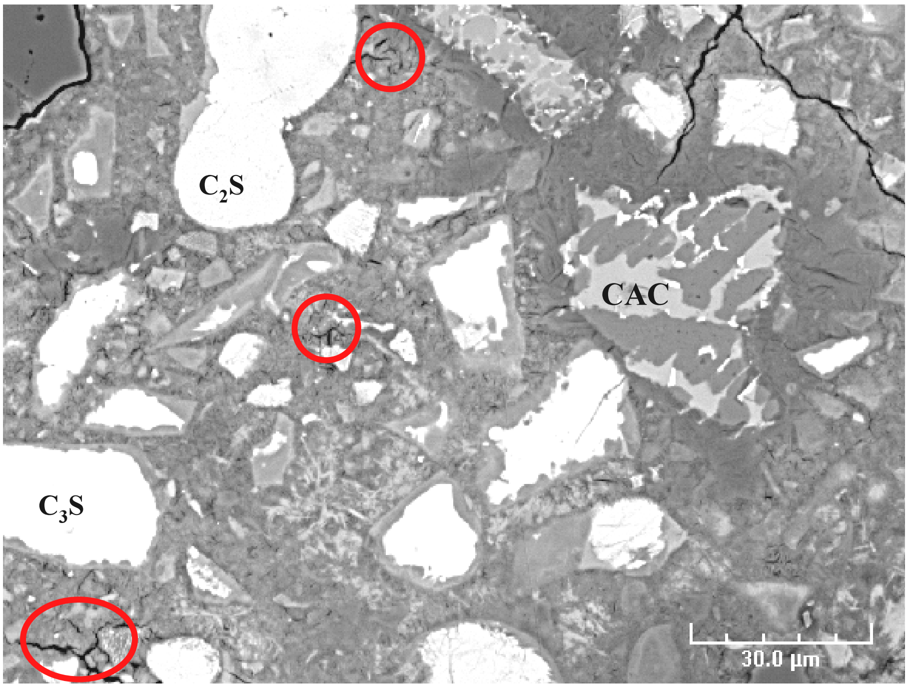

Figure 3- 20: BSE image of F16 – 3 years. Red circles indicate ettringite deposits.

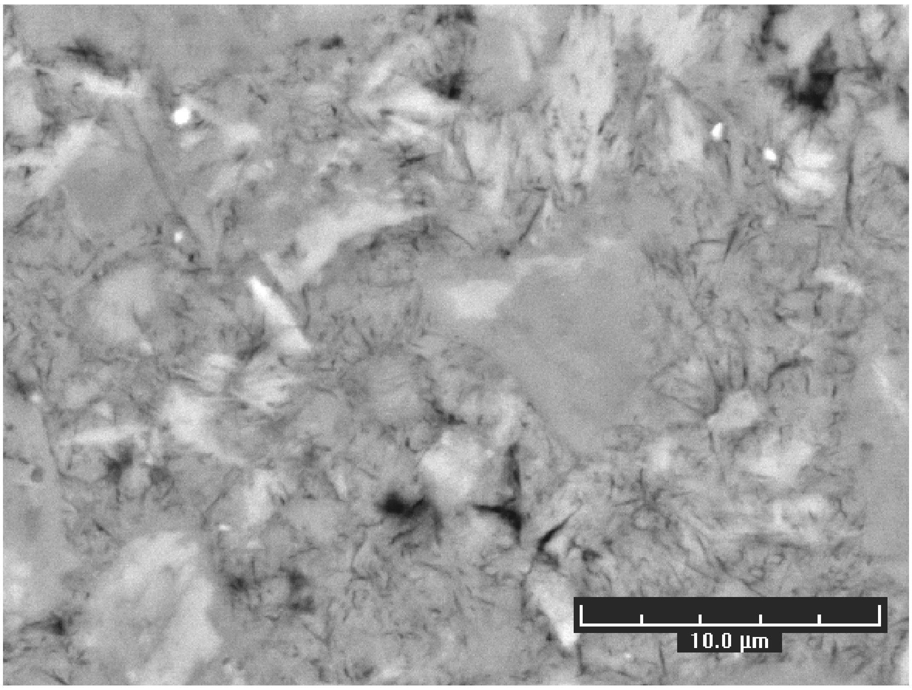

Figure 3- 21: High magnification of the matrix of F16. Portlandite appears light grey and the rest of the matrix is ettringite, monosulfate intermixed within C-S-H

The microstructure looks like that of plain Portland; clinker particles are surrounded by rims of inner C-S-H. The layer around belite grains is much thinner than that surrounding the alite grains indicating that belite hydrates slower than alite. However, at higher magnification figure 3-21, significant differences can be observed. Portlandite does not precipitate in clusters but is finely dispersed within the matrix and clear ettringite deposits are observed throughout the paste even after 3 years.

EDS microanalysis results are given in figures 3-22 and 3-23.

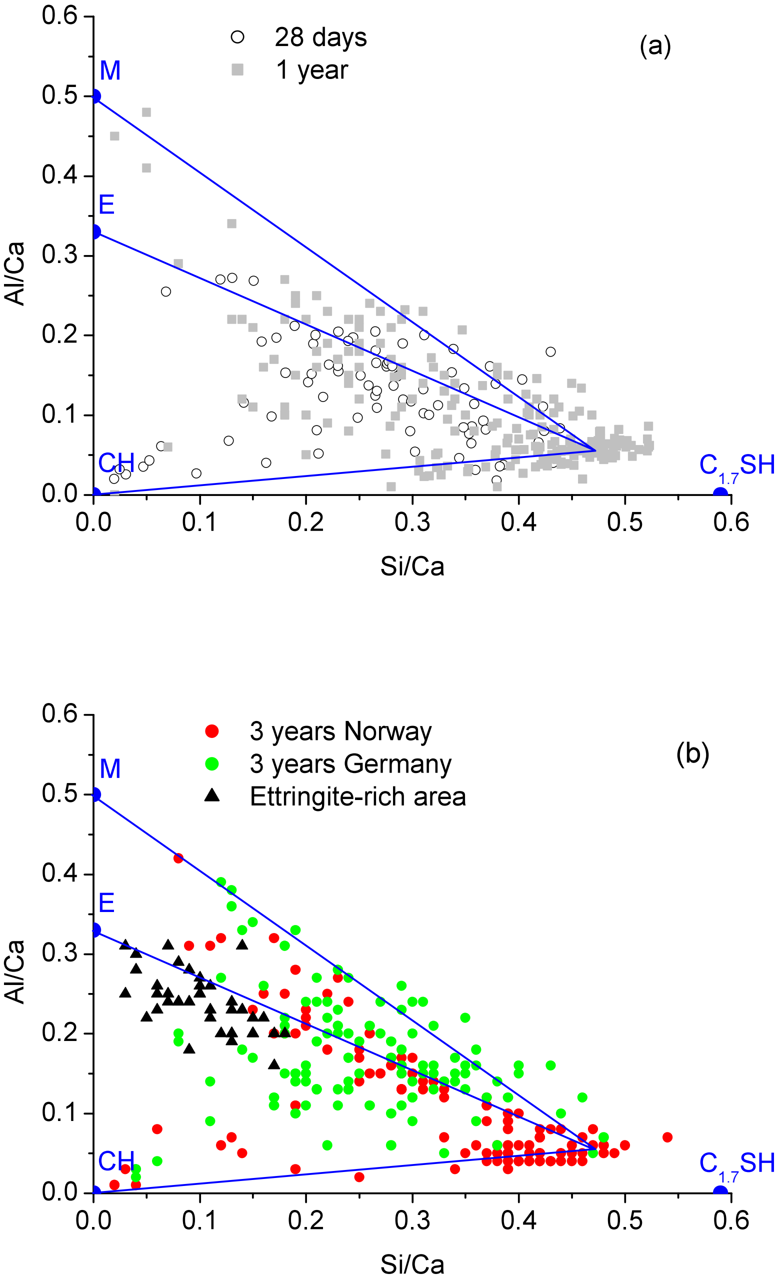

Figure 3- 22: Al/Ca atom ratios vs. Si/Ca atom ratios for the matrix of F16. .(a) Evolution between 28 days and 1 year. (b) 3 years. Comparison of 2 exposure sites and ettringite-rich area means EDS analysis close to anhydrite grain.

Due to the relatively large interaction volume contribution to the analysis in the SEM, phases intermixed at submicron scale can not be resolved by the microprobe and this leads to a scattering of the microanalysis. The high magnification of the matrix, image 3-21 illustrates this intermixing.

The C-S-H present in F16 is almost compositionally similar to that in F19; Ca/Si ratio ranges from 2 to 2.2 with a Ca/Si ratio~1.9 for no Al substitution and the content in alumina is comparable. Again, precipitation of microcrystallites of CH, ettringite or monosulfate embedded within C-S-H could explain the high content of Ca.

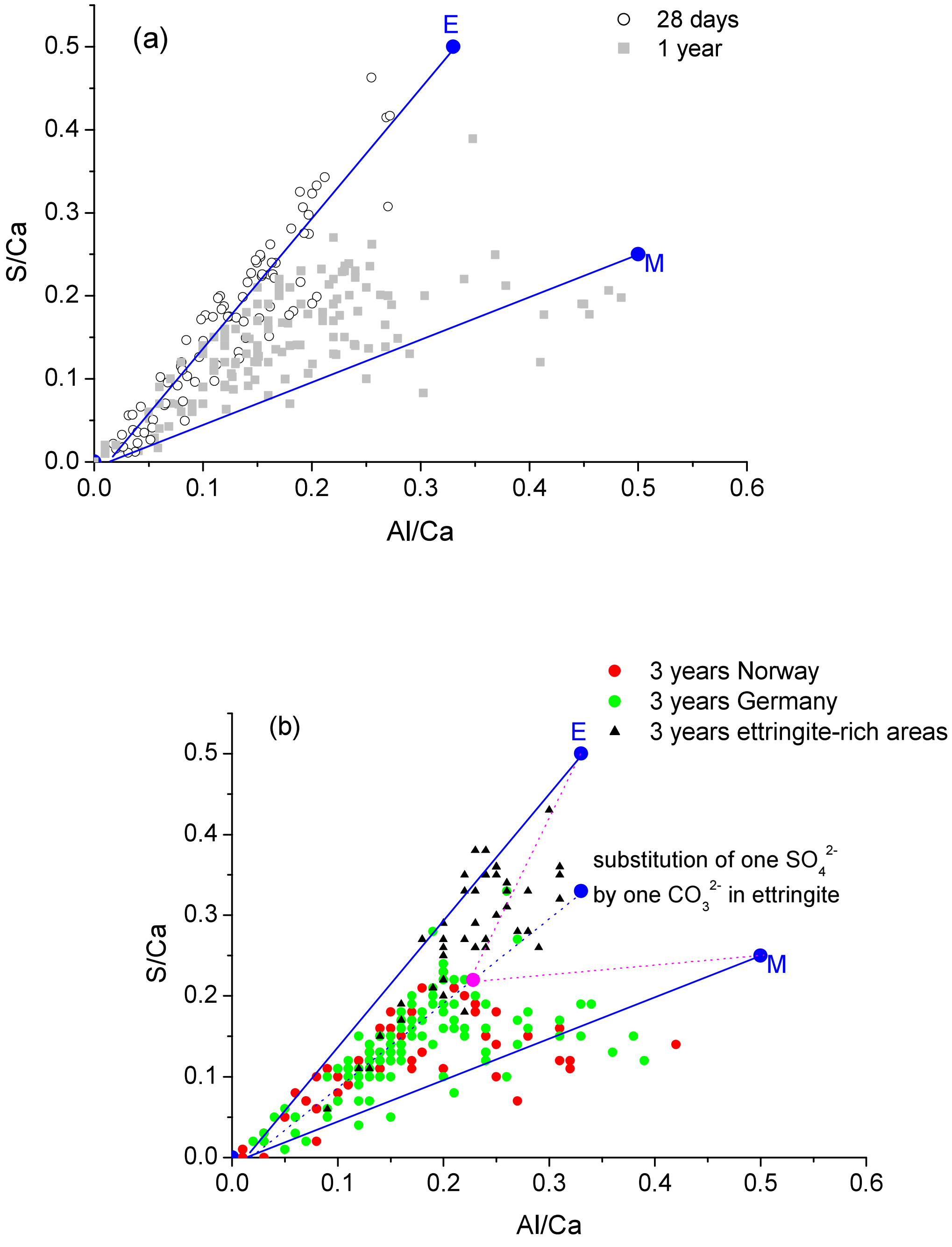

Figure 3- 23: S/Ca atom ratios vs. Al/Ca atom ratios for the matrix of F16. (a) Evolution between 28 days and 1 year. (b) 3 years. Comparison of 2 exposure sites and ettringite-rich area means EDS analysis close to anhydrite grain.

The 28-days points line almost exactly along a tie line connecting the C-S-H gel composition to the ettringite composition. The early hydration is dominated by the formation of extra ettringite compared to Portland. NMR results (figure 3-25) confirms the formation of ettringite but also reveals the presence of AFm. It could be monosulfate which surrounded CAC grains as discussed latter.

At 1 and 3 years, the points have shifted towards the line connecting C-S-H and monosulfate. Two hypotheses could be expressed:

① Ettringite partially further reacted into monosulfate and the scattering of points indicates that the microanalyses relate to C-S-H intermixed on a sub micrometer scale with ettringite and monosulfate. Indeed, if we consider the centre gravity of the triangle C-S-H, E and M on the graph 3-23(b) (pink point), EDS analysis fit well with the hypothesis of a mix of these three phases. XRD pattern, figure 3-24, confirm the presence of ettringite whatever the age while almost no monosulfate was detected. This latter is probably poorly crystalline; its low degree of crystallinity is well recognized [44, 45]. The formation of monosulfate is expected because in this formulation sulfate is depleted ($n_{C\overline{S}} / n_{CA} < 3$ cf. equation (3.8)).

② The other assumption to explain this shift is the partial replacement of sulfate by carbonate. Pöllmann [27] showed that the maximum extent of carbonate substitution is 2/3; on graph 3-23(b), a "virtual" point corresponding to a substitution of one SO_4^{2-} by CO_3^{2-} is plotted and the EDS analysis are rather consistent with this assumption but the latter is not detected by XRD, figure 3-24. According to Pöllmann a change in lattice parameter occurs with the substitution leading to a peak shift to higher 2θ, such a shift was not observed by XRD here.

Therefore the first hypothesis seems to be the most likely.

Nevertheless, whereas there is no shift peak to higher 2θ corresponding to a "carbonate ettringite", ettringite presents a double peak with a shift to smaller 2θ. This left shift means that the unit cell became larger and several assumptions were considered:

① Iron substitution: as already reported in section 3.1.2.3, Fe^{3+} substitution in place of Al^{3+} leads to a shift to smaller 2θ but, after checking with EDS analysis, no iron was detected.

②In the same way, ettringite may undergo other incorporations of elements into its crystal structure such as titanium, chromium or chlorine. EDS results did not confirm this hypothesis.

③The presence of solid solution with thaumasite. Ettringite can tolerate the replacement of ½ its Al by Si [46, 47] leading to a decrease of the unit cells (a=1.105 nm , c=1.041 nm), thus a shift to higher 2θ.

④Changes in crystal structure of ettringite due to dehydration. As already mentioned in 3.1.2.1, a lattice shrinkage occurs leading to a shift to higher 2θ and not to smaller 2θ.

Therefore, no relevant assumption has been found to explain this double peak of ettringite.

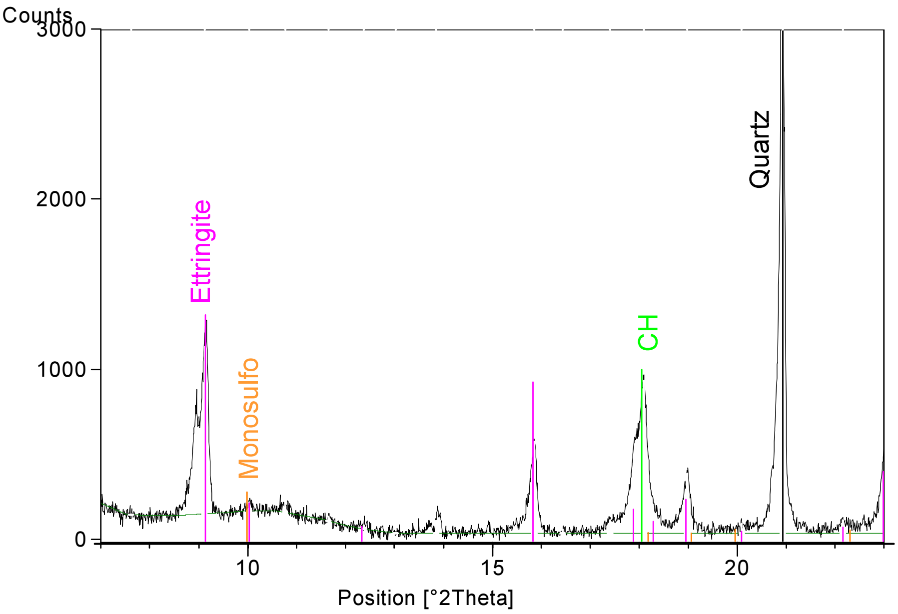

Figure 3- 24: XRD diffractogram of F16 - 3 years

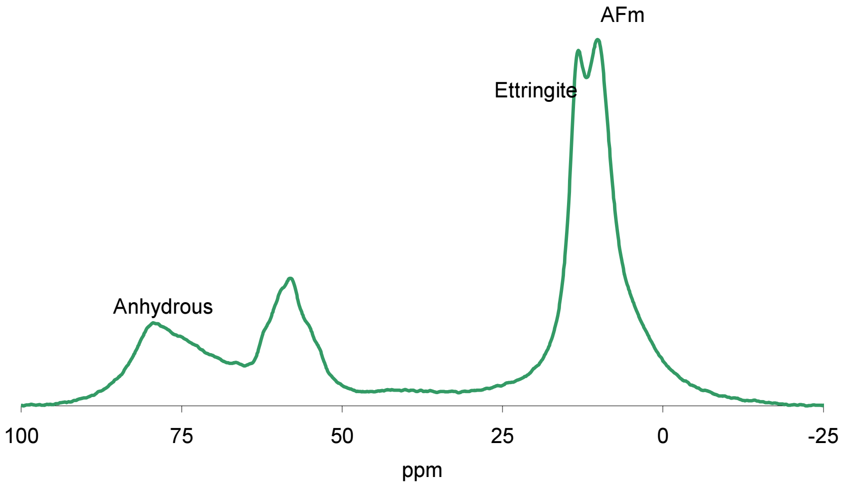

Figure 3- 25: ^{27}Al MAS NMR spectra of the 28-days old F16.

A focus on the evolution of CAC grains and their surrounding exhibits interesting features, image 3-26.

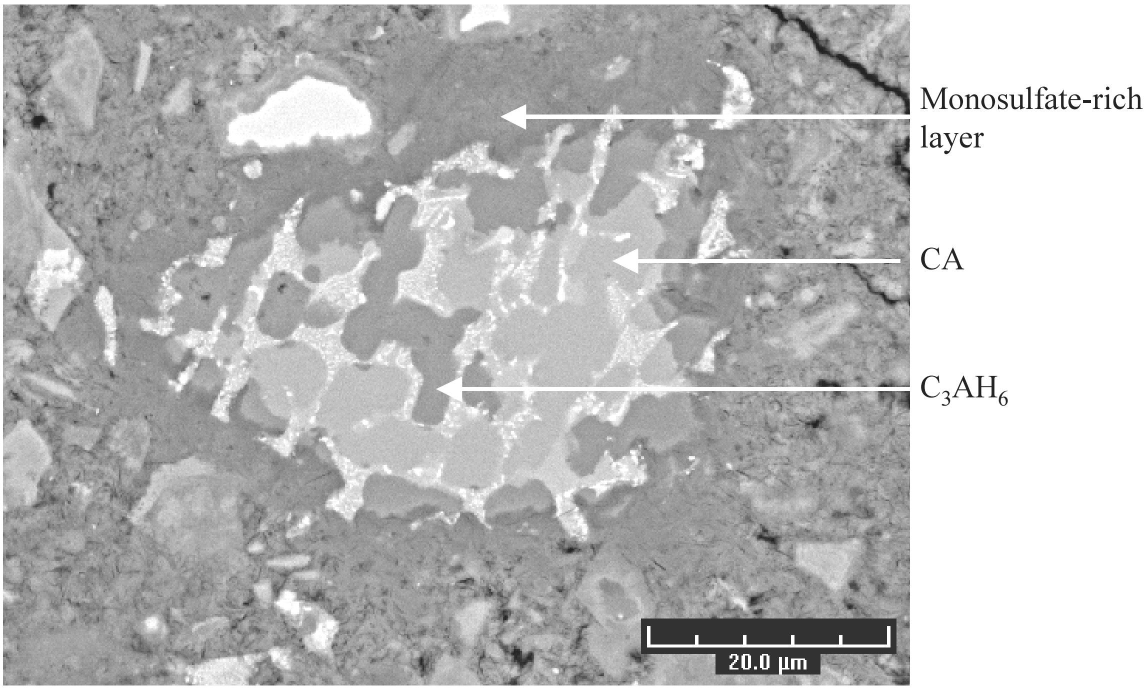

Figure 3- 26: BSE image of F16. Zoom on a polymineralic CAC grain, partially hydrated.

The area around aluminous grains is different and EDS analysis indicate that the phase is rich in monosulfate. The ettringite close to the CAC grains becomes locally the new source of sulphur and the reaction below can take place:

$$6CA + C_3A.3C\overline{S}.H_{32} + 16H \rightarrow 3C_3A.C\overline{S}.H_{12} + 4AH_3 \qquad (3.10)$$

Whereas the CAC grain is surrounded by a monosulfate rich phase, in the core of the CAC grain, the CA has been replaced by a inner product whose the composition corresponded to hydrogarnet, equation (3.11). The absence of this phase in XRD could be explain by the fact that C_3AH_6 is a minor hydrate and in the crushed sample rich in sand the amount could be under the detection limit.

$$CA + 2C + 6H \rightarrow C_3AH_6 \qquad (3.11)$$

3.2.3.1 Hydration degree and Inner C-S-H layer

As for Portland mortar, the hydration rate and the evolution of the inner C-S-H thickness have been measured.

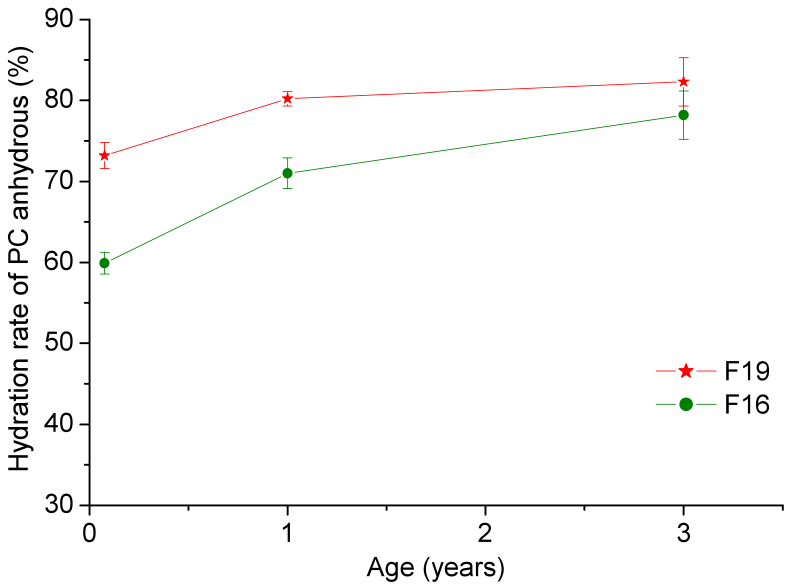

Figure 3- 27: Hydration degree of Portland anhydrous measured by BSE-IA for the mix F16 and F19

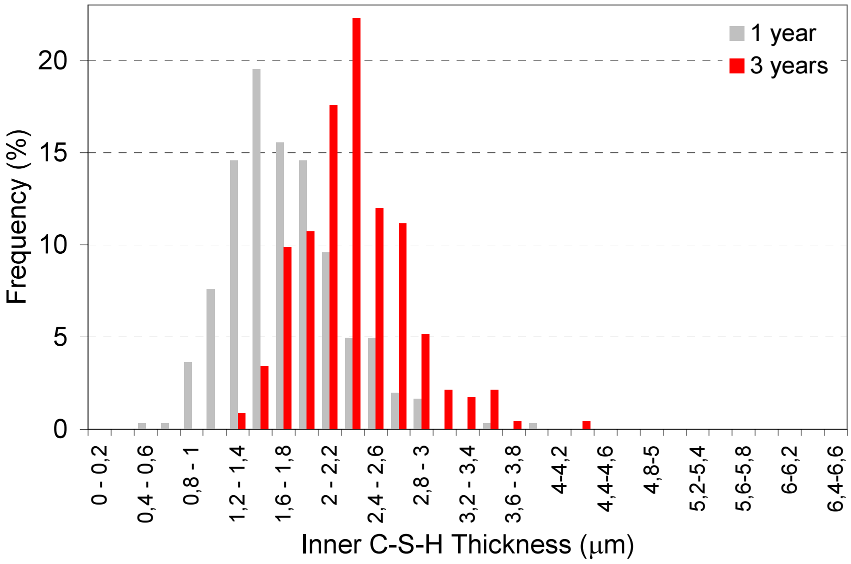

Figure 3- 28: Distribution of Inner C-S-H layers at 1 and 3 years of F16

At 28 days, only very little inner C-S-H has started to form around C_3S although some outer C-S-H has precipitated throughout the matrix, so no thickness could be measured. At 1 and 3 years, the inner C-S-H layers remain thinner than those in Portland. These results are coherent with the hydration degree of Portland anhydrous.

The degree of hydration is lower for F16 than for pure Portland at 28 days but the difference is reduced with time to end up at similar values after 3 years. The delay of silicate hydration has been previously reported [35, 42]; authors suggest to state that the origin of this delay is a diffusion barrier layer around anhydrous grains but reason for this is still discussed. We considered several hypotheses.

① The slowing down of the dissolution of silicates. The calculated solubility of C_3S is about 1 $mol.l^{-1}$ [49]. In the absence of barrier layer, the ”blocking” of silicates hydration could be explained only if the concentrations close to C_3S surface were of this order of magnitude. Stein found that bulk concentrations in the aqueous solution in C_3S + water systems are too low to make this solution saturated towards C_3S. It is doubtful whether the very high concentration gradients that implies could exist [50].

② A difference of the density of the inner C-S-H rims. As we observed, the C-S-H is product of variable composition, particularly in terms of the Ca/Si ratio. Variations may also occur in the degree of porosity. Both these factors affect the grey level in BSE images. As the average Ca/Si ratio of inner C-S-H is similar for F16 and F19, difference of grey level in BSE images will result in a difference of density (C-S-H with lower microporosity has a lighter appearance). Therefore, we compared the relative grey level of inner C-S-H of F19 and F16. The procedure is based on the histogram segmentation with sand and C_3S as references of the grey level. In a BSE picture, we selected manually sand, C_3S and inner C-S-H and we obtained the histogram graph 3-29. For both F19 and F16 the B/A ratio was calculated leading to a similar value 0.37.

As there is no difference between the B/A ratio, both inner C-S-H have the same density therefore this hypothesis is not plausible.

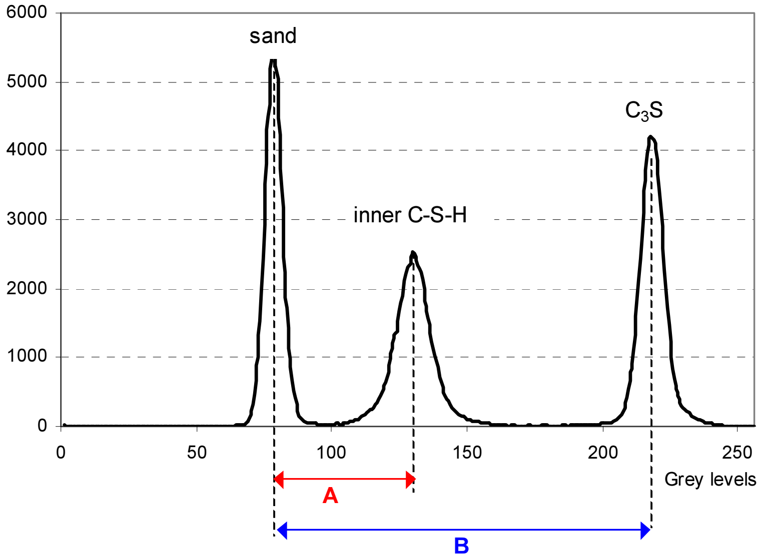

Figure 3- 29: Histogram of F19- 3 years

③ Variation of C-S-H growth. It is suggested by Minard [48] that the delay of silicates hydration is attributed to the variation in C-S-H growth which depends on the calcium concentration in the solution. If the concentration is low, lots of nucleation sites are created and the parallel rate of C-S-H growth around the anhydrous grain is widely favoured, thus the anhydrous grain surface is covered more quickly. The hydration then shifts to diffusion limited control earlier.

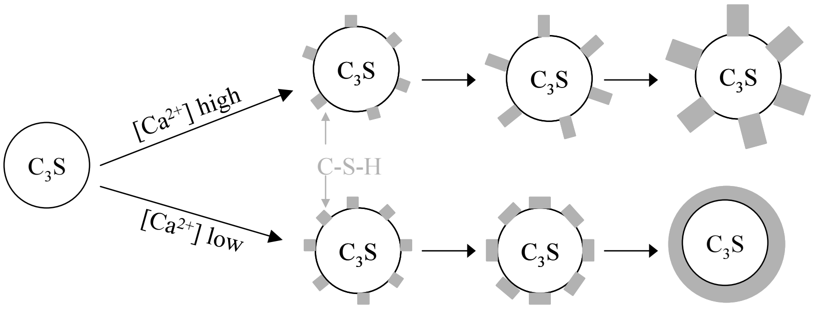

Figure 3- 30: Model of C-S-H growth

This hypothesis is not very probable because at 28 days, the rims of inner C-S-H around C_3S are very thin. Afterwards, we will see that although F21 and F15 have no inner C-S-H (section 3.2.4 and 3.2.5), the hydration of silicates was delayed; this evidence excludes this hypothesis.

④ A direct poisoning of the silicates surface. Sulfates or aluminates may play a role. The nature of the poisoning is still discussed.

3.2.3.2 Quantification

The impact of CAC and C$ on the hydration of Portland may also be assessed by the content of portlandite in the hardened cement paste. The quantification of CH is done by thermogravimetric analysis TGA; all experiments were carried out at a heating rate of 10°C.min^{-1} and in a nitrogen atmosphere.

The deshydroxylation of $Ca(OH)_2$ takes place between 400 and 600°C [51]:

$$Ca(OH)_2 \rightarrow CaO + H_2O \qquad (3.12)$$

Then the following equation is used to determine the calcium hydroxide content α_{CH} :

$$\alpha_{CH} = \frac{M_{CH}}{M_{H_2O}} \frac{\Delta M_{CH}}{M_{dry}} \qquad (3.13)$$

where M_{CH} and M_{H2O} correspond to the molar weights of calcium hydroxide and water respectively, ΔM_{CH} the weight loss recording by TGA analysis for CH.

α_{CH} (% weight)	F19	F16
28 days	12.3	5.1
1 year	15.8	6.3
3 years	17.2	10.8

Table 3- 3: Portlandite content measured by TGA in F16 and F19

The extra calcium supplied by the congruent dissolution of C_3S precipitates in CH in plain Portland but in F16, this calcium is consumed to form ettringite (equation 3.8) to the detriment of portlandite. Thus the content of CH is lower in the ternary binder than in Portland.

By assuming a Ca/Si ratio of 2 for the C-S-H (mean ratio found in EDS) and C_3S hydration degree is the overall hydration degree, the amount of calcium which participates in the formation of ettringite was calculated (in moles):

$$C_3S + 5H \rightarrow C_2SH + CH \tag{3.14}$$

t=0 0.172 -- --

t=28 days 0.069 0.103 if no consumption by ettringite

0.067 experimental (TGA)

Thus, 0.036 mole of C_3S ($n_{CH} = n_{C_3S}$) participated in ettringite formation which represents about 35% of that formed from the reacted C_3S. Then, we can deduce the amount of CA reacted with equation (3.8):

$$n_{CA} = \frac{n_{CH}}{2} = 0.018 moles \tag{3.15}$$

which corresponds to 85% of the initial mole of CA.

This degree of reaction seems to be overestimated because in BSE image, figure 3-20, there remains a non negligible amount of CA. The first uncertainty is the chosen Ca/Si ratio and the second error may come from the quantification of portlandite by TGA; the amount of CH could have been underestimated due to a possible carbonation.

3.2.4 Ternary binder (F21)

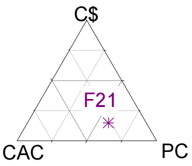

In order to see what happens for hydration mechanism when more aluminous cement and calcium sulfate are added, the binder F21 was studied.

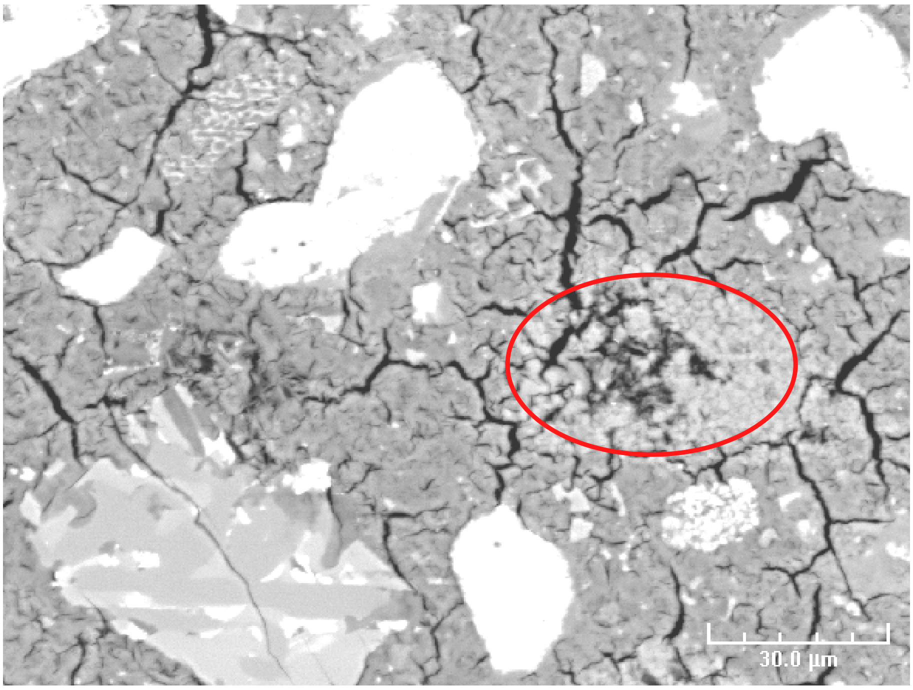

Figure 3- 31: BSE image of F21 – 3 years. The circle is CH and it is surrounded by an ettringite-rich area.

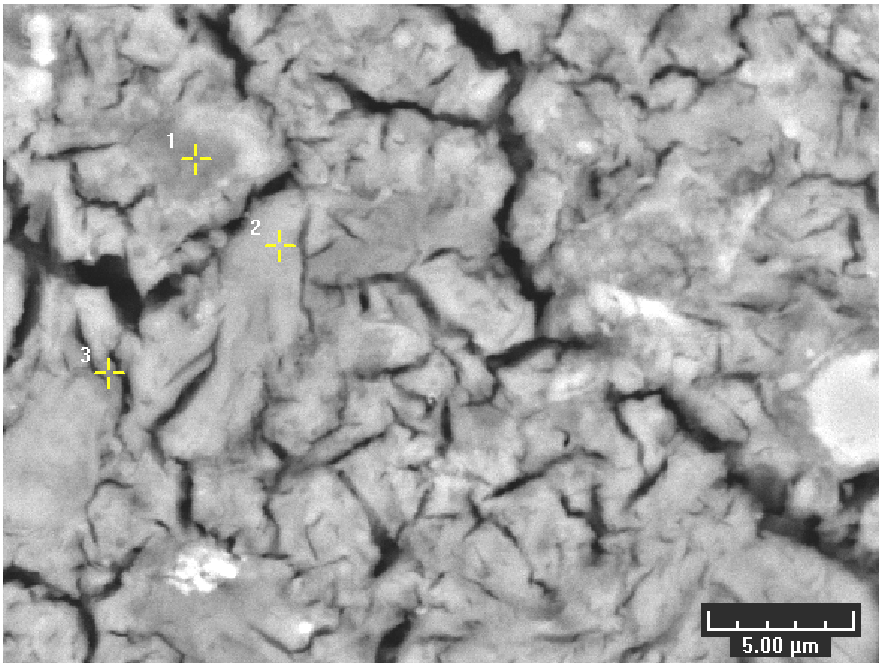

Figure 3- 32: High magnification of the matrix of F21

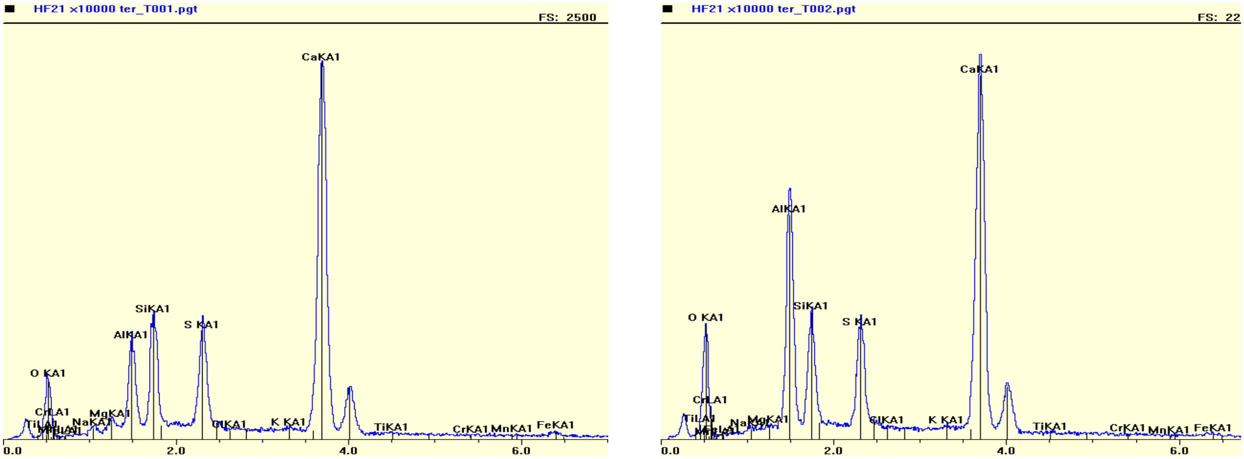
Point 1

Point 2

Point 3: ettringite

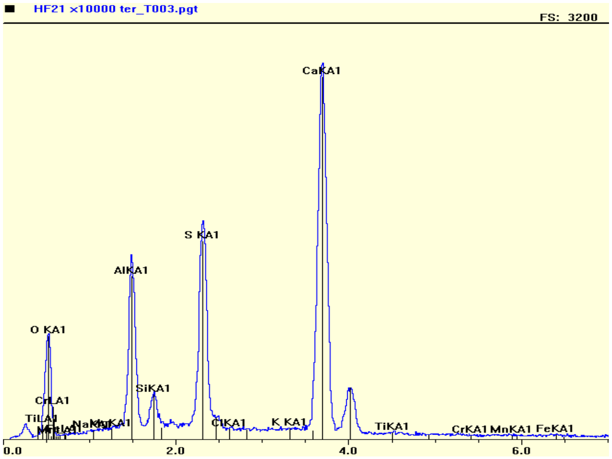

Figure 3- 33: EDS micronalysis

The microstructure displays completely different features compared to F19 and F16. The hydration of silicates are disturbed by the high content of CAC and C$. Whatever the hydration time, no inner C-S-H developed around silicate grains and only few outer C-S-H are analysed throughout the matrix, as shown by the graphs below.

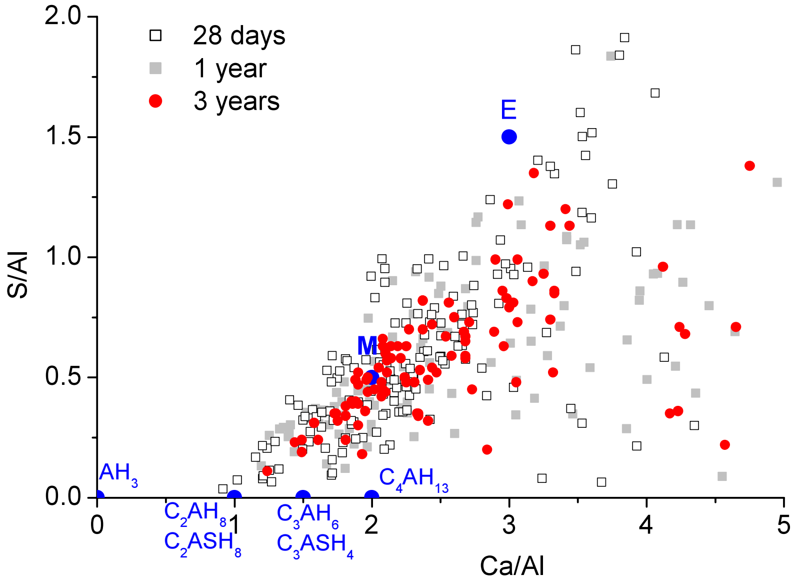

Figure 3- 34: S/Al atom ratios vs. Ca/Al atom ratios for the matrix of F21

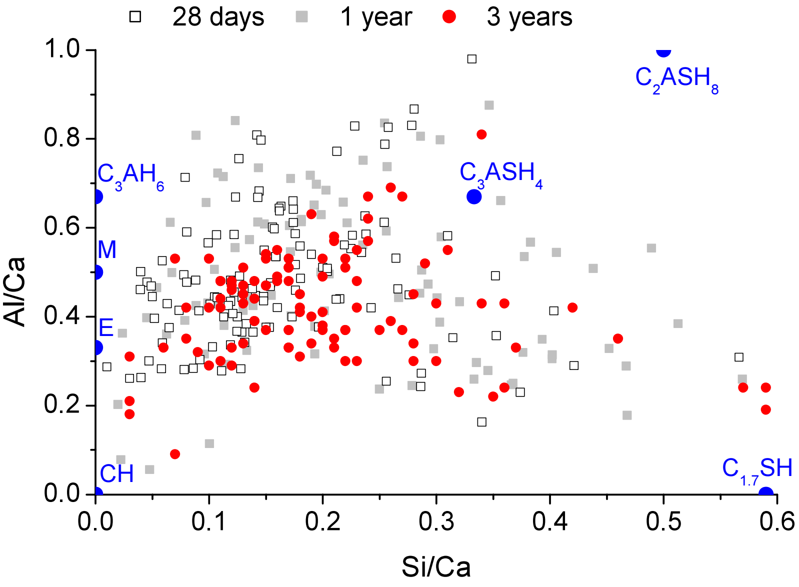

Figure 3- 35: Al/Ca atom ratios vs. Si/Ca atom ratios for the matrix of F21

The large scattering of the microanalysis points for the outer products indicates that there is a highly variable degree of phases intermixing. BSE image figure (3-32) with corresponding EDS analysis (figure 3-33) highlight the phases intermixing; several grey levels are identified but each grey level corresponds to a mix of Ca, Al, Si, S in different proportions.

No significant evolution in the nature of hydrates is noticed over time. The combination with XRD and NMR spectra are useful to identify these hydrates.

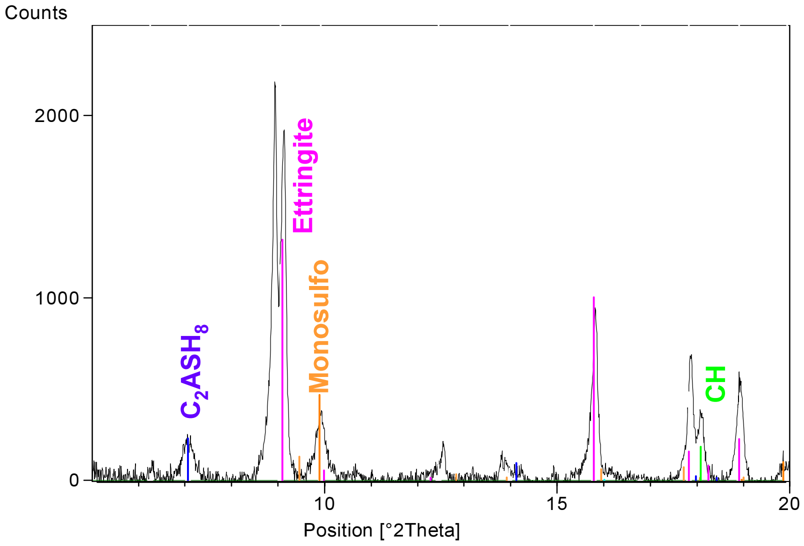

Figure 3- 36: XRD spectrum of the bulk of F21 – 3 years

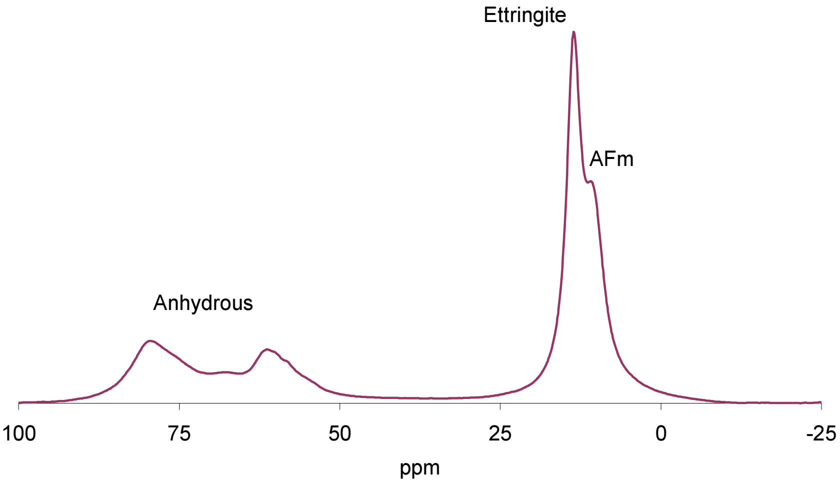

Figure 3- 37: ^{27}Al NMR spectra of F21 – 28 days

The matrix contains ettringite (point 3 graph 3-33) which is confirmed by XRD and NMR. NMR also reveals the presence of AFm phases which are found to be monosulfate and strätlingite by XRD. The double peak of ettringite in XRD has already been discussed, see section 3.2.3 An other crystalline phase, portlandite is found which is not intermixed within the outer products but seems to have precipitated in the place originally filled with anhydrite, figure 3-31. The dissolution- precipitation process could explain this: the solubility product of anhydrite is high so the limit of the solubility is never achieved. The anhydrite continuously dissolved into Ca^{2+} and SO_4^{2-} which migrate by diffusion throughout the matrix. As the interstitial solution was saturated with calcium, supersaturation with respect to CH is achieved and the former thus precipitates in the free space left by the anhydrite.

The EDS microanalysis are consistent with XRD results; ettringite and AFm phases, i.e. monosulfate and strätlingite, are finely intermixed. Silicates are found in strätlingite and in less extent in outer C-S-H. In this binder, sulfates are in deficit ($n_{C\bar{S}} / n_{CA} < 3$, Eq. (3.8)) therefore, ettringite becomes the new source of sulphur and reacts further with residual CA to form monosulfate.

As only few C-S-H and CH are detected in the matrix, it is interesting to estimate the hydration degree of Portland anhydrous, figure 3-38.

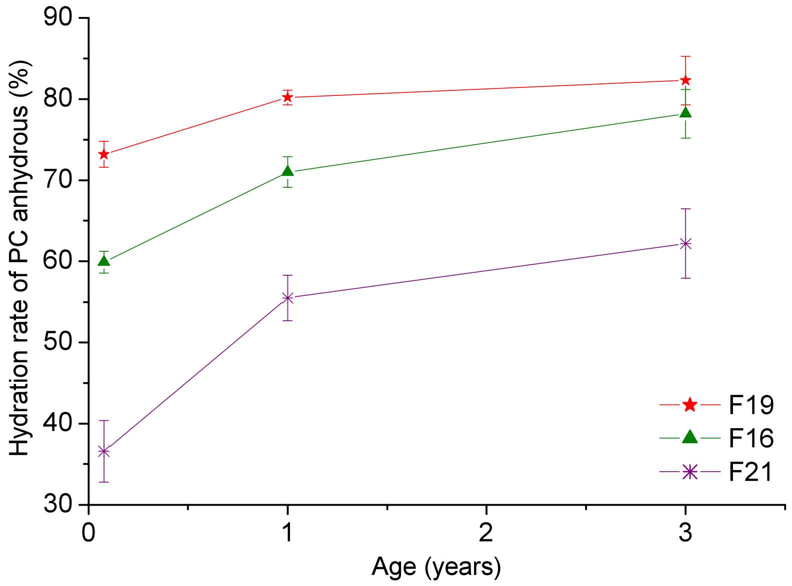

Figure 3- 38:Hydration degree of Portland anhydrous measured by BSE-IA for the mixes F19, 16 and 21

The classical hydration of silicates is disturbed by the aluminates; at 28 days, the degree of hydration of F21 was very low and contrary to F16, it did not end up to similar value as F19 over time. The hypothesis of the variation in C-S-H growth around C_3S grains to explain the “blocking” of silicates hydration (see section 3.2.3.1) is not consistent with the fact that F21 has no inner C-S-H.

3.2.5 Binary binder PC/CAC (F15)

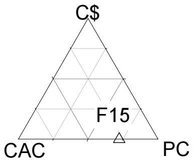

In this formulation 30% of Portland has been replaced by CAC.

The images of the samples displays a non-homogenous cementitious matrix; very porous layers alternate with dense layers as shown in pictures 3-39 and 3-40. This heterogeneity may result from a problem of mixing and casting.

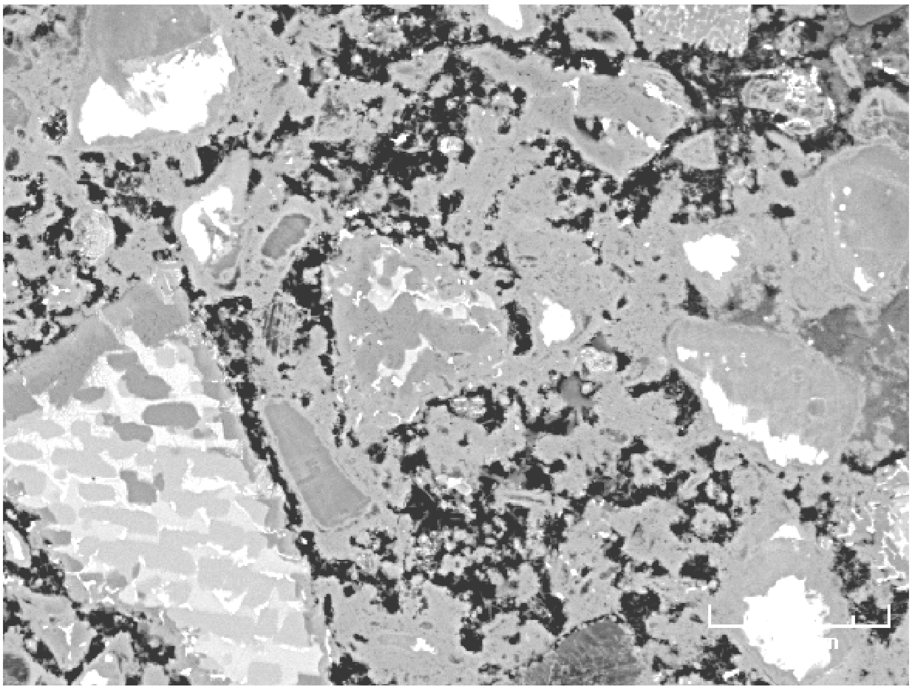

Figure 3- 39: BSE image of F15. Porous region

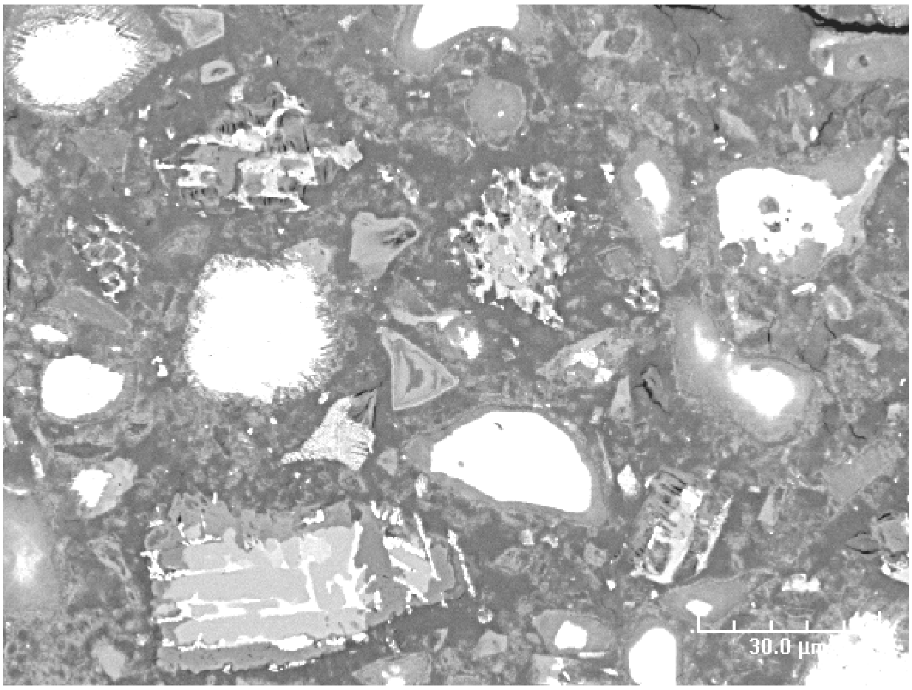

Figure 3- 40: BSE image of F15. Dense region

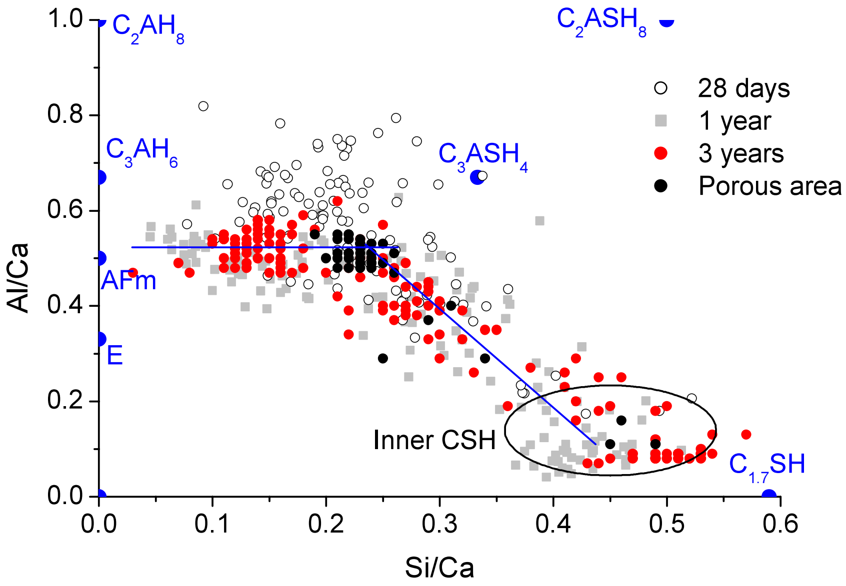

Figure 3- 41: Al/Ca atom ratios vs. Si/Ca atom ratios for the matrix of F15. The phases C_4AH_{13},, monocarbo and monosulfate are summarized under the name AFm.

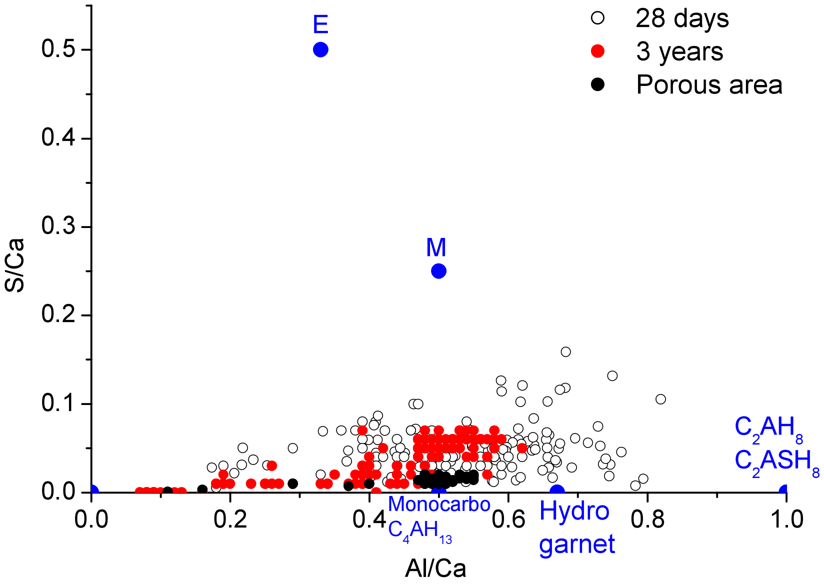

Figure 3- 42: S/Ca atom ratios vs. Al/Ca atom ratios for the matrix of F15 – 28 days and 3 years

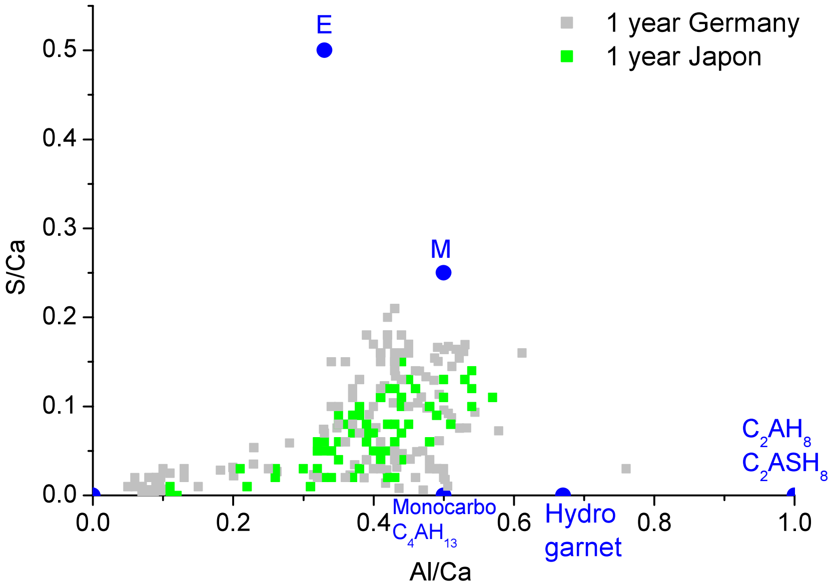

Figure 3- 43: S/Ca atom ratios vs. Al/Ca atom ratios for the matrix of F15 – 1 year

Like F21, there is a large scatter of the EDS microanalysis throughout the matrix indicating the presence of intermixing phases but some trends can be distinguished. XRD analysis is helpful for the identification of the hydrates.

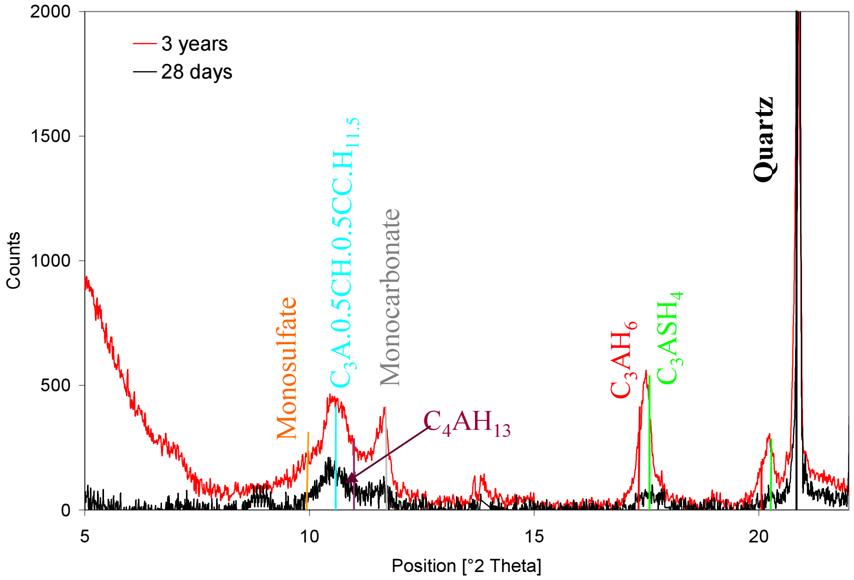

Figure 3- 44: XRD patterns of F15 – 28 days and 3 years

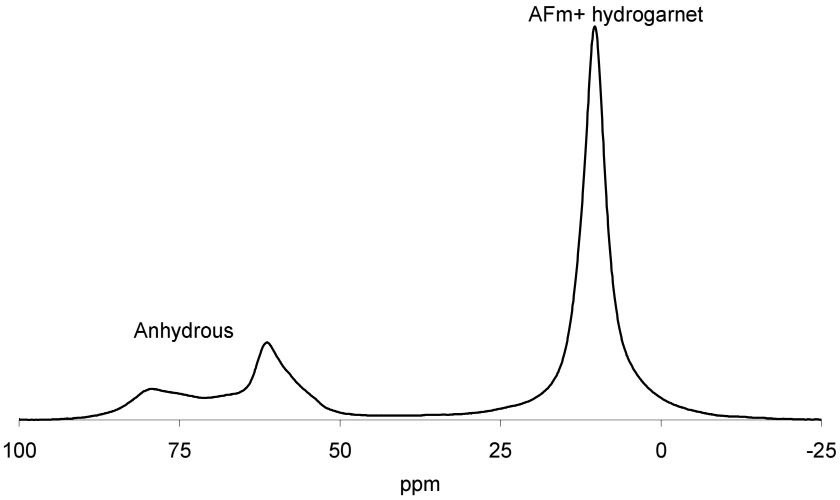

Figure 3- 45: ^{27}Al NMR of F15 – 28 days

The three techniques lead to the same conclusion: no ettringite was detected in this sample. ^{27}Al NMR reveals the presence of AFm which are confirmed by XRD and SEM. However, AFm phases discrimination is more difficult because a broad peak is detected in XRD indicating the presence of solid solutions between C_4AH_{13}, monocarboaluminate, hemicarbonate and monosulfate. The latter should be present to a small extent because sulfates only come from gypsum in the Portland cement. However, the one-year EDS microanalysis, figure 3-42, indicate high content of sulphur whose the origin is unknown.

The 28 days EDS analysis seems to be more centred on hydrogarnet

No trace of Portlandite is detected either in XRD, or in TGA whereas inner C-S-H are formed in the long-term.

The XRD highlights the coexistence of C_3AH_6 and C_3ASH_4. Damidot and Glasser [31] have demonstrated by thermodynamic calculations that hydrogarnet $C_3AS_xH_{6-2x}$ with low or high Si content may form instead of C_3AH_6 and are stable.

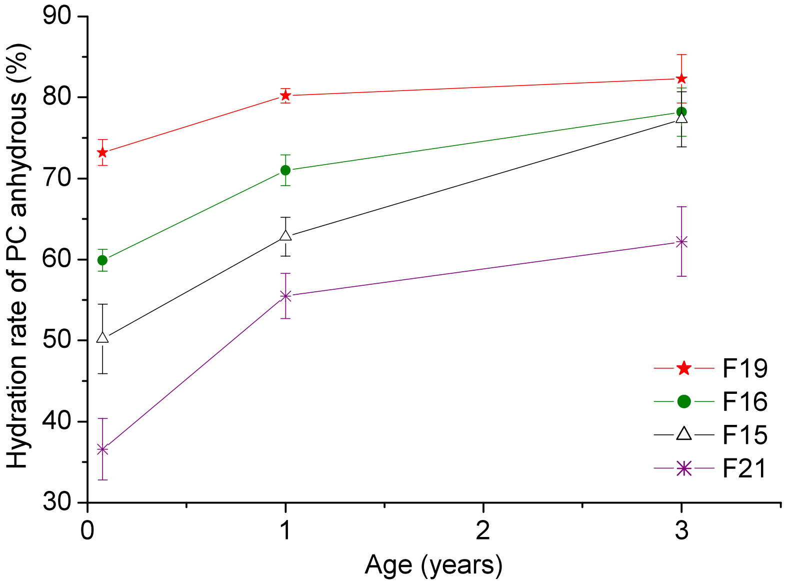

Figure 3- 46: Hydration degree of Portland anhydrous measured by BSE-IA for the mixes F19, 16, 21 and 15

As for F16, the long-term hydration rate of Portland anhydrous approaches that of plain Portland; C_3S is partially consumed to form inner C-S-H over time.

Gu and Beaudoin [39] have also observed the delay in hydration of PC/CAC 70/30 binder and have attempted to explain it by a hydrate barrier effect (mainly ettringite). This physical barrier impedes further contact between water and the inner surface of cement particles. The existence and the nature of this protective layer is still debated to explain the delay of silicates hydration.

3.3 HYDRATION MECHANISMS WHEN CAC IS THE MAJOR COMPONENT

3.3.1 Literature review

Before describing the hydration process for binary and ternary binders, it is important to consider the hydration of pure calcium aluminate cement.

3.3.1.1 Hydration of CAC

The hydration of CA is temperature dependent with three possible phase assemblages [30, 52, 53]:

Low temperatures: $CA + 10H \rightarrow CAH_{10}$ (3.16)

Intermediate temperatures: $2CA + 16H \rightarrow C_2AH_8 + AH_3$ (3.17)

High temperatures: $CA + 12H \rightarrow C_3AH_6 + 2AH_3$ (3.18)

The thermodynamically stable hydrates of CA are the hydrogarnet C_3AH_6 and gibbsite, AH_3, thus the metastable phases CAH_{10} and C_2AH_8 will convert to these phases over time.

The conversion reactions are:

$$2CAH_{10} \rightarrow C_2AH_8 + AH_3 + 9H \tag{3.19}$$

$$3C_2AH_8 \rightarrow C_3AH_6 + AH_3 + 9H \tag{3.20}$$

The conversion of metastable to stable hydrates is accompanied by a reduction in solid volume causing an increase in porosity but water is released which is available to hydrate any remaining anhydrous phases.

3.3.1.2 Hydration mechanisms in CAC/C$ system [54, 55]

As soon as the solids come in contact with water, the phases dissolve until the critical supersaturation of ettringite is reached, at which point the latter precipitates.

$$3CA + 3C\overline{S}H_x + (38-3x)H \rightarrow C_3A.3C\overline{S}.H_{32} + 2AH_3 \tag{3.21}$$

The stoichiometry of the reaction is such that alumina must be produced and this phase is characterized by a more or less crystalline nature.

When the calcium sulfate is depleted, ettringite reacts with remaining anhydrous CA to form calcium monosulfate (AFm phase).

$$C_3A.3C\overline{S}.H_{32} + 6CA + 16H \rightarrow 3C_3A.C\overline{S}.H_{12} + 4AH_3 \tag{3.22}$$

The hydration of calcium sulfate / calcium aluminate cement mixes has been studied with different varieties of calcium sulfate and as mentioned before (section 2.1.1), their dissolution rates are a key parameter for the morphology or spatial distribution of the hydrates. We distinguish hereafter two cases:

- CAC/"C$ rapid" (Gypsum or Hemihydrate): in this case, the calcium sulfate is more rapidly soluble than the calcium aluminate, so the solution is rich in Ca^{2+} and SO_4^{2-} and deficient in Al^{3+}. Short stubby crystals of ettringite are formed, preferentially on the surface of CAC grains.

- CAC/"C$ slow" (Anhydrite): this time, the calcium sulfate is less rapidly soluble than the calcium aluminate; the calcium sulfate solubilisation is the limiting parameter (solution poor in SO_4^{2-}) and it leads to the growth of long thin needles of ettringite.

Conclusions

The mechanisms of hydration of these binders are complex but the key is the initial concentration of C/A/$ in solution which determines:

- the kinetics of ettringite formation (massive precipitation, length of the dormant period)
- localisation of the hydrates either to the bulk of the solution, or on the surface of the anhydrous particles
- the morphology of the ettringite crystals (massive or very long needles) and its effects on the strength development, the dimensional variations and the final properties of the hardened product.
- potential blocking when the reaction is too fast

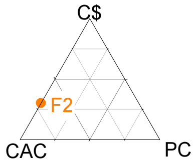

3.3.2 Hydration mechanism of the binary binder CAC / C$

This section deals with the microstructural development of F2, a 70/30 CAC/C$ mix. Figure 3-47 shows its microstructure.

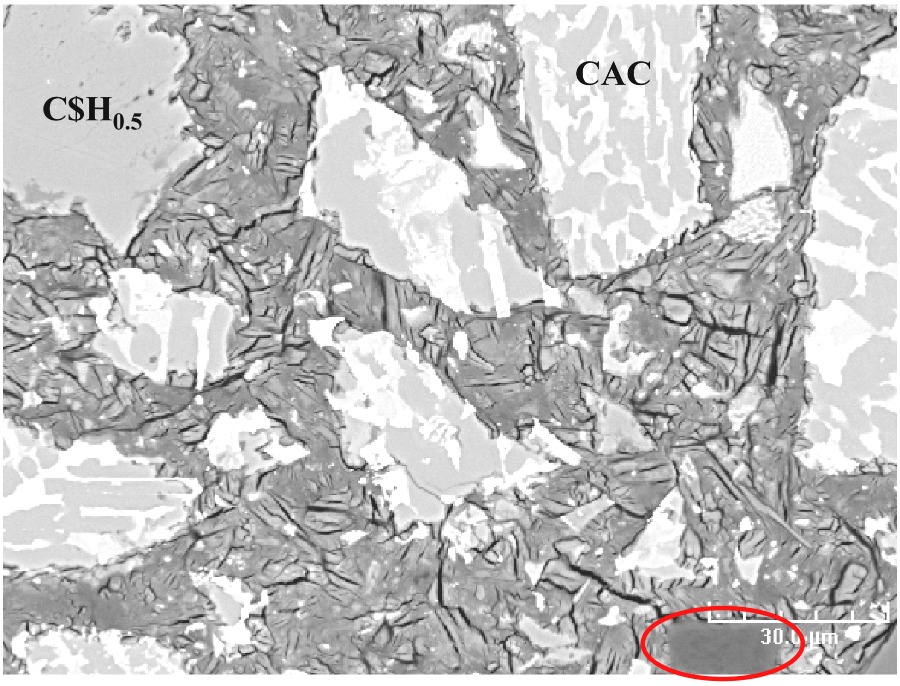

Figure 3- 47: BSE image of F2 -3 years. CAC grains are polymineralic; the brightest phase represents C_4AF, the light grey C_2AS and the darker grey CA. The circle indicates a AH_3 mass and microcrack-rich areas are ettringite. As mentioned before, ettringite is sensitive to vacuum and a lattice shrinkage is created, leading to microcracking.

As displayed on the picture 3-47, lots of anhydrous materials remains after 3 years. Masses of hemihydrate are still present.

The stoichiometry is respected ($n_{C\$H_{0.5}} / n_{CA} = 1$, cf. equation 3.22) in this binder but the limiting factor is the water. Lack of space for further hydration seems also to be relevant to explain the presence of large amounts of residual anhydrous. Indeed, the microstructure is very dense.

EDS microanalysis have been done throughout the matrix, graph 3-48.

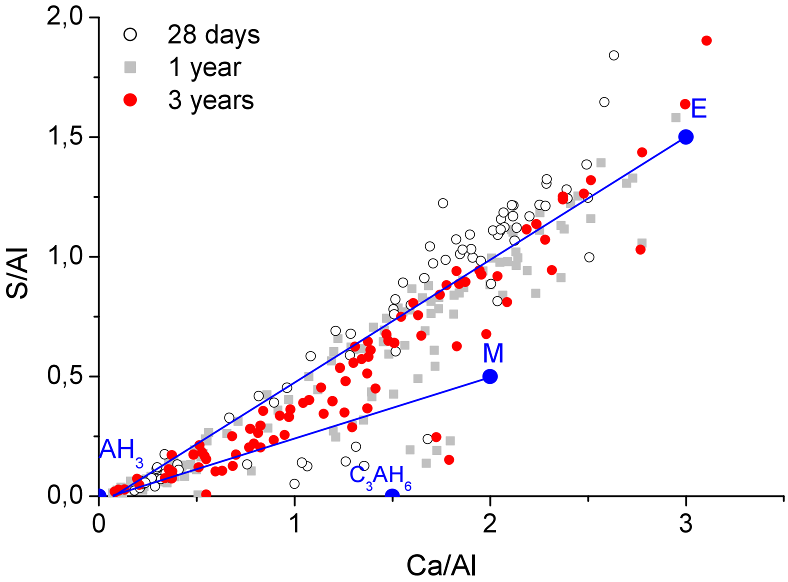

Figure 3- 48: S/Al vs. Ca/Al plot of mix F2

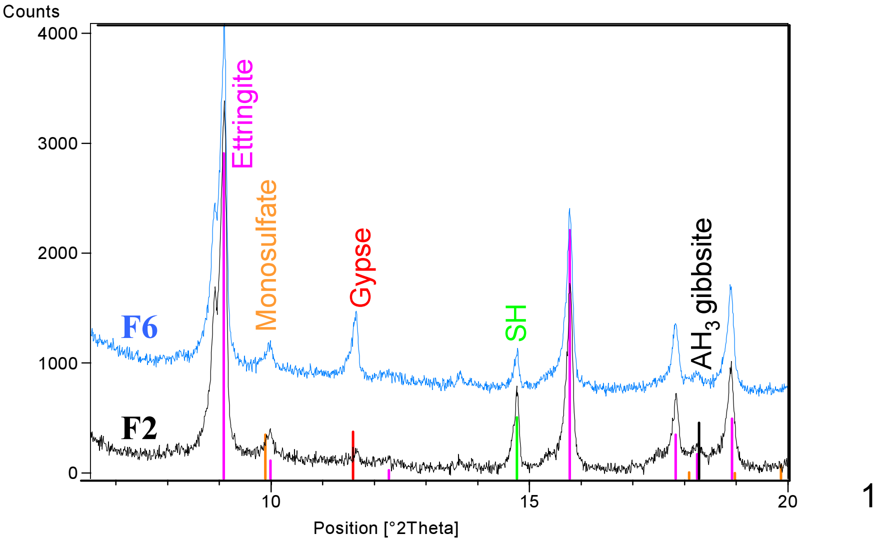

Figure 3- 49: XRD diffractograms of 3 years old F2 and F6. The double peak of ettringite is discussed in section 3.2.3.

At 28 days, all the EDS analysis can be interpreted as being of ettringite and AH_3.

Ettringite and AH_3 have precipitated throughout the matrix. As soon as the CAC and the calcium sulfate are in contact with water, $Al(OH)_4^-$, Ca^{2+} and SO_4^{2-} are produced until the

critical supersaturation of ettringite is reached, at which point the latter precipitates. This will increase the concentration in $Al(OH)_4^-$ in the solution and depress [OH$^-$] and [Ca^{2+}] which as a consequence will increase the saturation toward AH$_3$ till this second hydrate precipitate. The precipitation is immediately balanced by the dissolution of anhydrous until thermodynamic equilibrium is reached.
We confirm that AH$_3$ is a gel-like phase because almost no signal belonging to crystalline AH$_3$ is detected in XRD, graph 3-49.

At 1 and 3 years, there is still hemihydrate, so the reaction of ettringite with residual CA to form monosulfate should be limited but some monosulfate has been detected by EDS and confirmed by XRD (graph 3-49); this could be explained by a local depletion of sulfate and in presence of anhydrous aluminate, equation (3.23) takes place.

3.3.3 Influence of Portland addition to CAC/C$ system

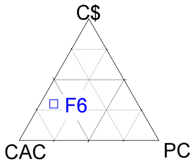

As the initial concentration of C/A/$ in solution determines the mechanism, it should be interesting to evaluate the impact of Portland addition; thus, in binder F2, 9.9% of CAC have been replaced by Portland cement and the amount of hemihydrate was unchanged.

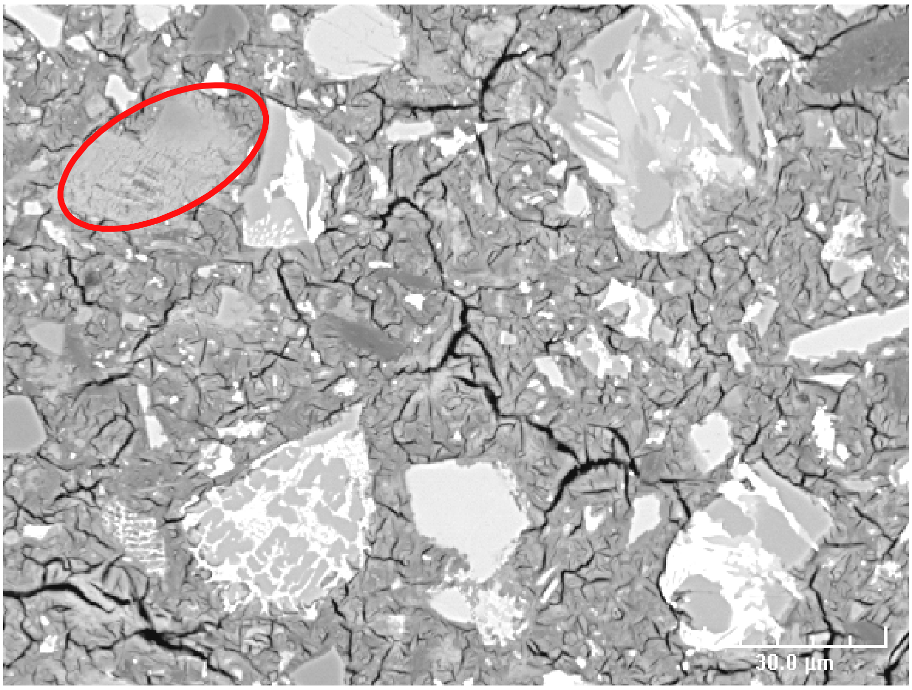

Figure 3- 50: BSE image of F6 – 3 years

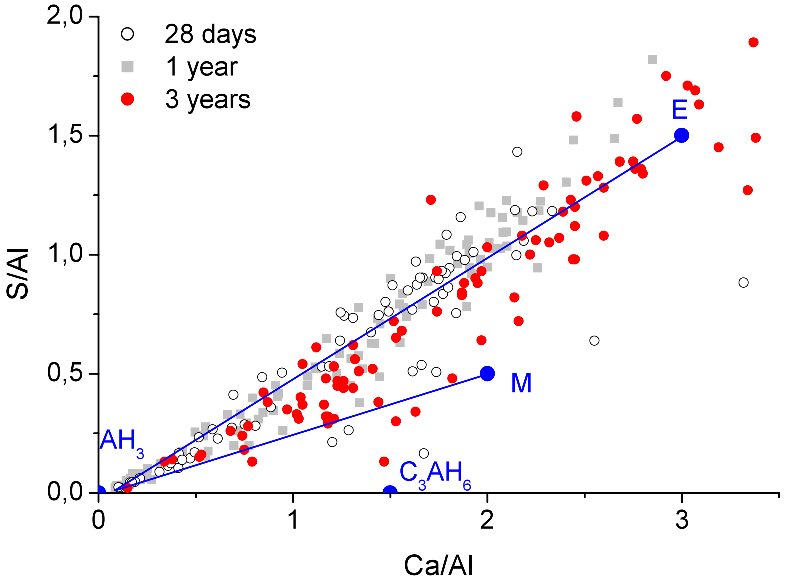

Figure 3- 51: S/Al vs.Ca/Al plot of F6

Reaction (3.22) is still valid but the supplementary calcium will be combined into ettringite formation through equation below:

$$CA + 3C\overline{S}H_x + 2C + (38-3x)H \rightarrow C_3A.3C\overline{S}.H_{32} \tag{3.23}$$

As for F2, all the analyses can be interpreted as being of ettringite, monosulfate and AH_3. However, because of equation (3.24), we expect a smaller amount of AH_3 which is confirmed by thermogravimetry analysis (TGA); the following equation is used to determine the AH_3 content α_{AH3} :

$$\alpha_{AH_3} = \frac{M_{AH_3}}{M_{H_2O}} \frac{\Delta M_{AH_3}}{M_{dry}} \tag{3.24}$$

where M_{AH3} and M_{H2O} correspond to the molar weights of aluminium hydroxide and water respectively, ΔM_{AH3} the weight loss recording by TGA analysis for CH.

AH_3 (% weight)	1 year	3 years
F2	12.7	14.1
F6	9.2	9.6

Table 3- 4: % weight of AH_3 measured by TGA

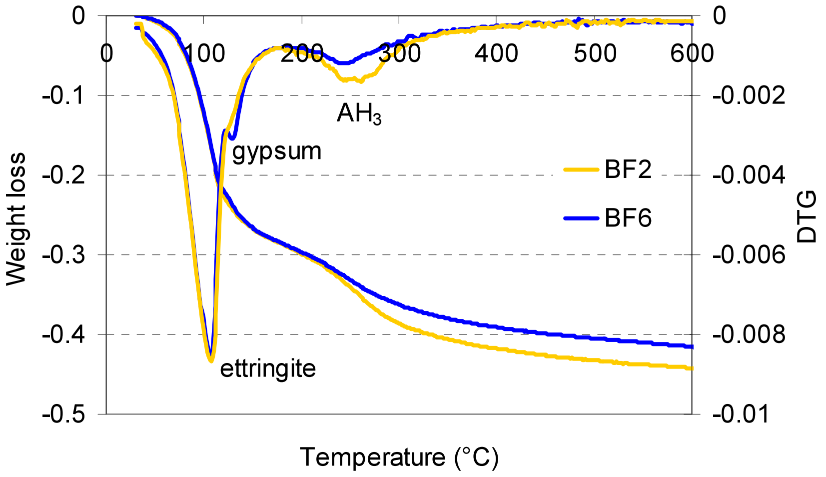

Figure 3- 52: TGA curves for F2 and F6 – 3 years

The comparison of XRD diffractograms, figure 3-49, provides more information; gypsum is detected in F6, confirmed by TGA and BSE image 3-50 (circle) whereas only traces are present in F2. In F6, hemihydrate is in excess compared to CA and thus reacts with water to form gypsum; this is confirmed by the smaller hemihydrate peak in F6 than in F2. The presence of hemihydrate instead of gypsum could be explained by a lack of water.

Bayoux [55] and Amathieu [35] have shown that there is an accelerating effect of a moderate calcium contribution in the reactional system and the existence of a value threshold beyond which the excess of reactional reactivity leads to a temporary blocking of the interfaces.

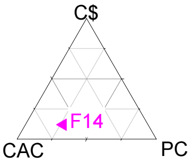

3.3.4 F14

F14 is mainly composed of CAC but the addition of slag (26%) brings additional complexity to the hydration pattern compared to F2 or F6.

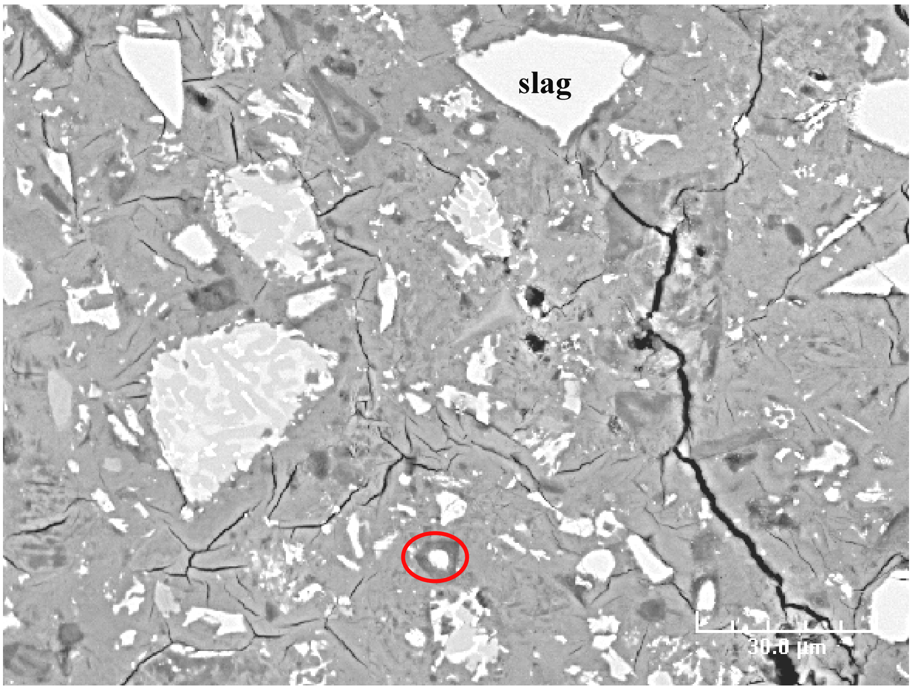

Figure 3- 53: BSE image of F14 – 3 years. The circle indicates a hydrotalcite rim around slag particles

Figures 3-54 and 3-55 show the microanalysis taken of the matrix.

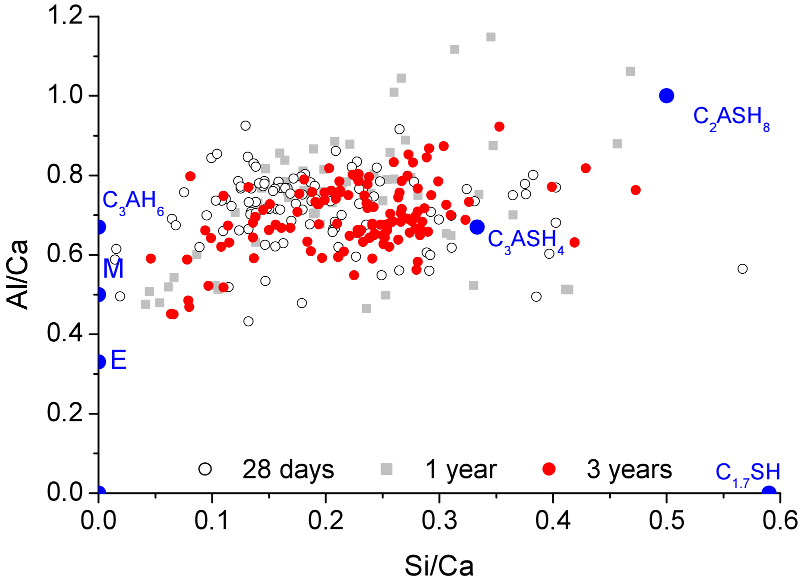

Figure 3- 54:Al/Ca vs. Si/Ca plot of F14

The microanalysis are scattered between AFm, hydrogarnet compositions; nevertheless, it is clear that no C-S-H and portlandite have precipitated. The graph S/Ca against Al/Ca is also difficult to interpret; the microanalysis are concentrated in the area between hydrogarnet and monosulfate. The nature of hydrates with the continuation of hydration remains the same.

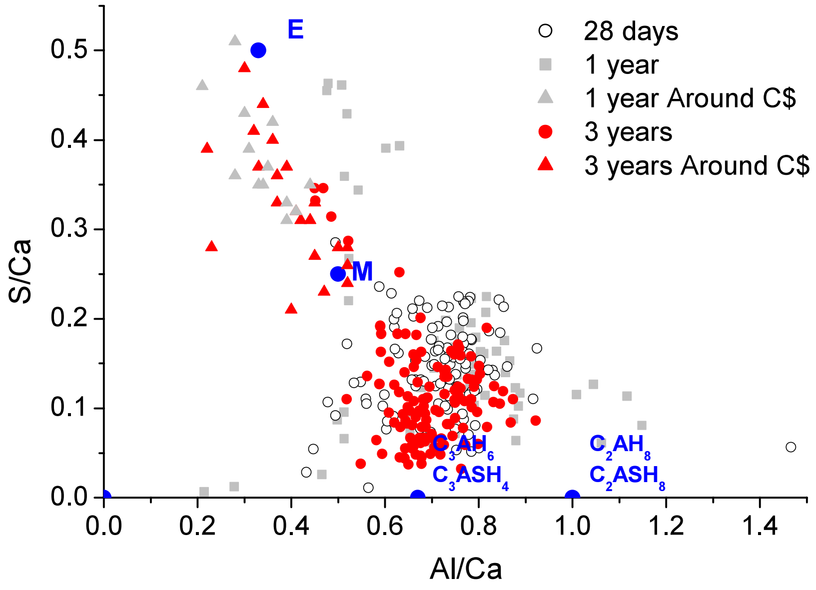

Figure 3- 55:S/Ca vs Al/Ca plot of F14

Ettringite is only detected in regions close to anhydrite grains as shown on figure 3-56. This result is consistent with the fact that sulfate is in deficit in F14 and throughout the matrix, ettringite further reacted with CA to form monosulfate.

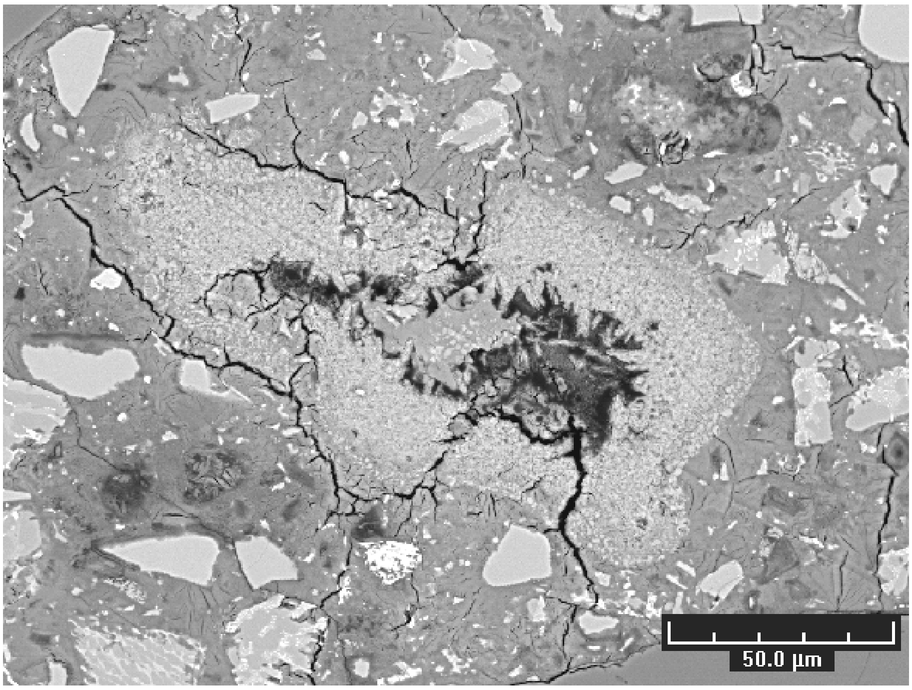

Figure 3- 56:Anhydrite grain surrounding by ettringite rich region (microcracked areas)

Combination of EDS analysis with NMR and XRD analysis is essential to better identify the hydrates.

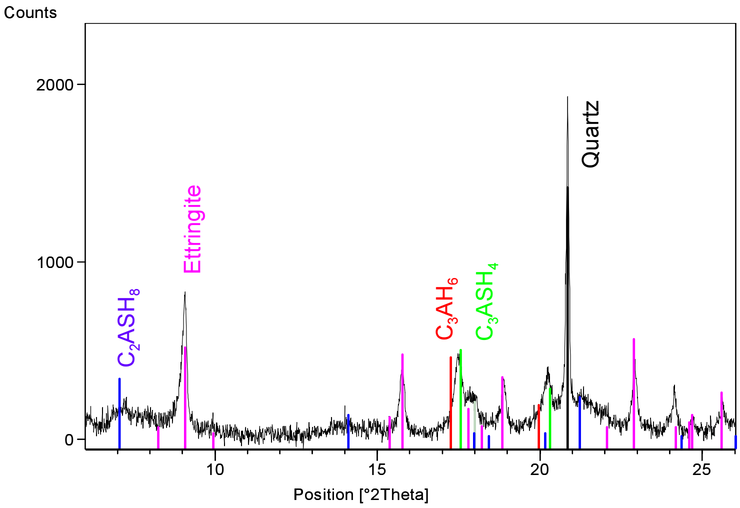

Figure 3- 57:XRD pattern of F14

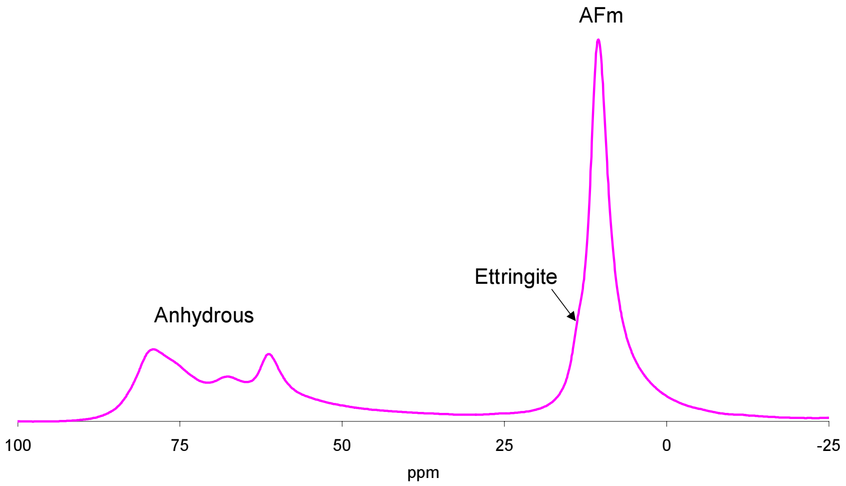

Figure 3- 58: ^{27}*Al NMR of F14 – 3 years*

The XRD spectrum exhibits relevant results with EDS microanalysis; ettringite and hydrogarnets are detected. Monosulfate is certainly poorly crystalline because no XRD signal is observed. Another AFm phase, the strätlingite is also identified.

No traces of hydrotalcite due to the presence of slag are detected either in XRD or throughout the matrix in EDS but BSE images show clearly rims around slag particles (figure 3-53, red circle) which are found to be an hydrotalcite-type phase intermixed with C-S-H which accounts for their darker appearance. In figure 3-59, there is a clear relationship between the two ratios with the points lying on a line with Mg/Al ratio of about 2 which are consistent with the ratio found in cementitious systems [56].

At early age, slag hydrates through solution and at later age, the presence of the rims suggests that the slag particles may form some in-situ products by a partially solid state mechanism.

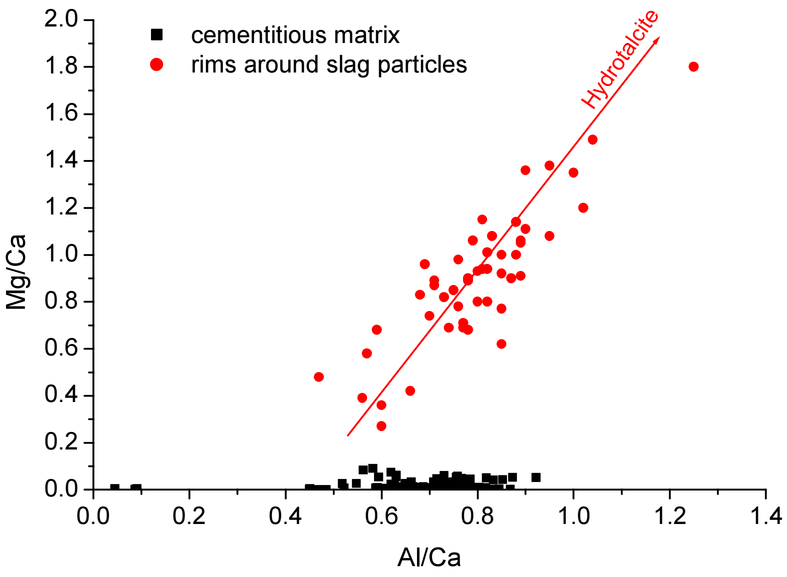

Figure 3- 59:Plot of Mg/Ca vs. Al/Ca for F14, 3 years

3.4 CONCLUSIONS

The PC/CAC/C$ blends behave very differently from plain Portland and mechanisms are sensitive to PC/CAC ratio. A significant delay of Portland hydration occurs resulting in a change of the hydration mechanism. This delay depends on the CAC content and reduces with time except for F21. However, previous investigations of the hydration behaviour of 80%PC-20%CAC paste [40, 42] using conduction calorimetry indicated that the delay of PC hydration results in poor strength development which is discussed in Chapter 2.

The binary system CAC and C$ leads to ettringite and AH_3 precipitation. Addition of supplementary lime source such as Portland cement, lowers the content of AH_3 but does not modify the hydration mechanism.

However, the hydration pattern becomes more complex when C$ is much lower and Portland cement is included in the mix; hydrogarnets seem to be the major hydrates and strätlingite is also detected.

In this chapter, the study was directed toward the hydration chemistry; phase composition and hydration mechanisms were identified for different formulations. The development of the microstructure also includes more physical properties such as porosity and transport properties which are the topics of the following chapter.

3.5 REFERENCES

1. Richardson, I.G. (1999). The nature of C-S-H in hardened cements. *Cement and Concrete Research* **29**, 1131-1147.
2. Taylor, H.F.W. (1986). Proposed structure for calcium silicate hydrate gel. *Journal of American Ceramic Society* **69**, 464.
3. Richardson, I.G., and Groves, G.W. (1992). Models for the composition and structure of calcium silicate hydrate (C-S-H) gel in hardened tricalcium silicate pastes. *Cement and Concrete Research* **22**, 1001-1010.
4. Richardson, I.G., and Groves, G.W. (1993). The incorporation of minor and trace elements into calcium silicate hydrate (C-S-H) gel in hardened cement pastes. *Cement and Concrete Research* **23**, 131-138.
5. Gauffinet, S., et al. (1998). Direct observation of the growth of calcium silicate hydrate on alite and silica surfaces by atomic force microscopy. *Comptes Rendus de l'Academie des Sciences - Series IIA - Earth and Planetary Science* **327**, 231-236.
6. Nonat, A. (2004). The structure and stoichiometry of C-S-H. *Cement and Concrete Research* **34**, 1521-1528.
7. Jennings, H.M. (2000). A model for the microstructure of calcium silicate hydrate in cement paste. *Cement and Concrete Research* **30**, 101-116.
8. Rayment, D.L., and Majumdar, A.J. (1982). The composition of the C-S-H phases in portland cement pastes. *Cement and Concrete Research* **12**, 753-764.
9. Richardson, I.G. (2000). The nature of the hydration products in hardened cement pastes. *Cement & Concrete Composites* **22**, 97-113.
10. Richardson, I.G., and Groves, G.W. (1993). Microstructure and microanalysis of hardened ordinary portland cement. *Journal of Materials Science* **28**, 265-277.
11. Andersen, M., et al. (2003). Incorporation of aluminium in the C-S-H of hydrated portland cements: a high field ^{27}Al and ^{29}Si MAS NMR investigation. *Inorganic chemistry* **42**, 2280-2287.
12. Faucon, P., et al. (1998). Triple-Quantum two-dimensional ^{27}Al Magic angle nuclear magnetic resonance study of the aluminium incorporation in calcium silicate hydrates. *Journal of American Chemistry Society* **120**, 12075-12082.
13. Odler, I. (1980). Interaction between gypsum and the C-S-H phase formed in C_3S hydration. In *7th International Congress on Chemistry of Cement*: Paris.
14. Courault, A.C. (2000). Simulation expérimentale des C-S-H dans les bétons modernes: etude de la composition et des propriétés à l'équilibre dans des milieux complexes. PhD thesis, Université de Bourgogne, Dijon.
15. Famy, C. (1999). Expansion of heat-cured mortars. PhD thesis, Imperial College, London.
16. Deng, M., and Tang, M. (1994). Formation and Expansion of Ettringite Crystals. *Cement and Concrete Research* **24**, 119-126.
17. Taylor, H.F.W. (1997). Hydrated aluminate, ferrite and sulfate phases. In Cement Chemistry, Chapter 6, T. Telford, ed.
18. Glasser, F.P. (2002). The stability of ettringite. In *Internal Sulfate Attack and Delayed Ettringite Formation* (K.L. Scrivener and J.P. Skalny, eds.). pp. 43-63, RILEM: Villars, Switzerland.
19. Damidot, D., and Glasser, F.P. (1993). Thermodynamic investigation of the CaO-Al_2O_3-$CaSO_4$-H_2O system at 25°C and the influence of Na_2O. *Cement & Concrete Research* **23**, 221-238.

20. Zhou, Q., et al. (2004). Metaettringite, a decomposition product of ettringite. *Cement and Concrete Research* **34**, 703-710.
21. Zhou, Q., and Glasser, F.P. (2001). Thermal stability and decomposition mechanisms of ettringite at < 120 °C. *Cement and Concrete Research* **31**, 1333-1339.
22. Skoblinskaya, N.N., et al. (1975). Changes in crystal structure of ettringite on dehydration.2. *Cement & Concrete Research* **5**, 419-432.
23. Skoblinskaya, N.N., and Krasilnikov, K.G. (1975). Changes in crystal structure of ettringite on dehydration.1. *Cement & Concrete Research* **5**, 381-394.
24. Lachowski, E.E., et al. (2003). Transmission electron optical study of ettringite and thaumasite. *Cement and Concrete Composites* **25**, 819-822.
25. Damidot, D., and Glasser, F.P. (1992). Thermodynamic investigation of the CaO-Al_2O_3-$CaSO_4$-H_2O system at 50°C and 85°C. *Cement and Concrete Research* **22**, 1179-1191.
26. Myneni, S.C.B., et al. (1998). Ettringite solubility and geochemistry of the $Ca(OH)_2$-$Al_2(SO_4)_3$-H_2O system at 1 atm pressure and 298 K. *Chemical Geology* **148**, 1-19.
27. Pöllmann, H., et al. (1990). Solid solution of ettringites part I: incorporation of OH^- and CO_3^{2-} in $3CaO.A1_2O_3.32H_2O$. *Cement and Concrete Research* **20**, 941-947.
28. Buhlert, R., and -J., K.H. (1971). The replacement of Al^{3+} and Fe^{3+} in ettringite. *Zement-Kalk-Gips* **24**, 83-85.
29. Glasser, F.P., et al. (1999). Stability and solubility relationships in AFm phases: Part I. Chloride, sulfate and hydroxide. *Cement and Concrete Research* **29**, 861-866.
30. Taylor, H.W.F. (1997). Cement Chemistry (London: Thomas Telford).
31. Damidot, D., and Glasser, F.P. (1995). Investigation of the CaO-Al_2O_3-SiO_2-H_2O System at 25°C by Thermodynamic Calculations. *Cement and Concrete Research* **25**, 22-28.
32. Siauciunas, R., and Baltusnikas, A. (2003). Influence of SiO_2 modification on hydrogarnets formation during hydrothermal synthesis. *Cement and Concrete Research* **33**, 1789-1793.
33. Pratt, P.L., and Jennings, H.M. (1981). The microschemistry and microstrucutre of portland cement. *Annual Review of Materials Science* **11**, 123-149.
34. Scrivener, K.L. (1984). The development of microstructure during the hydration of Portland cement, University of London.
35. Amathieu, L., et al. (2001). Mechanisms of set acceleration of portland cement through CAC addition. In *Calcium Aluminate Cement 2001.*
36. Bayoux, J.P., et al. Shotcrete- Understanding of the hydration process of mixes containing CAC and OPC and proposal for a simple rheological characterization. 208-216.
37. Cottin, B., F (1980). Hydratation des mélanges silicates - aluminates de calcium. In *Congès Chimie des Ciments*, vol. 3,5. pp. 113-118: Paris.
38. Zhang, X., et al. (1997). Study of early hydration of OPC-HAC blends by microwave and calorimetry technique. *Cement and Concrete Research* **27**, 1419-1428.
39. Gu, P., and Beaudoin, J.J. (1997). A conduction calorimetric study of early hydration of ordinary Portland cement high alumina cement pastes. *Journal of Materials Science* **32**, 3875-3881.
40. Gu, P., et al. (1994). A Study of the Hydration and Setting Behavior of OPC-HAC Pastes. *Cement and Concrete Research* **24**, 682-694.
41. Gu, P., et al. (1993). Electrochemical-Behavior of Portland-Cement High-Alumina-Cement Systems at Early Hydration Times. *Journal of Materials Science Letters* **12**, 1771-1773.

42. Gu, P., et al. (1997). Early strength development and hydration of ordinary Portland cement calcium aluminate cement pastes. *Advanced Cement Based Materials* **6**, 53-58.
43. Garces, P., et al. (1998). Hydration characteristics of high alumina cement Portland cement mixtures. *Zkg International* **51**, 646-649.
44. Taylor, H.F.W. (1997). Hydration of Portland cement. In Cement Chemistry, Chapter 7, T. Telford, ed.
45. Odler, I., and Abdulmaula, S. (1984). Possibilities of Quantitative-Determination of the AFt (Ettringite) and AFm (Monosulfate) Phases in Hydrated Cement Pastes. *Cement and Concrete Research* **14**, 133-141.
46. Barnett, S.J., et al. (2003). Extent of immiscibility in the ettringite-thaumasite system. *Cement and Concrete Composites* **25**, 851-855.
47. Barnett, S.J., and Macphee, D.E. (2002). XRD, EDX and IR analysis of solid solutions between thaumasite and ettringite. *Cement & Concrete Research* **32**, 719-730.
48. Minard, H. (2003). Etude intégrée des processus d'hydratation de coagulation, de rigidification et de prise pour un système C_3S-C_3A-sulfates-alcalins. PhD thesis, Université de Bourgogne, Dijon.
49. Stein, H.N. (1972). Thermodynamic considerations on the hydration mechanisms of Ca_3SiO_5 and $Ca_3Al_2O_6$. *Cement and Concrete Research* **2**, 167-177.
50. Gartner, E.M. (1989). Hydration mechanisms I. In *Materials Sciences of Concrete I* (J.P. Skalny, ed.).
51. Mounanga, P., et al. (2004). Predicting $Ca(OH)_2$ content and chemical shrinkage of hydrating cement pastes using analytical approach. *Cement and Concrete Research* **34**, 255-265.
52. Scrivener , K.L., and Capmas, A. (1998). Calcium Aluminate Cement. In Lea's Chemistry of Cement and Concrete, Volume 13, 4th Edition, P.C. Hewlett, ed. pp. 709-778.
53. Sorrentino, D., et al. (1995). Mechanisms of hydration of calcium aluminate cements. In Materials science of concrete IV, Volume IV, S.M. Jan Skalny, ed. pp. 41-90.
54. Bayoux, J.P., et al. Thermodynamic approach to understand the CaO-Al_2O_3-SO_3 system. In *9th ICCC*.
55. Bayoux, J.P., et al. (1990). Study of the hydration properties of aluminous cement and calcium sulfate mixes. In *Calcium aluminates cement* (Mangabhai, ed.). pp. 320-334: London.
56. Wang, S.D., and Scrivener, K.L. (1995). Hydration products of alkali activated slag cement. *Cement and Concrete Research* **25**, 561-571.

Chapter 4. Porosity and Transport Properties

It is generally recognised [1-4] that the facility of penetration of water or other species is one of the most important factors in determining durability. Ingress of water through pore spaces provides a path for the transport of deleterious substances such as chlorides, or gaseous CO_2 which can initiate the corrosion of reinforcing steel. These transport properties are known to be strongly dependent on the total porosity and pore size distribution. The first part of this chapter describes the measurement of the porosity of the formulations by various techniques. The samples were equilibrated at different relative humidities (33, 55, 76 and 86%) and then various transport tests were applied namely oxygen diffusivity, oxygen permeability and water absorption. This gives complementary information on the pore size distribution.

4.1 POROSITY IN CEMENTITIOUS MATERIALS

Investigation of the porosity of cementitious materials poses two major problems. First, the dimensions of the pore sizes range over several order of magnitude with an important fraction of the pores having dimensions in nm range, figure 4-1. Second, the hydrated paste contains a substantial content of water. The state of the water varies between free water, adsorbed water and chemically bound water and the transitions between these states are not well defined. As a consequence the hydrated cement paste changes during drying. All drying techniques will provoke some changes but it is known that some are more damaging than others.

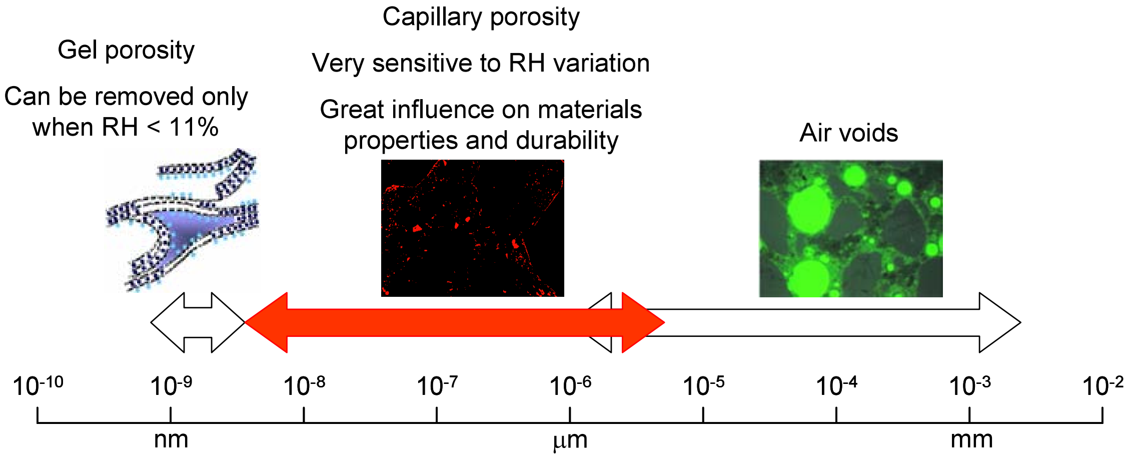

Figure 4- 1: Range of porosity in hardened cement paste

4.1.1 Methods for investigation of porosity in concrete

A wide range of methods are available for the investigation of the porous network, some of which are listed below. Each of these methods has the ability to describe specific aspect of porosity, however none of these can fully characterize all aspects of the pore space:

- Evaporable water content: direct oven drying tends to collapse the microstructure due to the effects of the receding water meniscus and removes some chemically bound water [5, 6].

- Water resaturation of dried samples: this process has a double negative effect; the specimen needs to be dried and some of the products may rehydrate.

- Image analysis [7]: it is a powerful tool to assess the total porosity but in CAC-rich binders, ettringite is the main hydrate and due to its sensitivity to the vacuum in the SEM microscope, microcracks appear in the matrix, figure 4-2, and the segmentation will not distinguish the true porosity and that created by the vacuum.

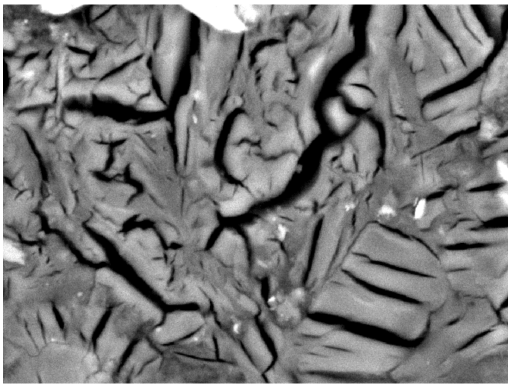

Figure 4- 2: BSE image of an ettringite based system

- Mercury Intrusion Porosimetry : MIP is widely used because of its ease and simplicity and also leads to a pore size distribution but it needs prior drying. MIP technique and the impact of the drying are discussed in paragraph 4.1.2.

- Desorption isotherms, using water, N_2 or other sorbates have been widely used to study the pore structure [8-10].

- Solvent exchange: This method is based on water counter diffusion with a miscible solvent. It appears to be a good method for pores analysis [9, 11, 12] and one of the most suitable method for drying samples.

In our project, after a pre-study of the porosity by MIP, we have chosen these two last methods which seem to be less damaging both for Portland systems and aluminous rich binders.

4.1.2 Mercury Intrusion Porosimetry

This technique is based on the fact that for a non-wetting fluid to enter a pore of diameter *d*, a pressure *P* inversely proportional to the diameter of this pore must be applied. For a cylindrical pore, this pressure is given by the Washburn equation, as seen in equation 4.1:

$$P_{H_g} = \frac{-4\gamma \cos\theta}{d} \tag{4.1}$$

where γ is the surface energy of the mercury and θ the contact angle.

MIP requires a pre-treatment to remove all water in pores generally achieved through various drying procedures. However, cement paste drying may introduce damage such as microcracking, changes in the capillary porosity, collapse of fine pores. In the literature, numerous papers [5, 6, 13, 14] have been published on the drying effects for plain Portland cement or with additives (slag, silica fume, fly ash) but no data is available for PC/CAC/C$ binders. Thus, a preliminary study was done on a ettringite-rich binder (F2) and on a Portland-rich binder (F16) to find out the impact of different drying techniques on MIP measurements.

Three methods of drying were used:

- oven-drying for 60 hours at 60°C,
- freeze-drying (sublimation with liquid nitrogen at –196°C and under vacuum 10^{-4} bars) for 1 week
- solvent exchange for 10 days (with isopropanol) followed by drying in dessicator.

The porosity was measured with a Carlo Erba Porosimeter 2000 at 1, 28 days and 1 year, figure 4-3.

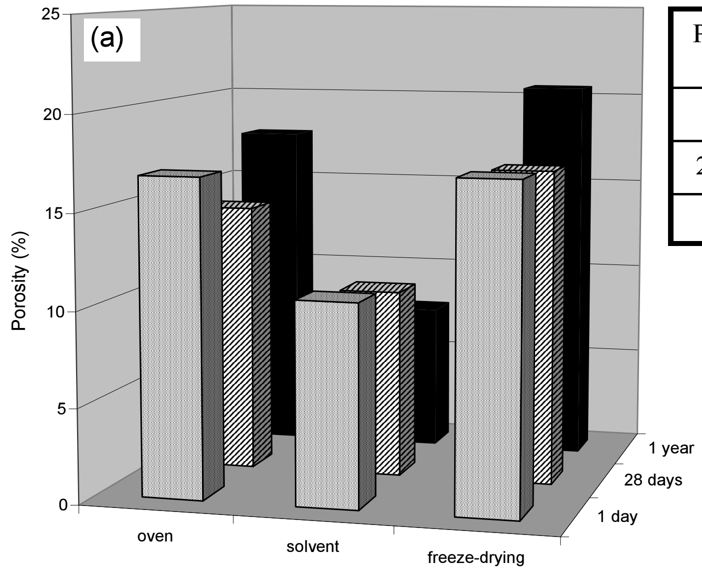

Porosity (%)	Oven	Solvent	Freeze-drying
1 day	16.8	10.7	17.1
28 days	14.3	10.0	16.7
1 year	17.7	7.8	20.6

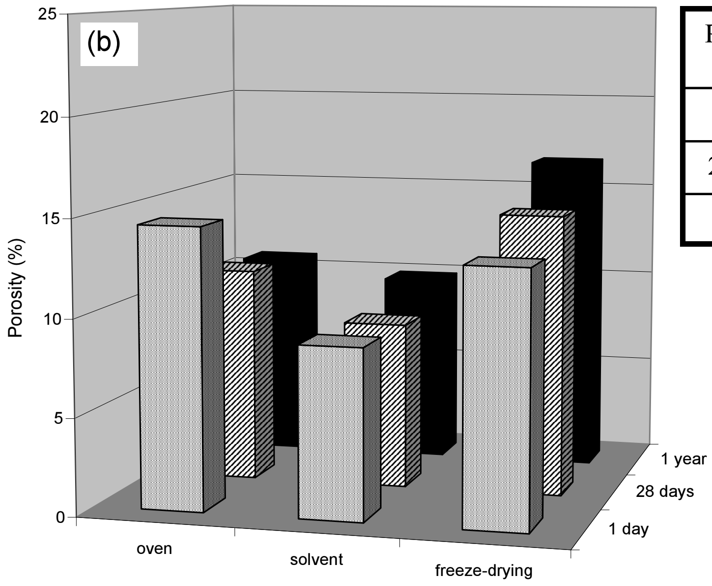

Porosity (%)	Oven	Solvent	Freeze-drying
1 day	14.5	8.8	13.0
28 days	11.2	8.6	14.6
1 year	10.7	9.8	16.6

Figure 4- 3: Comparison of the total porosity values with time according to the drying. (a) F2. (b) F16

The freeze-drying is usually considered as a reasonable drying mode for Portland cement [6], however, for F2 and F16 which are rich in ettringite, it seems to overestimate the porosity.

For instance, for both one-year old samples, the value of porosity doubles between solvent and freeze dryings. Since ettringite has 32 water molecules, water could be removed during sublimation, creating extra pores. The oven-drying is the most common specimen preparation for Portland cement because it is fast and easily performed but it leads to severe disruption of pore structures [15]. Most researchers [13-15] agree that solvent exchange is the least-damaging drying technique but requires more time. Removal of the solvent after it has replaced the water does not produce large surface tension forces within the pore structure (the surface tension of isopropanol is about 30% of that of water) and even if complete exchange does not occur in practice, the collapse of the structure due to removal water is therefore moderate. No drying method is damage free but solvent exchange minimizes the microstructure change.

We noticed that for F2 oven dried and freeze dried, the one-year porosity increased which is unexpected.

The pore size distributions of the mortars influenced by the various drying methods are shown in the form of histograms in figures 4-4 and 4-5.

The pore size distribution of F2 is much coarser than F16; the main range of pore size is 0.1-1 μm for F2 whereas it is 0.01-0.1 μm for F16.

The volume of the coarse pores (r >1 μm), was larger for F2 sample freezing -dried whereas the solvent dried one showed less proportion of pores in the region 0.1-1 μm. The proportion of finer pores is similar for oven and solvent dryings.

For F16, the finer pores are better preserved with freeze-drying and solvent exchange than those in the case of direct oven drying. The difference between the dryings comes from the proportion of pores in the range 0.01-0.1 μm which is the lowest for solvent replacement. Konecny [14] observed the same trend for Portland mortar with fly ash. The solvent replacement seems to be the best with respect to preserving the pores in the finest pore size region.

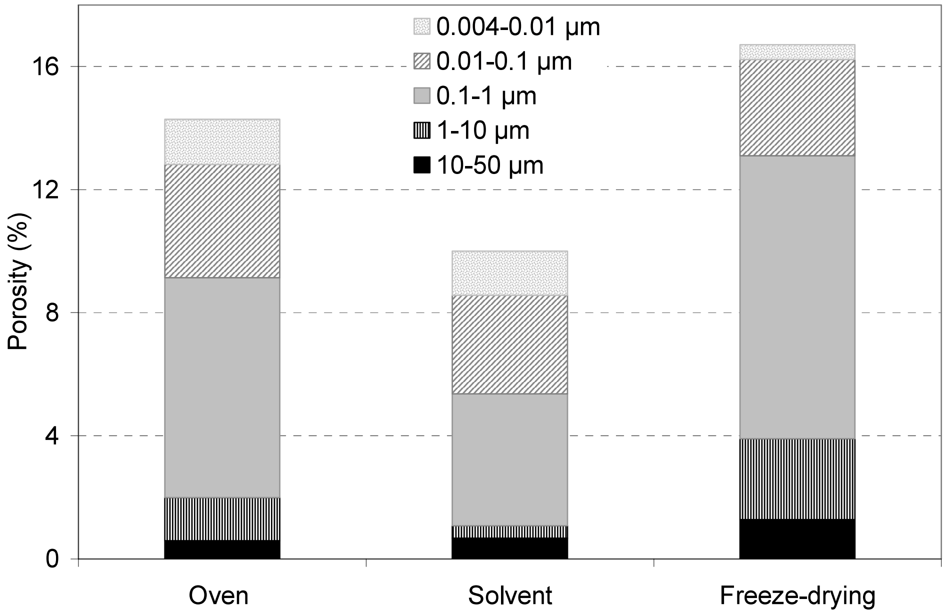

Figure 4- 4: MIP pore size distribution of F2 28 days dried in oven, freezing and solvent replacement technique.

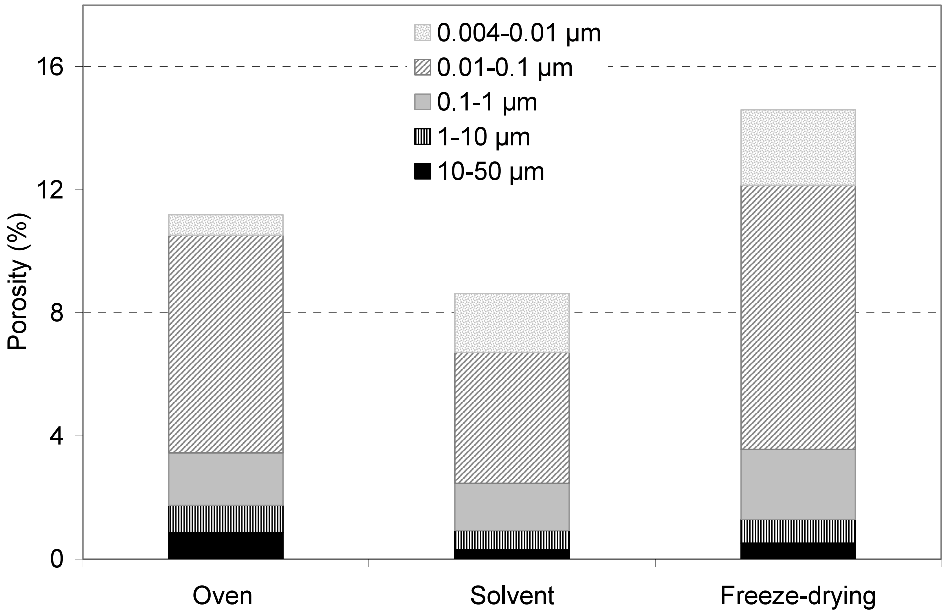

Figure 4- 5: MIP pore size distribution of F16 28 days dried in oven, freezing and solvent replacement technique.

Nevertheless, concerning the pore size distribution, Diamond [16] claims that MIP measurements systematically misallocates the sizes of almost all of the pores volume; this problem of MIP comes from the lack of direct accessibility of most of the pore volume to the mercury surrounding the specimen, figure 4-6. Numerous authors [16-20] share this point of view but the discussion on the validity of the MIP is still open when dealing with the ingress pore opening is relevant.

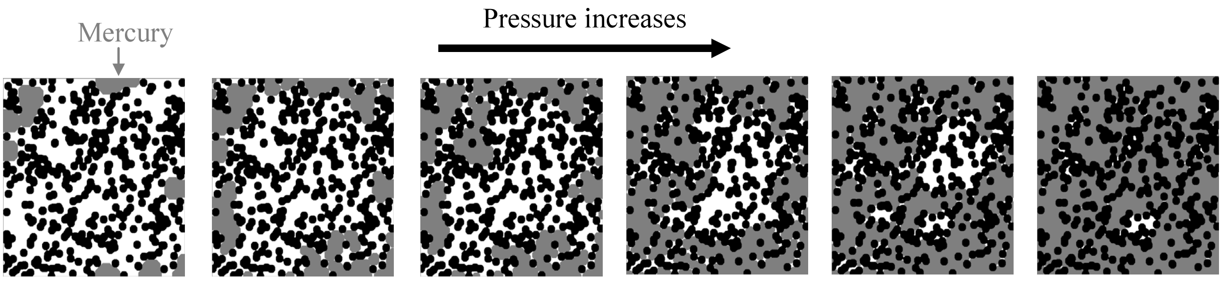

Figure 4- 6: Illustrative diagram of the accessibility of pores

Given the limitations of MIP, it was decided to abandon this method.

4.1.3 Solvent exchange

4.1.3.1 Principle

Solvent exchange has been proposed as a suitable method to assess porosity and to simultaneously yield a coefficient for the counter diffusion of water and solvent. The success to get diffusion parameters depends on the solvent exchange process being one of simple counter diffusion. Several organic fluids have been investigated such as methanol, ethanol, propan-1-ol and propan-2-ol [11, 21-25]. Several workers have suggested that methanol can interact with both $Ca(OH)_2$ [26] and C-S-H by penetration of the layered silicate structure [24]. It is felt [24, 27] that isopropanol shows negligible interaction with the cement paste and is therefore an appropriate solvent for the exchange technique.

4.1.3.2 Experimental procedure

The dimensions of the samples must be closely controlled and a 3 mm thick mortar slice sawed out of 4×4×16 cm^3 prism is convenient; the edge of the slice was removed to eliminate the edge effects. The samples must be water-saturated initially; this was achieved by immersing the samples in distilled water for 2 days.

All measurements must be made at a constant temperature to eliminate the variation of the Archimedean thrust in the solvent.

4.1.3.3 Exchange technique

The slices were surface dried in moist tissue and initially weighed W_{ws}. The samples were then weighed immersed in water W_{wsw}. These weighing results are used in equation (4.2) to give the volume of the water saturated mortar slice:

$$V_{ws} = (W_{ws} - W_{wsw}) / \rho_w \tag{4.2}$$

After these initial weightings, the slice was immersed in isopropanol and the counter diffusion was monitored by measuring the weight changes with time. An automated weighing technique was developed to follow the counter diffusion in-situ; data from the scale are transferred to an application program at particular times fixed by the operator.

As the water is replaced by isopropanol in the pores, the weight decreases due to the lower density of isopropanol (ρ_{IP}=0.7851 g.cm^{-3}). The exchange process reached a steady level after different periods depending on the tested samples.

4.1.3.4 Calculation of total porosity

Parrott [22] showed that almost all of the pore water in plain or hardened cement pastes can be replaced by alcohol. However, the limitation is the size of isopropanol molecule, ≈9Å which is bigger than that of water (2.7Å).

The total porosity accessible to isopropanol molecule is calculated from equation (4.3):

$$P_{IP} = (W_{IP}^{0} - W_{IP}^{f}) / (\rho_w - \rho_{IP}) / V_s \tag{4.3}$$

where P_{IP}: pore volume

W_{IP}^{0} : initial weight in isopropanol (g)

W_{IP}^{f} : final weight in isopropanol (g)

ρ_{IP} : density of isopropanol (g.cm^{-3})

ρ_w: density of water (g.cm^{-3})

V_s: volume of the samples (cm^3)

4.1.3.5 Experimental Results

The evolution of the solvent exchange was similar from one sample to another; typical solvent exchange curves are illustrated in figure 4-7.

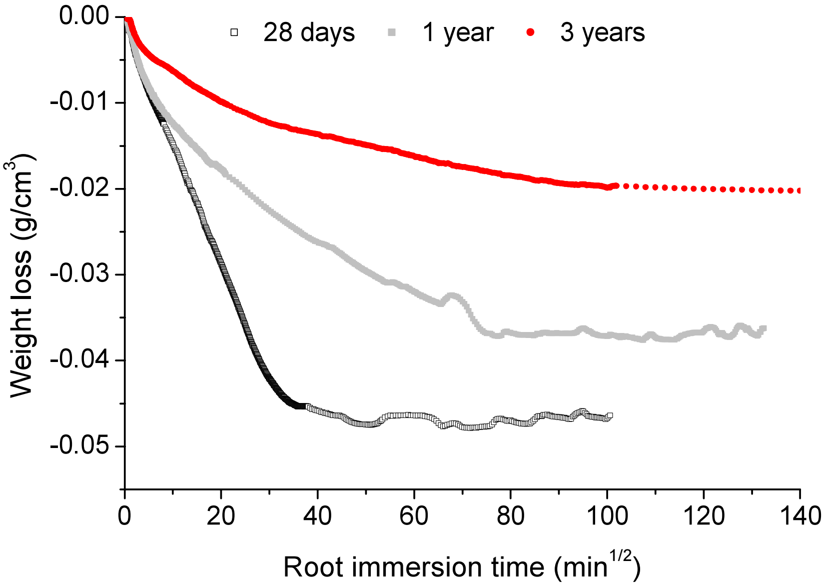

Figure 4- 7: Solvent exchange curves for the binder F14

The 28 days curve exhibits two parts, the first one being linear determining a diffusion process and the second part being constant meaning that an equilibrium state was achieved. This curve shape is characteristic of a simple counter diffusion phenomena governed by Fick's First Law. The behaviour at 1 and 3 years is different; the solvent exchange profile deviates from simple counter diffusion and as a consequence the exchange data cannot be used to determine diffusion coefficients as originally intended. Hughes [28] has also concluded that the solvent technique is unable to yield diffusion coefficients for slag/PC grouts because there is not a simple counter diffusion process.

Almost all studied binders present a non simple counter diffusion process so no kinetic parameters will be deduced. Despite this, one has to remember that the first goal was the porosity whose values are extracted from exchange curves as described in equation (4.3); the histogram below gathers the results. The total porosity are expressed as percentages of the specimen bulk volume.

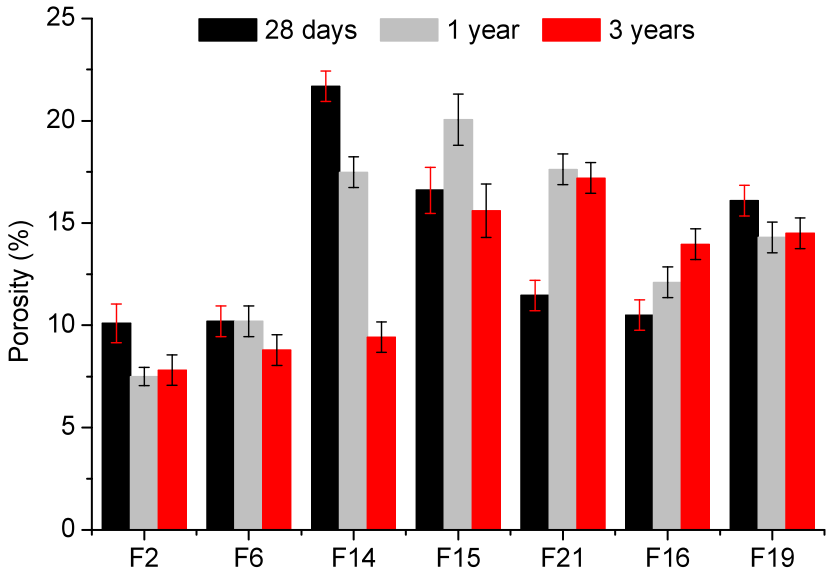

Figure 4- 8: Total porosity values extracted from solvent exchange curves

Before examining these results, few examples of the reproducibility are given.

As we can see on the graph 4-9, generally the reproducibility is relatively acceptable but it is quite poor for F15; there is almost 20% error between the three values. Source of errors are:

- the samples volume [23]: the thickness variation between the slices is unavoidable due to the inaccuracy of the saw.
- the water saturated state: perhaps the investigated slice is not fully saturated.
- the sand content in the slice; the idea was to find if the plot of the weight loss per gram of cement paste would be more appropriate than weight loss per cm^3 of sample volume. To check this, the three slices of F15 28 days were immersed in hydrochloric acid (diluted 1:9) which dissolved the cement paste component and we obtained the sand content. The graph using weight loss per gram of cement paste was replotted and the scattering was similar. So this source of error is not significant.

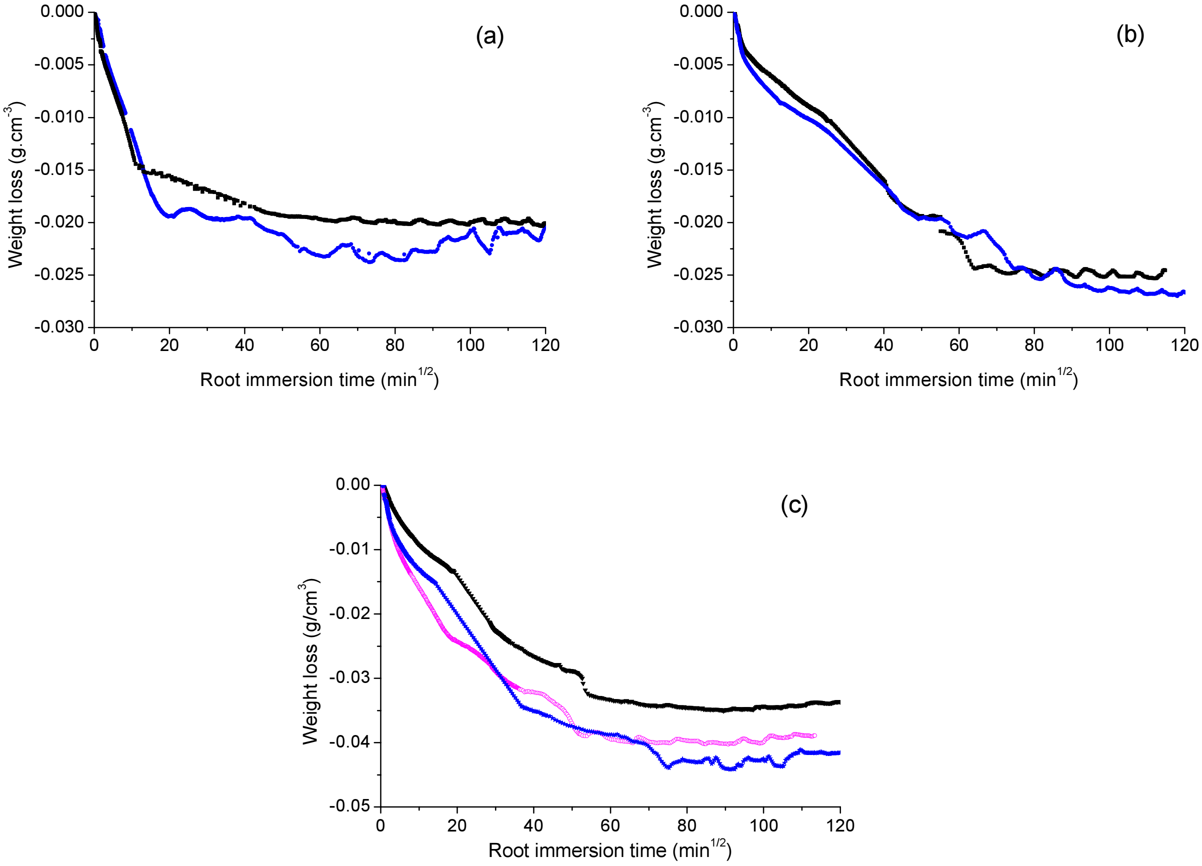

Figure 4- 9: Reproducibility of exchange solvent of slices extracted from the same prism. (a) F6 28 days, (b) F21 28 days, (c) F15 28 days

Consequently, the absolute values of the porosity have to be considered with caution and the trend of the curves should be seen as the major factor of assessment. After a rapid examination of the histogram, figure 4-8, we notice that binders rich in CAC, i.e. F2 and F6, are less porous than Portland-rich systems.

We would expect a decrease of the porosity as the hydration time increases; only F14 follows this trend with a total porosity divided by 2. Taking into account the experimental error the evolution between 28d, 1 and 3 years of F2, F6, F16 and F19 seems to be slight.

It is known that the total porosity is widely reduced during the first days of hydration by the rapid and extensive formation of hydration products through solution and with subsequent hydration to 28 days, the total porosity is further reduced. Then the extent of this is less significant and becomes progressively more restricted and slower. As we measured the porosity after 28 days, in the later stages of hydration, it is relevant to find no or little evolution with time; very little product forms within the remaining capillary pore network.

Crumbie [11] also observed no further change to the total porosity from 28 days 1 year by solvent exchange.

However, the results of F15 and F21 were unexpected: porosity of F15 increased at 1 year to decrease afterwards and the 28-day porosity of F21 seems too low compared to 1 and 3 years. As observed in section 3.2.5, the one-year EDS microanalysis of F15 indicated high content of sulphur whose the origin was unknown. Either it is a simple coincidence or an external factor modified the microstructure. The low porosity of F21 could be explained by the fact that an operator cast the 1 and 3 year samples whereas the 28-day prism was cast by the author.

4.1.4 Relationship between porosity and compressive strength

Numerous strength-porosity relations for hydrated cement have been proposed. Three types of semi empirical equations have been widely used. These are [29, 30]:

Balshin equation $$\sigma = \sigma_{P_0}(1-P)^y \quad (\sigma_{P_0} = 540, y = 14.47) \tag{4.4}$$

(modification of Powers model $\sigma = \sigma_{P_0}(1-P)^3$)

Ryshkewitch equation $$\sigma = \sigma_{P_0} e^{-kP} \quad (\sigma_{P_0} = 636, k = 17.04) \tag{4.5}$$

Schiller equation $$\sigma = k \ln \frac{P_0}{P} \quad (P_0 = 0.31, k = 81.5) \tag{4.6}$$

where σ represents the strength, σ_0 the strength at zero porosity, P the porosity and k an empirical constant.

These functions were tested on the strength and solvent exchange porosity data obtained and on data from the literature for Portland Cement [31] and CAC [32]; the comparison is given on the graph 4-10.

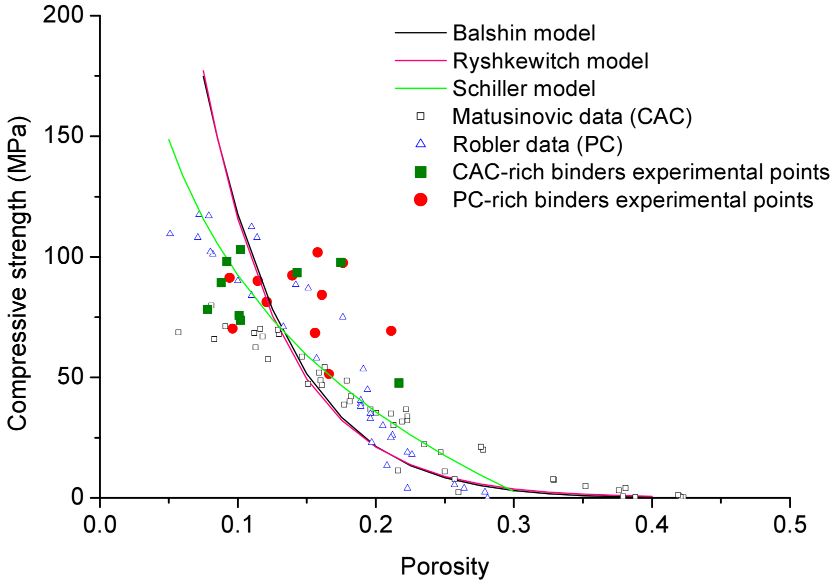

Figure 4- 10: Relationship between porosity and compressive strength. Range of our experimental data and from the literature and calculated functions.

Although there is a large amount of scatter, the points full in the same region as the data from the literature. The CAC rich and PC rich binders also full in the same range. Nevertheless it is clear that it is not possible to predict a value of strength from porosity alone.

4.1.5 Water sorption isotherms

The second method used to characterize the pore space was water desorption isotherms. The basic principle lies in the fact that upon drying a sample to a given relative humidity, one empties a particular range of pores. Many of the pores in concrete are sufficiently small such that condensation will occur at RH values much less than 100%. The relationship between the smallest pore radius in which water condenses, r_k, and RH is described by the Kelvin-Laplace equation:

$$r_K = -\frac{2V_m.\gamma}{R.T.Ln(RH)} \tag{4.7}$$

where RH is the relative humidity at temperature T, γ is the specific surface energy of water, V is the molar volume of water, R the gas constant and r_k the capillary radius.

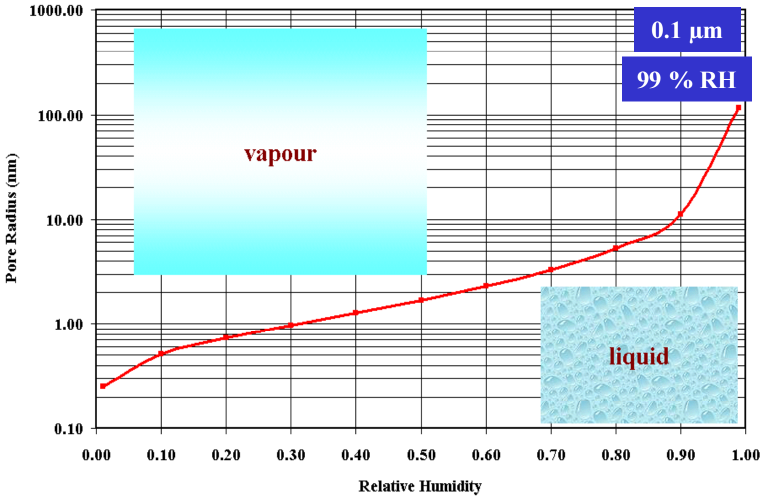

Figure 4- 11: Kelvin pore radius vs. relative humidity. Under the red curve, water condenses in the pores.

The different transport processes involved in water flow through pores systems have been reviewed by numerous authors [33-35]. Different stages may be distinguished and are summarized below:

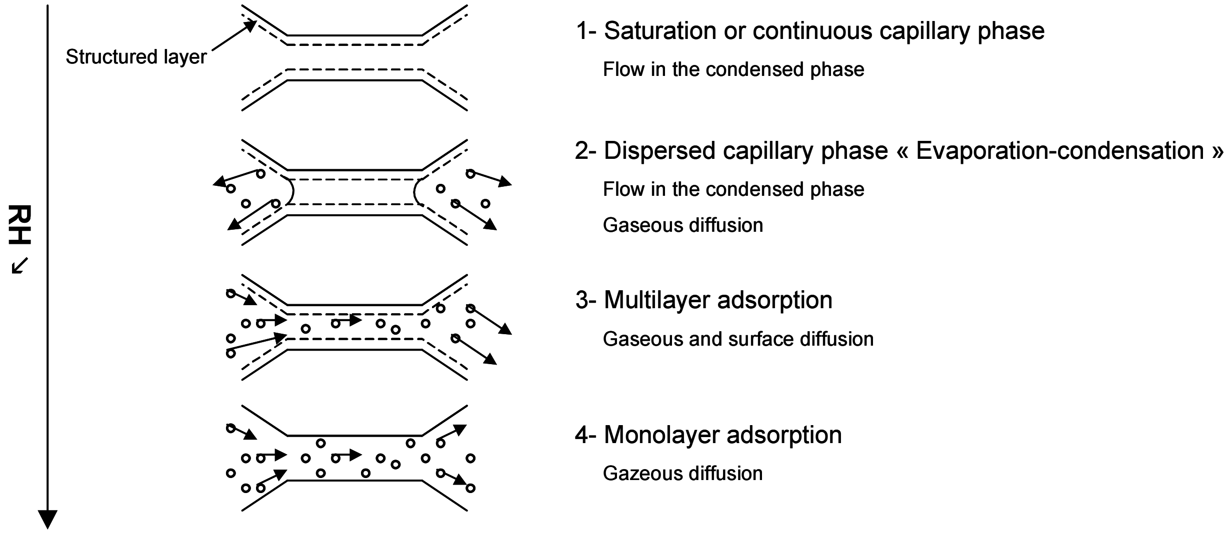

Figure 4- 12: Movement of water in a cylindrical pore

At high RH (stage 1), the porous network is entirely water-filled (continuous capillary phase) but concrete is rapidly unsaturated by self-dessication.

At intermediate RHs (stage 2), gaseous and liquid phases coexist. As the RH decreases, the pores empty and the liquid water becomes discontinuous. Capillary water is present in the network but does not form a continuous phase in the medium.

At low RH (stage 3), transfer occurs mainly in gaseous phase but the adsorbed film is highly structured.

At very low RH (stage 4), transfer in gaseous phase dominates and only a monolayer of water molecules is adsorbed.

4.1.5.1 Materials and mortar mixes used

The selection of formulations was different to the subset described in 4.1.3 in order to measure the impact of the water cement ratio. Nevertheless, the plain Portland F19 and the CAC rich binder F6 are common to both methods. Diagram 4-13 shows the details of formulations chosen.

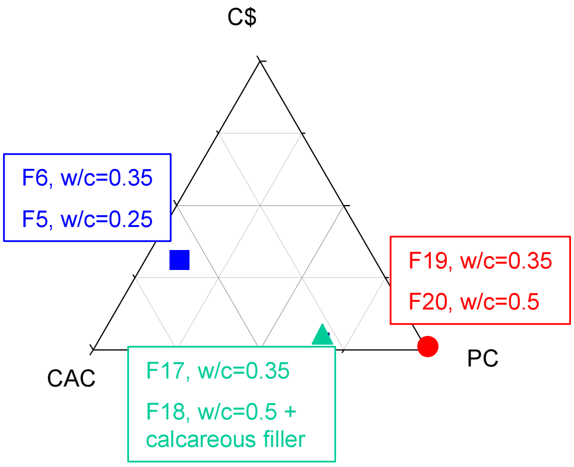

Figure 4- 13: Binders compositions for desorption tests

4.1.5.2 Preparation of test specimens

2 cylinders 250 mm long, 100 mm diameter were cast for each formulation. From each of these cylinders, eight 20 mm thick slices were cut. For each mortar mix, 4 replicate discs specimens (20 mm×100 mm) were cured for 7 days at 100% RH and then exposed to varying relative humidities, 33%, 55%, 76% and 86% RH, at a constant temperature. The samples weight was monitored over 810 days.

4.1.5.3 Water desorption results

The drying leads to progressive emptying of the pores. For a temperature T, a specimen with an initial weight m_0 at relative humidity of H_0 is immersed into an environment H_1 such that $H_1<H_0$, thus causing moisture exchange. Water evaporates into the atmosphere, causing weight loss [35].

The global change of weight can be expressed by:

$$\Delta_{0\to1}(t)=\frac{[m_0-m(t)]}{m_0} \tag{4.8}$$

The kinetics of water vapour desorption are plotted below.

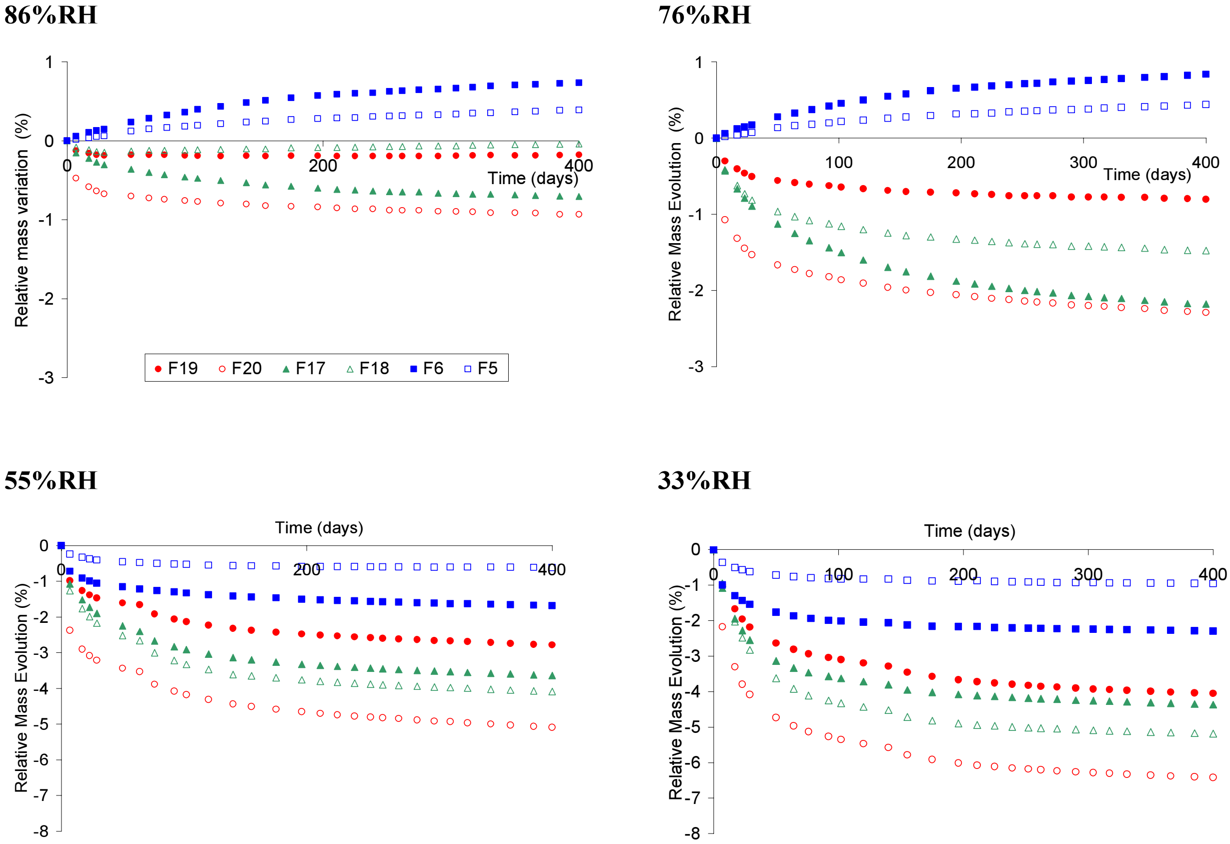

Figure 4- 14: Water vapour desorption kinetics

We first note that all binders have lost weight at all RHs except for CAC-rich binders namely F6 and F5 at 76% and 86%RH. For the latter, the weight increase indicates a reabsorption of water leading to a possible continuation of the hydration; F18 also seems to gain weight in the long-term. Alternatively the samples may not have been fully water saturated when they were put in climatic chambers. For the other samples, at the end of the conditioning, the plateau suggest that an equilibrium moisture state was achieved. For the highest RH, the time required to achieve the equilibrium moisture is low; this could be explained by the fact that the transfers occur in liquid phase (the pore space is occupied by a capillary connected phase) and the transfer coefficient is higher in liquid than in gas. The lower the relative humidity, the higher the weight lost.

The mass variation after equilibrium was reached is plotted versus RH in figure 4-15.

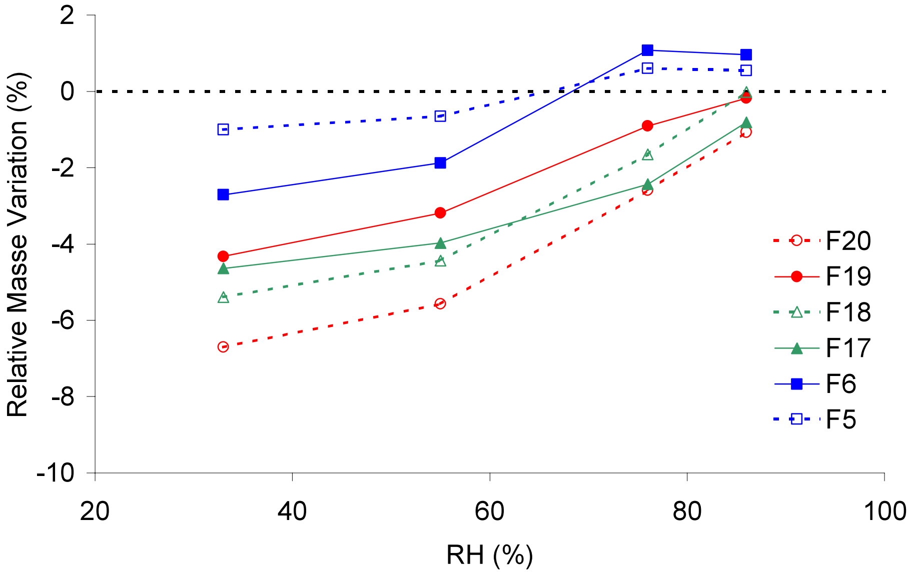

Figure 4- 15: Relative mass variation up 33% to 86% RH at t= 810 days

In order to estimate the water content, dry samples are needed but after the desorption test, all the samples were tested for water sorption and it is likely that for this, water modifies the microstructure, so it is impossible to know the correct dry weight. Therefore, as a compromise 33% RH was taken as the reference state and curves are replotted as water content per gram of dry hardened cement paste (hcp), graph 4-16.

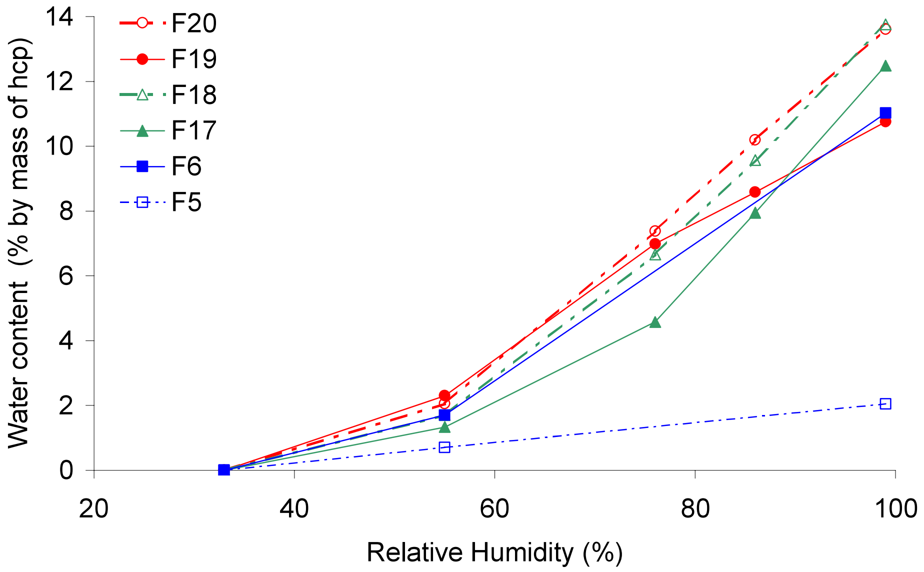

Figure 4- 16: Desorption curves up 33% to 86% RH at t= 810 days (33% RH= reference state)

The water content at 100% RH have been determined by water resaturation under vacuum of the 33%RH dried samples.

Desorption isotherms could lead to some information on porosity. For instance, it is possible to compute a total volumetric porosity p_v as follows:

$$p_v(\%) = V_{des}(RH = 100\%) \times \rho \times 100 \qquad (4.9)$$

ρ: density of the mortar specimen

V_{des} : adsorbed volume of water determined from the desorption isotherm for RH= 100% which is supposed to be the required volume to saturate all pores.

Mix	F20	F19	F18	F17	F6	F5
V_{des} (mm^3/g dry hcp)	136.2	107.6	137.6	124.9	110.2	18.8
p_v (% of dry sample)	20.1	13.4	20.3	16.1	12.6	2.4

Table 4- 1: Volumetric porosity of the samples (r_K> 9.6 nm)

The influence of the w/c ratio is as follows- the higher the w/c, the higher the porosity. All systems have a porosity of the cement paste in the range 12-20% except the mix F5; its very low porosity is explained by the low w/c ratio (0.25). Thereafter, we will see that this binder presents low permeation properties.

A pore size distribution was calculated using Kelvin – Laplace equation (Eq. (4.7)) and the volume of water desorbed for an interval of pore radius.

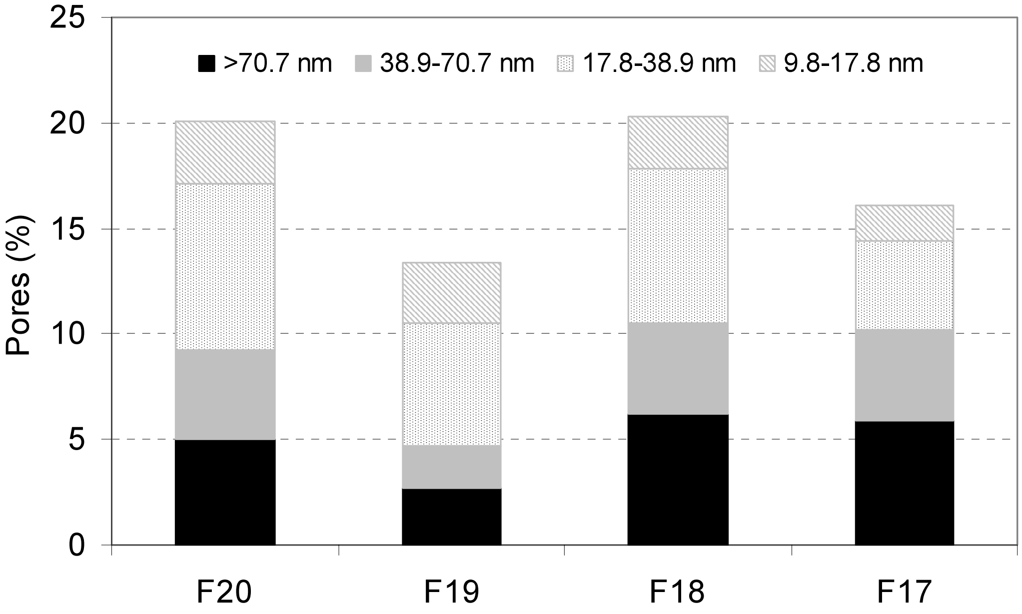

Figure 4- 17: Pore size distribution. Due to the weight gain of F5 and F6 for RH>76% i.e. pores >38.9 nm, pore size distribution could not be calculated.

For both Portland cement, F20 and F19, the main range of pores is 17.8 – 38.9 nm; the higher water-cement ratio for F20 creates more coarse pores than for F19. F18 has similar coarse pores than the equivalent binder with a lower w/c ratio F17 but more fine pores.

4.1.5.4 Determination of the cumulative pore volume and the specific surface

The reduction in relative pressure will result not only in emptying the largest pore of its capillary condensate, but also in a reduction in thickness of the physically adsorbed layer. So, the water desorption isotherms can be analysed by considering the coexistence of an adsorbed and a capillary phase in the pores which are supposed to be cylindrical = model BJH (Barrett – Joyner – Halenda) [35, 36]

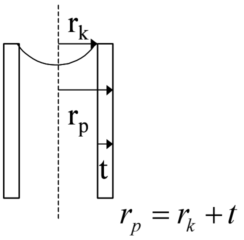

Figure 4- 18: BJH model

Adsorbed phase t

The adsorbed layer is characterised by the thickness according to the relative humidity. The values t on the whole RH range for non-porous adsorbents are drawn from the literature [37, 38]. Baroghel- Bouny [35] has compared these values with those she obtained for cement paste and curves fit almost perfectly at RH<70% and then diverge a little bit. For our calculations, the results from Baroghel-Bouny study are used.

Capillary phase r_k

In a porous material, in addition to the adsorption, evaporation or condensation is also observed at a RH corresponding to radius r_k calculated by the Kelvin – Laplace equation (Eq. 4.7).

For water at 296K:

$$\begin{aligned} &\sigma_{l/g} = 0.0729 N.m^{-1} \\ &\rho_w = 10^3 kg.m^{-3} \\ &M = 18.10^3 Kg.mol^{-1} \\ &R = 8.3144 J.mol^{-1}.K^{-1} \end{aligned} \qquad \rightarrow r_k = -\frac{10.6637}{\ln(RH)} \tag{4.10}$$

The calculation is based on a step by step analysis (desorption curves are divided in 3 intervals). For each interval, the desorbed water amount comes from:

- the emptying of a pores category with a radius r_p
- the decrease of the adsorbed multilayer t left behind in the first empty pores

The equation of B.J.H link the relative humidity to the porous volume:

$$V_{P_n} = \frac{\mathbf{r}_{\mathbf{P_n}}^2}{[\mathbf{r}_{\mathbf{k_n}} + (\Delta t_n)]^2} \left[(\Delta V_{des})_n - (\Delta t_n).\sum_{j=1}^{n-1} A_{P_j} \right] \tag{4.11}$$

with V_P: porous volume (mm^3/g dry hcp)

t: adsorbed layer (Å)

r_k: Kelvin radius (Å)

r_p: pores radius (Å) $r_P(RH) = t(RH) + r_k(RH)$

A_P: area of pores $A_p = 2V_p / r_P$

V_{des}: adsorbed volume determined from the experimental desorption curves (mm^3/g dry hcp)

The parameters in bold character indicate an average value: $\mathbf{x_n} = (x_n + x_{n-1})/2$

The variables *(Δx)* is calculated as following: $(\Delta x)_n = x_{n-1} - x_n$

Despite the fact that the desorption curves have only a few experimental points, it is sufficient for a comparative study; results are summarized in the following table:

Formulation	V_{des} (mm^3/g of dry hcp) Desorption curves	V_{Pcum} (mm^3/g of dry hcp) BJH method	S_{Scum} (m^2/g of dry hcp) BJH method
F20	136.2	132.9	95.1
F19	107.6	108.8	77.9
F18	137.6	131.8	91.7
F17	124.9	117.6	70.1

Table 4- 2: Comparison of adsorbed liquid volume V_{des} from desorption curves and porous volume calculated by BJH method and cumulative specific area S_{Scum} by BJH

The desorption data for F5 and F6 could not be exploited because of the weight gain at high RH.

The values provided by BJH method correlate well with these obtained by desorption curves.

The binders with the higher w/c ratio present the higher specific surface.

In Portland cement, the major contribution to the specific surface is provided by the C-S-H.

4.1.6 Comparison of the porosity values obtained with different methods

4.1.6.1 Solvent exchange and MIP with solvent as drying

F2 and F16 were measured by both these methods.

It is known that each method describes specific range of porosity; MIP technique includes pores from about 4 nm to 50 µm whereas the solvent exchange measures finer pores (theoretically down to the size of the solvent molecule, i.e. about 0.9 nm for isopropanol). The histogram below presents the comparison of the total porosity for F2 and F16.

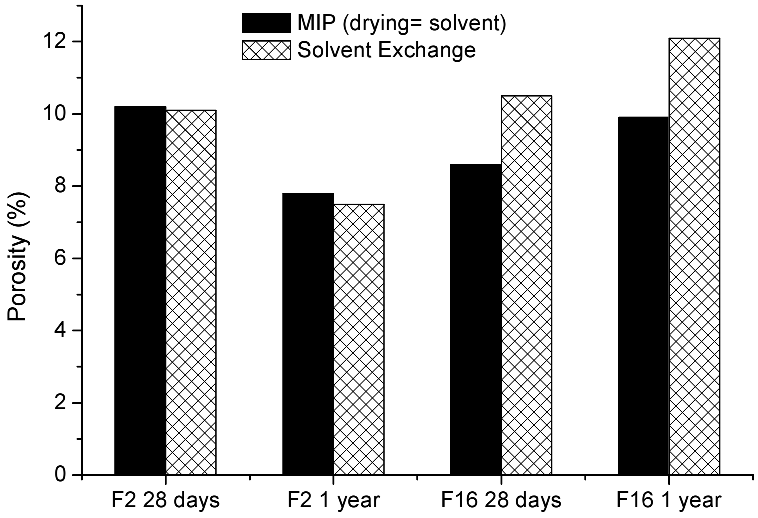

Figure 4- 19: Total porosity obtained by MIP with solvent as drying and solvent exchange for F2 and F16.

For the ettringite-rich binder, the porosity values is similar for both methods whereas for F16, MIP gives a lower value; this could be explained by the fact that the matrix of F16 may have a large volume of finer pores which are available for solvent replacement whereas MIP does not have access to this range of pores.

4.1.6.2 Solvent exchange and water desorption

F19 and F6 were measured by both methods.

Porosity (% volume sample)	F19	F6
Water desorption (~2.2 years)	13.4	12.6
Solvent exchange (3 years)	14.5	8.6

Table 4- 3: Comparison of the porosity obtained by water desorption and solvent exchange

Porosity measured by water desorption up to 33% RH takes into account pores with a radius >9.8 nm; therefore the interlayer water in the C-S-H is not included. In solvent exchange, the water in gel porosity of C-S-H is not replaced because of problem of charges; therefore a similar porosity value for both techniques is expected.

The higher porosity measured by water desorption of F6 could be explained by the loss of water from ettringite at 33%RH. As already reported, ettringite is sensitive to dehydration and loses progressively water molecules. For instance, after 100 days at 50%RH, the water content of ettringite decreases down to 10-13 H_2O per formula unit [39]. As the porosity value was calculated from the weight loss at 33%RH, it is certainly overestimated.

4.2 TRANSPORT PROPERTIES

The interaction of the surface layer of the concrete with the immediate external environment is a paramount importance in many degradation processes such as ingress of chlorides and sulfates, carbonation or wetting/drying cycles. For this reason, an evaluation of the transport properties should provide a valuable indication of the durability. The theory of transport in concrete has been reviewed by numerous authors [40-42]. A brief summary is presented below.

4.2.1 Transport mechanisms in concrete

Depending on the driving force, the transport of fluids into concrete is usually classified into four mechanisms namely diffusion, permeation, capillary absorption and wick action.

4.2.1.1 Diffusion

The diffusion of gas, ion or liquid is stimulated by a concentration gradient and can be described in a porous solid by Fick’s Law as

$$J = -D \frac{\delta c}{\delta x} \tag{4.12}$$

J represents the flow, D the diffusivity and $\frac{\delta c}{\delta x}$ the concentration gradient.

A factor to consider while dealing with the diffusion process is the chemical reactions taking place between the penetrating substances and concrete. For example, the diffusion of chloride ions is accompanied by a physical and chemical binding with the hardened cement paste whereas oxygen is an inert gas [43, 44].

Oxygen diffusion was chosen for this work because it is fast and is a good indicator for other diffusion processes. It also affects the progress of corrosion of reinforcement in concrete. Corrosion reaction progresses by an electro-chemical mechanism and oxygen plays the role of accelerating cathodic reaction.

4.2.1.2 Permeation

Permeation can occur in liquid or gaseous state and plays an important role in the concrete deterioration by mechanisms such as alkali-aggregate reaction, sulfate attack or freeze-thaw damage.

Permeability is defined as the ease with which a fluid will pass through the specimen under the action of a pressure gradient. Darcy’s law states that the steady-state rate of flow is directly proportional to the pressure gradient and can be expressed by the following equation:

$$Q = -\frac{kA}{\mu} \frac{dP}{dz} \tag{4.13}$$

where Q is the flow, μ the viscosity, A the sample surface area and dP/dz the pressure gradient. Latter may either be externally applied or by the capillary forces.

Water permeability measurement is a relevant indicator of durability in deep sea or water retaining structures such as dams. Nevertheless, measurement of oxygen permeability has been preferred in this work because for measuring liquid permeability, the specimen should be completely saturated prior to testing to minimize the time required to reach a steady state. In this work with conditionings at RH<86%RH, weeks or months could be required to achieve a measurable cumulative flow in the downstream collection volume.

4.2.1.3 Capillary absorption

Transport of liquids, in particular water, in porous solids due to surface tension acting in capillaries is called water absorption. The force which drives the water results from the difference in pressure between the two sides of the menisci formed by water in the pores. Absorption is related not only to the pore structure, but also to the moisture condition of the concrete.

The invasion of water provides a preferential path for the penetration of deleterious materials like chloride, therefore water sorption plays a strong role in durability.

4.2.1.4 Wick Action

Wick action is the transport of water from a face in contact with water to a dry face. Species dissolved in the water are transported to the zone where drying occurs and may result in salt crystallization.

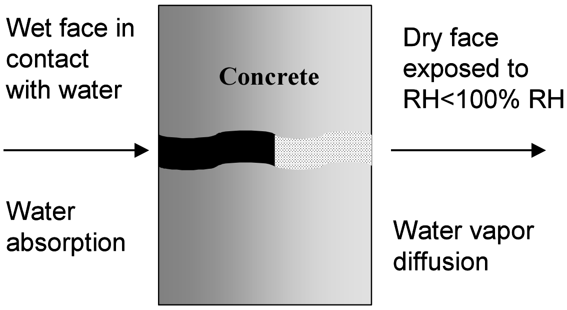

Figure 4- 20: Wick action through concrete [45]

It is worth pointing out that the situation is complicated by the fact that concrete will often be below the fully saturated state so that transport will be a combination of vapour and liquid diffusion.

4.2.2 Laboratory investigations

Many test methods and techniques can be used to carry out the assessment of penetration properties of concrete and the results depends strongly on the chosen experiments. Long et al. [4] give an outline of various methods.

All experiments were carried out at Imperial College under the direction of Dr. Nick Buenfeld. The employed techniques are described below. The mortars mixes are described in 4.1.5.1; they were kept in varying relative humidity (33, 55, 76 and 86%RH) up to the test time (810 days).

4.2.2.1 Measurements of oxygen diffusivity [46]

With the apparatus (figure 4-21), oxygen and nitrogen gases were continuously fed under a constant pressure to the two sides of a specimen mounted in a cell. Traces of oxygen are detected in the stream of the nitrogen. When the test was started, the oxygen concentration in the nitrogen gas changed and several minutes later became more or less constant. The time at which the oxygen concentration became a constant value was judged to be the steady state and concentration, pressure and flow were measured and the average diffusion coefficient D_n of oxygen was determined by the following equation:

$$D_n = \frac{Q_A.t}{A(C_2 - C_1)} \tag{4.14}$$

C_2 represents the concentration of oxygen in oxygen stream, C_1 the oxygen concentration in nitrogen stream and Q_A the diffusion rate of oxygen (m^3/s). t and A are respectively the thickness and the area of the sample.

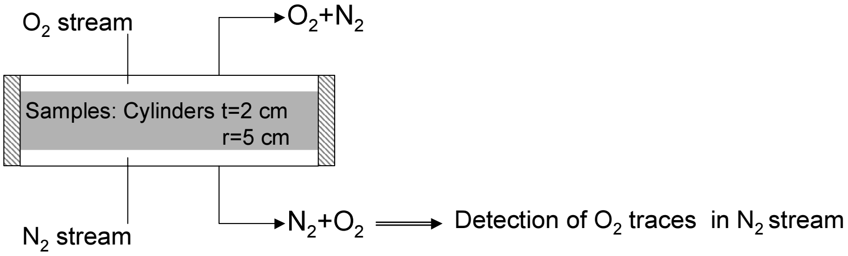

Figure 4- 21: Schematic set-up for O_2 diffusion

4.2.2.2 Measurements of oxygen permeability

The test was carried out by applying a constant pressure head to the test sample, and the flow rate of gas through the sample at steady state was measured, figure 4-22. A pressure regulator is used to get the inlet a the desired value with the outlet pressure being atmospheric. A gas flowmeter in the downstream flow path is used to monitor the gas flow rate. A set of 3 test pressures (0.5, 1.5 and 2.5 bars) was used in this study.

With this set-up, the gas permeability is given by:

$$Q = \frac{k.A(P_1^2 - P_2^2)}{2\eta.t.P_2} \tag{4.15}$$

where: t = specimen thickness (m)

A = specimen cross-sectional area (m^2)

η = viscosity of oxygen

P_1 = absolute pressure on inlet face (N/m^2)

P_2 = absolute pressure on outlet face (N/m^2)

Q = outflow rate (m^3/s)

k = permeability coefficient (m^2)

With $\eta_{oxygen} = 2{,}02.10^{-16} Ns/m^2$ and $P_2 = 1bar$, the equation (4.16) becomes

$$k = \frac{4{,}04.10^{16} Qt}{A(P_1^2 - 1)} \tag{4.16}$$

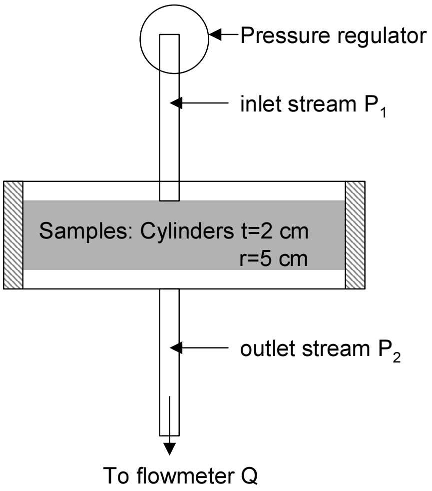

Figure 4- 22: Basic experimental set-up for O_2 permeability

4.2.2.3 Capillary water absorption test

The measurement of water capillary sorption is in principle, a very simple experiment. The cylindrical specimen was exposed to distilled water on one of the face by placing them in a tray as shown in figure 4-23. To avoid excessive leaching of calcium hydroxide, some researchers recommend using saturated calcium hydroxide solution as the sorbing fluid [47], while others have noted little or no difference between this solution and distilled water[48]. For our binders, distilled water was chosen.

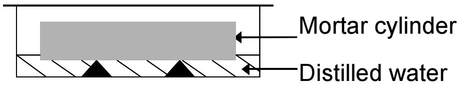

Figure 4- 23: Experimental set-up for water absorption

The uptake of water by capillary absorption was measured through the weight gain of the mortar surface in contact with water at the set time intervals of 3, 5, 10 min, 1h…1 day…It is usually admitted that the uptake of water per unit area of concrete surface W follows a linear relationship with the square root of time for the suction period [48]:

$$\frac{W}{A\rho_{eau}} = S\sqrt{t} + S_0 \tag{4.17}$$

where W is the volume of water absorbed, A is the sample surface area exposed, t the time, S is the sorptivity (the slope of the W/A vs. $t^{1/2}$ plot) and S_0 is a correction term added to account for surface effects at the time the specimen is placed in contact with water.

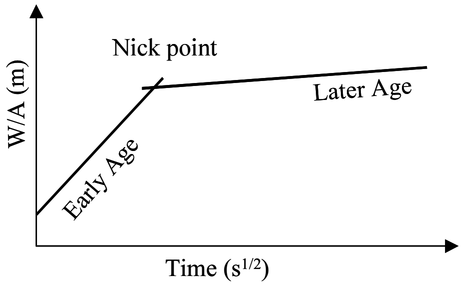

Figure 4- 24: Calculation of the sorption coefficient

As shown by the schema above, the capillary sorption is divided into two different regimes, both linear with time. The later age sorption coefficient is usually attributed to phenomena such as filling of larger pores and air voids. The Nick-point represents the time at which a percolated path of water forms in the specimen.

4.2.3 Experimental results

4.2.3.1 Oxygen diffusivity

The average coefficient of oxygen diffusivity obtained from 4 replicate specimens are presented in figures 4-25.

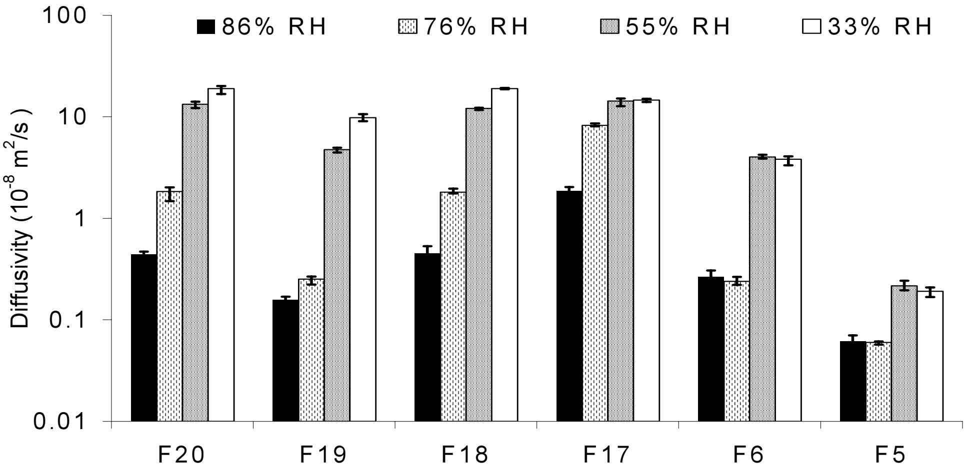

Figure 4- 25: Oxygen diffusion coefficient of different mortars

The results show the same trend for all binders: the diffusivity increases with the decrease of the relative humidity. On drying the pore system will gradually empty and an increasing volume of the pore space is available for the gas flow; the diffusion is faster in gas than in liquid. Large increases of diffusivity are observed for drying from saturation down to 55%RH but further drying to 33%RH had little effect. This is in agreement with the dependence of oxygen diffusivity and moisture reported by Kobayashi [49] shown below.

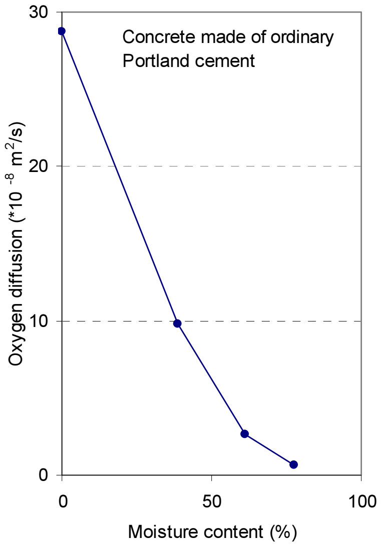

Figure 4- 26: Relations between moisture content and diffusion [49]

The influence of water-cement ratio is also apparent. The oxygen diffusivity becomes larger as the porosity increases. These results coincide with the trend indicated in research on Portland cement pastes [49, 50]. However, the couple F17 / F18 do not follow the same trend; F17 presents higher oxygen diffusion coefficients while it is the binder with the lower porosity. It is because of the addition of lime filler which modifies the pore size distribution; as we noticed in section *4.1.5.4*, F17 has a majority of coarse pores, thus diffusion could be facilitated.

If we compare binders with the same w/c ratio (F19/F17/F6), the coefficients of oxygen diffusion exhibit some variation; the diffusivity of F17 is the highest under all curing conditions, while F6 and F19 are generally equivalent. These results coincide with the calculated porosity (Table 4-1); F17 is the most porous and the porosity of F19 and F6 is in the same range.

4.2.3.2 Oxygen permeability

The data for the oxygen permeability are presented in the histogram below. For specimen F5 the steady-state condition could not be established due to its low permeability, for this reason the values are not reliable.

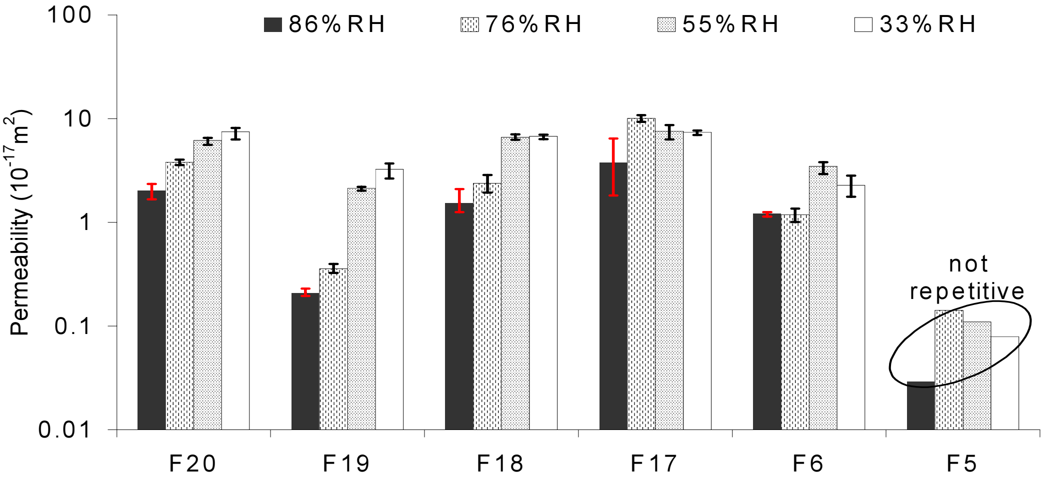

Figure 4- 27: Oxygen permeability coefficient of different mortars

As it was mentioned for the diffusion results, there is a variation of the results depending on the RH, the water-cement ratio and the binder composition. The permeability is significantly increased as the capillary pores are emptied, in other words as the RH is lowered; the channels available for gas flow increase in volume and connectivity.

For Portland mortar, the permeability of 33%RH conditioned samples is 15 times higher than of their corresponding 86%RH cured samples while F6 is less sensitive to the drying. The permeability of F6 is increased at high RH by 4-5 times as compared to that of Portland sample while at low RH, the values are nearly similar. The binders F17/F18 exhibit smaller variations between the conditioning; the influence of the pore size distribution is less than for oxygen diffusion.

Afterwards, the permeability for the 0.5 w/c ratio Portland sample is determined in the range 7-10 times higher than for the 0.35 w/c ratio. It is known that the permeability is mainly dependent on capillary pores volume [50-52], consequently the w/c ratio.

The link between oxygen permeability and degree of saturation is well-established in the studies of Abbas [53, 54] .This dependence has been also studied by Villain [55] who also found a decrease of permeability with the increase of the saturation degree.

The graph 4-28 illustrates the permeability versus the degree of saturation of our experimental results and data from Abbas [54] were also shown.

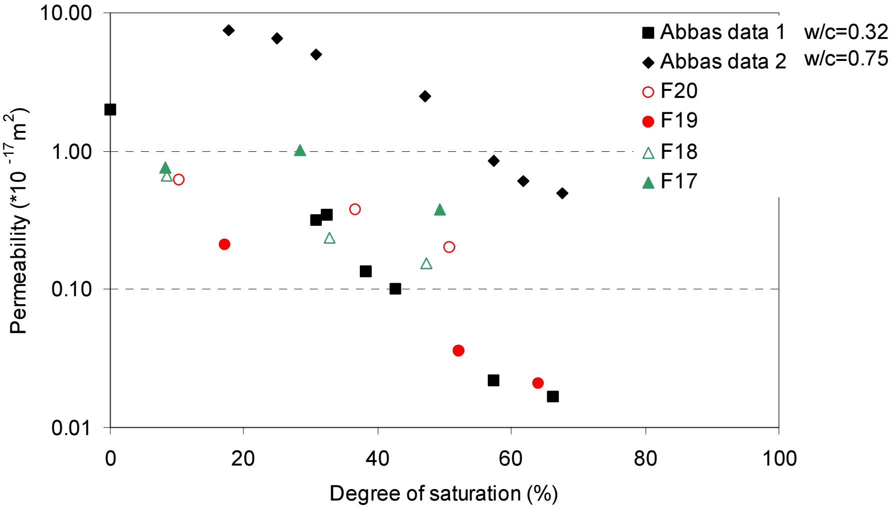

Figure 4- 28: Oxygen permeability as a function of degree of saturation. Abbas data 1: concrete with R_c 28d=100 MPa, w/b=0.32, silica fume, porosity =8.4%. Abbas data 2: concrete with R_c 28d=25 MPa, w/b=0.75, porosity =12.9% [54].

The results from Abbas study show a difference of one order of magnitude in the values of permeability at the same values of saturation which can be explained by porosity. Porosity is not the single parameter to be taken into account because the porosity of our binders range from 13 to 20% and permeability values are in the same range for different degree of saturation. This can be explained by considering the fact that there is a strong effect of the connectivity of the pores and of the tortuosity of the percolation path on the value of the permeability. However, considering Abbas's data for a w/c ratio of 0.32 which is close to our experimental w/c, a trend can be drawn (blue line). Permeability depends on the degree of saturation but there is no unique relationship between permeability value and degree of saturation.

4.2.3.3 Capillary water absorption

The cumulative sorption (i.e. the volume of water/surface) μ (cm) is calculated by the following formula:

$$\mu = \frac{m_t - m_0}{A\rho_{eau}} \tag{4.18}$$

where m_t, m_0 are the weight at the time t and the initial weight (g) respectively, A the surface area (cm^2) and ρ_{eau} the water density ($g.cm^{-3}$).

The figure 4-29 summarizes the cumulative water sorption for all specimen for each relative humidity.

Note that both the short and long time moisture sorptions are consistent with a $t^{1/2}$ behaviour, However F6 33%RH deviates from the square-root of time behaviour and this may be attributed to interactions of water with the cement paste. The break of the slope in figure 4-28 corresponds to the time when the top of the samples becomes wet.

As water invades the pore space, it encounters smaller pores and thus slows down the rate of sorption. There is a moderate difference in the total water taken up for the different samples. Clearly, the degree of saturation of the material plays an important role in controlling the uptake water. Hall [56] and Martys [48] have published similar observations.

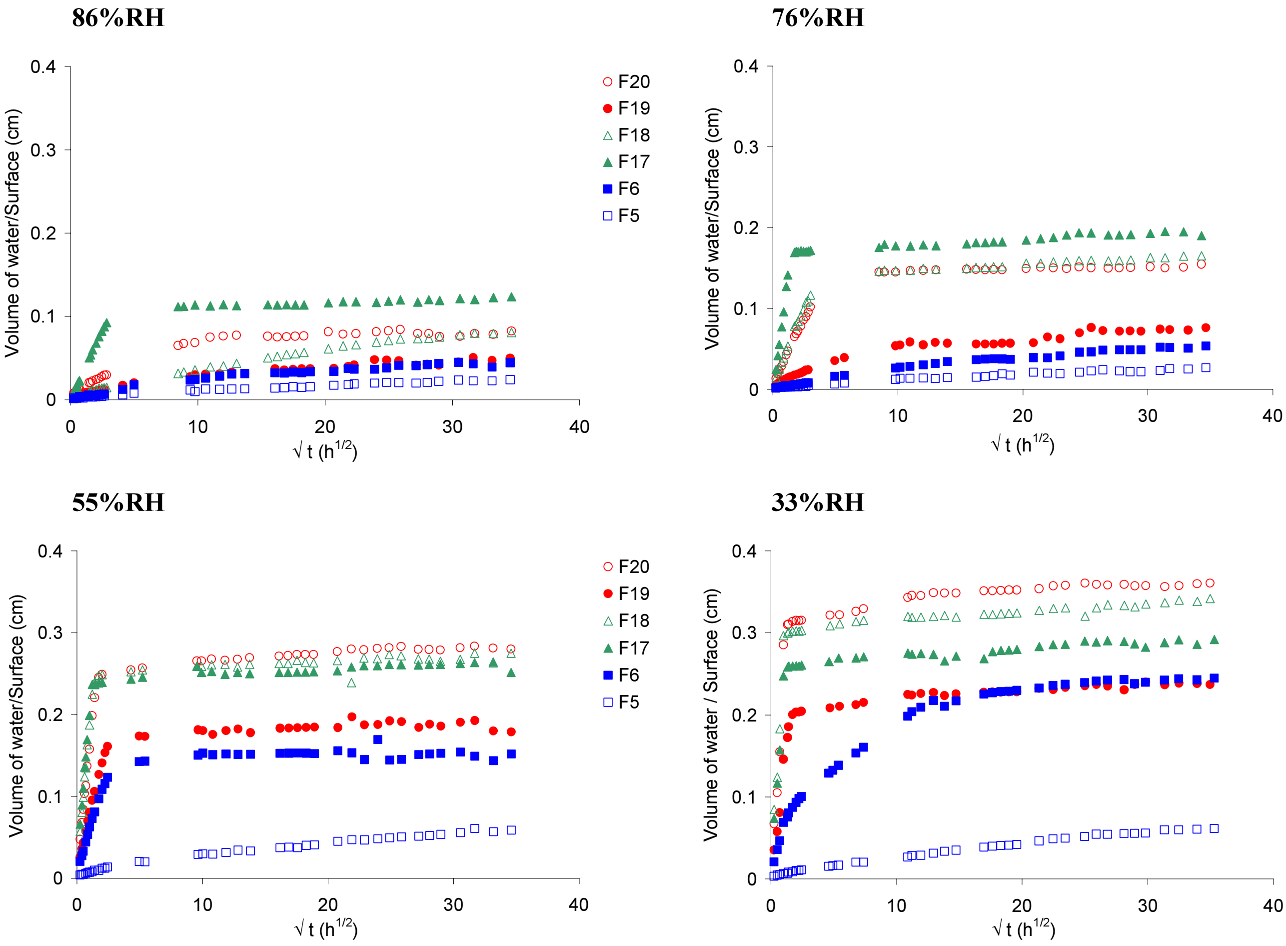

Figure 4- 29: Rate of absorption versus time at different RH

The average coefficients of sorptivity obtained from fits of the data in figure 4-29 are plotted in figure 4-30.

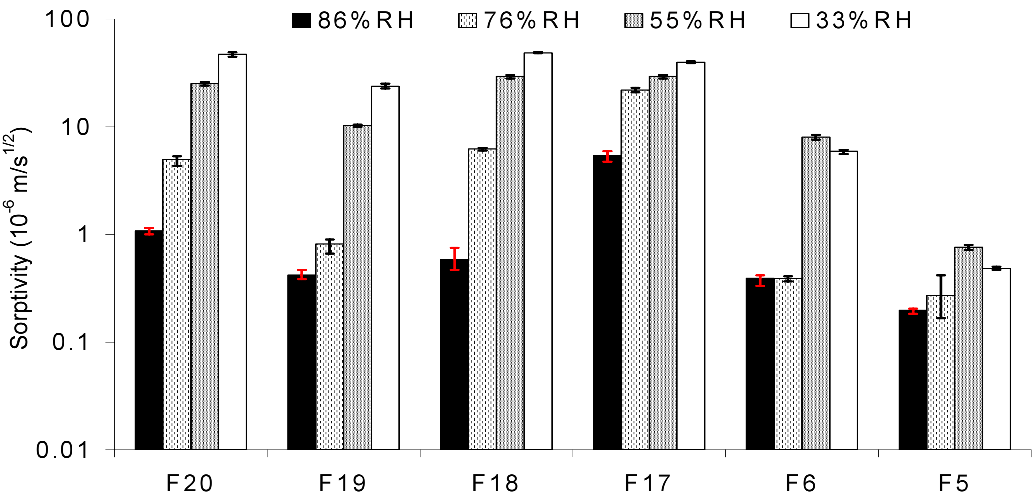

Figure 4- 30: Early age sorptivity

The higher the relative humidity, the lower the sorptivity, indicating that the pores are initially partially filled with water; the possible flow paths are blocked or hampered.

The amount of water sorption depends on mixture design. F5 was designed to produce lower porosity mortar which results in a lower absorption. Sorptivity is more sensitive to the porosity or pore size distribution at high degree of saturation for the couple F18/F17 while for F5/F6 it is at low degree of saturation.

4.2.4 Discussion

The equilibrium moisture conditions plays a significant role in the state of saturation filling of pores, whatever the binder composition be. Shafiq [57] has recently published results on this influence: the porosity becomes higher as the relative humidity in the environment decreases. We know that the porosity is directly connected to the w/c ratio, so if we focus on our binders by pair (F19/F20 and F5/F6), the results are in good agreement with Shafiq; by increasing the w/c and thus the porosity, the permeation properties increase. However, for the couple F17/F18, the explanation is a little more complicated because lime filler was added in F18; the lowest transport properties is for F18 which presents the highest porosity. This behaviour underlines the complexity of the relationship between transport properties, total porosity and pore size distribution.

The curing conditions also play a role in the moisture content; the higher the degree of saturation, the lower the penetration properties. These observations are related to the size of the accessible pores: the macropores are drained first and represent a preferential way for the transfers. The range of studied conditioning simulates more or less the real exposure conditions for mortars.

To highlight the disparities between the binders for the same w/c ratio at 33%RH, it is interesting to draw a summary table.

w/c=0.35, 33%RH	**F19 (Portland)**	**F17 (rich in PC)**	**F6 (rich in CAC-C$)**
$\mathbf{D_{O2}}$ (10^{-8} m^2/s)	9.8	14.6	3.8
$\mathbf{k_{O2}}$ (10^{-17} m^2)	3.2	7.4	2.3
S (10^{-8} $m/s^{1/2}$)	23.8	39.7	5.9

Table 4- 4: Comparison of the different coefficients at 33%RH

The water sorption and oxygen diffusion of the binder rich in calcium aluminate cement F6 are fairly low compared with that of Portland whereas the permeability is very close. F17 always presents the highest values.

4.2.4.1 Relationships between transport properties

The flow of liquids or gases should be interrelated to some extent since these flow processes occur in the same pore system.

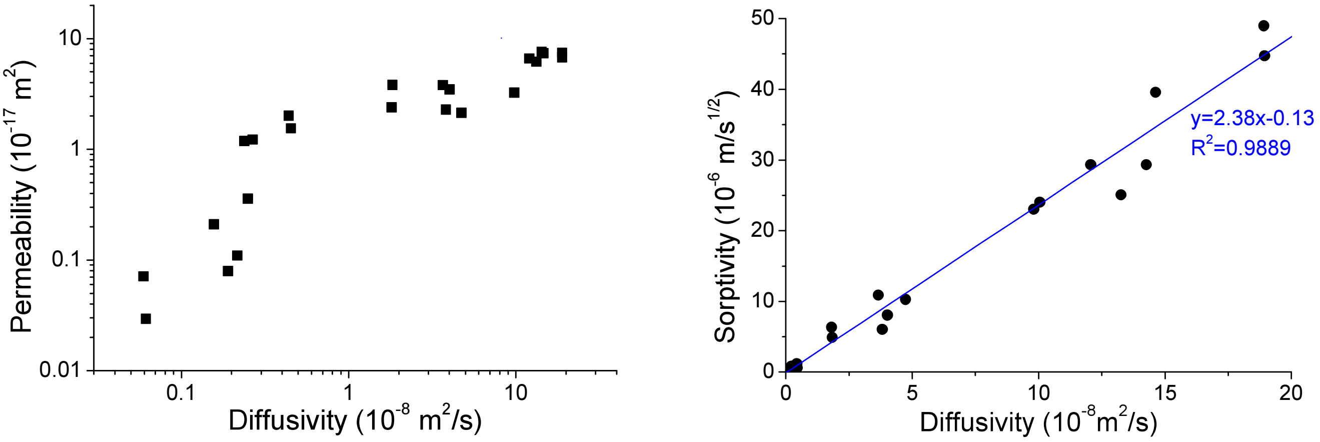

Figure 4- 31: Relations between diffusivity, permeability and sorptivity

The relationship found between diffusivity and permeability is illustrated in Figure 4-31. All the points seem to follow the same trend, a linear one in a log-log scale, indicating a power law dependence. Lawrence [46] has established the same relationship for Portland systems. Nyame [50] and Halamickova [58] have previously published that permeability can be represented by a power-law function of critical pore radius (maximum of the dV/dp curve in MIP) while diffusivity itself has been shown to be a linear function of critical radius; the power law we found experimentally between permeability and diffusivity expresses the same trend.

As shown on the second graph, there is a linear relationship between diffusivity and sorptivity. Data collected by the simpler sorption test appear to be readily convertible to the theoretically useful measurements of diffusivity.

Moreover, whatever the composition of the binder, the same relationships governs the transport properties, we can conclude that the ettringite based systems behave similarly to Portland systems at equivalent porosity.

4.2.4.2 Correlation between porosity and transport properties

As mentioned before, it is often considered that as a first approximation, porosity governs the transport properties; the graphs below display the relation transport properties vs. porosity obtained in this study.

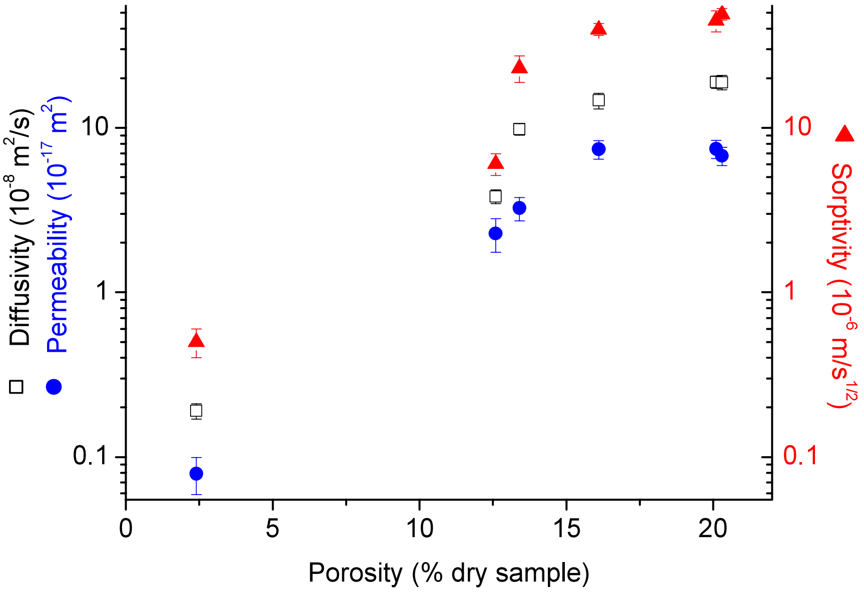

Figure 4- 32: O_2 diffusivity; O_2 permeability and water sorption at 33% RH vs. porosity measured by water desorption

We have too few data points to establish a trend but it seems that the total porosity is not uniquely related to transport properties because no simple relationship could be found, graph 4-32. Along this study we have demonstrated that the transport properties also depends on the saturation state of the samples. Moreover, the transport properties for F18 was found to be lower than F17 in spite of the fact that the former had a greater total pore volume. On examining the pore size distribution and transport properties data, it is apparent that large pores played an important role in determining the different coefficients than the smaller pores.

This shows that to develop a more reliable relationship between transport properties and pore structure, it would be better to take into consideration several parameters such as pore size distribution or degree of saturation, rather than depend on the total porosity alone.

4.2.5 Conclusion

Results including oxygen diffusivity and permeability and water absorption of a range of different mortars have been presented. The following conclusions can be drawn:

- The main factors that control the permeation properties of cementitious materials are the pore structure, the pore size distribution and the environment. Indeed, as we have discussed, the degree of filling of the pore structure greatly affects diffusion, permeability and sorption processes.
- The degree to which the oxygen diffusion, oxygen permeability and water sorption is influenced by the curing environment depends on the type of the cement used.
- Among the different mixes, it appeared that the binder F5 with the lowest w/c is the most impermeable.
- It was found that at similar porosity, Portland and CAC-C$ rich binder have similar properties.

4.3 CONCLUSION

Porosity and transport properties were investigated in this chapter. The combination of these results with those of hydration chemistry (Chapter 3) provides basic knowledge to better understand the degradations of the cementitious materials in controlled atmosphere.

4.4 REFERENCES

1. Buenfeld, N.R. Measuring and modelling transport phenomena in concrete for life prediction. In Prediction of concrete durability, N. Glanville, ed. pp. 77-90.
2. Basheer, L., et al. (2001). Assessment of the durability of concrete from its permeation properties: a review. *Construction and Building Materials* **15**, 93-103.
3. Bentz, D.P., et al. (2001). Sorptivity-based service life predictions for concrete pavements. In *7th International Conference on Concrete Pavements.* (NIST, ed.), vol. 1. pp. 180-193: Orlando- Florida.
4. Long, A.E., et al. (2001). Why assess the properties of near-surface concrete? *Construction and Building Materials* **15**, 65-79.
5. Moukwa, M., and Aitcin, P.C. (1988). The Effect of Drying on Cement Pastes Pore Structure as Determined by Mercury Porosimetry. *Cement and Concrete Research* **18**, 745-752.
6. Galle, C. (2001). Effect of drying on cement-based materials pore structure as identified by mercury intrusion porosimetry - A comparative study between oven-, vacuum-, and freeze-drying. *Cement and Concrete Research* **31**, 1467-1477.
7. Lange, D.A., et al. (1998). Characterization of cement pore structure using Wood's metal and mercury porosimetry. In *Imaging Technologies - Techniques and Applications in Civil Engineering* (M.S. Frost F., ed.). pp. 197-206.
8. Abdel-Jawad, Y. (1988). Pore structure of hydrated cement determined by mercury porosimetry and nitrogen sorption techniques. In *Pore structure and permeability of cementitious materials* (R.a. Skalny, ed.), vol. 137. pp. 105-118: Boston.
9. Day, R.L., and Marsh, B.K. (1988). Measurement of Porosity in Blended Cement Pastes. *Cement and Concrete Research* **18**, 63-73.
10. Juenger, M.C.G., and Jennings, H.M. (2001). The use of nitrogen adsorption to assess the microstructure of cement paste. *Cement and Concrete Research* **31**, 883-892.
11. Crumbie, A.K. (1994). Characterisation of the microstructure of concrete. PhD thesis, Imperial College, London.
12. Thomas, M.D.A. (1989). The suitability of solvent exchange techniques for studying the pore strucutre of hardened cement paste. *Advances in Cement Research* **2**, 29-34.
13. Feldman, R.F., and Beaudoin, J.J. (1991). Pretreatment of Hardened Hydrated Cement Pastes for Mercury Intrusion Measurements. *Cement and Concrete Research* **21**, 297-308.
14. Konecny, L., and Naqvi, S.J. (1993). The Effect of Different Drying Techniques on the Pore-Size Distribution of Blended Cement Mortars. *Cement and Concrete Research* **23**, 1223-1228.
15. Marsh, B., et al. (1997). The effect of solvent replacement upon the pore structure characterization of portland cement paste. *Principles and Applications of Pore Structural Characterization: Proceedings of the RILEM Milan*, 365-374.
16. Diamond, S. (2000). Mercury porosimetry - An inappropriate method for the measurement of pore size distributions in cement-based materials. *Cement and Concrete Research* **30**, 1517-1525.
17. Chatterji, S. (2001). A discussion of the paper "Mercury porosimetry - an inappropriate method for the measurement of pore size distributions in cement-based materials" by S. Diamond. *Cement and Concrete Research* **31**, 1657-1658.
18. Cook, R.A., and Hover, K.C. (1999). Mercury porosimetry of hardened cement pastes. *Cement and Concrete Research* **29**, 933-943.

19. Willis, K.L., et al. (1998). Image-based characterization of cement pore structure using wood's metal intrusion. *Cement and Concrete Research* **28**, 1695-1705.
20. Moro, F., and Bohni, H. (2002). Ink-bottle effect in mercury intrusion porosimetry of cement- based materials. *Journal of Colloid and Interface Science* **246**, 135-149.
21. Parrott, L.J. (1984). An examination of two methods for studying diffusion kinetics in hydrated cements. *Materials and Structures*, 131-137.
22. Parrott, L.J. (1981). Effect of Drying History Upon the Exchange of Pore Water with Methanol and Upon Subsequent Methanol Sorption Behavior in Hydrated Alite Paste. *Cement and Concrete Research* **11**, 651-658.
23. Marcdargent, R.A., et al. (1983). Water-methanol exchnage in mortars and concrete: a method of studying mass transfer. In *International Colloquium "Materials Science and Restoration"* (L.u. Chemie, ed.). pp. 51-55: Germany.
24. Feldman, R.F. (1987). Diffusion Measurements in Cement Paste by Water Replacement Using Propan-2-ol. *Cement and Concrete Research* **17**, 602-612.
25. Gran, H.C., and Hansen, E.W. (1998). Exchange rates of ethanol with water in water-saturated cement pastes probed by NMR. *Advanced Cement Based Materials* **8**, 108-117.
26. Beaudoin, J.J., et al. (1998). Solvent replacement studies of hydrated portland cement systems: The role of calcium hydroxide. *Advanced Cement Based Materials* **8**, 56-65.
27. Beaudoin, J.J., et al. (2000). Solvent exchange in partially saturated and saturated microporous systems - Length change anomalies. *Cement and Concrete Research* **30**, 359-370.
28. Hughes, D.C., and Crossley, N.L. (1994). Pore Structure Characterization of GGBS OPC Grouts Using Solvent Techniques. *Cement and Concrete Research* **24**, 1255-1266.
29. Takahashi, T., et al. (1997). Relationship between compressive strength and pore trucutre of hardened cement pastes. *Advances in Cement Research* **33**, 25-30.
30. Beaudoin, J.J., et al. (1994). Pore structure of hardened portland cement pastes and its influence on properties. *Advanced Cement Based Materials* **1**, 224-236.
31. Robler, M., and Odler, I. (1985). Investigations on the relationship between porosity, structure and strength of hydrated portland cement pastes I. Effect of porosity. *Cement and Concrete Research* **15**, 320-330.
32. Matusinovic, T., et al. (2003). Porosity-strength relation in calcium aluminate cement pastes. *Cement and Concrete Research* **33**, 1801-1806.
33. Rose, D.A. (1965). Water movement in unsaturated porous materials. *Bulletin RILEM* **29**, 119-124.
34. Wong, S.F., et al. (2001). Study of water movement in concrete. *Magazine of Concrete Research* **53**, 205-220.
35. Baroghel-Bouny, V. (1994). Caractérisation des pâtes de ciment et des bétons. Méthode, analyse, interprétations., LCPC Edition.
36. Barrett, E.P., et al. (1951). The determination of pore volume and area distributions in porous substances. I- Computations from nitrogen isotherms. *Journal of American Chemical Society* **73**, 373-380.
37. Badmann, R., et al. (1981). The statistical thickness and the chemical potential of adsorbed water films. *Journal of Colloid and Interface Science* **82**, 534-542.
38. Hagymassy, J., et al. (1969). Pore structure analysis by water vapor adsorption. *Journal of Colloid and Interface Science* **29**, 485-491.
39. Zhou, Q., and Glasser, F.P. (2001). Thermal stability and decomposition mechanisms of ettringite at < 120 °C. *Cement and Concrete Research* **31**, 1333-1339.

40. Bentz, D.P., et al. (1999). Transport properties and durability of concrete: lietrature review and research plan. *NIST* **NISTIR 6395**.
41. Kropp, J., et al. (1995). Transport mechanisms and definitions. In Performance criteria for concrete durability, Volume Rilem Report 12, J. Kropp, ed. (E& FN Spon), pp. 4-13.
42. Hall, C. (1994). Barrier performance of concrete: a review of fluid transport theory. *Materials and Structures* **27**, 291-306.
43. Taylor, H.W.F. (1997). Cement Chemistry (London: Thomas Telford).
44. Chandra, S. (1988). Hydrochloric-Acid Attack on Cement Mortar - an Analytical Study. *Cement and Concrete Research* **18**, 193-203.
45. Aldred, J.M., et al. (2004). Effect of initial moisture content on wick action through concrete. *Cement and Concrete Research* **34**, 907-912.
46. Lawrence, C.D. (1984). Transport of oxygen through concrete. In *Chemistry and Chemicaly-related properties of cement*, vol. 35. pp. 277-293.
47. Sosoro, M. (1998). Transport of organic fluids through concrete. *Materials and Structures* **31**, 162-169.
48. Martys, N.S., and Ferraris, C.F. (1997). Capillary transport in mortars and concrete. *Cement and Concrete Research* **27**, 747-760.
49. Kobayashi, K., and Shuttoh, K. (1991). Oxygen Diffusivity of Various Cementitious Materials. *Cement and Concrete Research* **21**, 273-284.
50. Nyame, B.K., and Illston, J.M. (1980). Capillary pore structure and permeability of hardened cement paste. In *7th International Symposium on Chemistry of Cement*, vol. 3. pp. 181-186: Paris.
51. Mehta, P.K., and Manmohan, D. (1980). Pore size distribution and permeability of hardened cement pastes. In *7th International Symposium on Chemistry of Cement*, vol. 3. pp. 1-5: Paris.
52. Goto, S., and Roy, D.M. (1980). The effect of w/c ratio and curing temperature on the permeability of hardened cement paste. *Cement & Concrete Research* **11**, 575-579.
53. Abbas, A., et al. (1999). Gas permeability of concrete in relation of its degree of saturation. *Materials and Structures* **32**, 3-8.
54. Abbas, A., et al. (2000). The importance of gas permeability in addition to the compressive strength of concrete. *Magazine of Concrete Research* **52**, 1-6.
55. Villain, G., et al. (2001). Mesure de la perméabilité aux gaz en fonction du taux de saturation des bétons. *Revue Francaise de Génie Civil* **5**, 251-268.
56. Hall, C. (1994). Tightness of concrete with respect to fluids. *Materials and Structures* **27**, 291-306.
57. Shafiq, N., and Cabrera, J.G. (2003). Effects of initial curing condition on the fluid transport properties in OPC and fly ash blended cement concrete. *Cement and Concrete Composites* **26**, 381-387.
58. Halamickova, P., et al. (1995). Water permeability and chloride ion diffusion in portland cement mortars: Relationship to sand content and critical pore diameter. *Cement and Concrete Research* **25**, 790-802.

Chapter 5. Degradation mechanisms. Accelerated ageing

The sources of deterioration in cement-based systems can be divided into two main groups: chemical and physical degradations. We will focus here on the former one. To obtain durability results in reasonable experimental times, accelerating ageing is often used. This is generally a simplified version of the natural weathering with a relatively stable and controllable environment which allows a single degradation mechanism to be isolated. Nevertheless, although it is useful to understand a specific process, it has to be checked against field ageing which takes into account the possible synergies between all degradations mechanisms. This double approach (accelerated ageing and natural weathering) was applied here to identify and understand the potential degradation mechanisms of ternary systems. Chapter 5 deals with the accelerated ageing and Chapter 6 the natural ageing.

The sources of deterioration are numerous and so a limited number were selected among the possible degradation mechanisms. First, attention is directed toward the influence of the storage environment and carbonation and then two more specific tests are examined, acid attack and external sulfate attack. Freezing thawing cycles were also done but as this accelerated test is more physical than chemical, results were not thoroughly analysed; experimental data are given in Appendix B.

5.1 INFLUENCE OF THE STORAGE CONDITIONS

Field experience indicates that materials exhibiting a high degree of drying shrinkage are likely to crack and fail prematurely. For repair mortars, high shrinkage affects their compatibility with concrete. Moreover, concerns have been expressed about the dimensional stability of ettringite-based systems because of possible excessive expansion. As no data are available on these ternary binders, it is indispensable to consider the effect of the storage environment on their stability.

5.1.1 Experimental conditions

Mortar prisms were cast and stored under three different conditions:

- Wet conditions (20°C, under water)

- Dry conditions (20°C at 50%RH)
- Cycles – alternating between one week at 50°C, 50%RH and one week at 20°C, 90%RH.

The formulations subjected to this testing regime were F1, F4, F8, F12, F14, F16, F17, F19, F21, figure 5-1. All specimen were initially cured for 7 days at 90%RH. Their long term behaviour under the storage conditions described above was characterised by mean of:

- Dimensional variations measurements
- Effective Young's modulus E (obtained by Grindosonic measurements)
- Compressive strength tests at end of testing period

The initial time t=0 was taken just after demoulding (4h) except for F19 which was demoulded after 24h.

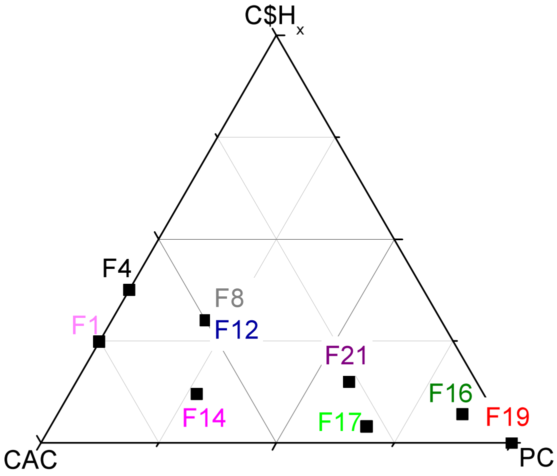

Figure 5- 1: Investigated systems in the test "Influence of the storage conditions"

5.1.2 Dimensional variations

5.1.2.1 20°C under water

Over the long term, the results show that in all cases except F4 and F21 the dimensional variation becomes stable and ranges from 500 to 2000 µm/m, figure 5-2. If we focus on the very early age, F16 presents a higher initial expansion (1750 µm/m after 1 day) which remains stable over time. Formulation F4 exhibits excessive swelling, 9000 µm/m after one year; calcium sulfate in excess in this formulation and the new source of water could lead to expansive formation of ettringite. F21 also exhibits expansion over time but in a lesser extent.

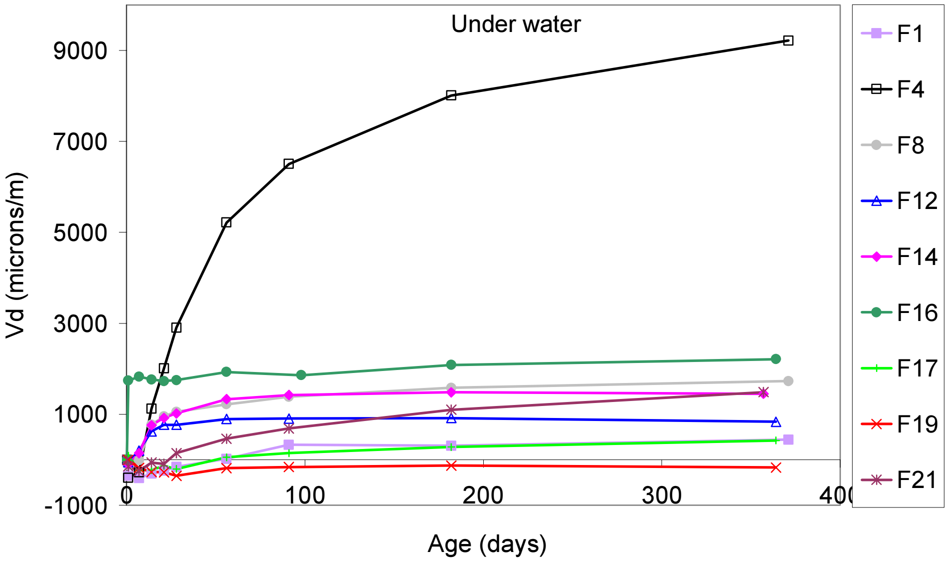

Figure 5- 2: Dimensional variations of the mortars stored under water. For F19, t_0=24h instead of t_0=4h for the other blends

5.1.2.2 Dry conditions

The passage of wet storage to dry conservation leads to shrinkage. After one year, this is between -500 µm/m to -1300 µm/m for almost all formulations as shown on figure 5-3. Two binders, F17 and F16, exhibit higher shrinkage, -2700 µm/m and -1800 µm/m respectively. For F16, the shrinkage is compensated by the initial expansion between 0 and 7 days.

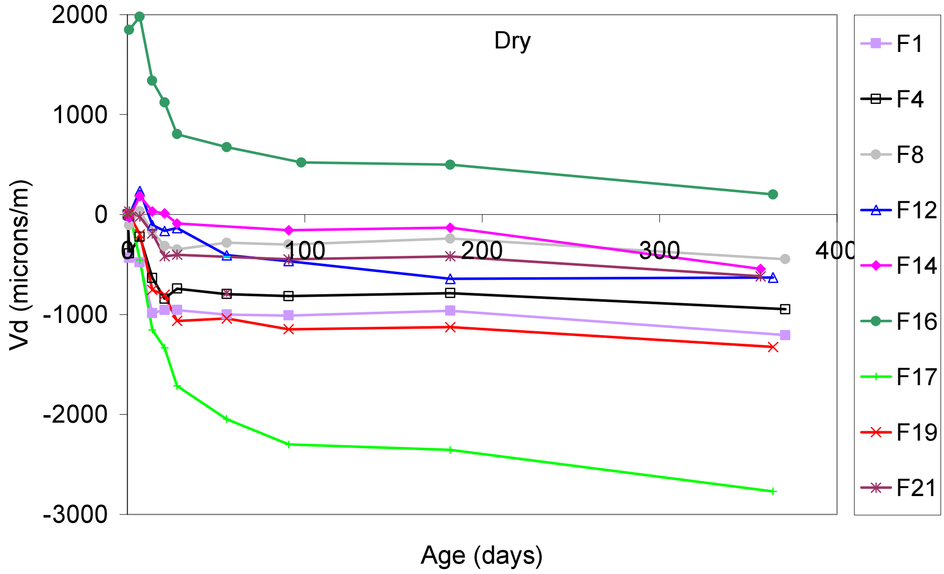

Figure 5- 3: Dimensional variations of the mortars stored in dry condition. For F19, t_0=24h instead of t_0=4h for the other blends

5.1.2.3 Cycles

The cycling samples (1 week 50°C, 1 week 90%RH) were measured at the same ages as those in dry and wet storage but were also measured the week before and week after (corresponding to one cycle) to ascertain the degree to which dimensional variations changed under the cycling conditions. After 100 days, only one cycle was done per month (2 weeks 50°C, 2 weeks 20°C, 90%RH).

The mortars stored under severe thermohygrometric cycles exhibit cyclic dimensional variations (shrinkage/expansion), figure 5-4. The systems are more or less sensitive to the cycles; F14 and F17 present the greatest amplitude of dimensional variations (figure 5-5).

The average dimensional variations after one year are generally not very different with these obtained in dry conditions.

Dimensional variations (µm/m)	F1	F4	F8	F12	F14	F17	F21	F16	F19
Dry environment	-1210	-950	-450	-630	-545	-2770	-620	200	-1325
Cycles	-1620	-1160	-585	-220	-270	-2630	-1200	1200	-910

Table 5- 1: Comparison of the 1-year dimensional variations between dry storage and cycles

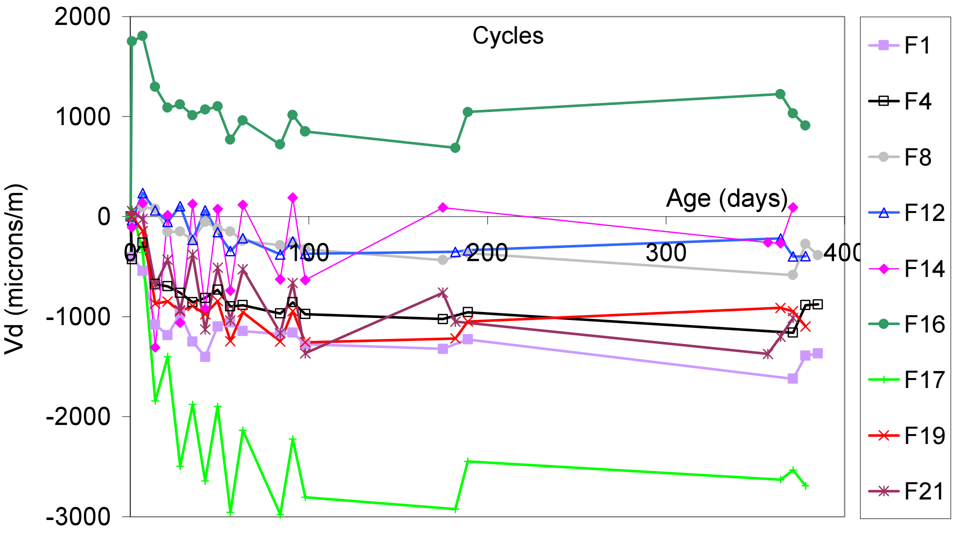

Figure 5- 4: Dimensional variations of the mortars stored under cycles. For F19, t_0=24h instead of t_0=4h for the other blends

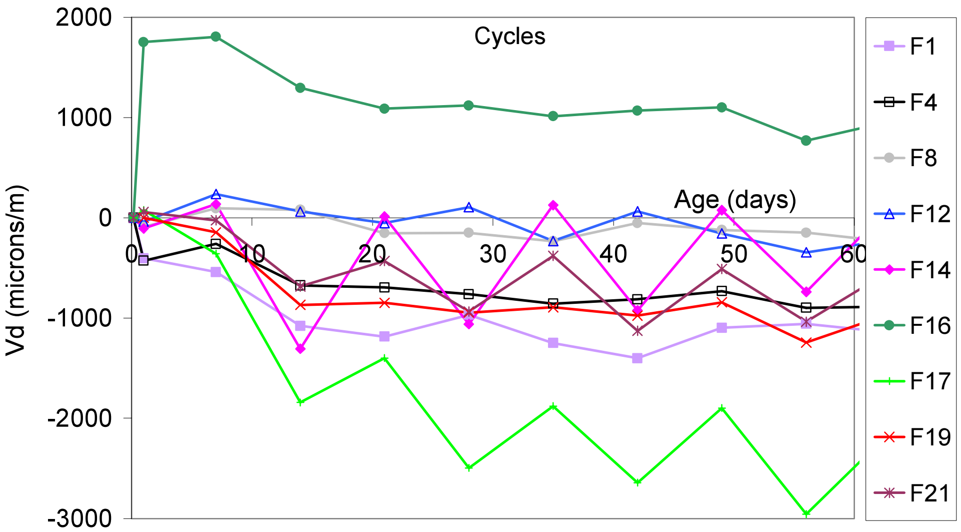

Figure 5- 5: Enlargement of the dimensional variations up to 2 months

5.1.3 Young's modulus

Under water storage, the Young's modulus increases up to a plateau close to 41 GPa for all formulations except F14 whose value is lower (30 GPa); this could be explained by the finer sand granulometry. In dry conditions, the Young's modulus decreases slightly, probably because of the drying shrinkage which creates microcracks in the samples. F14 is characterised by a lower Young's modulus both in dry conditions and under cycles. The elastic modules of other samples are more or less sensitive to thermocycles, but that no general trend is apparent.

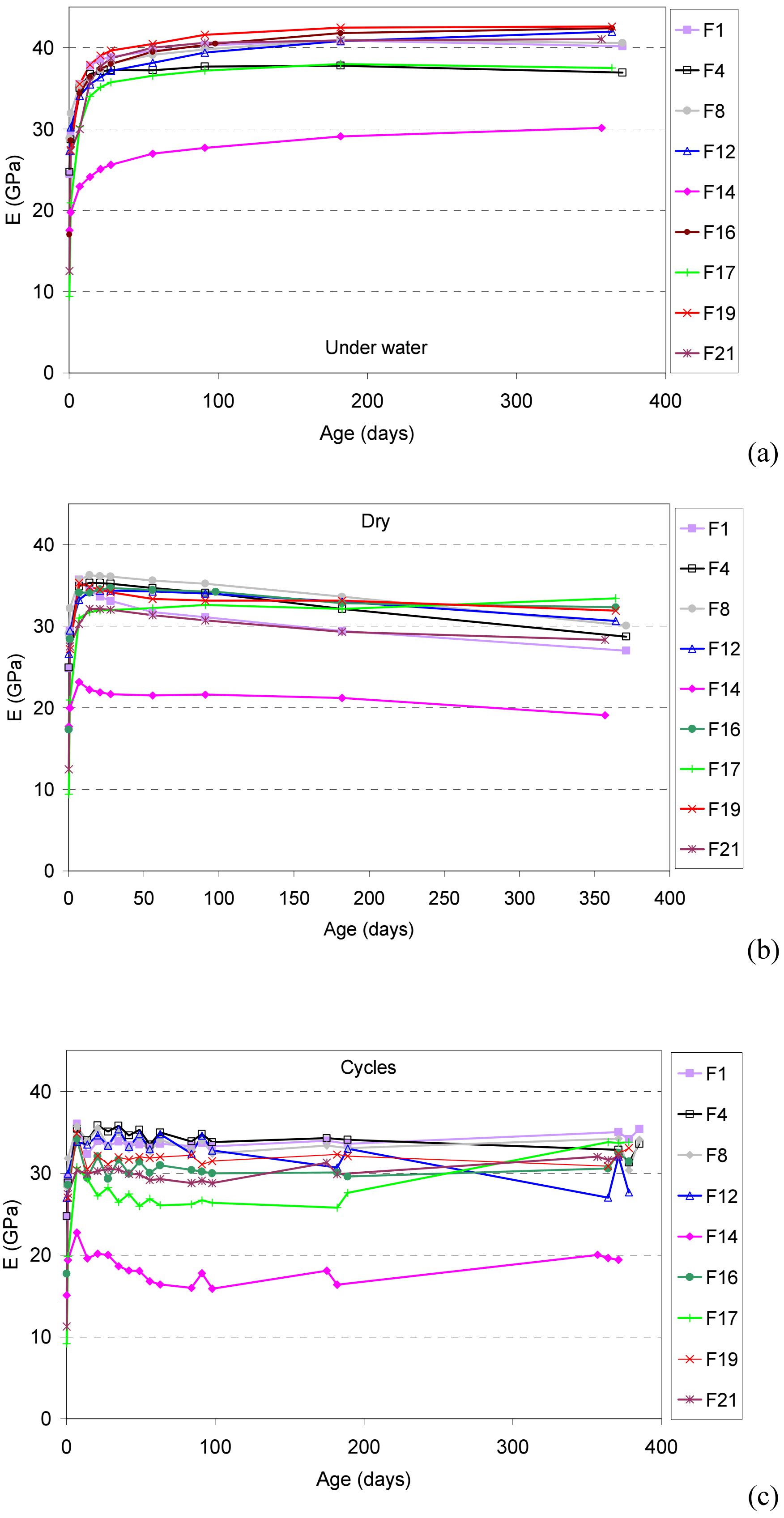

Figure 5- 6: Evolution of the effective Young's modulus over time for samples stored (a)under water, (b) in dry conditions and (c) cycles

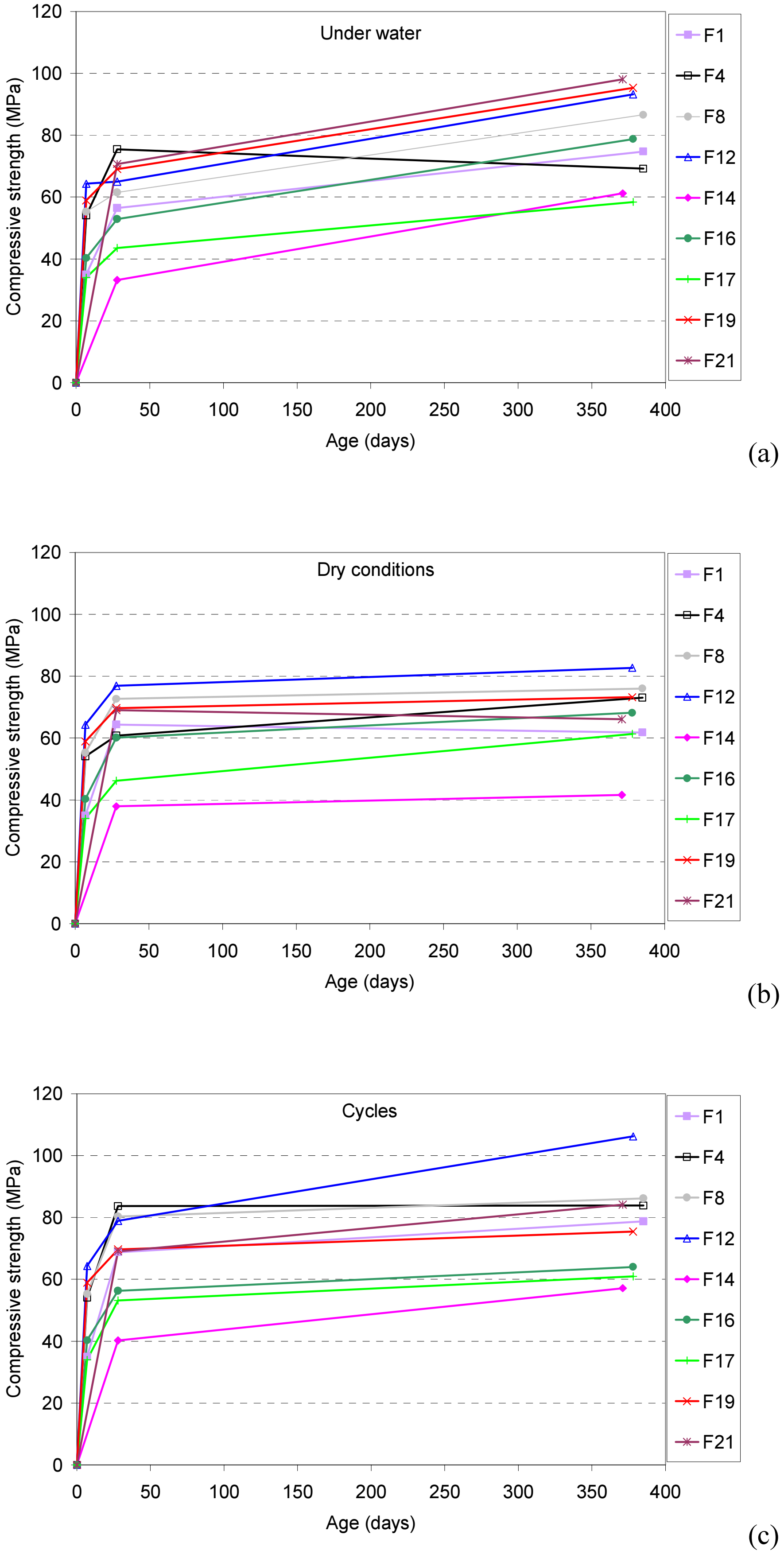

Figure 5- 7: Compressive strength of the samples stored (a) under water, (b) in dry conditions and (c) cycles

5.1.4 Compressive strength

Figure 5-7 summarizes the compressive strength results. The 28-days measurements highlight that whatever the conditions are, the compressive strengths continuously increase after the initial curing of one week. Nevertheless, the effect of the storage is observed over the long-term: under water, the samples gain approximately 35% in R_c between 28 days and 1 year except F4 whose compressive strength decreases. This is linked with its excessive swelling. The storage in dry conditions leads to lower compressive strengths than in wet conditions. In the case of the cycles, the compressive strengths generally increase slightly and are similar to those in wet conditions.

5.1.5 Conclusions

Depending on the storage conditions, the development of mechanical strengths and dimensional variations differ. No system seems to be better or worse than the others except F4 and F21 to a lesser extent. We may also point out that F17 and F16 present a high drying shrinkage. Ettringite-rich compositions are dimensionally stable whatever the environment and the presence of abundant ettringite is not invariably associated with physical expansion if the composition has a correct stoichiometry between CAC and C$ (no C$ in excess).

5.2 CARBONATION

5.2.1 Introduction

Carbonation itself does not damage the concrete; it leads to a drop in the pH of the interstitial solution, down to a value such that the passive oxide film protecting the steel is no longer stable. Whereas the detailed carbonation of Portland cement has been widely studied, the effects of carbonation on ternary binders are not known in detail. According to the application of mortar, carbonation may affect durability differently. In “Building Chemistry” e.g. floor overlays, the mechanical properties and microstructural evolution are the main parameters whereas in “Concrete” applications the main concern is the corrosion of steel reinforcement bars. The corrosion starts when the pH becomes lower than 8: the passive film of Fe_2O_3 is the destroyed according to the Pourbaix diagram.

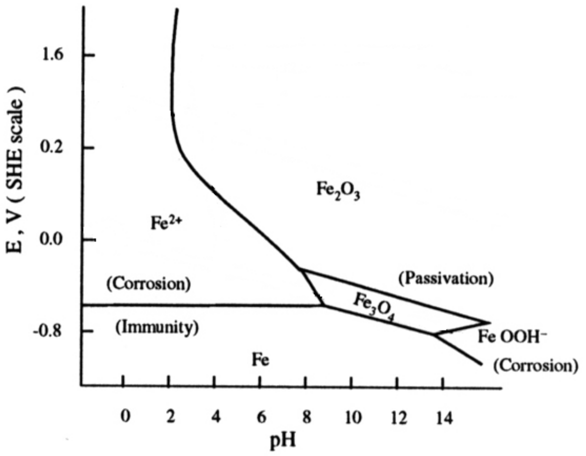

Figure 5- 8: Pourbaix diagram for Fe-H_2O *system at* 25°C

The principal objective of this study was to examine the carbonation reaction of the different binders with emphasis on the microstructure and to investigate the stability of ettringite-based mortars subject to carbonation and the impact on the mechanical properties.

5.2.2 Mechanisms of carbonation

5.2.2.1 Portland cement

Carbon dioxide dissolves in water to form carbonic acid. This acid then reacts with $Ca(OH)_2$ and leads to the formation of $CaCO_3$ [1, 2].

$$CO_2 + 2OH^- \rightarrow CO_3^{2-} + H_2O \tag{5.1}$$

$$Ca(OH)_2 + CO_3^{2-} \rightarrow CaCO_3 + 2OH^- \tag{5.2}$$

In addition to the dissolution of portlandite, the Ca/Si ratio of the C-S-H is lowered leading eventually to silica gel formation, equation.(5.3). As still more CO_2 goes into solution, all OH^- ions are used up and the solution becomes acidic, which results in a drop of pH. Therefore, portlandite acts as a buffer for maintaining the pH (release of OH^- ions, Eq. (5.2)).

$$C_xSH_y + xCO_2 \rightarrow xCaCO_3 + SiO_2.nH_2O + (y-n)H_2O \tag{5.3}$$

The volume of the calcium carbonate exceeds that of the hydrates from which it is formed (the volume increase is approximately 11% for calcite formation, equation (5.4)). Calcite precipitates in free space, and thus contributes to a clogging of the porous network. As a consequence, the increase of the depth of the carbonated layer in Portland cement leads to reduce the rate of further carbonation.

$$\underbrace{Ca(OH)_2}_{33.3cm^3} + CO_2 \rightarrow \underbrace{CaCO_3}_{39.1cm^3} + H_2O \tag{5.4}$$

The rate of carbonation is greatly slowed down if the pore network is filled with water, which will hinder the diffusion of CO_2, or if the pores system is completely dry. Optimum conditions for the carbonation reaction are in the humidity range of 55-75% RH [3, 4].

5.2.2.2 Calcium Aluminate Cement

The carbonation of hydrogarnet leads to formation of calcite and alumina gel according to Eq. (5.5).

$$\underbrace{C_3AH_6}_{150cm^3} + 3CO_2 \rightarrow \underbrace{3CaCO_3 + AH_3}_{180cm^3} + 3H_2O \tag{5.5}$$

This reaction leads to a solid volume increase of 20% with the assumption of calcite and gibbsite precipitation. Monocarbonate may also be formed as a transient reaction product [5].

5.2.2.3 Ettringite

It is generally accepted that ettringite decomposes into calcite, gypsum and alumina gel by carbonation, as follows [6-10]:

$$\underbrace{C_3A.3C\overline{S}.H_{32}}_{708.5\text{ cm}^3} + 3CO_2 \rightarrow \underbrace{3CaCO_3 + 3C\overline{S}H_2 + AH_3}_{402.6\text{ cm}^3} + 23H_2O \tag{5.6}$$

Calcium and sulfate ions dissolve into the pore solution; dissolved ions are consumed to form crystalline gypsum and calcium carbonate. The aluminium ions are found in alumina gel;

gibbsite is generally not observed. Due to the differences in the molar volumes of the solid reactant (ettringite) and the solid products, a decrease of the solid volume is to be expected:

- ~ 44% assuming that AH_3 precipitates as gibbsite
- ~ 31% considering AH_3 as a gel with a density of 1

A carbonation profile for ettringite pellets has been proposed by Zhou and Glasser [10] (zone 1 is the nearest to the surface)

Zone 1	Gypsum, $CaCO_3$ and AH_3
Zone 2	Gypsum, $CaCO_3$, AFm and AH_3?
Zone 3	Gypsum, $CaCO_3$, AFm and AFt
bulk	AFt

Figure 5- 9: Zoning developed in ettringite pellets carbonated at 25-40°C, 66-88%RH. AFm corresponds to monosulfate but solid solutions with monocarboaluminate are not excluded

5.2.2.4 Monosulfate

Monosulfate probably disappears as a result of the interlayer exchange $SO_4^{2-} \rightarrow CO_3^{2-}$ leading to monocarbonate. However, the final carbonated products are calcium carbonate, alumina gel and the sulphur is found in gypsum. As the pH drops, monosulfate is stable at pH down to 11.6 while ettringite is stable down to pH= 10.6 [11].

5.2.3 Accelerated test

7 formulations were studied: F1, F8, F12, F21 , F17, F16, F19. 4×4×16 prisms were cast, cured for 28 days at 90% RH, 20°C and then placed in a climatic chamber at 25°C, 65% RH, 0.3% CO_2. The level of 0.3%CO_2 (ten times more than the atmospheric level) was chosen because previous research has indicated that too high concentration in CO_2 induces a somewhat different degradation mechanism expected with carbonation under natural atmospheric conditions [7]. The humidity, 65% RH was in the optimum range for the carbonation reaction process as previously mentioned.

5.2.4 Results

5.2.4.1 Carbonation depth

One easy and rapid way to determine if carbonation has occurred is to spray phenolphthalein which turns to pink at pH above 8.5, onto a freshly broken surface of the sample. This method captures the colour change boundary between the uncarbonated (pink) and carbonated areas (colourless). It is useful as it reveals a continuous carbonation front in a visual form but it may underestimate the level of carbonation because partially carbonated areas are generally not detected.

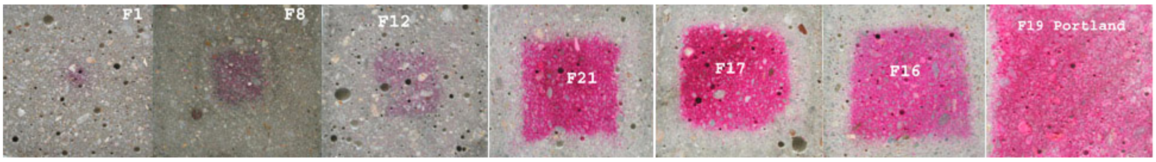

Figure 5- 10: Slice sections of the one year-carbonated sample sprayed with phenolphthalein

The simple observation of samples sprayed with phenolphthalein, figure 5-10, indicates that the Portland mortar is almost not affected by the carbonation whereas CAC-C$ rich binders present an advanced carbonation state.

The phenolphthalein test is widespread in the case of Portland cement but it may be questioned if this method is also appropriate for ternary binders because of the different hydrates, the pH evolution may changed. Indeed, Andrade [12] showed that the alkalinity of the pore solution of CAC measured with phenolphthalein indicator is a function of the degree of water saturation of the pores. So a carbonated CAC paste is not always colourless to phenolphthalein.

SEM observation is the second tool to check the carbonation depth due to the microstructural changes which accompany the carbonation process. The carbonation depth by SEM is defined from the external surface by progressing inward till we reach the bulk microstructure. The comparison between both techniques is shown in the graph below.

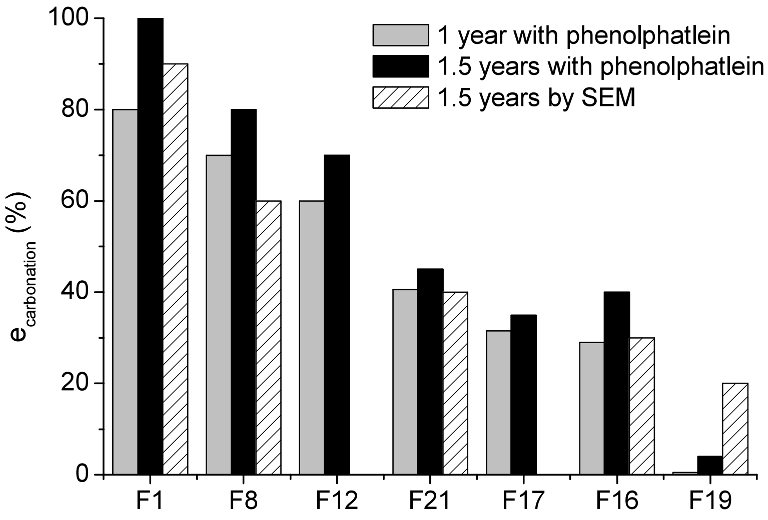

Figure 5- 11: Carbonation depth measured with phenolphthalein test and by SEM

From 1 year to 1 ½ years, carbonation has progressed inwards for all mixtures but slowed up. The main result is that CAC-rich binders are more sensitive to carbonation than Portland; the higher the CAC content, the greater the carbonation depth.

Compared to SEM observations, the phenolphthalein test slightly overestimates the carbonation depth for all specimens except the plain Portland one which is underestimated. This confirms the buffering role of Portlandite which dissolves to restore the equilibrium of the cement paste and pore solution; the matrix could be partially carbonated but with a pH>8.5 thus not visible by phenolphthalein. In conclusion, although it is more difficult to distinguish the pink colour from the dark grey matrix, the phenolphthalein test seems to be relevant and adapted to CAC-C$ rich systems.

5.2.4.2 Mechanical strength

Figures 5-12 displays the evolution of compressive strengths for the 28 days-cured samples and at the end of the accelerated test, 1.5 years. A comparison with the 1 year natural weathering is also given.

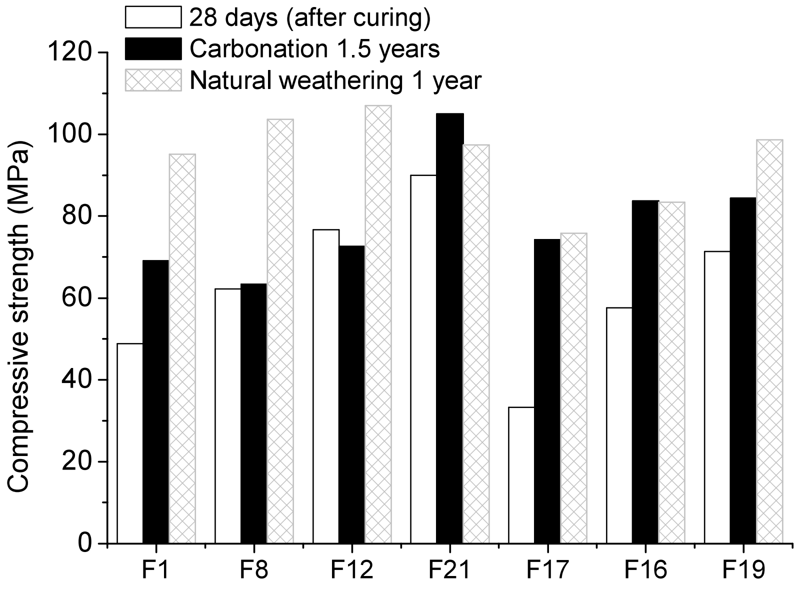

Figure 5- 12: Comparison of compressive strengths just before the storage in the carbonation chamber i.e. 28 days, after 1.5 years in the carbonation chamber and after 1 year under natural weathering

Between the beginning and the end of the accelerated carbonation test, the compressive strength has generally increased. It is widely accepted that Portland or CAC cement become denser when carbonated, which results in a mechanical strength gain [13, 14], but only very few data are available for ternary binders [7]. Scrivener et al. reported that the carbonation of a self-levelling flooring compound based on CAC/PC/C$ led to a coarsening of the porosity but this does not have negative effect on strength, which remained constant rather than decreasing. Microstructural changes or the continuation of hydration could also explain this behaviour. Despite of the high degree of carbonation of CAC-rich binders, the mechanical strengths of the fully carbonated sample F1 remain very good with a value of 70 MPa. This is perhaps linked to the formation of AH_3 which may contribute to the cohesion between the various hydrates. Further study by SEM was carried out to better understand the carbonation mechanisms.

5.2.4.3 Microstructural investigations

a. Portland

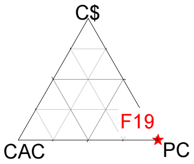

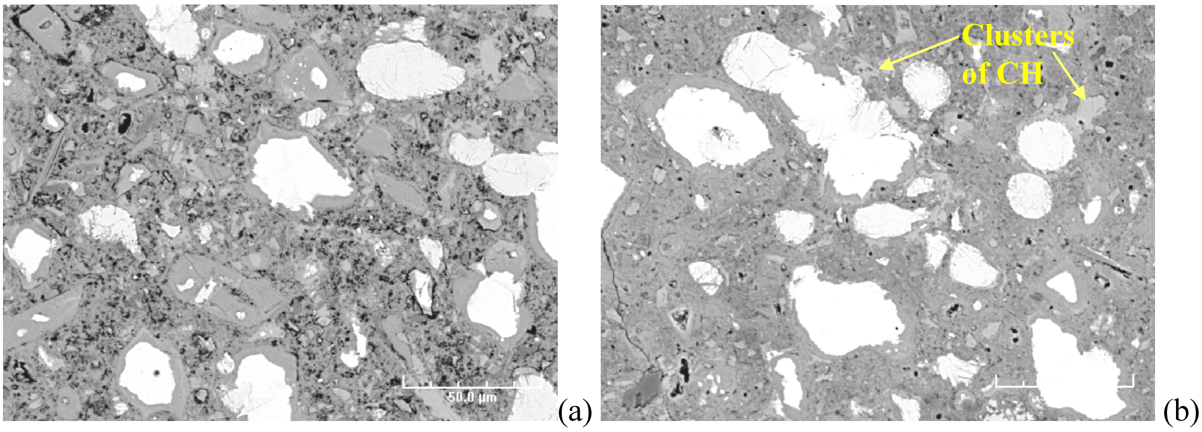

Figure 5- 13: BSE images of a non carbonated (a) and carbonated matrix (b) of a Portland mortar exposed 1.5 years to accelerated carbonation

While the phenolphthalein indicates a carbonation depth less than 1 mm, SEM observations show microstructural changes up to 4.5 mm from the surface. As we move away from the surface, Portlandite disappears progressively. EDS microanalysis in the undifferentiated products, indicate significantly higher contents of calcium and oxygen which was interpreted as calcite mineral. The characteristic features of Portland carbonation were observed such as disappearance of portlandite and densification of the matrix; this is consistent with results reported in the literature.

b. F16

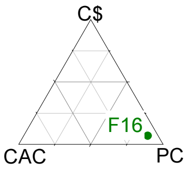

As reported in section 3.2.3, the main hydrates present before carbonation are ettringite, monosulfate, CH and C-S-H. The process starts from the surface and propagates inward, creating a front. The outer matrix is illustrated by the following SEM images.

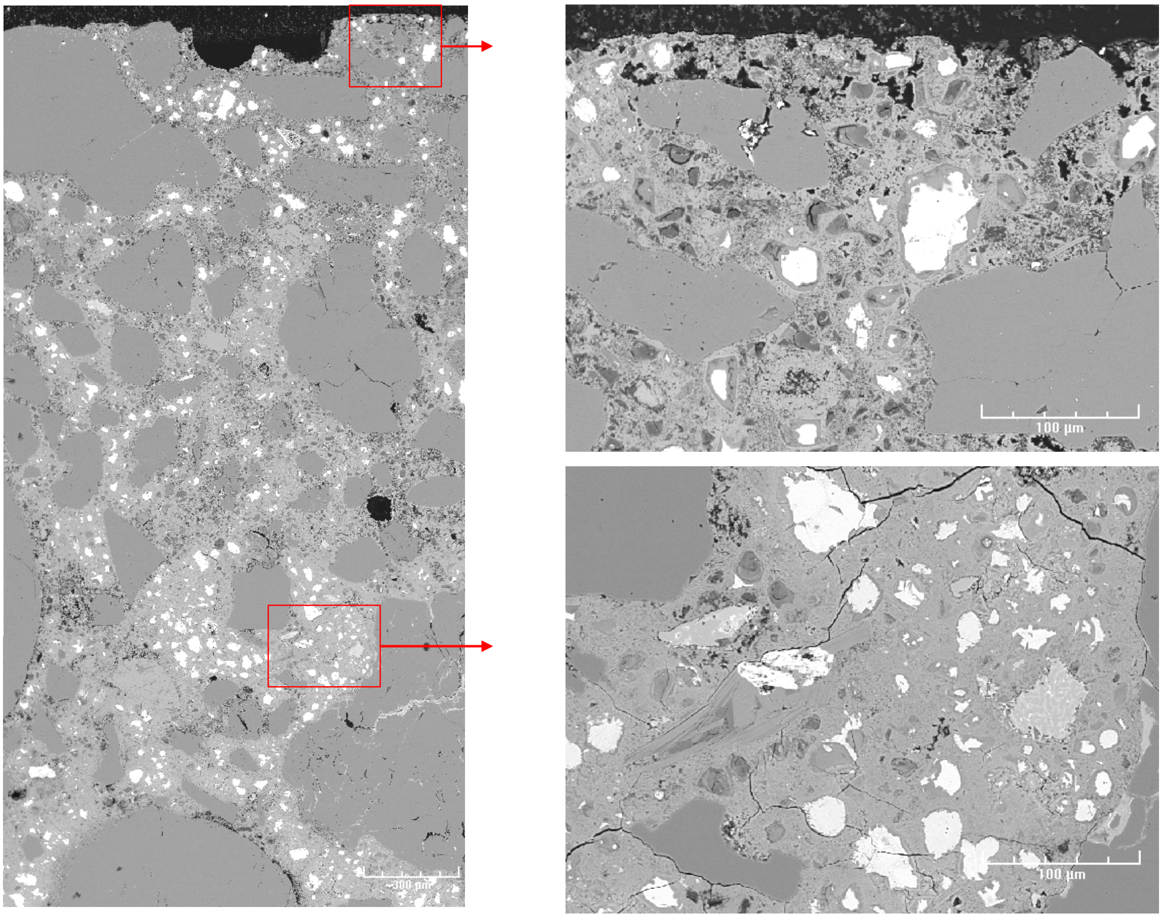

Figure 5- 14: BSE pictures showing the carbonated matrix of F16

Dark grains are residual clinker particles which have been decalcified. There is no significant amount of CH and the disappearance of CH is confirmed by TGA analysis and XRD.

EDS point analysis are represented on the graphs 5-15 and 5-16; the first one highlights the presence of C-S-H finely intermixed with $CaCO_3$; the initial CH microcrystallites embedded in the outer C-S-H have reacted into $CaCO_3$. The Ca/Si ratio of the inner C-S-H is lowered from the value of about 2 (section 3.2.3) to 0.8 and further reaction will destroy the C-S-H with formation of hydrous silica. However, in the long term, this decalcification of C-S-H leaves a residual skeleton of silica gel [15].

The second graph, figure 5-16 underlines the presence of gypsum (blue ring). The source of gypsum formation is the carbonation of ettringite and monosulfate (equations (5.6)). The concentration of gypsum around aluminous grain is explained by the carbonation of the monosulfate-rich layer surrounding CAC particles in the non-carbonated area.

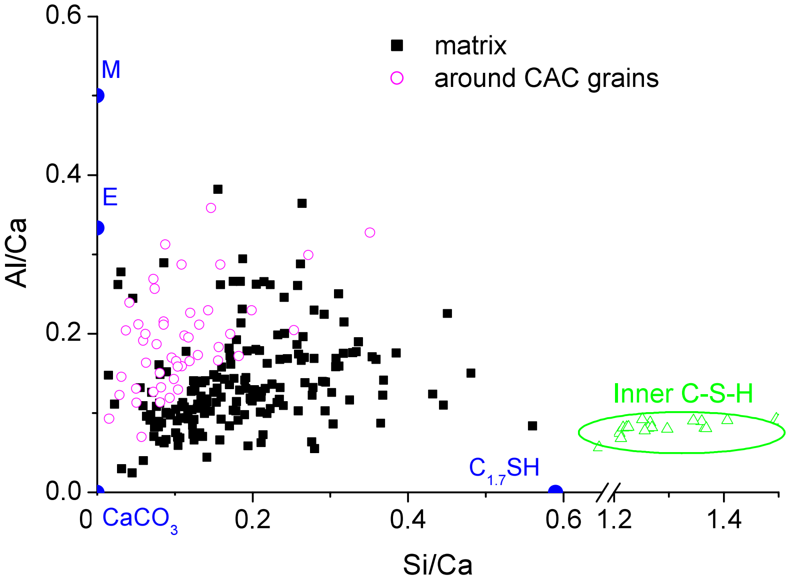

Figure 5- 15: Al/Ca atom ratio versus Si/Ca ratios of the carbonated matrix. Pink points have not been chosen arbitrarily but around CAC grains.

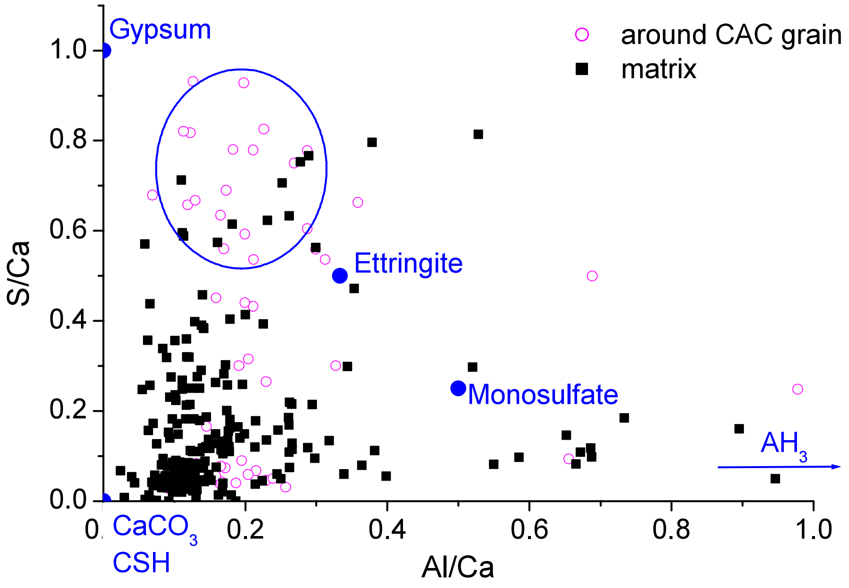

Figure 5- 16: S/Ca atom ratio versus Al/Ca ratios of the carbonated matrix. Pink points have not been chosen arbitrarily but around CAC grains.

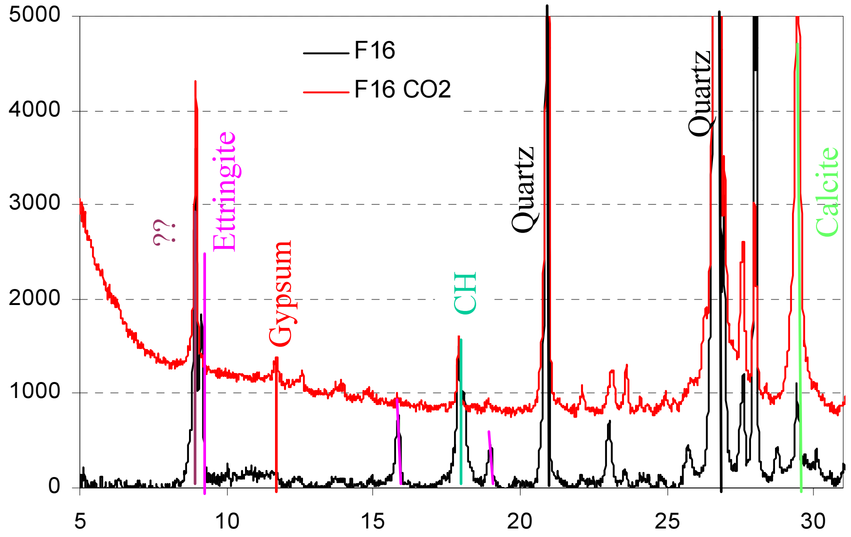

Figure 5- 17: XRD diffractogram of the carbonated F16 (red curve) and the bulk of F16 (black curve) The "double peak of ettringite" is still present in the carbonated F16.

c. F21

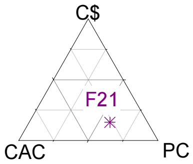

The hydrates in the bulk matrix have been identified as a finely mixture of ettringite, AFm and hydrogarnet phases (Chapter 3, section 3.2.4). In contact with CO_2, these phases should progressively develop into calcium carbonate, AH_3 and gypsum.

As previously, the carbonation propagates inward leading to microstructural changes which are illustrated below.

Near the surface, the smallest alite grains are completely hydrated and appear totally dark in BSE images meaning that they are composed of light elements; only silica is detected in these dark zones which can be inferred to consist of silica gel.

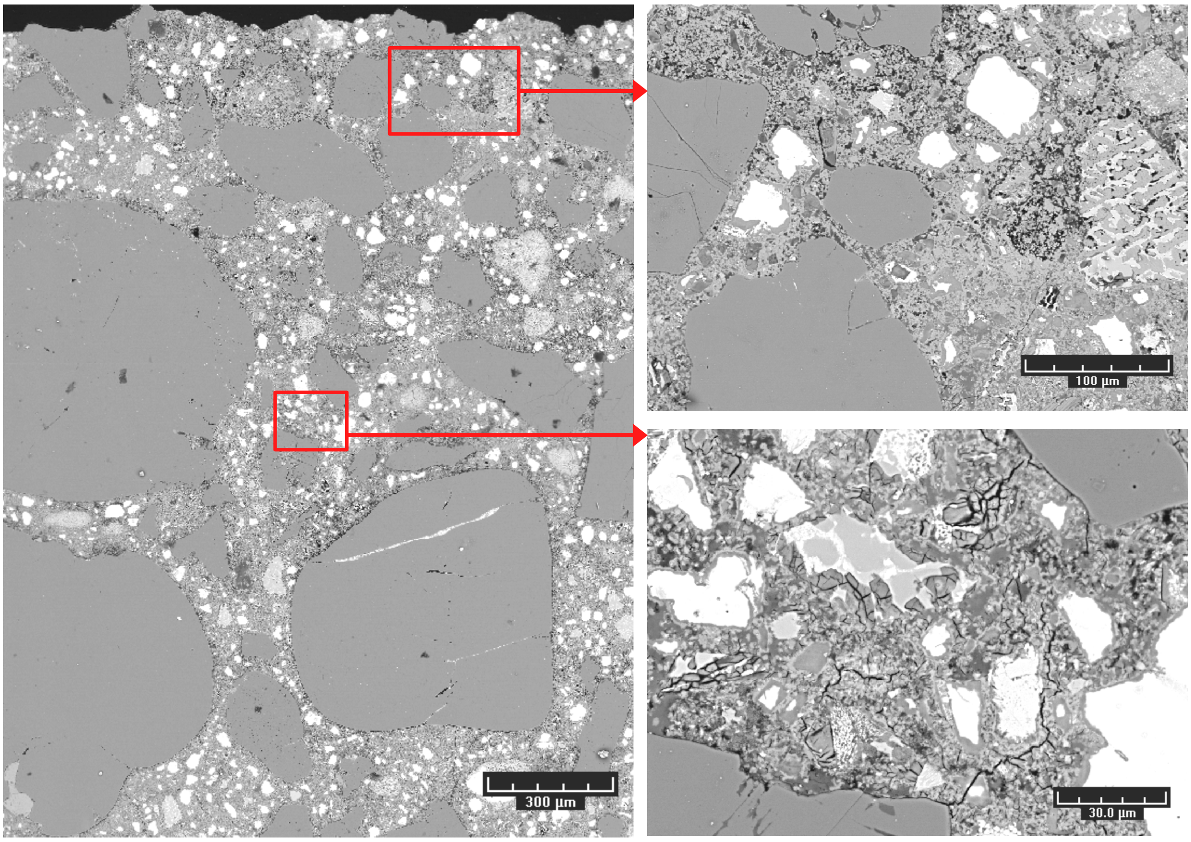

Figure 5- 18: BSE pictures showing the carbonated matrix of F21. The darkest zones are AH_3 and the lightest, calcium carbonate

The EDS analysis plotted in figures 5-20 and 5-21 confirm the decalcification of the C-S-H, the presence of calcium carbonate and the formation of AH_3 which was not detected by XRD because of its low crystallinity. In theory, AH_3 and SiO_2 points are located at infinity but because of the analysed volume, points belonging to mixtures of these hydrates with other phases are visible on the graph 5-20.

Analysis points close to the origin in figure 5-21 belong to calcium carbonate; calcium sulfate is also detected. These results are consistent with XRD data.

The comparison of XRD diffractograms between the bulk and the carbonated matrix, figure 5-19, shows the disappearance of monosulfoaluminate, the depletion of the ettringite peak and the formation of gypsum and calcium carbonate as calcite and aragonite.

The presence of ettringite in the carbonated part (regions striated by drying cracks) could be justified by some residual ettringite (non carbonated) or ettringite newly formed. As stated by Kuzel [16, 17] the interlayer SO_4^{2-} groups in the crystal structure of monosulfate are replaced by CO_3^{2-}, thus the sulfate concentration in the pore solution increases and ettringite could be formed.

$$C_3A.C\overline{S}.H_{12}\ +2Ca^{2+} + CO_3^{2-} + 2OH^- \rightarrow\ C_3A.3C\overline{S}.H_{32} + 2C_3A.0{,}5C\overline{C}.0{,}5CH.H_{11.5} \qquad (5.7)$$

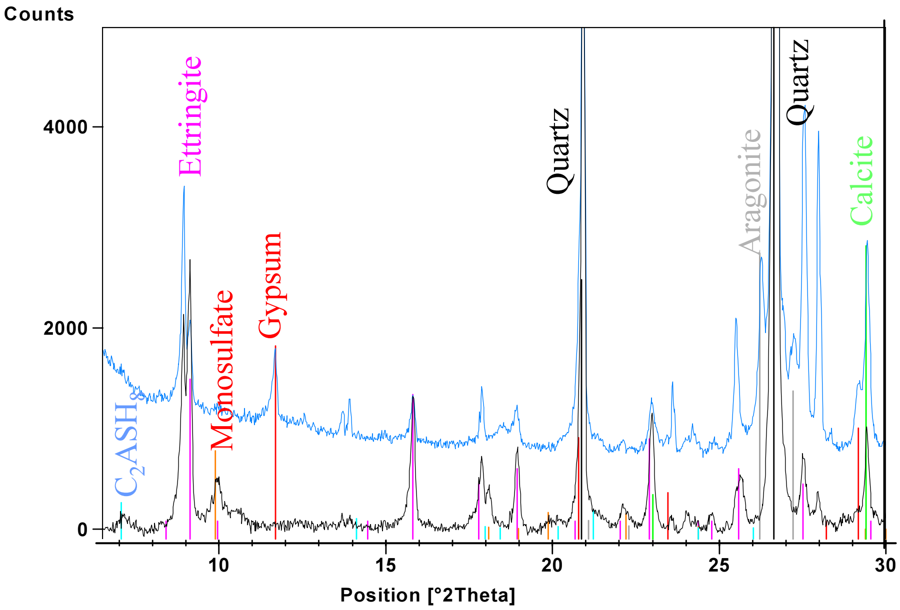

Figure 5- 19: XRD diffractograms of carbonated matrix (blue curve) and the bulk (black curve) of F21

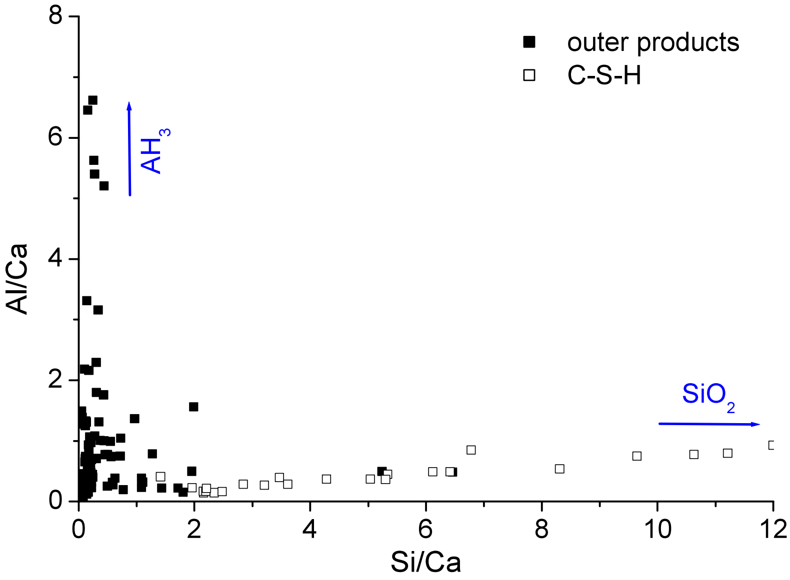

Figure 5- 20: Al/Ca atom ratio versus Si/Ca ratios of the carbonated matrix of F21. Empty squares represent EDS analysis in hydrated alite grains.

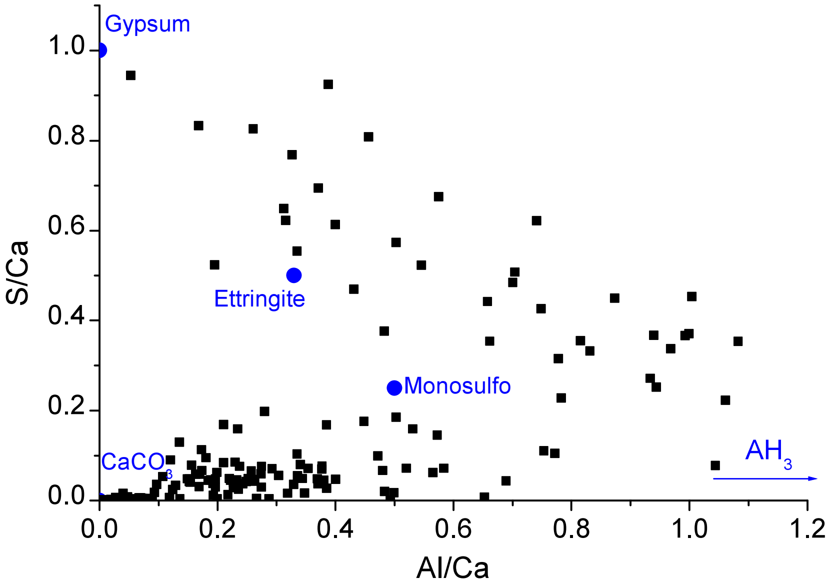

Figure 5- 21: S/Ca atom ratio versus Al/Ca ratios of the carbonated matrix of F21

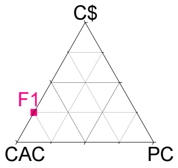

d. F1

F1 is very similar to the binder F2; some EDS analysis have been done on the unaltered part and the main hydrates are ettringite and AH_3 like F2. The carbonated matrix appears totally different than the non-carbonated (F2, section 3.3.2); regions striated by drying cracks typical of ettringite have disappeared and large areas of AH_3 are scattered throughout the matrix, figure 5-22.

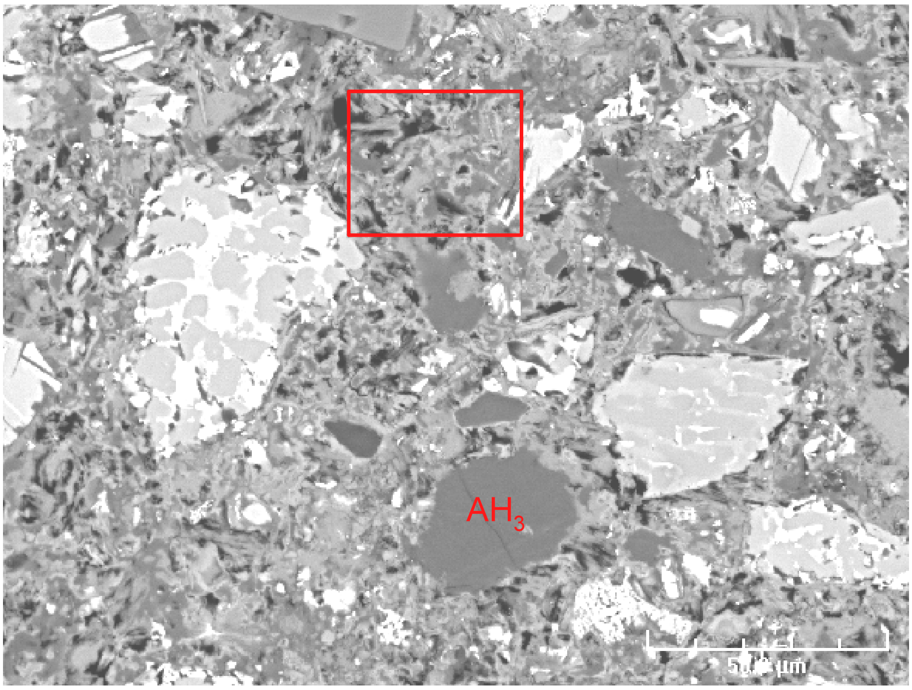

Figure 5- 22: BSE image of the carbonated area of F1

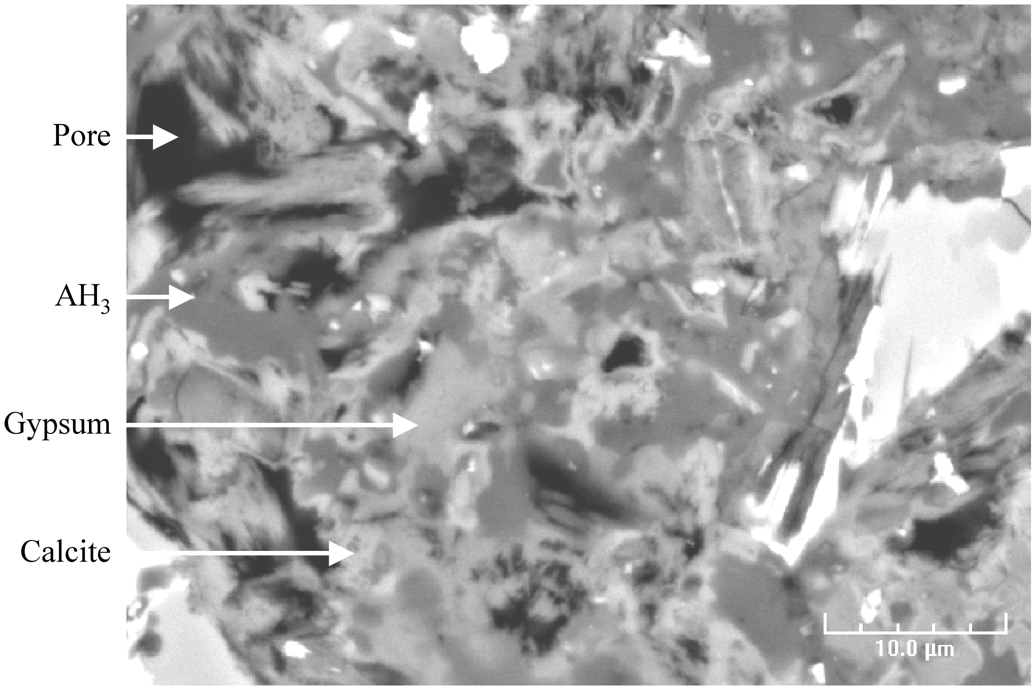

Figure 5- 23: Magnification of the square in picture 5-22. The darkest regions correspond to AH_3, the brightest ones to calcite and the intermediate grey level to gypsum.

EDS results of the intermediate grey level zone indicate high contents of Ca and S which is interpreted as gypsum after correlation with XRD results, figure 5-25.

The matrix is an intimate mixture of $CaCO_3$ and gypsum crystallites embedded in a fine textured alumina gel as confirmed by SEM microanalysis. The finely dispersed carbonate crystallites were found from the XRD patterns to be aragonite and calcite, figure 5-25. The XRD peak belonging to ettringite has totally disappeared whereas some gypsum is detected; there was also residual hemihydrate. These results were expected because in presence of CO_2 ettringite decomposes into calcium carbonate, gypsum and AH_3 (Eq. (5.6)) and are consistent with Zhou and Glasser' study [10].

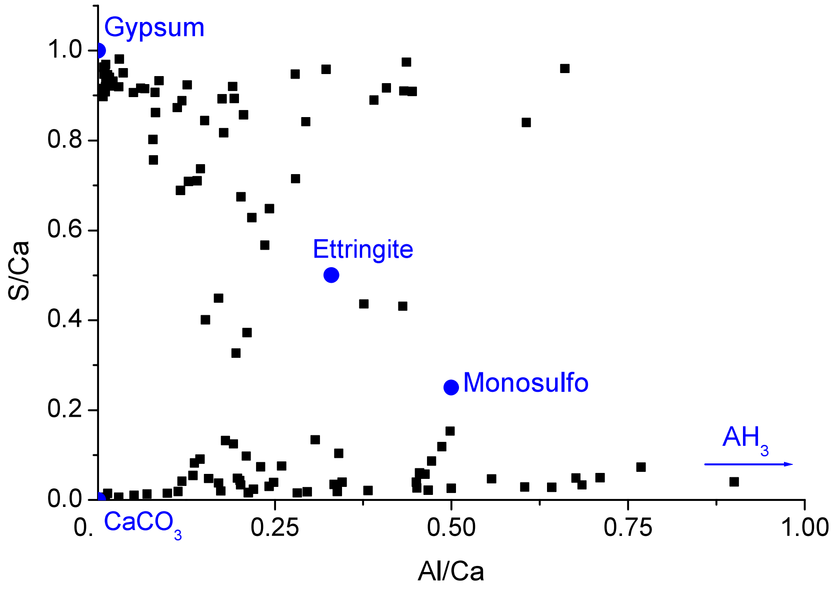

Figure 5- 24: S/Ca atom ratio versus Al/Ca ratios for F1

However, as mentioned before, the carbonation of ettringite is accompanied by a decrease of the solid volume and it was interesting to assess the porosity of the totally carbonated slice by solvent exchange. We found 16% of porosity while for uncarbonated F2, binder very similar to F1, the 1-year porosity was about 8%. The porosity doubled but remains reasonable and this could explain the good compressive strength even after total carbonation. The decrease of solid volume could be overestimated due to the fact that gibbsite does not crystallise but alumina gel, and in the presence of local excess of water released by carbonation (equation (5.6)), further hydration may occur. The new hydrated products may also seal some pores and thus counterbalances the loss of solid due to carbonation.

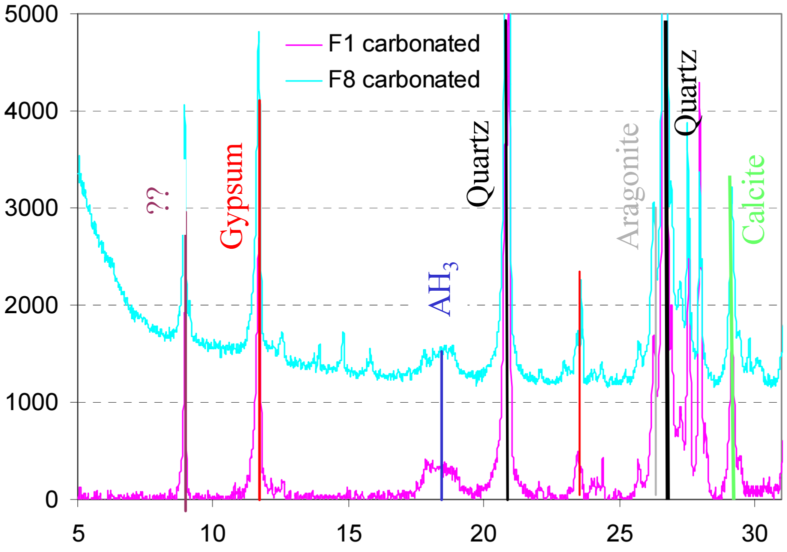

Figure 5- 25: XRD of F1 and F8 carbonated. The peak "??" is not ettringite.

e. F8

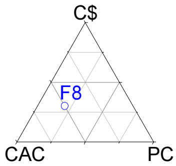

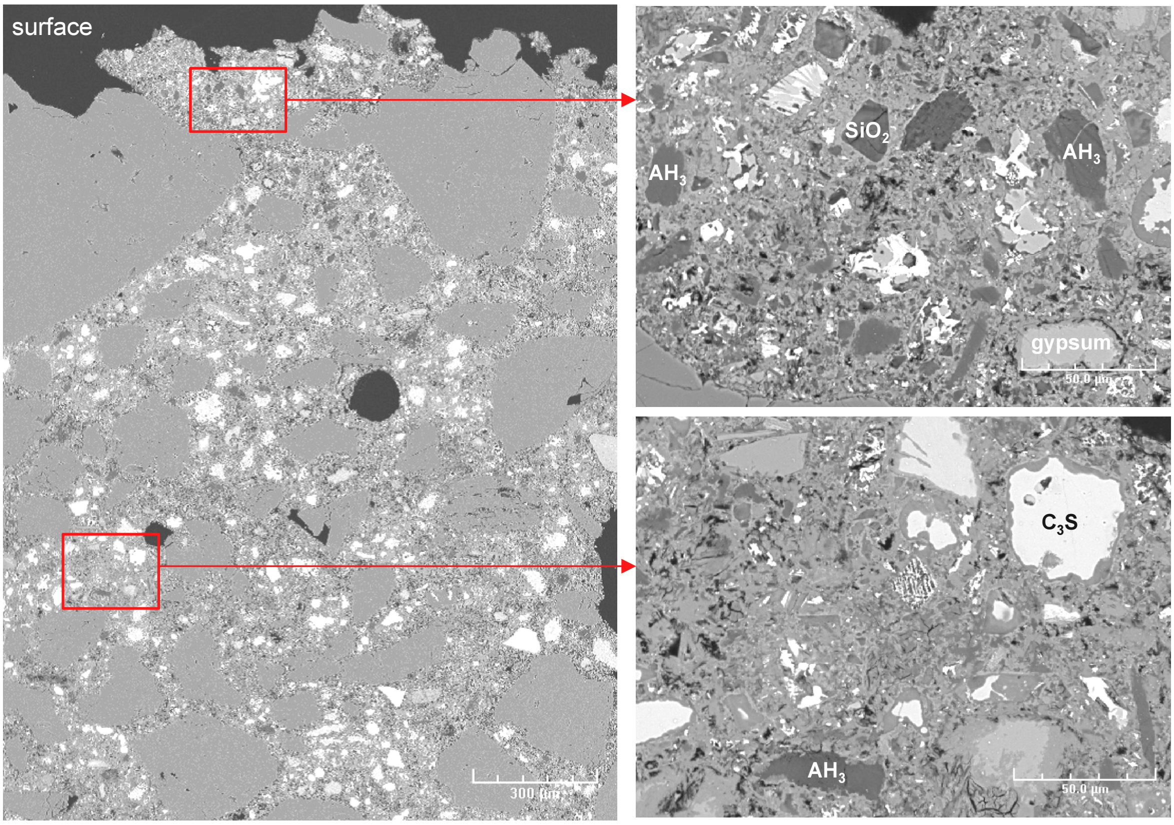

Figure 5- 26: BSE image of F8 carbonated

The microstructure looks like that of F1; as expected because the initial hydrates are similar (ettringite, AH_3). The outer microstructure appears to be almost completely devoided of unhydrated C_3S which has been decalcified and as for F1, the matrix consists of calcite, AH_3 and gypsum. However, the addition of Portland leads to lower depth of carbonation.

5.2.5 Conclusions

The microstructural characteristics of carbonated samples were investigated. Different phases formation were observed by SEM and the results were supported by chemical and structural analysis using EDS, XRD and TGA. It is confirmed that portlandite plays a key role due to its buffering effect and that ettringite is decomposed into calcite, gypsum and alumina gel. Clearly, a carbonation front occurs whatever systems but the rate of the carbonation is faster for ettringite-rich binders. In spite of a advanced state of carbonation, the mechanical strengths of these latter remain good.

5.3 ACID ATTACK

The better resistance of calcium aluminate cement in acidic media compared to that of Portland cement is generally acknowledged. This property enables the use of CAC in aggressive environments such as dairyworks, chemicals plants and sewage pipe. However, no data are available on CAC-rich binders. The aim of this study is to define the performance of binders with different contents of CAC and calcium sulfate.

5.3.1 Acidic corrosion model

5.3.1.1 Portland cement

The reactions which lead to its degradation may be summarized as follows:

- Acid dissociation (example of sulphuric acid):

$$H_2SO_4 \rightarrow 2H^+ + SO_4^{2-} \tag{5.8}$$

- Attack of the most vulnerable part of the binder, portlandite:

$$Ca(OH)_2 + 2H^+ \rightarrow Ca^{2+} + 2H_2O \tag{5.9}$$

- Decomposition of the C-S-H:

$$C_x - S - H_y + 2xH^+ \rightarrow xCa^{2+} + SiO_2 + (2y+1)H_2O \qquad (5.10)$$

Attack by sulphuric acid could lead to gypsum formation; Ca^{2+} ions generated in (5.9) and (5.10) will react with SO_4^{2-} ions from (5.8) but sulfates could also be leached by the flow of acid.

5.3.1.2 Calcium aluminate cement

CAC owes its stability against many aggressive agents not only to the nature of the hydrates and absence of portlandite but also to its greater neutralization capacity and to the reduced amount of acid formed by bacteria on a CAC substrate.

Acid attack of the aluminates hydrates occurs in two stages as follows. Above pH=3.5, Eq. (5.11) takes place.

$$C_3AH_6 + 6H^+ \rightarrow 3Ca^{2+} + AH_3 + 6H_2O \qquad (5.11)$$

The precipitation of AH_3 whose solubility threshold is about pH=3.5, creates locally a barrier layer which reduces further acid ingress. Below pH=3.5, AH_3 dissolves but in doing so neutralises more acid, as seen in Eq. (5.12).

$$AH_3 + 6H^+ \rightarrow 2Al^{3+} + 6H_2O \qquad (5.12)$$

5.3.1.3 Ettringite

Ettringite exposed to sulphuric acid is decomposed as Eq. (5.13)[18].

$$C_3A.(C\overline{S})_3.H_{32} + 12H^+ \rightarrow 3Ca^{2+} + AH_3 + 3C\overline{S}H_2 + 26H_2O \qquad (5.13)$$

This decomposition leads to gypsum and alumina gel formation; Ca^{2+} may be leached.

5.3.2 Neutralisation capacity

The neutralisation capacity (NC) is often used in acidic corrosion; it corresponds to the quantity of H^+ required to neutralize a given quantity of materials (mM H^+ vs. g. material); depending on the material, the greater the quantity of acid necessary to destroy a given amount of material, the longer the material is able to tolerate an aggressive environment. The capacity of neutralisation of CAC considerably exceeds that of similarly designed Portland systems in acid environment (pH<5) as shown on the graph below.

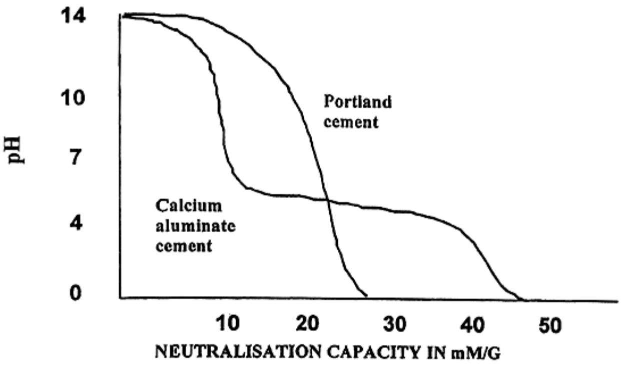

Figure 5- 27: Development of neutralisation capacity [19]

The full neutralisation capacity of CAC is developed in two stages, figure 5-27:

1. the first at a pH above 3.5, where C_3AH_6 is attacked to give precipitated AH_3
2. the second at a pH below 3.5, where the precipitated AH_3 together with that formed on initial hydration is attacked, further contributing to the overall neutralisation capacity of the cement

As the composition of the binder is known, its neutralisation capacity is easily calculated. Details about the calculations are given in [20].
The table below represents the NC for the binders by ascended order. Slag acts as a sacrificial phase.

Binders	F16	F19	F8	F4	F10	F6	F2	F17	F15	F1	F14 (slag)	F12 (slag)
NC(mM/g)	7.9	10.0	10.0	10.1	10.2	10.6	11.2	11.4	11.7	12.0	13.6	14.3

Table 5- 2: Capacity of neutralisation of the different binders

5.3.3 Test

The resistance to acid attack was evaluated using a drip-by-drip method. A picture of the experiment set-up is shown in figure 5-28. Two replicates mortar samples (10×5×2 cm^3 in size) were tested on all formulations and the samples were cured for 28 days at 20°C, 90% RH.

The run-off acid solution was collected, weighed and analysed for pH; this step enables calculations of acid consumed to be made. The samples were also intermittently washed and weighed to determine the weight loss of the samples with acid passed.

The test was run using sulphuric acid solution at pH=3. Sulphuric acid is particularly corrosive due to the sulfate ion participating in sulfate attack, in addition to the dissolution by the hydrogen ion.

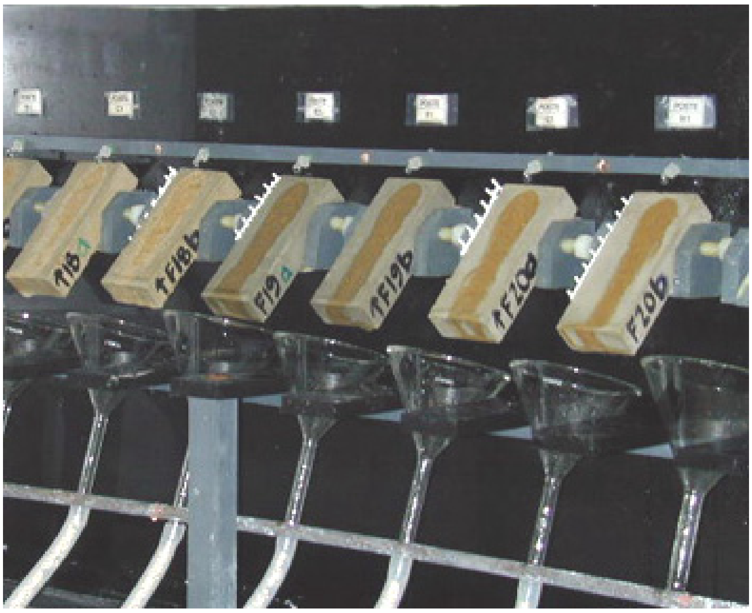

Figure 5- 28: Acid corrosion set-up placed in a chamber at saturated humidity

5.3.4 Results and discussion

After contact with the samples, the acid has used up its H^+ ions to a certain point. The pH of the effluent solutions tells us about the residual H^+ ions but acid corrosion is analysed with regard to acid consumption (corrosion kinetic). Flowed volume is a variable more appropriate than the time itself.

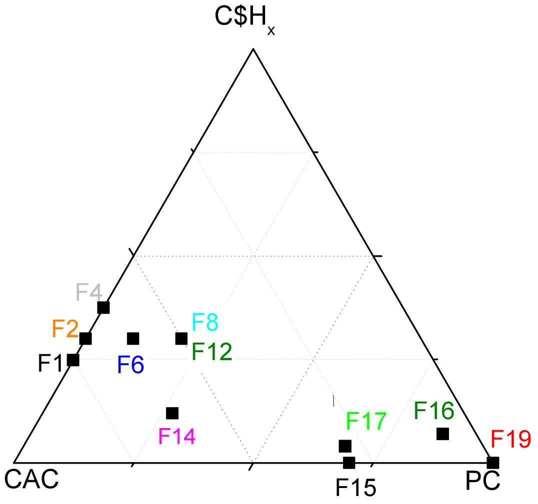

Figure 5- 29: Formulations tested in acid corrosion

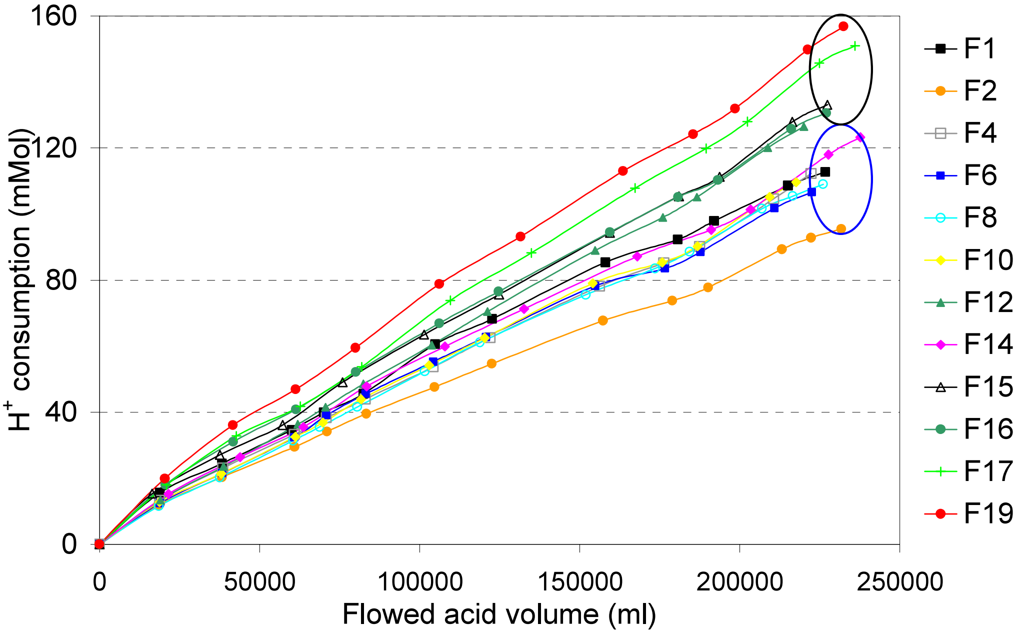

Figure 5- 30: Hydrogen ion consumption with flowed acid volume

As we can see on the diagram showing the consumption of acid as a function of the volume of acid which has flowed over the sample, corrosion is active as soon as the first drop of acid flows on the sample. The linearity indicates that the reaction rate is constant; the surface of the sample is continuously attacked. Binders can be classified into two groups: Portland rich binders (black circle) and CAC-C$ rich binders (blue circle). Portland mortar has the largest consumption, 160 mM for 230L, whilst a binary system CAC/C$ only consumes 95 mM. The kinetics of attack are thus essentially different and in favour of CAC/C$; indeed, higher the consumption, higher the loss of solid. For CAC-C$ rich systems, the most obvious explanation is that there still exists a zone of intermediate pH between the pH at the surface and the unaffected core in which AH_3 provides a barrier to penetration of acid.

Corrosion expressed as weight loss remains a useful indicator even if the measurement may be biased by the formation of secondary products or by sample washing. The final weight losses are presented in the following graph.

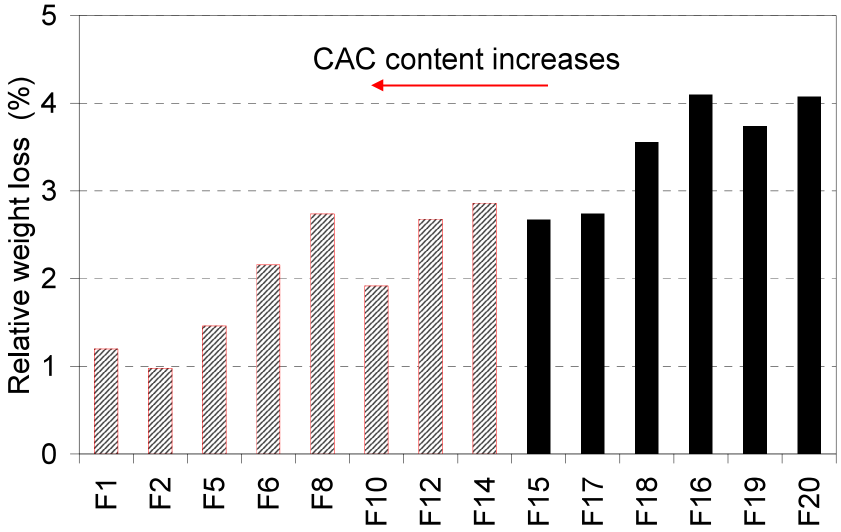

Figure 5- 31: Weight loss of mortars samples after 230 litres of H_2SO_4. Blue colour represents CAC-C$ rich binders while black indicates Portland-rich binders.

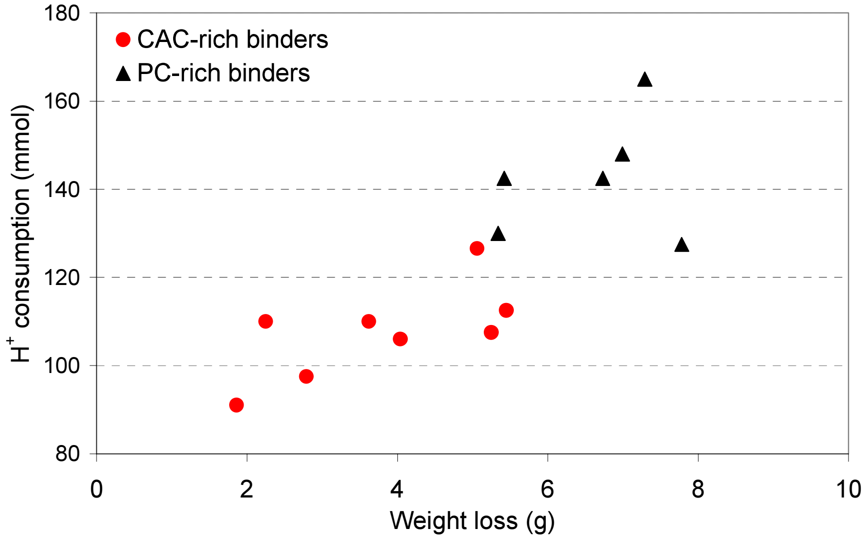

Figure 5- 32: Consumption of H^+ vs. the weight loss recorded at the end of the test

The weight losses follow a similar trend as the hydrogen consumption; it is linked to the CAC content. Portlandite formed in F16, F19 and F20 is readily attacked by acid, this causing the decomposition of the matrix and the washing away of sand grains. Plain Portland mortar F19 loses 4 times more weight than the binary binder F2.

By plotting the consumption of H^+ as a function of the mass loss after the passage of 230 litres of sulphuric acid, figure 5-32, one notes a logical correlation; the materials destroyed in proportion to the consumption of acid .

Concerning the neutralizing capacity is important if the amount of acid is limited, for example in a closed system. In the drip-by-drip test, the system is open so the neutralisation capacity does not play a key role and no relationship between H^+ consumption and the neutralisation capacity is seen, as shown on the graph below.

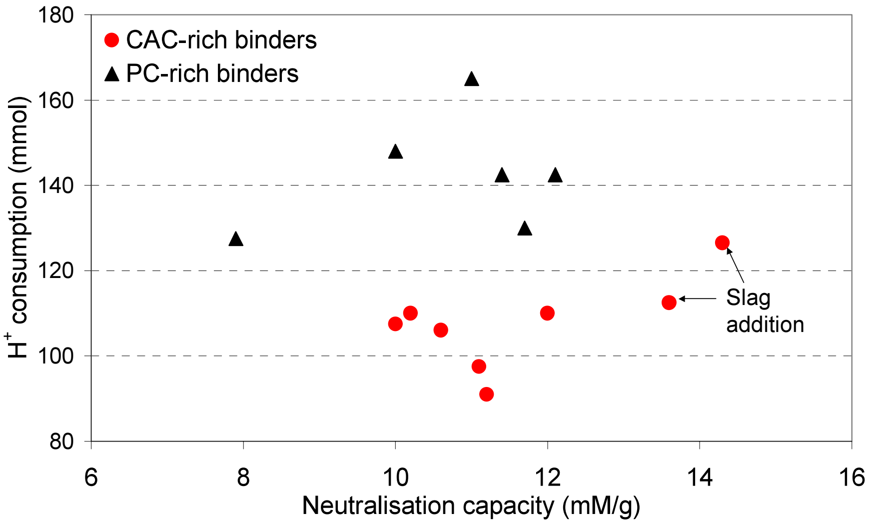

Figure 5- 33: H^+ consumption vs. neutralisation capacity

5.3.5 Conclusions

Corrosion by sulphuric acid proceeds by consumption of acid to different extents according to the nature of the hydrates and the presence of barrier layer, then this destroys the matrix. The good performance of CAC-C$-rich binders is explained by the precipitation of alumina gel throughout the matrix during hydration, which acts as a barrier layer because of its insolubility threshold at pH=3.5. It was already known that pure CAC mortars have good acid resistance and this study demonstrated that CAC/C$ binders show good resistance to acid attack.

5.4 EXTERNAL SULFATE ATTACK

Sulfates commonly known to cause deterioration of cement paste include sodium, calcium, and magnesium sulfate which can come either from natural (soil, groundwater, salt water) or artificial sources (fertilisers, sewers, industrial effluents, de-icing salts). The ions can be carried to inner sections of concrete by diffusion or capillary absorption. The nature of the cations involved in the sulfate-bearing environment is important and attack proceeds differently [21, 22]. Many research reports have been published on the complex mechanism of sulfate attack which is still not well understood [23, 24]. Expansion is most widely recognized but loss of adhesion and strength should also be considered; both aspects are treated below.

Although mechanisms are disputed, the deleterious reactions of sulfate attack basically agreed upon include [21, 25]:

$$C_3A.C\overline{S}.H_{12} + 2SO_4^{2-} + 2Ca^{2+} + 20H_2O \rightarrow C_3A.3C\overline{S}.H_{32} \qquad (5.14)$$

Alongside this reaction to form ettringite, there is the possibility for calcium ions to combine with sulfate to form gypsum:

$$Ca^{2+} + SO_4^{2-} + 2H_2O \rightarrow CaSO_4.2H_2O \qquad (5.15)$$

Both these reactions consume calcium, which is leaching from the other hydrates. Whether this reaction is expansive or not depends on the degree of supersaturation which can provide the driving force for expansion. The expansive force results from crystallization pressure which comes from the interaction between the solid product of a chemical reaction, e.g. ettringite and the cement paste [26, 27]. Two conditions are required for the occurrence of crystallization pressure [26]:

1- Confined crystal growth of the solid product

2- “Activity product” of reactants in the pore solution greater than the “solubility product” of the solid product

5.4.1 Accelerated test

As mentioned in Chapter 2, the sulfate resistance was carried out at the University of Berkeley under the direction of Dr. Paul Monteiro.

Test specimens consists of 1.3 cm cubes of hydrated cement paste, immersed in a circulating 4% Na_2SO_4 solution where the pH is maintained at 7.2. Because of the constant pH, the leaching of CH is maximized which better replicates field conditions.

Compressive strength is tested after curing (28 days, 100%RH) and after sulfate exposure (28 days of curing + 28 days or 90 days of immersion). While in laboratory studies, much attention has been paid to expansion and cracking, in this test, loss in compressive strength is used as a measure of the susceptibility of the cement to sulfate attack; both forms of sulfate attack are considered, i.e. softening- spalling and expansion.

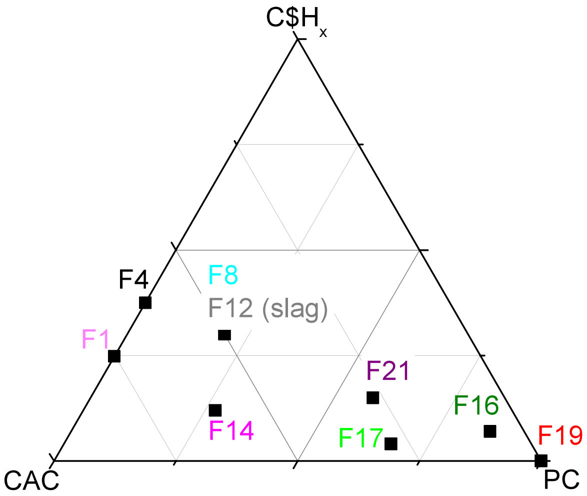

Figure 5- 34: Formulations tested in sulfate attack

5.4.2 Results and discussion

Results show a wide range of performances with the strength of some cement pastes relatively unaffected by sulfate exposure, while others experienced enough damage that they could not be tested in compression; this is the case of F4 and F8.

Figure 5-35 shows the relative change in compressive strength measured after 28 and 90 days of immersion.

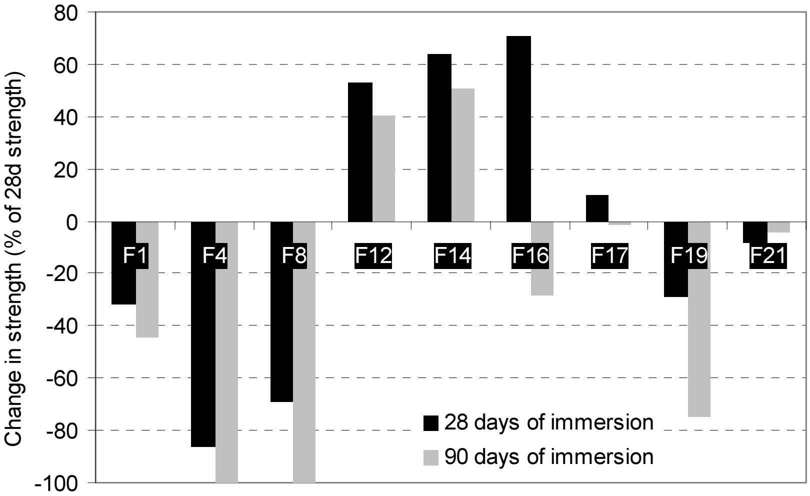

Figure 5- 35: Results of accelerated sulfate test after 28 and 90 days of exposure. Change in strength is based upon strength measured at 28 days of age, prior to exposure.

Increases in strength do not provide any information about sulfate resistance; such results only show that the cement continues to hydrate in sulfate solution over the test period and should not be interpreted as increased resistance to attack; F12 and F14 follow this behaviour.

It is difficult to identify general trends. After 90 days of immersion, the plain Portland F19 has lost about 70% of the 28-days strength while F17 and F21 remained quasi intact; the addition of CAC and C$ in Portland systems improves the sulfate resistance. On the other hand, binders with addition of slag (F14, F12) are less affected than the others; Khatri [28] and Lawrence [25] have already found that binders with slag provide significantly better chemical resistance to sulfate attack than Portland cement.

Loss in strength can be attributed to the decalcification of C-S-H which leads to a softening of the matrix and to cracking caused by expansion of ettringite and gypsum formation.
When portlandite is depleted, C-S-H, the primary strength-giving phase of the hydrated cement paste, undergoes decalcification and may become unstable. Loss of adhesion and strength are indicative of this form of sulfate attack.

5.4.3 SEM examination of polished sections

A brief SEM observation may give us more information to better understand the chemical degradation by sodium sulfate and the differences between the binders. As the samples tested at Berkeley were not available, new paste samples 1.3×1.3×1.3 cm^3 were cast and stored 90 days in 4% Na_2SO_4 solution.

5.4.3.1 Portland cement paste F19

The following BSE image was obtained from the Portland cement paste immersed 90 days in Na_2SO_4 solution.

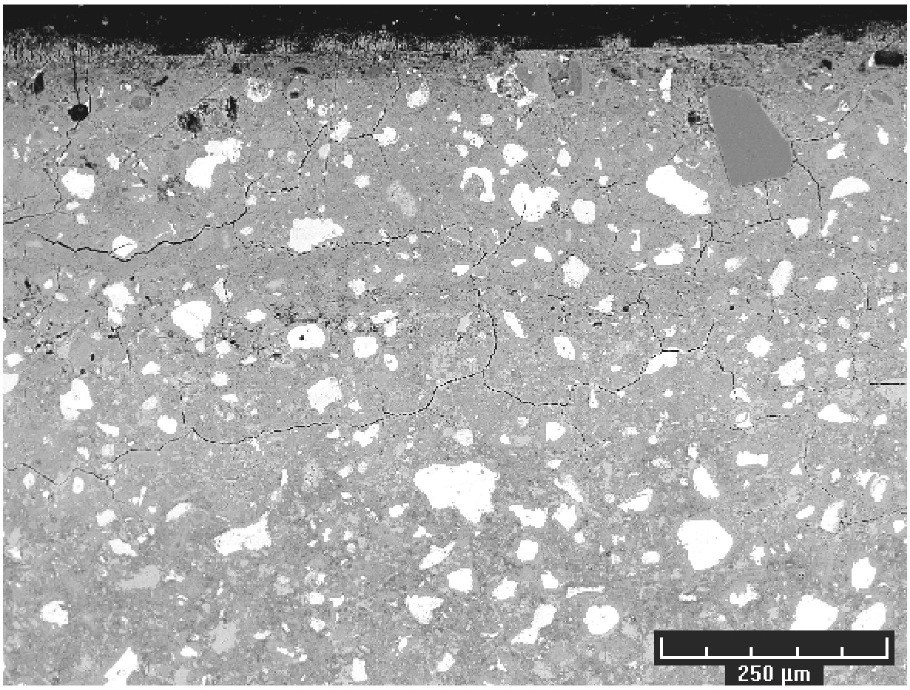

Figure 5- 36: BSE image of Portland cement paste immersed 3 months in Na_2SO_4 solution

Networks of cracks radiate through the paste to a depth of about 500 µm in a manner typical of that observed as a result of sulfate attack [29]. If we focus on the extreme surface, we can easily distinguish some precipitation of ettringite, red circles in image 5-37. Evidence of calcium hydroxide masses is absent.

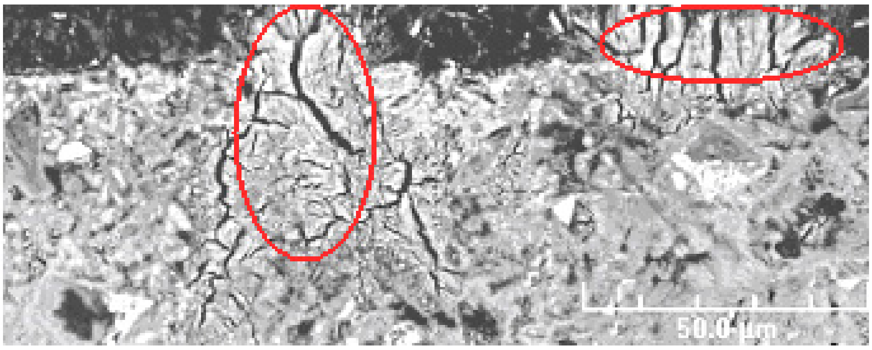

Figure 5- 37: High magnification of the extreme skin of F19. Red circles are ettringite rich areas

Figure 5-38 presents the sulphur mapping which reveals the presence of a sulphur-rich band located in veins parallel to the exposed surface. EDS microanalysis showed that the band is made of gypsum. The precipitation of gypsum is relevant with the disappearance of Portlandite. The zonal formation of ettringite and gypsum in samples exposed to sodium sulfate solution have already been observed by Maltais [30] and Brown [31].

Until now, there has been no clear documentation this gypsum formation leads to expansion or not; published papers either support or contradict this idea [32]. This study tends to support this idea; as the gypsum-rich layer corresponds to the cracked layer, the formation of gypsum could be the source of the expansion.

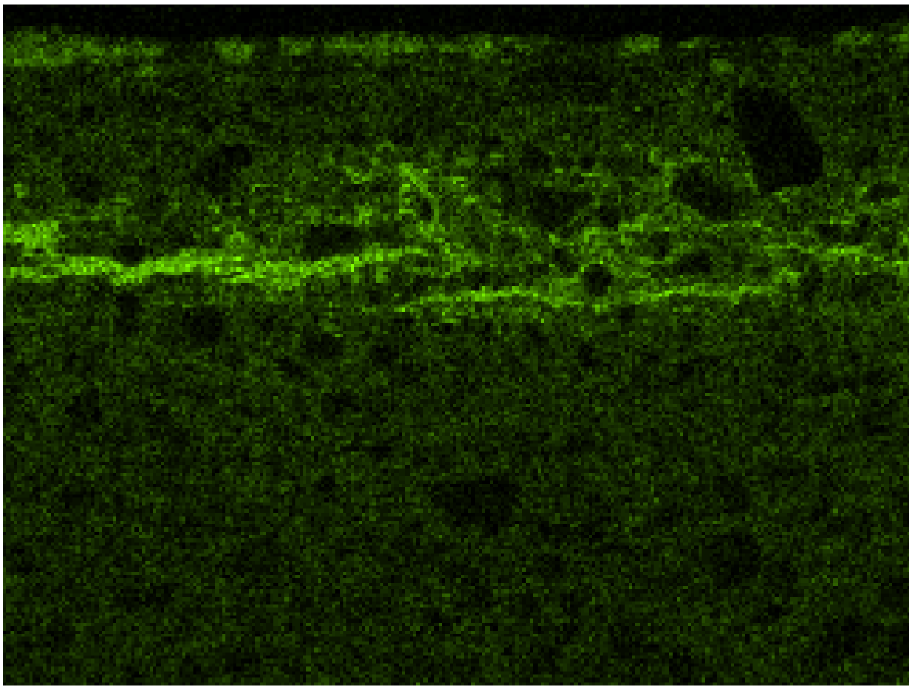

Figure 5- 38: Sulphur content mapping for F19

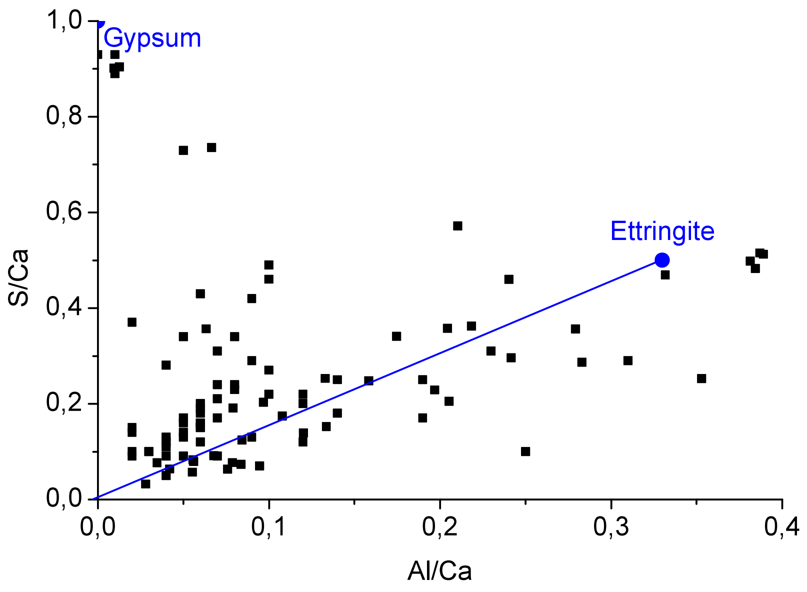

Figure 5- 39: EDS microanalysis in the degraded matrix of F19. S/Ca vs. Al/Ca plot.

The EDS X-ray analysis approximate to mixture of C-S-H and ettringite on the one hand and gypsum formation on the other hand; in this region, monosulfate has been replaced by ettringite. Calcium hydroxide is no longer present; it is the first calcium-bearing phase to be dissolved to restore the pore solution equilibrium. These results are consistent with Santhanam [22, 33] and Gollop's studies [34].

5.4.3.2 F16 cement paste

Figure 5-40- presents the microstructure of F16 immersed 3 months in Na_2SO_4 solution.

F16 exhibits more cracking than neat Portland. The presence of veins of gypsum (blue circle) is noteworthy and after EDS X-ray analysis, the dark regions have been identified to be ettringite, figure 5-41 (spectrum shows Si peak indicative of an adjacent Si-containing solid). Ettringite is formed by the reaction of the sulfate with alumina-bearing phases such as residual CAC grains or monosulfate. With the ingress of sufficient sulfate, sources of alumina will be locally exhausted and gypsum forms instead of ettringite. Gypsum precipitation also occurs by reaction of calcium hydroxide with the sulfate.

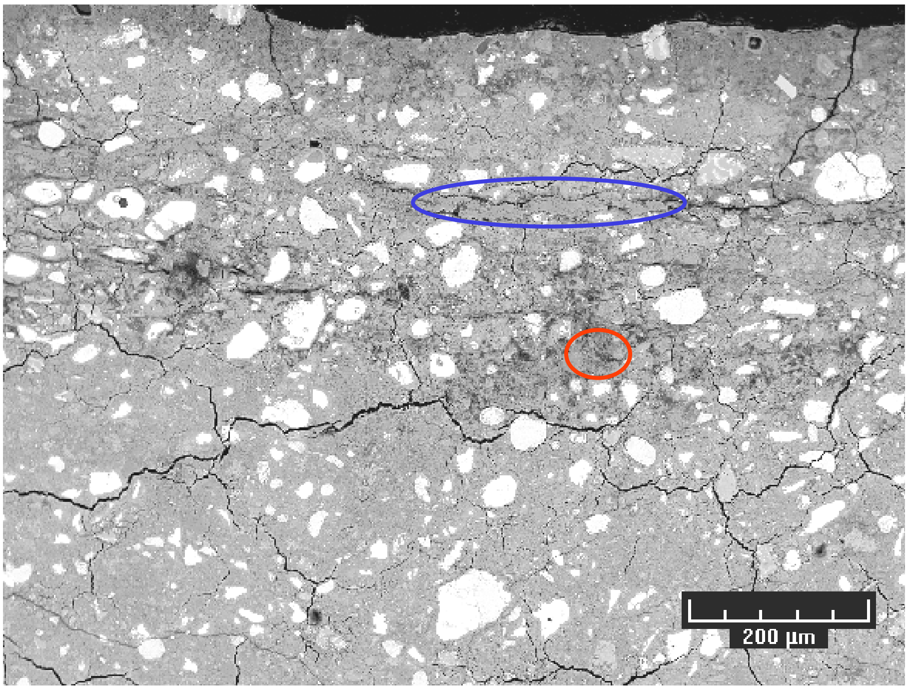

Figure 5- 40: BSE image of F16 cement paste immersed 3 months in Na_2SO_4 solution. Blue circle indicates gypsum vein and the red one ettringite-rich area.

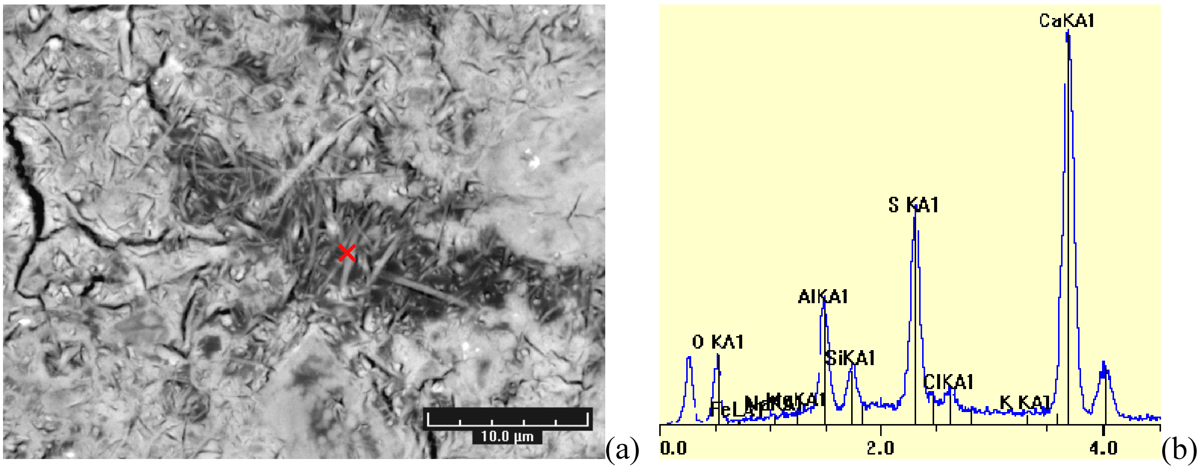

Figure 5- 41: (a) High magnification of the dark area (red circle in figure 5-?). (b) EDS spectrum corresponding to the red cross in (a)

5.4.3.3 Binary CAC/C$ cement paste F1

The BSE image shows a dense microstructure but a network of microcracks developed in the surface layer. The cracks may be due to formation of expansive ettringite; indeed it remains anhydrous aluminous grains which may react with sulfate from Na_2SO_4 solution.

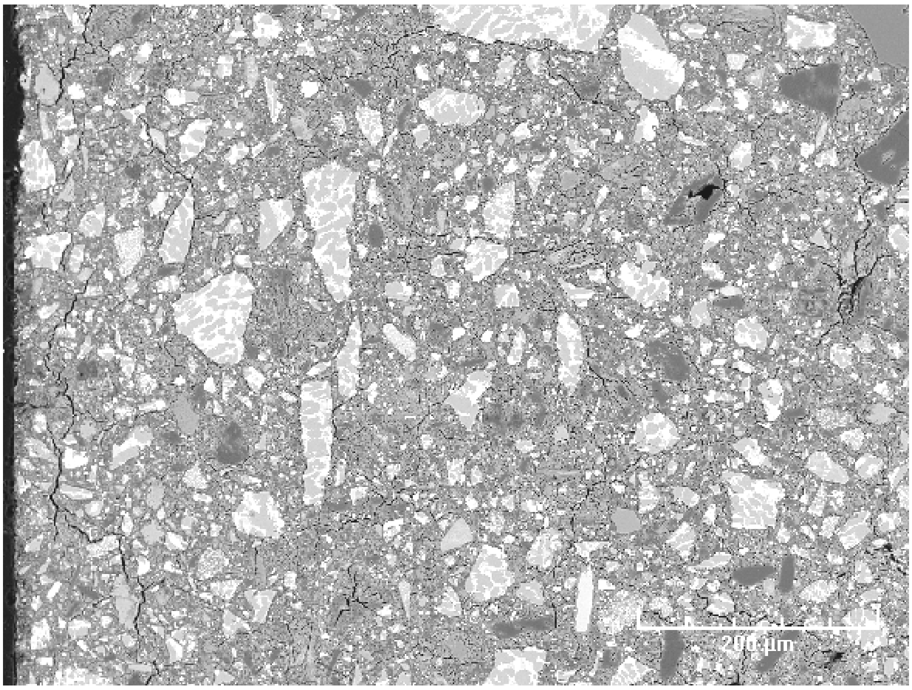

Figure 5- 42: BSE image of F1 cement paste immersed 3 months in Na_2SO_4 solution

5.4.3.4 F14 cement paste

The BSE picture also displays a very dense cementitious matrix and the extreme skin seems to be unaffected. Brown et al. [29] have attributed the elevated sulfate resistance of slag cement system to a reduction in diffusion of aggressive ions.

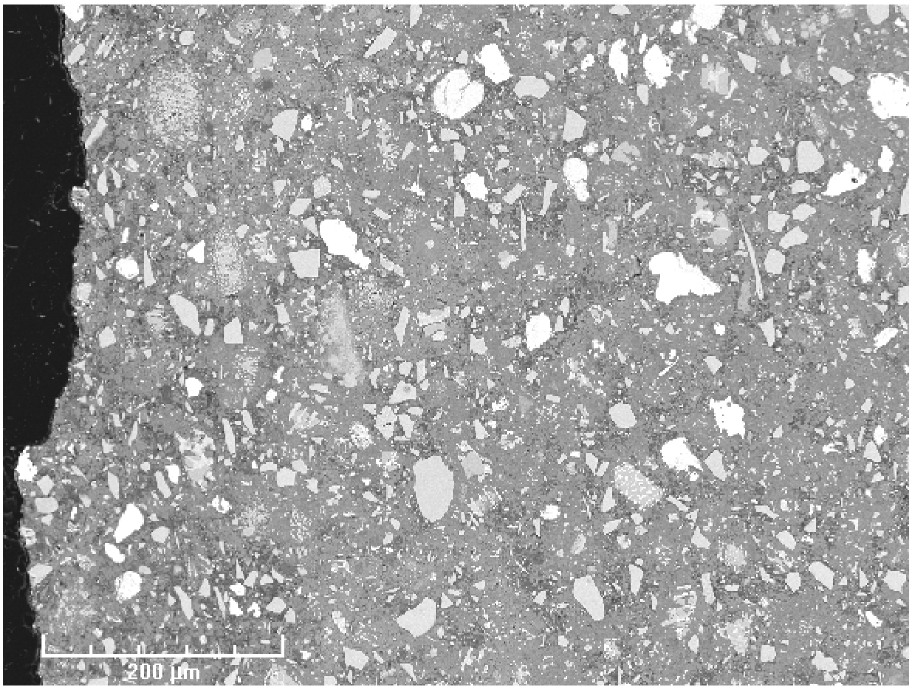

Figure 5- 43: BSE image of F14 cement paste immersed 3 months in Na_2SO_4 solution

5.4.4 Conclusions

The sulfate attack is accompanied by a decrease of mechanical strengths which results from expansion and/or softening of the cement paste. For CAC-C$ rich binders (F1, F4 and F8), expansion is the main consequence of sulfate attack whereas for PC-rich systems, softening is added. The softening comes from the decalcification of the matrix whose the calcium ions are consumed to form gypsum and ettringite. We confirm the formation of a cracks network in the examined binders, which is typical of sulfate attack. Moreover, addition of slag significantly improves the sulfate resistance, certainly because the diffusion of sulfates through pores is limited by the dense matrix.

5.5 CONCLUSIONS

Throughout this chapter, the behaviour of different binders in various environments were studied and the important points are reviewed below:

- Well-formulated CAC-C$ rich binders (C$ not in excess) are dimensionally stable whatever the storage and for all studied binders except F17 which presents high drying shrinkage, the dimensional variations are in the same range.

- Carbonation of CAC-C$ rich binders is faster than that for Portland rich systems. Portlandite plays a buffering role and ettringite carbonates into gypsum, AH_3 and calcium carbonate.

- Although an advanced state of carbonation, ettringite-rich systems keep good mechanical strengths.

- CAC-C$ systems present a better resistance to acid corrosion than Portland binders; AH_3 acts as a local protective barrier.

- Sulfate attack leads to a decrease of the mechanical strength in different extent according to the systems and slag addition increases the performance.

These accelerated tests have given data on the performance of different ternary systems in controlled atmospheres. This provide basic knowledge to better understand the complex degradation processes which take place during natural weathering.

5.6 REFERENCES

1. Johannesson, B., and Utgenannt, P. (2001). Microstructural changes caused by carbonation of cement mortar. *Cement and Concrete Research* **31**, 925-931.
2. Taylor, H.W.F. (1997). Cement Chemistry (London: Thomas Telford).
3. Lo, Y., and Lee, H.M. (2002). Curing effects on carbonation of concrete using a phenolphthalein indicator and Fourier-transform infrared spectroscopy. *Building and Environment* **37**, 507-514.
4. Roy, S.K., et al. (1999). Durability of concrete - accelerated carbonation and weathering studies. *Building and Environment* **34**, 597-606.
5. Scrivener , K.L., and Capmas, A. (1998). Calcium Aluminate Cement. In Lea's Chemistry of Cement and Concrete, Volume 13, 4th Edition, P.C. Hewlett, ed. pp. 709-778.
6. Xiantuo, C., and Ruizhen, Z. (1994). Kinetic study of ettringite carbonation reaction. *Cement & Concrete Research* **24**, 1383-1389.
7. Scrivener, K., et al. (1997). Effect of CO_2 and humidity on the mechanical properties of a formulated product containing calcium aluminate cement. In *13 internationale baustofftagung*, vol. 1. pp. 1-0745, 0741-0751: Weimar.
8. Nishikawa, T., et al. (1992). Decompostion of synthesized ettrinigte by carbonation. *Cement & Concrete Research* **22**, 6-14.
9. Grounds, T., et al. (1988). Carbonation of ettringite by atmospheric carbon dioxyde. *Thermochimica Acta* **135**, 347-352.
10. Zhou, Q., and Glasser, F.P. (2000). Kinetics and mechanism of the carbonation of ettringite. *Advances in Cement Research* **12**, 131-136.
11. Gabrisova, A., et al. (1991). Stability of Calcium Sulfoaluminate Hydrates in Water Solutions with Various Ph Values. *Cement and Concrete Research* **21**, 1023-1027.
12. Andrade, C., et al. (2001). Effect of humidity in the natural carbonation of CAC. In *Calcium Aluminate Cements 2001*. pp. 361-369.
13. Gaztanaga, M.T., et al. (2001). Accelerated Carbonation of calcium aluminate cement paste. In *Calcium Aluminate Cements* (M.a. Glasser, ed.).
14. Goni, S., et al. (2002). Role of cement type on carbonation attack. *Journal of Materials Research* **17**, 1834-1842.
15. Carde, C., and Francois, R. (1997). Effect of the leaching of calcium hydroxide from cement paste on mechanical and physical properties. *Cement and Concrete Research* **27**, 539-550.
16. Kuzel, H.J. (1996). Initial hydration reactions and mechanisms of delayed ettringite formation in Portland cements. *Cement & Concrete Composites* **18**, 195-203.
17. Kuzel, H.J., and Pollmann, H. (1991). Hydration of C_3A in the Presence of $Ca(OH)_2$, $CaSO_4.2H_2O$ and $CaCO_3$. *Cement and Concrete Research* **21**, 885-895.
18. Shi, C., and Stegemann, J.A. (2000). Acid corrosion resistance of different cementing materials. *Cement and Concrete Research* **30**, 803-808.
19. Letourneux, R., and Scrivener, K.L. (1999). The resistance of calcium aluminate cements to acid corrosion in sea water applications. In *Modern concrete materials: binders, additions and admixtures* (T.E.D. R.K. Dhier, ed.): Dundee.
20. Espinosa, B., et al. Acid attack of hydraulic cement-bound materials: corrosion kinetics and neutralisation capacity. In *13th Int. corrosion Congress*. pp. 1-10: Melbourne.

21. Hime, W.G., and Mather, B. (1999). "Sulfate attack," or is it? *Cement and Concrete Research* **29**, 789-791.
22. Santhanam, M., et al. (2003). Mechanism of sulfate attack: a fresh look: Part 2. Proposed mechanisms. *Cement and Concrete Research* **33**, 341-346.
23. Neville, A. (2004). The confused world of sulfate attack on concrete. *Cement and Concrete Research* **34**, 1275-1296.
24. Mehta, P.K. (2000). Sulfate attack on concrete: separating myths from reality. In *5th CANMET/ACI International Conference on Durability of Concrete*. pp. 57-61: Barcelona, Spain.
25. Lawrence, C.D. (1990). Sulfate attack on concrete. *Magazine of Concrete Research* **42**, 249-264.
26. Ping, X., and Beaudoin, J.J. (1992). Mechanism of sulfate expansion I. Thermodynamic principle of crystallization pressure. *Cement and Concrete Research* **22**, 631-640.
27. Scherer, G.W. (1999). Crystallization in pores. *Cement and Concrete Research* **29**, 1347-1358.
28. Khatri, R.P., et al. (1997). Role of permeability in sulfate attack. *Cement and Concrete Research* **27**, 1179-1189.
29. Brown, P., et al. (2004). Microstructural changes in concretes with sulfate exposure. *Cement and Concrete Composites* **26**, 993-999.
30. Maltais, Y., et al. (2004). Predicting the durability of Portland cement systems in aggressive environments. Laboratory validation. *Cement and Concrete Research* **34**, 1579-1589.
31. Brown, P.W., and Badger, S. (2000). The distributions of bound sulfates and chlorides in concrete subjected to mixed NaCl, $MgSO_4$, Na_2SO_4 attack. *Cement and Concrete Research* **30**, 1535-1542.
32. Tian, B., and Cohen, M.D. (2000). Does gypsum formation during sulfate attack on concrete lead to expansion? *Cement and Concrete Research* **30**, 117-123.
33. Santhanam, M., et al. (2002). Mechanism of sulfate attack.A fresh look. *923-929* **32**, 915-921.
34. Gollop, R.S., and Taylor, H.F.W. (1992). Microstructural and Microanalytical Studies of Sulfate Attack .1. Ordinary Portland-Cement Paste. *Cement and Concrete Research* **22**, 1027-1038.

Chapter 6. Natural ageing

Accelerated ageing provides some data on the performance of ternary binders in well-controlled environments; this allows us to better understand the degradation mechanisms. This background will be helpful to clarify the behaviour in natural exposure.

6.1 INTERACTIONS OF MORTARS WITH THE ENVIRONMENT

6.1.1 Main features of weather influence

The exposed surface has a direct interaction with the surrounding environment. Natural weather usually implies irregular changes of temperature and relative humidity, which induce a non-steady state regime in the sample. The interaction is much more complicated than laboratory tests as it involves a great number of climatic parameters such as diurnal cycles, seasonal cycles, effect of rainfall and CO_2,...

6.1.2 Processes occurring in concrete during hydrothermal cycles

When it rains, the amount of water in the concrete changes dramatically in short periods of time. It is absorbed at the concrete surface. The drying afterward will cause a reverse water movement although depending on the length of the dry period, not all water taken up dries out. Part of the water and vapour diffuses towards the bulk while the rest evaporates out. To sum up, three main mechanisms are involved in the water exchange with exterior:

- Evaporation / condensation
- Diffusion of water vapour across the empty pores or as liquid phase by diffusion along the pore walls
- Exchange with the exterior; water can also enter the concrete by diffusion as vapour phase or by absorption when raining.

6.2 PHYSICAL ASPECTS

6.2.1 Samples

The first collection of samples on the 4 sites was planned after 1 year and the second one after 3 years. After one year, the surfaces were relatively undamaged compared to 3 years, figure 6-1, so the thorough study of the surface microstructure was undertaken only on the 3-years old samples. Investigation focussed on the samples exposed in Norway as these were the earliest samples available and they also showed the highest degradation.

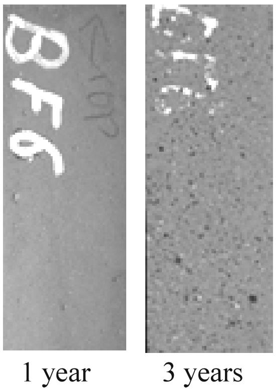

Figure 6- 1: Exposed surface of F6 after 1 year and 3 years of exposure in Norway

6.2.2 Mechanical behaviour

The mechanical behaviour is a very important engineering property since many in-service applications require a specific strength. Here the mechanical strength evolution under natural exposure was measured.

The compressive strengths under outdoor exposure up to 3 years are shown in figure 6-2. The 28 days value corresponds to the curing time 100%RH and serves as reference.

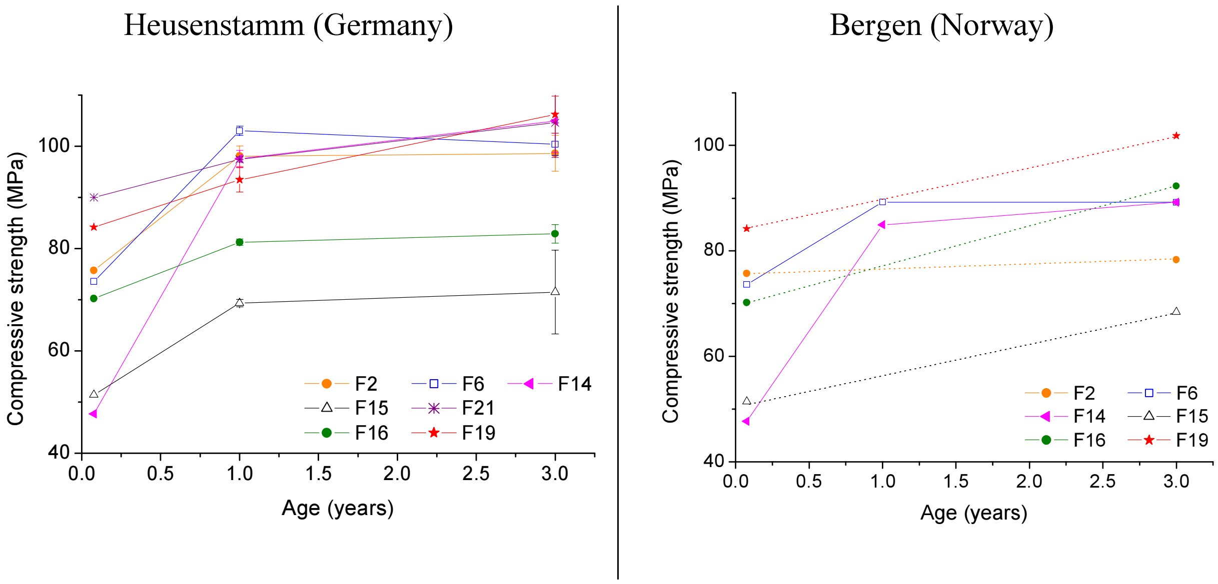

Figure 6- 2: Compressive strength of German and Norwegian samples (1 year samples of Norway were not available)

Whatever the exposure site, after the curing time, the compressive strength still increased and between 1 and 3 years, all binders remain stable. The 28-days strength of F14 was low but strength gain at 1 year is important. Whatever the age, small addition of CAC and C$ in Portland cement reduced the compressive strength; reductions were about 20% and 40% for F16 and F15 respectively stored in Germany; however as more CAC and C$ were added (F21), the compressive strength is equivalent than that of Portland.

After 3 years of exposure, small differences appears between the location of the exposure site; as the Norwegian climate is more aggressive (snow, freezing thawing cycles, rain) than that in Germany, mechanical strengths in Norway are slightly lower. It is worth pointing out that CAC-rich systems behave as well as PC-rich systems.

6.2.3 Surface aspects of the 3 years-old samples

6.2.3.1 Visual observations

The following pictures show the appearance of the exposed surface after 3 years which is a sufficient time to notice differences between Norwegian and German sites. For the sake of clarity, only compositions of the “main“ list (F2, F6, F14, F15, F21, F16, F19) or compositions which present particular features are shown.

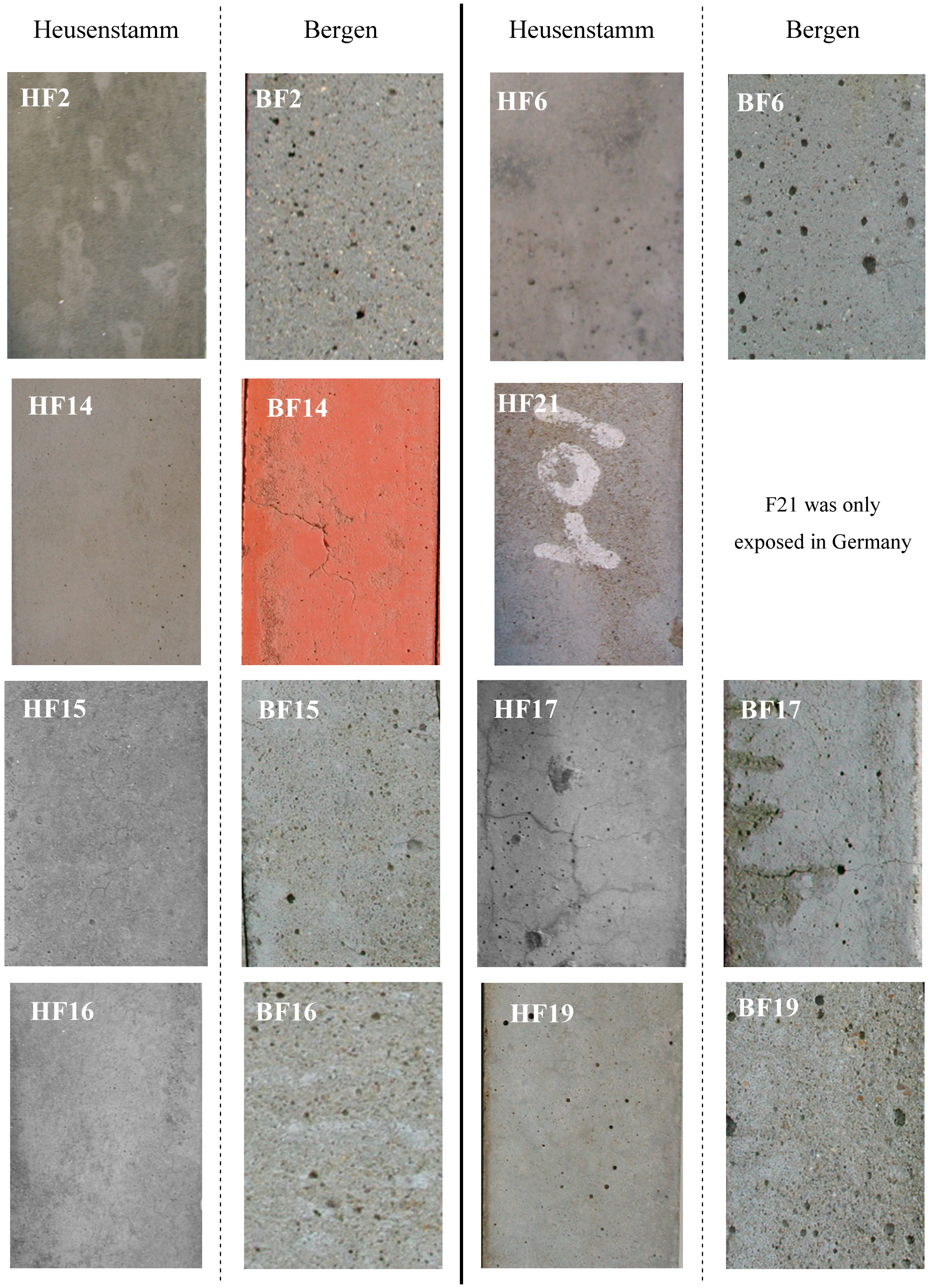

Figure 6- 3: Visual aspect of the exposed surface. Comparison between Germany (Heusenstamm) and Norway (Bergen) after 3 years of outdoor exposure. The red colour of BF14 is due to a pigment which has been removed from the formulation later.

It is clear that the Norwegian prisms are more eroded due to the high rainfall in Bergen. Regardless of the initial formulation, the degree of erosion is similar except for F14 which seems to be less affected but presents microcracks. Microcracks are also observed for F17 on both sites. It may be due to expansion, freeze-thaw cycles or drying shrinkage. The latter is likely because we observed in Chapter 5 that F17 presented a high drying shrinkage.

Among all systems stored under outdoor conditions, one formulation stands out, namely BF5, figure 6-4; its surface is practically intact whereas BF6 with a similar composition but a different w/c ratio is eroded. This good behaviour is attributable to the lower water cement ratio.

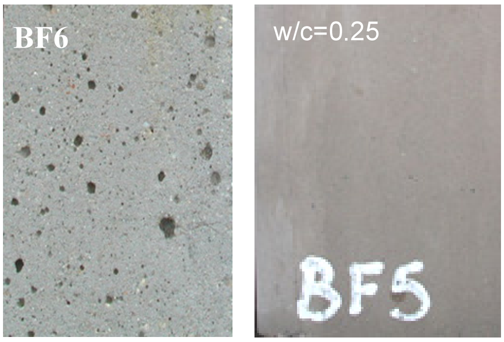

Figure 6- 4: Surface aspect of F6 and F5 after 3 years under natural exposure in Norway

6.2.3.2 Thickness of the microstructure carbonated by the environment and degree of erosion

The pictures in figure 6-5 exhibit general views of the different profiles. The thickness of the microstructure modified by the environment was measured by SEM; from the external surface, we progress inward till we reach the bulk microstructure (cf. Chapter 3). The values are reported on the graph 6-6.

The degree of erosion is simply assessed by examination of the following polished cross sections .

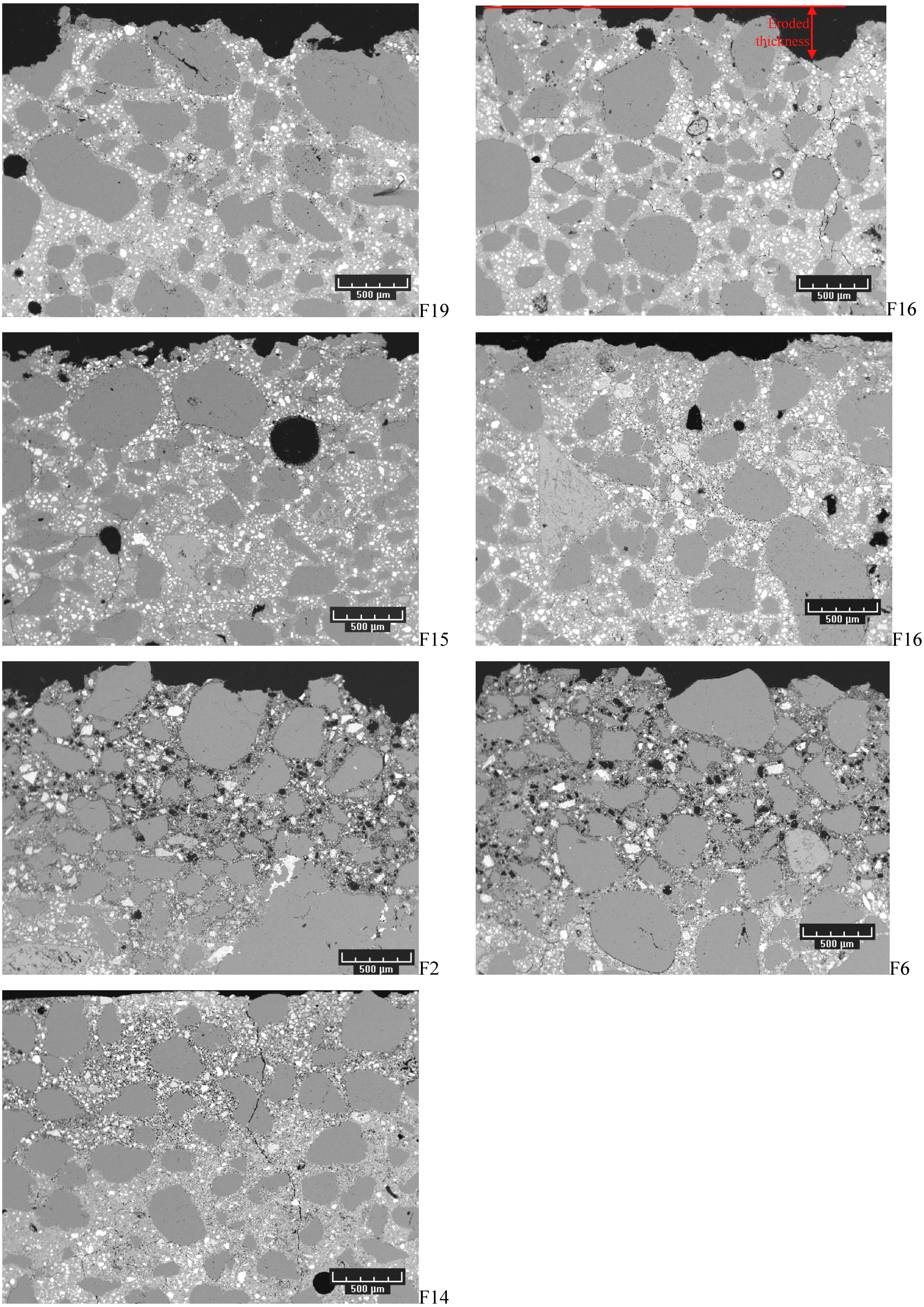

Figure 6- 5: BSE images of the eroded surface after 3 years under natural exposure in Norway.

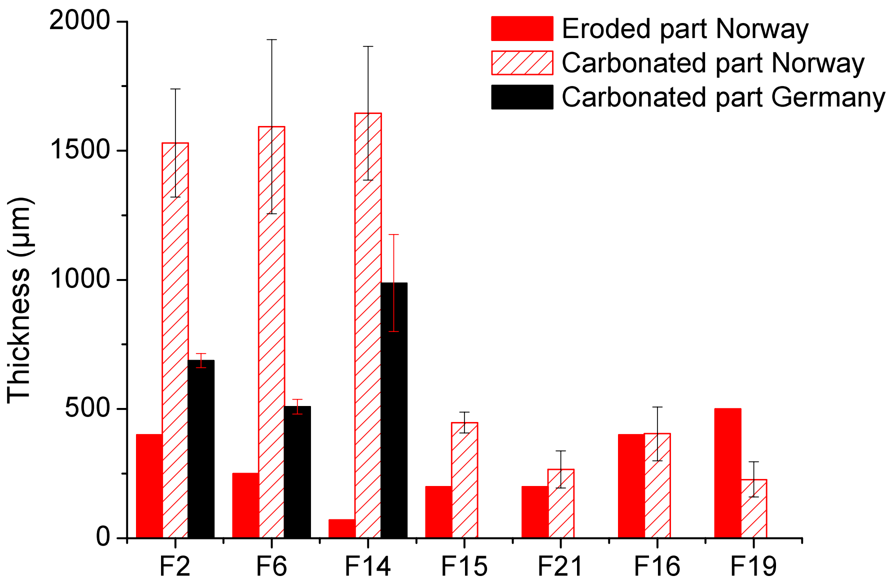

Figure 6- 6: Thickness of the carbonated microstructure after 3 years of exposure in 2 different climates. The thickness of the eroded part was added on the graph but the values are approximate because the removed material could not be quantified.

The error bars are high due to the presence of sand grains or microcracks which can locally modify the thickness. Another source of error is the eroded part; the amount of material which has been removed is unknown (the greater the eroded part, the greater the thickness is underestimated). It is worth pointing out that for CAC-rich systems, the carbonated microstructure becomes darker because of precipitation of alumina gel and not because of higher porosity.

We first notice a clear difference between binders with high content of CAC-C$ namely F2 and F6 and F14, which have a thickness of about 1.5 mm and Portland-rich binders whose the thickness are lower than 0.5 mm. However, this modification of microstructure have no impact on the mechanical behaviour of F2, F6, F14;

Quantification of erosion is quite tricky but we can compare the flatness of the surface and assess the thickness of the eroded part; an example of the measurement is given for F16 in figure 6-5. A simple look to figure 6-5 indicates that erosion of F14 is limited; the skin is not very damaged. For the other samples, the eroded thickness is in the range 250-500 µm and only small distinctions appear between Portland-rich systems and CAC-C$ rich binders; cementitious matrix and sand grains are more or less removed.

As already mentioned, 3 years of exposure is sufficient to observe the impact of the climate; German climate is less aggressive than the Norwegian one. This confirms the influence of the environment which has to be taken into account in durability prediction.

6.3 EVOLUTION OF THE MICROSTRUCTURE NEAR THE EXPOSED SURFACE AFTER 3 YEARS

As for the bulk characterisation, SEM combined with XRD were used to investigate the evolution of the microstructure under natural ageing.

As explained before, the detailed microstructural study has been done on the 3 years old Norwegian samples.

6.3.1 Plain Portland F19

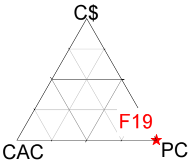

Figure 6-7 illustrates the microstructure of the sample surface.

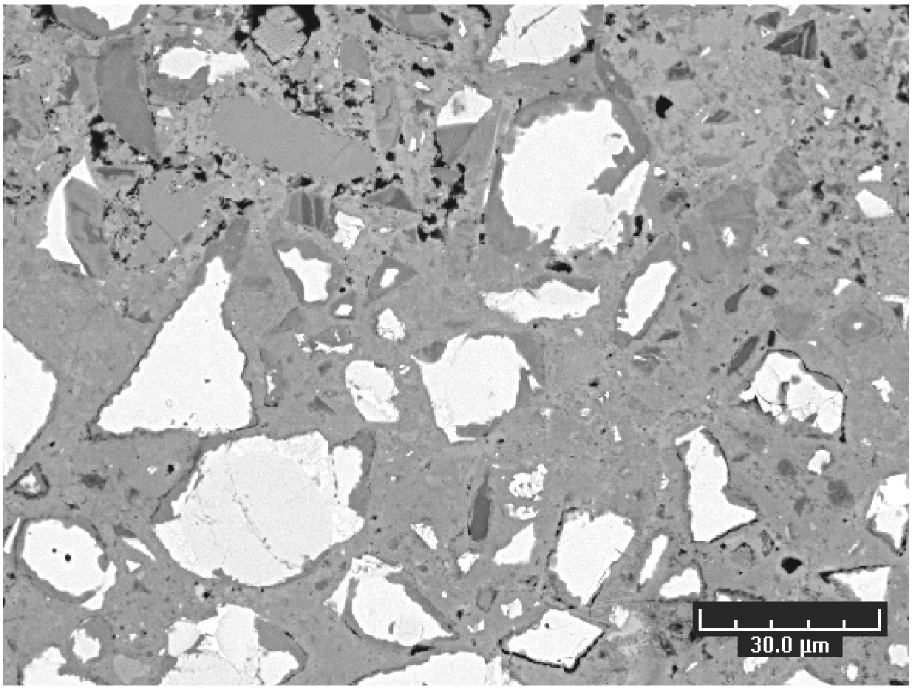

Figure 6- 7: BSE image in the modified part of F19

The matrix aspect of the surface is reminiscent of that observed for Portland in accelerated test of carbonation. With a simple observation of the surface microstructure, the signs of carbonation can be recognised such as homogenous and dense matrix, disappearance of portlandite and decalcified C-S-H. As for accelerated carbonation, there is a progressive disappearance of portlandite as we progress inward. Okochi [1] also established that after 2-years atmospheric exposure, mortar specimen were carbonated and the variation in the ratio of $CaCO_3$ to $Ca(OH)_2$ is function of distance from the exposed surface.

No traces of CH are detected by XRD or TGA, therefore EDS analysis, graph 6-8 (a), can be interpreted as being calcite and C-S-H. The graph 6-8 (b) highlights the disappearance of monosulfate; the sulfates were leached.

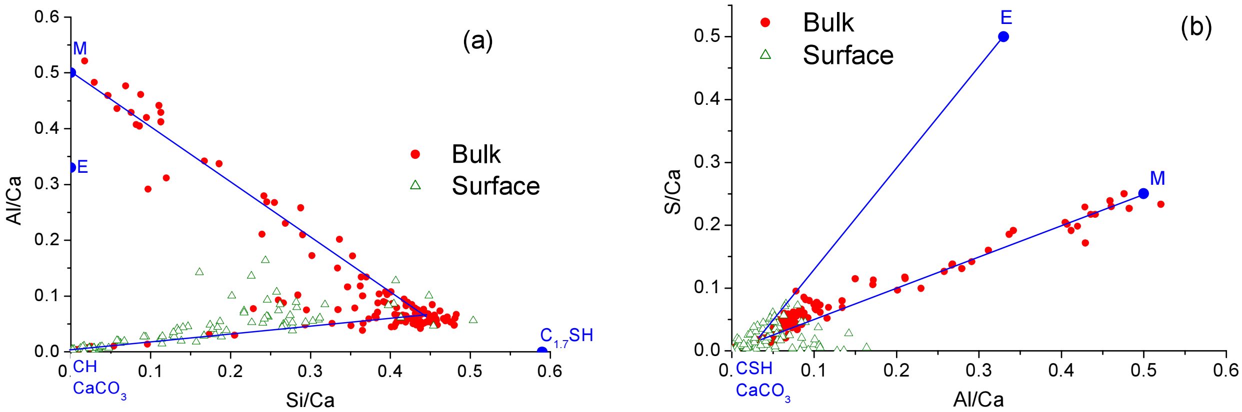

Figure 6- 8: EDS microanalysis in the modified part of F19. (a) Al/Ca vs. Si/Ca. (b) S/Ca vs. Al/Ca

We should also take into account that samples are washed by rainwater leading to a leaching of certain phases: portlandite dissolves and C-S-H are progressively decalcified. Thus, on the one hand, the leaching increases the porosity and on the other hand the carbonation fills the pores. A “competition” of these two mechanisms occurs and leaching dominate in the extreme surface leading to a more porous layer.

6.3.2 F16

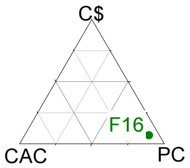

As we found previously, addition of CAC and C$ leads to precipitation of extra ettringite and decrease of Portlandite content. The picture below illustrates the microstructure of F16.

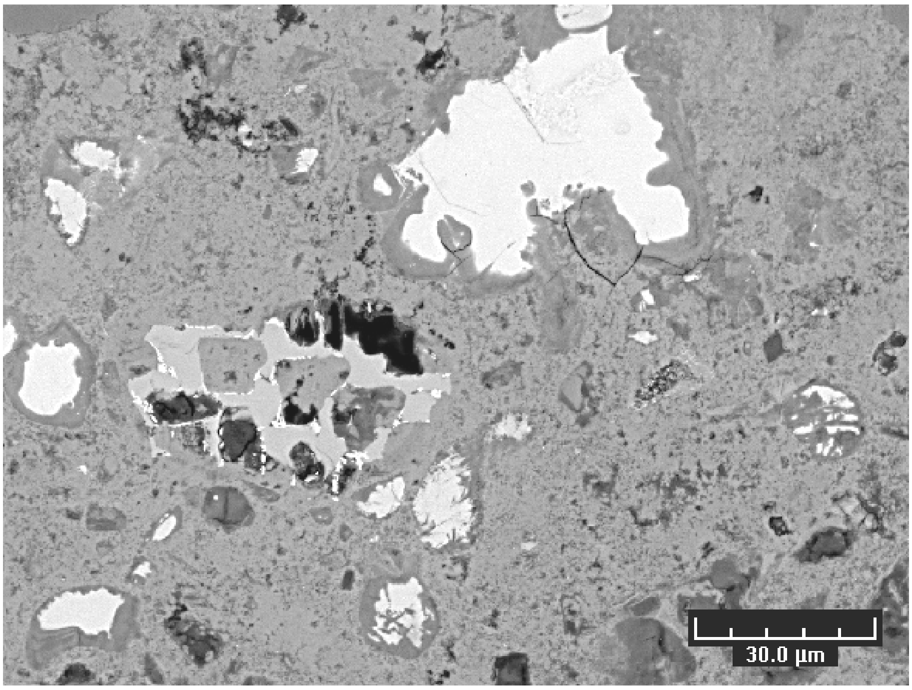

Figure 6- 9: BSE image of the modified part of F16

As previously, by studying the near surface microstructure of F16, we notice that the microstructure shows signs of carbonation such as the homogeneity of the matrix, the absence of CH and monosulfate-rich layer surrounding CAC grain or large regions of C-S-H exhibiting a dark colour.

Graph 6-10 (b) indicates that ettringite and monosulfate are no longer present in the matrix at the surface; they have also been carbonated. EDS analysis suggest that the matrix consists $CaCO_3$ and AH_3. The silica detected in graph 6-10 (a) comes from the decalcification of C-S-H.

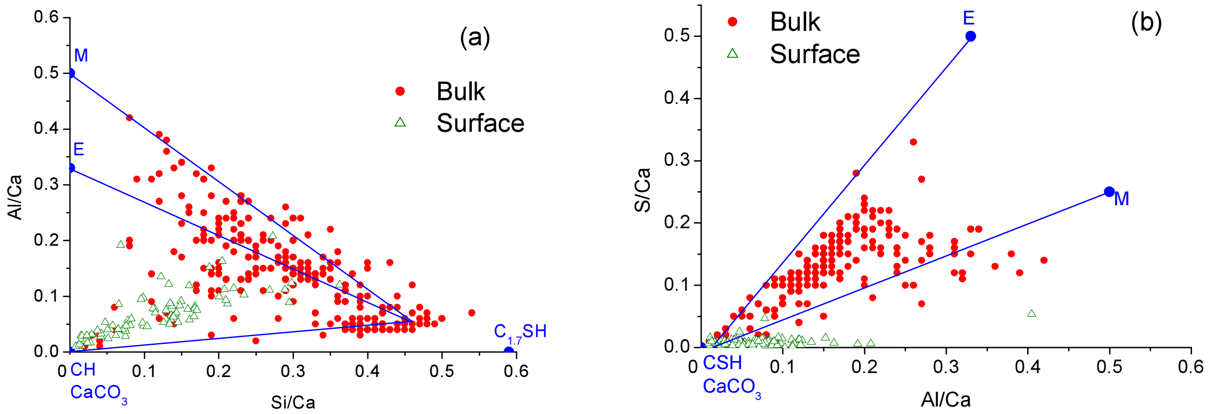

Figure 6- 10: EDS microanalysis in the modified part of F16. (a) Al/Ca vs. Si/Ca. (b) S/Ca vs. Al/Ca

However, according to Eq (5.6) we are expected gypsum formation as a carbonated product of ettringite and monosulfate but there is no existence of sulfate phase in the modified part, as confirmed by X-ray mapping, figure 6-11. Gypsum was thus dissolved by the rainwater. This is in agreement with Moranville [2] who has also observed sulfate leaching.

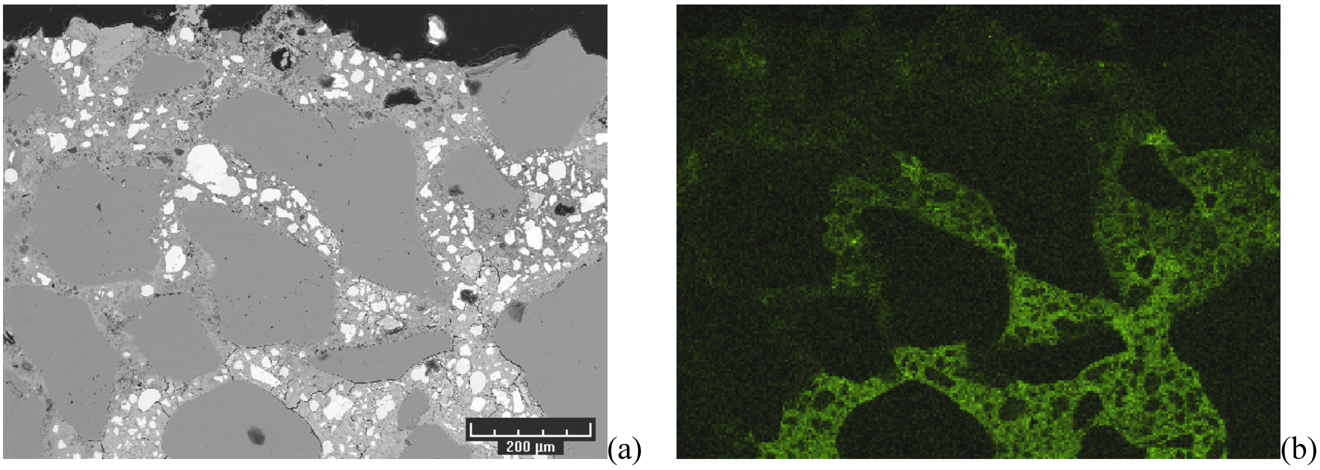

Figure 6- 11: Mapping of sulphur of the exposed surface. (a) original image, (b) sulphur mapping

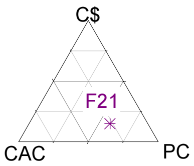

6.3.3 F21

As discussed (Chapter 3, section 3.2.4), further additions of CAC and C$ modify the hydration pattern. As the core of the sample has been identified as being ettringite, monosulfate, and strätlingite; $CaCO_3$ and alumina gel are expected if carbonation and leaching occur.

The near surface microstructure is shown in picture 6-12. AH_3 clusters are easily visible through the matrix (dark regions) while the light grey phase is calcium carbonate.

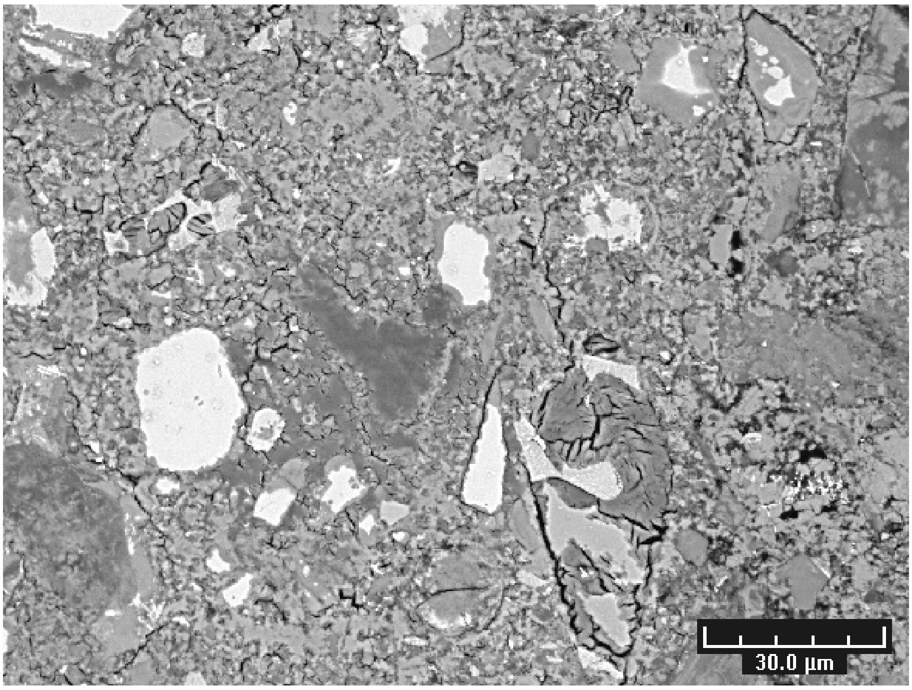

Figure 6- 12: BSE image of the modified part of F21

EDS analysis, figure 6-13, support the presence of calcite and AH_3.

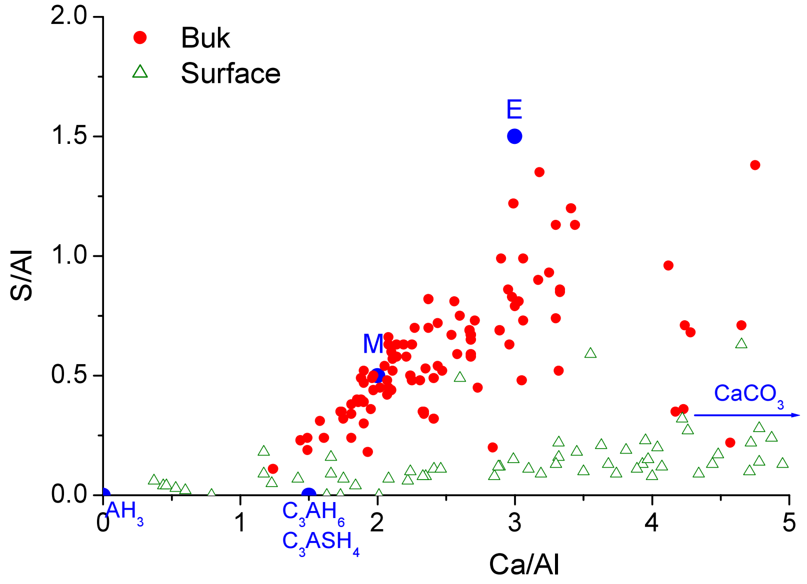

Figure 6- 13: EDS microanalysis in the modified part of F21

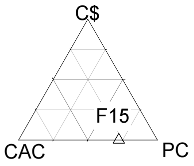

6.3.4 F15

A characteristic image of the near surface microstructure is given in figure 6-14.

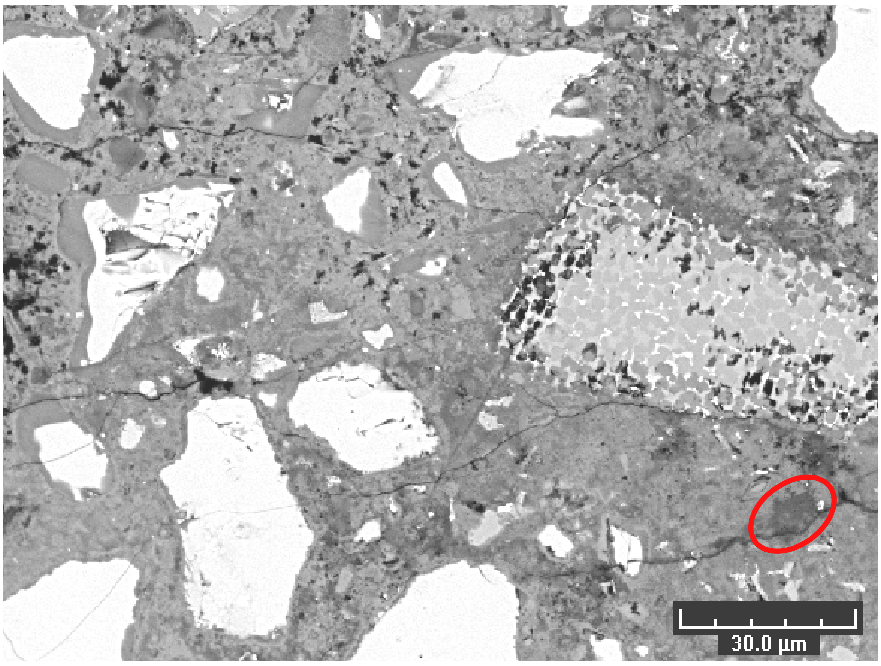

Figure 6- 14: BSE image of the modified part of F15. The circle indicates an Al-rich area.

The outer products seem to be composed of 3 phases defined by specific grey levels. The lightest phase has been identified to be calcium carbonate and the darkest one to be Al-rich phase such as AH_3 (red circle). The EDS analysis indicates that the intermediate grey corresponds to mixtures of these phases.

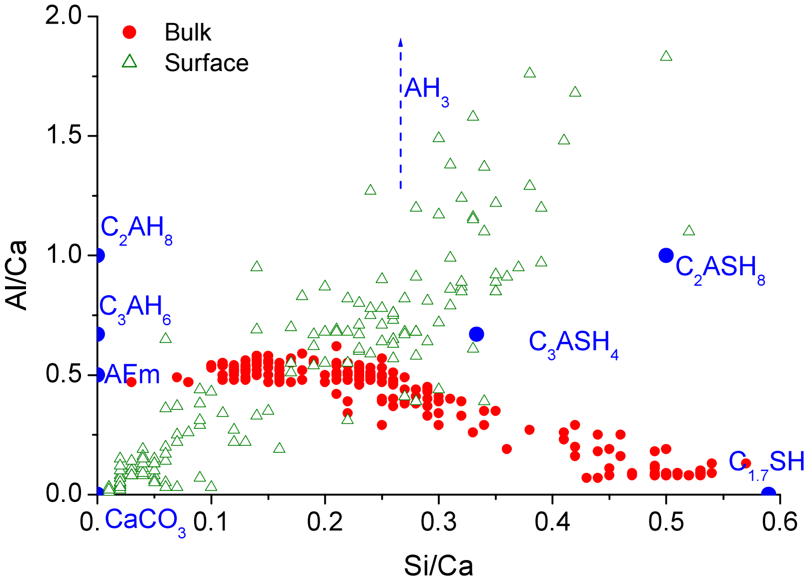

Figure 6- 15: EDS microanalysis in the modified part of F15

Many points are concentrated around the origin of the plot which corresponds to calcite. C-S-H is no longer detected. Other points can be interpreted as hydrogarnet intermixed with AH_3; this is consistent with a partial carbonation of hydrogarnet which is known to lead to calcite and AH_3 (Eq. 5.6). Presence of strätlingite is also probable.

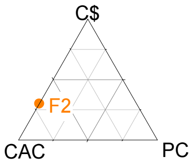

6.3.5 F2

The following image exhibit the microstructure of the modified part of F2.

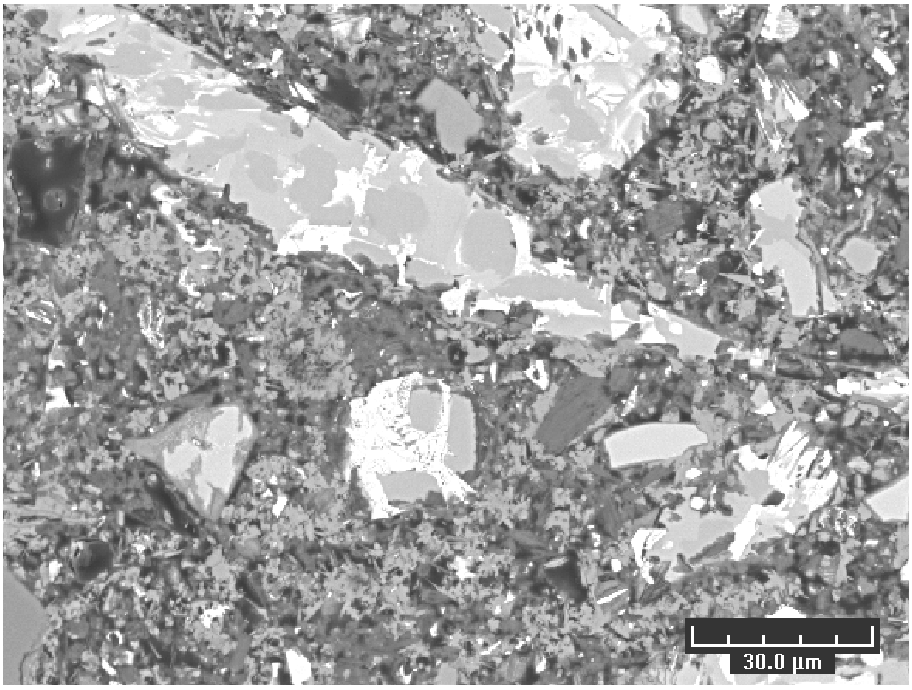

Figure 6- 16: BSE image of the modified part of F2. The darkest areas are alumina gel and the lightest one calcite.

The matrix aspect is completely different than that of the bulk (Chapter 3, section 3.3.2). Regions striated by drying cracks due the shrinkage of ettringite under vacuum have disappeared; ettringite is therefore certainly no longer present in the matrix.

This is confirmed by the EDS results. The points line almost exactly along a tie line connecting AH_3 to $CaCO_3$ showing that ettringite has been carbonated.

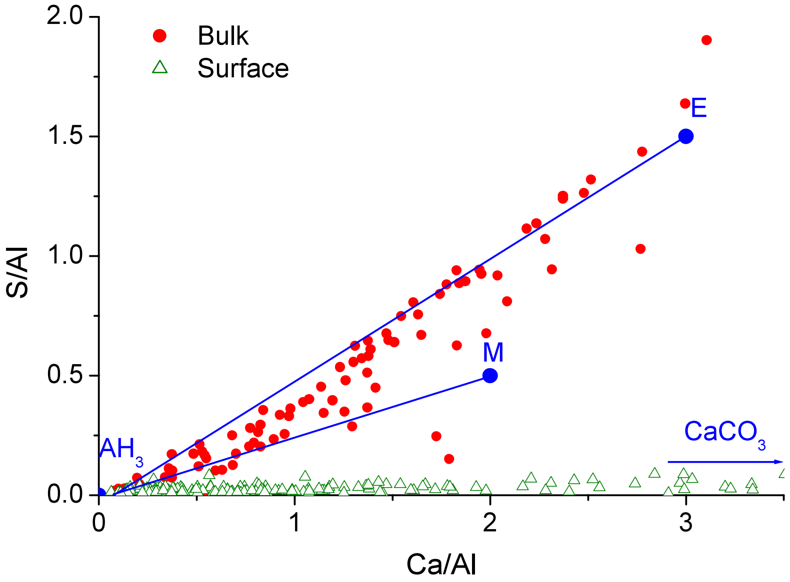

Figure 6- 17: EDS microanalysis in the modified part of F2

Referring to Eq (5.6), gypsum is expected but as mentioned before, sulfate is dissolved by rainwater. The leaching of sulphur is clear on the mapping presented below.

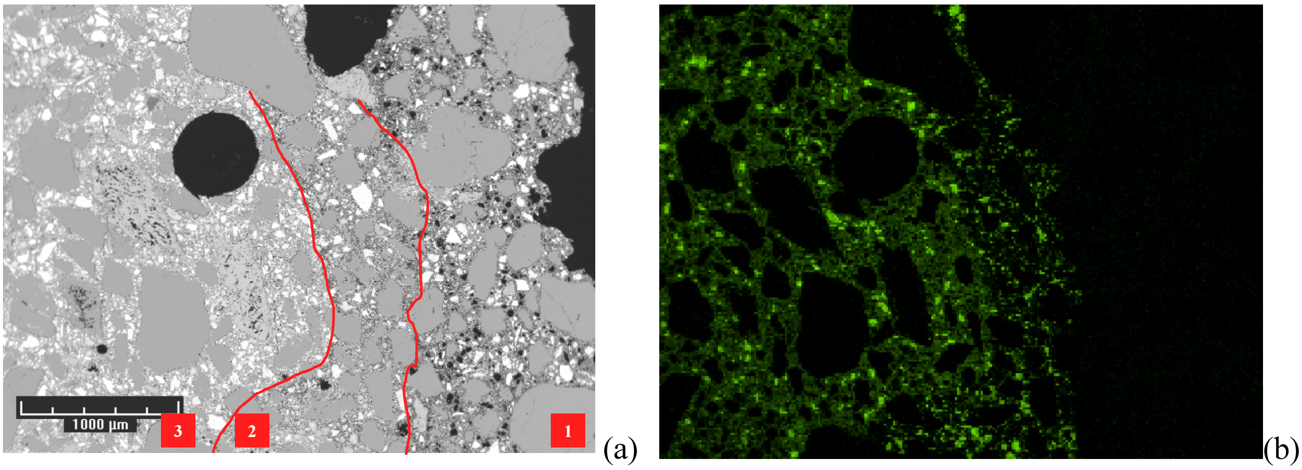

Figure 6- 18: Mapping of sulphur of the exposed surface. (a) original image, 1: lixiviated zone, 2: carbonated zone, 3: core. (b) sulphur mapping

On the mapping, 3 distinct regions are visible outward from the unaffected zone: the core (zone 3), the carbonated area (zone 2) and the leached away one (zone 1). In zone 1, areas initially occupied by gypsum leave empty space which increases the porosity. The thickness of the zone where sulphur is almost totally dissolved represents 2/3 of the total modified depth.

6.3.6 F6

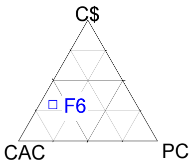

The figure 6-19 illustrates the surface microstructure of F6.

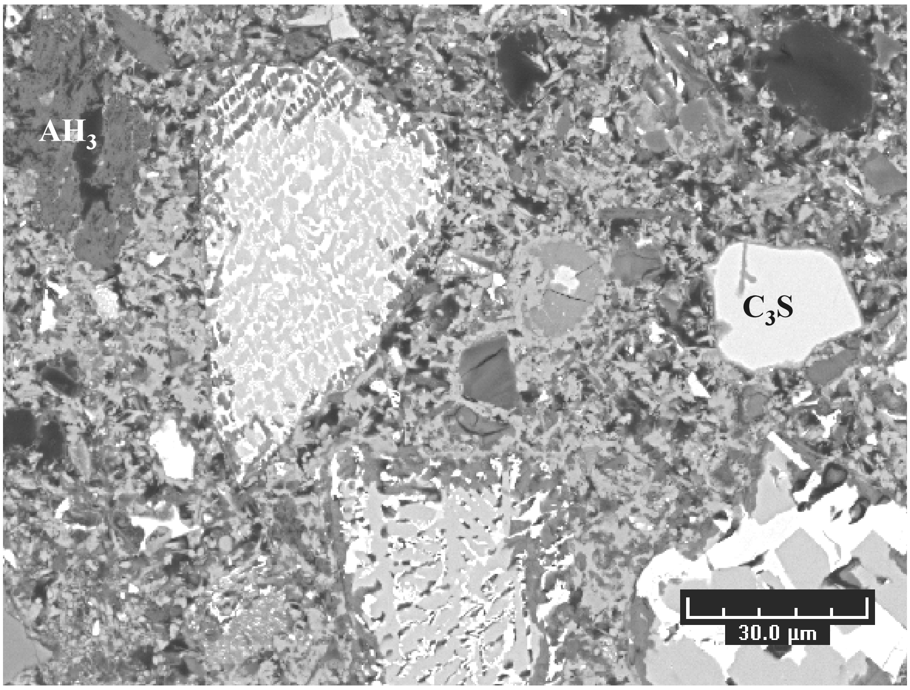

Figure 6- 19: BSE image of the modified part of F6.

As seen in Chapter 3, the bulk hydrates of F2 and F6 are similar, therefore an analogous microstructure in the modified part was expected.

As F2, EDS analysis can be interpreted as AH_3 and $CaCO_3$. No traces of gypsum are detected either in SEM or in XRD because of its leaching by the rainwater as it was shown for F2.

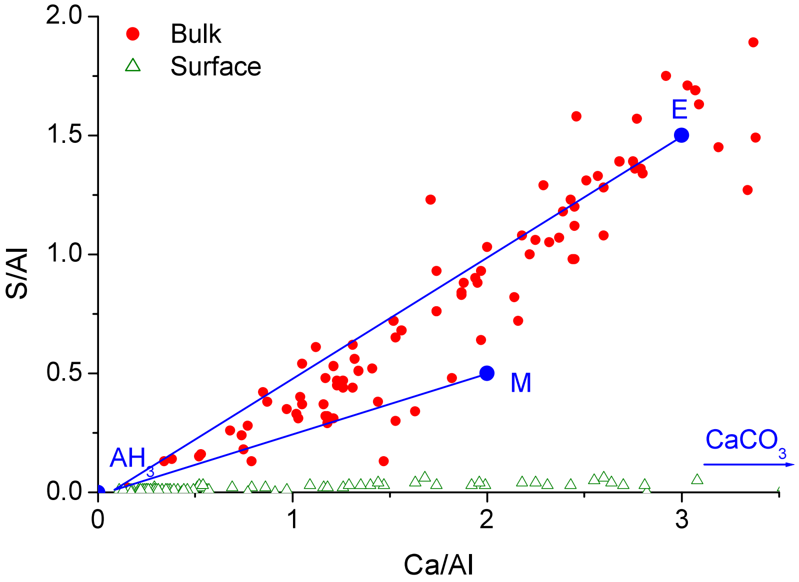

Figure 6- 20: EDS microanalysis in the modified part of F6

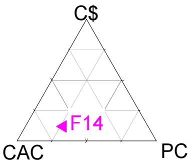

6.3.7 F14

The microstructure of the modified part of F14 is shown on figure 6-21.

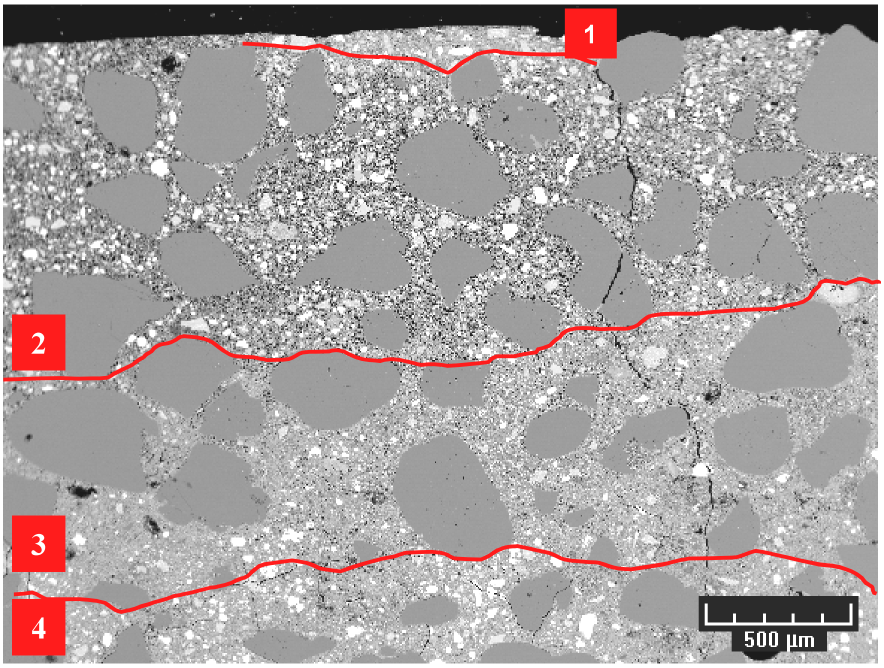

Figure 6- 21: BSE image of the modified part of F14

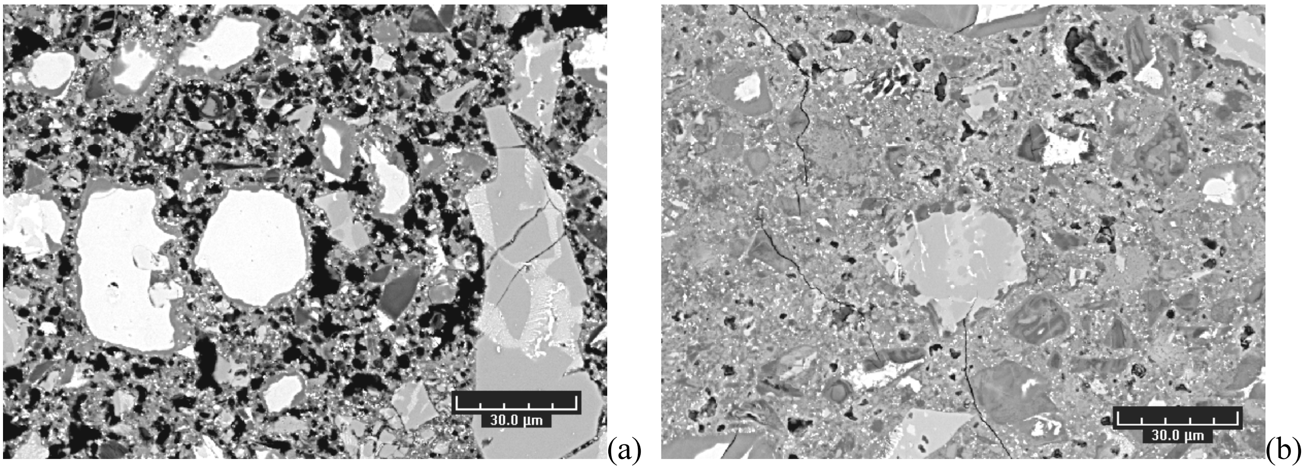

Figure 6- 22: Surface microstructure of F14. (a) Enlargement of zone 2. (b) Enlargement of zone 3

A zonation is clearly identified in figure 6-21: the external surface, zone 1, represents a calcite layer. Immediately beneath this layer there is a highly porous region about 1 mm thick, figure 6-22(a). Then, the 500 µm thick zone 3 is determined with a lower porosity, figure 6-22(b). The last zone, zone 4 corresponds to the bulk of the sample.

The total carbonated depth includes zone 1, 2 and 3. The high porosity of zone 2 is certainly due to the leaching of hydrates. EDS analysis were done in this zone and zone 3, figure 6-23.

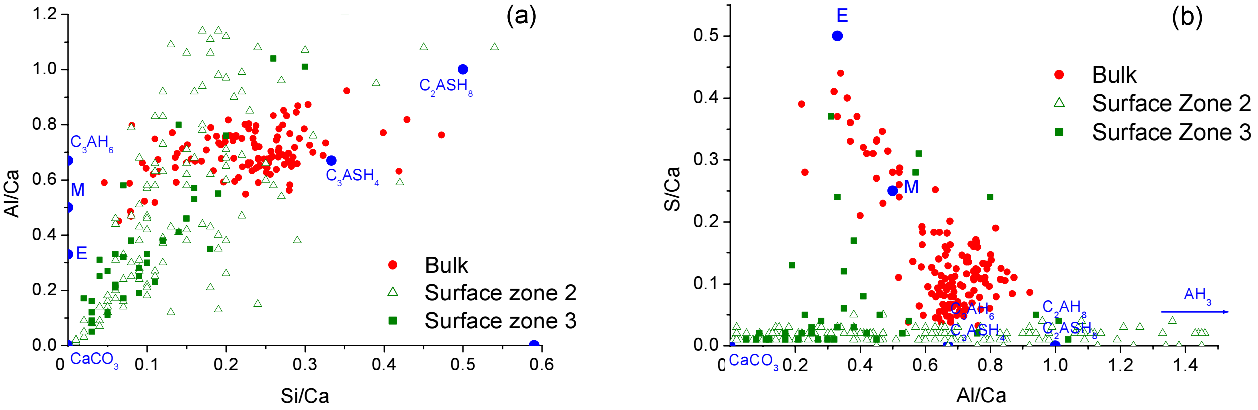

Figure 6- 23: EDS microanalysis in the modified part of F14. (a) Al/Ca vs. Si/Ca. (b) S/Ca vs. Al/Ca

EDS analysis in zone 2 can be interpreted as being $CaCO_3$ and AH_3. Sulfate is no longer present because of the leaching as we shown for F2.

For zone 3, the phases identification is more complicated; calcium carbonate and AH_3 are present and certainly intermixed with hydrogarnet. Some sulfate is still detected.

6.4 SUMMARY OF THE MICROSTRUCTURAL CHANGES UNDER NATURAL AGEING

The maximum depth at which any microstructural changes were observed was typically 1.5 mm for CAC-rich systems and less than 0.5 mm for Portland-rich binders. However, this microstructural modification had no impact on the mechanical strength; the CAC-rich systems behave as well as Portland-rich systems.

For all formulations, the SEM observations clearly demonstrated that the microstructure was affected by carbonation and leaching in different extent according to the binder. The schematic profile below illustrates the different layers.

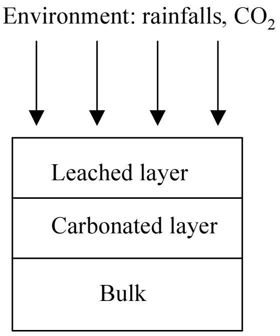

Figure 6- 24: Schematic profile of the microstructure in surface

For F19 and F16, the first substantial phase changes are a gradual depletion of calcium hydroxide which is replaced by calcium carbonate and a decalcification of the C-S-H.

For CAC-rich systems, on moving toward the surface, ettringite and monosulfate were replaced by calcite and AH_3.

6.5 CONCLUSIONS

Natural weathering samples underwent carbonation and leaching. The main leached phase is gypsum. The carbonation rate of CAC-C$ rich systems is higher and the carbonation mechanisms are similar either under accelerated test or under natural weathering. Thus, the accelerated test is relevant with the reality. Although a carbonation rate higher, the mechanical strengths of CAC-C$ rich systems remain as good as Portland-rich binders.

6.6 REFERENCES

1. Okochi, H., et al. (2000). Deterioration of concrete structures by acid deposition - an assessment of the role of rainwater on deterioration by laboratory and field exposure experiments using mortar specimens. *Atmospheric Environment* **34**, 2937-2945.
2. Moranville, M., et al. (2004). Physicochemical equilibria of cement-based materials in aggressive environments--experiment and modeling. *Cement and Concrete Research* **34**, 1569-1578.

Chapter 7. Discussion

In the preceding chapters, the experimental findings on the microstructural evolution during weathering of a wide range of binders has been presented. In this chapter, on overview of the findings is given and the strengths and weaknesses of the different systems are identified.

7.1 HYDRATION MECHANISMS

7.1.1 Nature of the hydrates

Regarding to the initial composition of the system, some trends on the hydrates nature can be drawn, figure 7-1. In the CAC-C$ rich region, we thoroughly studied the systems F2 and F6 but the hydration mechanism can be extrapolated to the whole region as the initial components are similar.

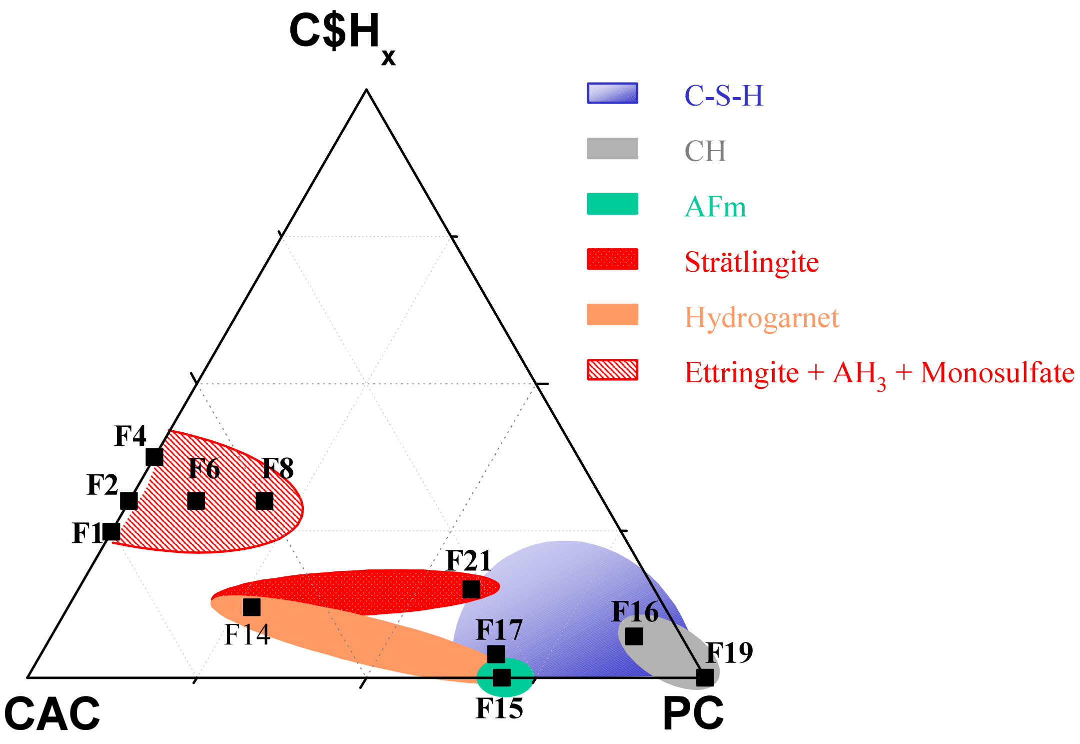

Figure 7- 1: Map of the hydrates nature

7.1.2 Hydration reactions

7.1.2.1 Theoretical water cement ratios

The amount of water required for complete hydration is different for a plain Portland and CAC-C$ systems (ettringite combines a large amount of water). The theoretical water cement ratio of the binders F19 (plain Portland) and F2 (binary system 70% CAC/30% $C\$H_{0.5}$) was calculated for a full hydration.

F19:

Here the equations considered for the calculations:

$$C_3S + 5.3H \rightarrow C_{1.7}SH_4 + 1.3CH \tag{7.1}$$

$$C_2S + 4.3H \rightarrow C_{1.7}SH_4 + 0.3CH \tag{7.2}$$

$$C_3A + 3C\overline{S}H_2 + 26H \rightarrow C_3A.3C\overline{S}.H_{32} \tag{7.3}$$

$$2C_3A + C_3A.3C\overline{S}.H_{32} + 4H \rightarrow 3C_3A.C\overline{S}.H_{12} \tag{7.4}$$

$$C_3A + 6H \rightarrow C_3AH_6 \tag{7.5}$$

F19 contains 61.7% C_3S, 12.2% C_2S, 10% C_3A, 5.6% C_4AF and 3.8 $C\$H_2$.

	Reactions by mass (g)					
Phases	Eq. (7.1)	Eq. (7.2)	Eq. (7.3)	Eq. (7.4)	Eq. (7.5)	Total
C_3S	61.7					
C_2S		12.2				
C_3A			2	4	4	
water	25.8	5.5	3.4	0.5	3.2	**38.4**

Table 7- 1: Theoretical amount of water for the different reactions in 100g of F19 (reaction of C_4AF is not taken into account)

F2:

F2 contains 50%CA and 30% $C\$H_{0.5}$.

$$3CA + 3C\overline{S}H_{0.5} + 36.5H \rightarrow C_3A.3C\overline{S}.H_{32} + 2AH_3 \tag{7.6}$$

Phases	CA	$C\$H_{0.5}$	Water
Eq. (7.6)	35	30	**46.0**

Table 7- 2: Theoretical amount of water for a total hydration of 100g F2 (CA is considered as the only reactive phase)

For a complete hydration of F19, a water/cement ratio of about 0.38 is required whereas F2 requires w/c= 0.46. With the w/c ratio used in this work, i.e. 0.35, the maximum of F19 hydration would be 92% and 73% of CA could be hydrated in F2. This explains why lots of anhydrous remained throughout the matrix.

As measured in Chapter 3, after 3 years, the degree of hydration of F19 was 82.3%; the maximum hydration degree is achieved in the very long term because the hydration becomes rapidly diffusion-controlled.

7.1.2.2 Volume balance

Knowing the molar volumes of all relevant cement phases and the expected hydration reaction, volume balance can be calculated. It illustrates the apparent paradox of the hydration: with hydration the solid volume increases whereas the total volume decreases. It is interesting to compare the volume balance of F19 and F2 as the hydration is totally different. The calculation is done with the stoichiometic amount of water, figure 7-2, and then with the used w/c in this work, i.e. 0.35, figure 7-3.

These volume balance calculations are subjected to assumptions:

① A Ca/Si ratio of 1.7 is taken for C-S-H

② AH_3 is considered as the crystalline form, i.e. gibbsite (density=2.4g.cm^{-3}) whereas AH_3 has been found to be poorly crystalline in these systems; the volume occupied by AH_3 is thus underestimated

③ The description is linear with the hydration degree and does not take into account the stoichiometric variations of the reaction

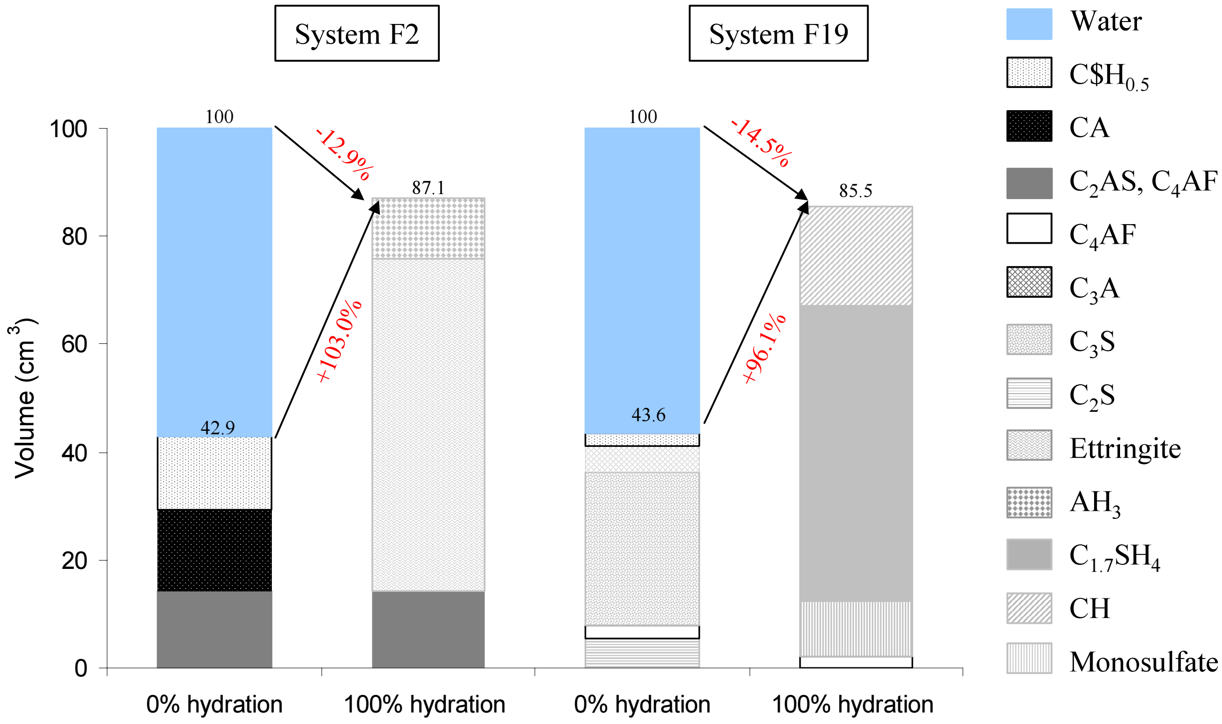

Figure 7- 2: Volume balance for the binders F2 and F19. "100% hydration" corresponds to w/c=0.46 for F2 and 0.38 for F19

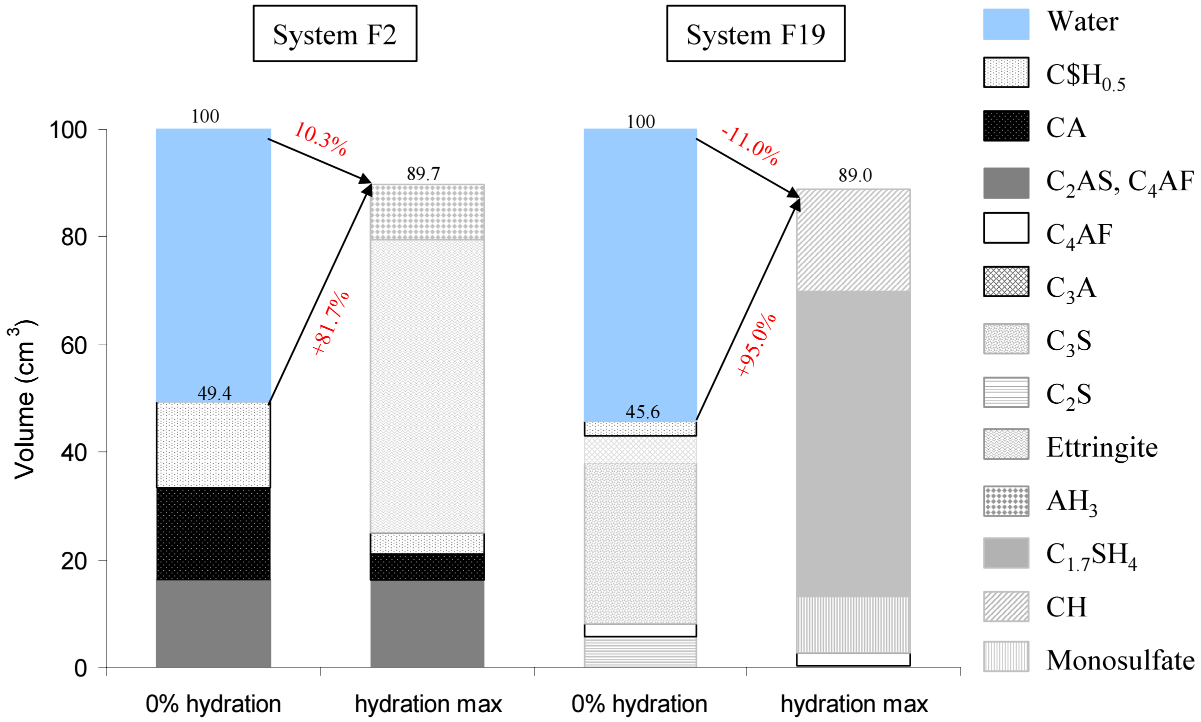

Figure 7- 3: Volume balance for the binders F2 and F19. "Hydration max" corresponds to the maximum of hydration with w/c=0.35

For full hydration of F2 and F19 systems, the reaction products occupy a volume around 13% and 14.5% smaller than the reactant; this effect is termed “chemical shrinkage” or Le Chatelier effect. As mentioned before, the calculated chemical shrinkage of F2 should be overestimated because of the formation of AH_3 gel instead of gibbsite. For a w/c ratio of 0.35, the chemical shrinkage is the same for both systems.

However, it is worth pointing out that the total volume decrease is not representative of the variation of the external apparent volume. CAC-C$ systems are known to provide shrinkage compensating properties but instead of volumetric increase, reduction in volume should occur on the basis of stoichiometric equations (F2, figures 7-2 and 7-3). Special conditions must exist to bring about an expansion of the system. The numerous theories and models that aim at explaining the mechanism of formation of ettringite and expansion due to ettringite can be divided into two schools of thought; observations supporting and contradicting the two schools are reviewed by Cohen [1].

- The swelling theory [2]: expansion is caused by the swelling of the ettringite particles that are of colloidal size. It is proposed that colloidal ettringite is able to attract a large number of water molecules which cause interparticle repulsion, thus causing an overall expansion of the system.

- The crystal growth theory: expansion is caused by the growth of ettringite crystals formed on the surface of the expansive particles or in the solution. The growth of these crystals is responsible for the crystallisation pressure and hence expansive force. Scherer [3-5] reviewed the thermodynamics of crystallisation within porous materials. Deng [6] also discussed the expansion mechanism associated to ettringite formation from a physico-chemical point of view.

In F2, initially ettringite crystals grow randomly in the bulk and as the hydration proceeds, growth becomes confined which gives rise to pressures exerting both on the ettringite crystals and the surroundings. Consequently little expansion is expected. Expansion is closely related to the distribution of ettringite crystals in cement paste.

7.1.3 Portland based systems

The microstructural investigations of plain Portland mortar confirm the characteristic features of Portland hydration, i.e. precipitation of ettringite which further reacts with anhydrous aluminate to form monosulfate, formation of calcium hydroxide and calcium silicate hydrates C-S-H.

Relatively low additions of calcium aluminate cement and calcium sulfate to Portland mortar lead to slight modifications of the microstructural development. Extra ettringite is produced and the lime consumed to form ettringite, i.e. the portlandite content is reduced. The other change is the retardation of silicates hydration. When CAC and C$ are added, hydration of calcium silicates is temporarily “blocked”. The cause is still discussed.

When more CAC and C$ are added, the hydration mechanism becomes more complicated. Precipitation of ettringite and monosulfate occur in substantial quantities and silicates ions are found in strätlingite and in outer C-S-H. The binary system Portland, aluminous cement has also a complex hydration pattern with the formation of C-S-H, hydrogarnets and AFm phases (carbonated AFm).

7.1.4 CAC-C$ based systems

We have determined that in CAC-C$ rich binders, ettringite and AH_3 precipitate. The most important hydration reaction is shown below:

$$(3-y)CA + 3C\overline{S}H_x + yC \xrightarrow{H_2O} C_3A.3C\overline{S}.H_{32} + (2-y)AH_3 \tag{7.7}$$

As the amount of lime in the system increases, more ettringite is formed and less AH_3; ettringite yield per CA is improved but there are some limits which are discussed later.

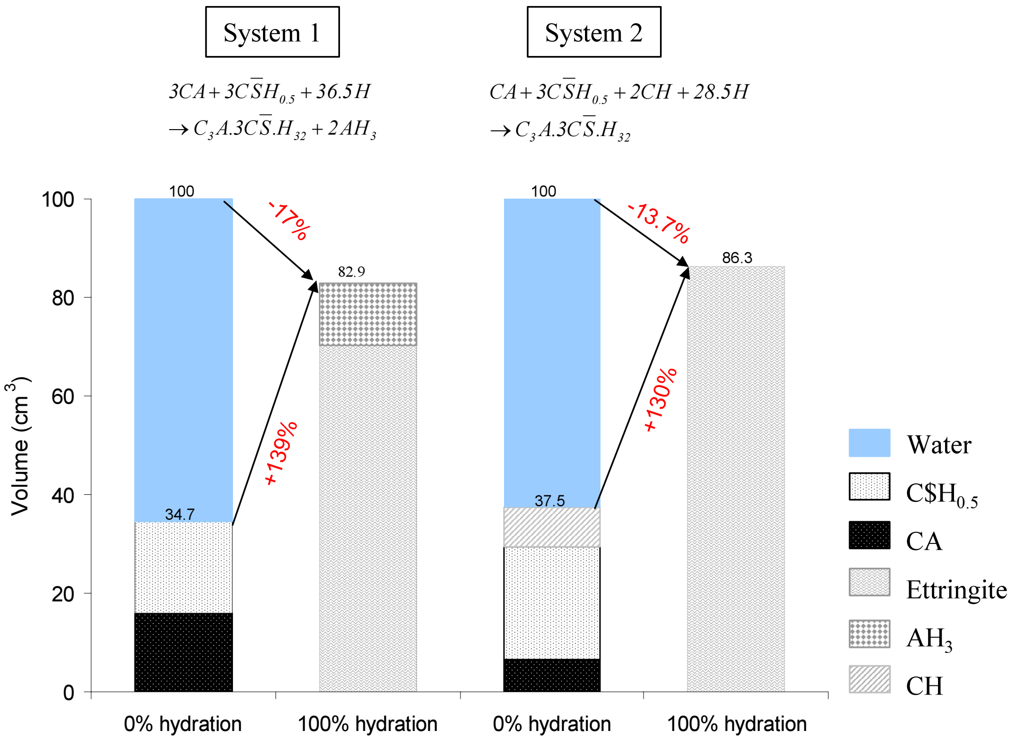

Figure 7- 4: Volume balance of the simple systems with the stoichiometric amount of water (0.72 and 0.69 for system 1 and 2 respectively)

By adding extra calcium in the binary system $\text{CAC+C\$H}_{0.5}$, the chemical shrinkage is lowered.

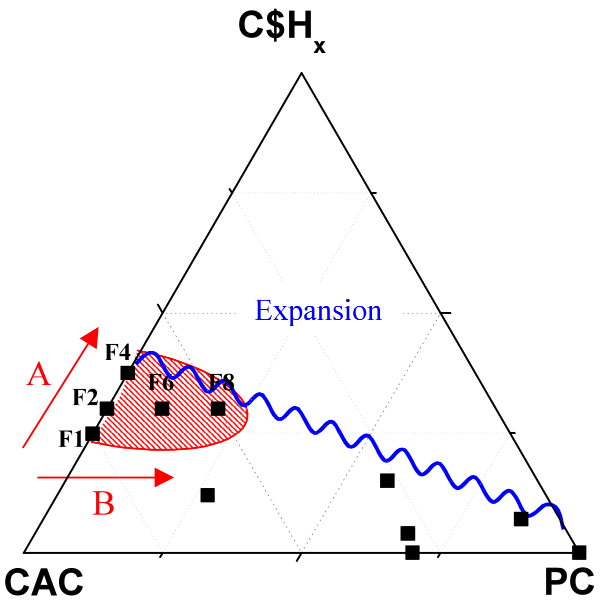

Figure 7- 5: Some trends for the CAC-C$ rich systems

Earlier internal studies at Lafarge Aluminates indicate that formulations rich in calcium sulfate are prone to uncontrolled expansion. This zone is roughly delimitated by the blue line; around this line, the behaviour is not well defined.

Changes in the A direction, figure 7-5: A moderate increase of the sulfate content will lead to a better shrinkage compensation due to more formation of ettringite but too much addition of calcium sulfate will lead to an excessive expansion. The binary systems F1 and F4 illustrate this effect; sulfate are in hyperstoichiometry in F4 resulting in instable swelling (figure 7-6)

Changes in the B direction, figure 7-5: addition of Portland in binary binders CAC/C$ will lead to favour the formation of ettringite at the expense of AH_3.
A moderate increase of the PC/CAC ratio will lead to higher strengths; F2, F6 and F8 illustrate this situation, figure 7-7.

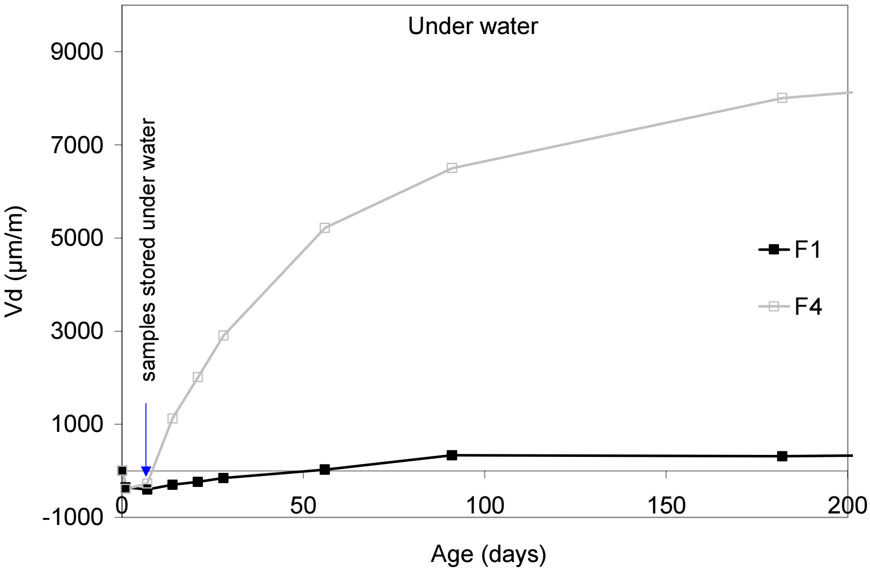

Figure 7- 6: Dimensional variations of F1 and F4 under water storage

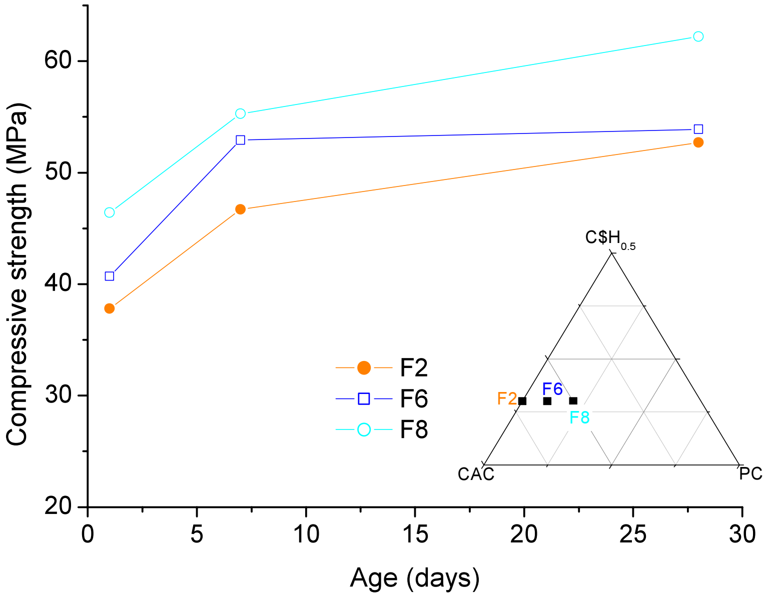

Figure 7- 7: Compressive strength evolution for the CAC-C$ rich systems w/c=0.35 (curing 28 days 75%RH)

CAC-C$ based formulations present a high capacity to combine water in the hydrates and so to rapidly reduce the internal relative humidity. This phenomenon was confirmed by the weight gain of the samples stored at 76%RH for the desorption measurements. The internal RH should be lower than 76%RH and as the external RH was higher than the internal RH, water vapour movement occurred inward the sample leading to reabsorption.

7.2 OVERVIEW OF THE RESULTS FROM ACCELERATED TESTS

The following table summarizes the performance of each binder in the different accelerated tests.

Binders	Hydrates	Storage influence	Carbonation	Acid attack	Sulfate attack
F19	C-S-H, CH Monosulfate	+	+ + +	– –	–
F16	C-S-H, CH (-) Monosulfate Ettringite	Drying shrinkage compensated by the high initial expansion	+ +	– –	–
F21	Ettringite Monosulfate Strätlingite	+ under water?	+ +	–	+ +
F17		Drying shrinkage	+ +	–	+ +
F15	C-S-H Hydrogarnets AFm			–	
F14	Ettringite (-) Hydrogarnets Strätlingite	+		+	+ + +
F12		+	–	+	+ + +
F8		+	–	+	– –
F6	Ettringite AH_3 (-) Monosulfate	+		+	
F4		Swelling under water storage		+	– –
F2	Ettringite AH_3 Monosulfate	+		+ + +	
F1		+	–	+ +	–

Table 7- 3: Performance of the different binders

7.3 ROLE OF THE HYDRATES IN DURABILITY

7.3.1 Role of portlandite in different environments

As already reported in Chapter 5, portlandite plays a key role in carbonation process; the higher the calcium hydroxide content, the lower the carbonation rate. CH acts as a buffer and its presence in F16 and F19 explains their good behaviour with respect to carbonation.

Portlandite content should also plays a role in sulfate attack. Precipitation of gypsum and ettringite requires calcium ions and the first source of Ca^{2+} is portlandite. Once this source is locally depleted, C-S-H becomes the preferred source of Ca^{2+} and this decalcification tends to soften the matrix, leading to loss of strength and disintegration. The absence of portlandite in F21 and F17 could be one of the causes of their good performance in sulfate environment. It has also been proposed by Mehta that the presence of portlandite is essential to the expansive formation of ettringite [2].

Hydroxide calcium dissolves at $pH<12.5$ so is soluble in water and may be removed by leaching creating a new porosity in the matrix. Portlandite is also no longer stable in acidic media.

7.3.2 Ettringite behaviour

7.3.2.1 Dimensional stability of ettringite containing systems

An issue related to ettringite is that of dimensional stability. Ettringite formation is related to the process of shrinkage compensation in type K cements and also to undesirable expansion during external sulfate attack and so called internal sulfate attack or delayed ettringite formation which may occur after exposure to temperatures>70°C during curing. There is no simple relationship between amount of ettringite and expansion [7]; the absence of such correlation indicates that ettringite can form without expansion. Extensive studies have shown that the crystallisation of ettringite only leads to expansive forces if its forms in small pores (50 nm) [8].

In this work, we have investigated the dimensional stability of ettringite containing systems in three environments:

- Wet conditions (under water)
- Dry conditions (20°C, 50% RH)
- Wetting and drying conditions (1 week 20°C / 90% RH, 1 week 50°C)

Only F4 presented excessive swelling and F21 is also suspected to expand under water. Otherwise, systems that were correctly formulated, i.e. systems with no excess of sulfates, were found to be dimensional stable over time as Portland-rich binders, whatever the severity of the environment.

Indeed, BSE images indicated that there remained considerable quantities of CA and $C\$H_{0.5}$ and an external source of water could lead to ettringite precipitation. It was experimentally seen that, during the water storage no significant expansion occurs. This potentially newly formed ettringite was not expansive or the ingress of water was limited; as we observed in Chapter 4, the transport properties of CAC-C$ rich systems are good.

7.3.2.2 Stability of ettringite containing systems

We confirmed in chapter 5 that the carbonation of ettringite leads to calcite, aluminium hydroxide and gypsum:

$$C_3A.3C\overline{S}.H_{32} + 3CO_2 \rightarrow 3CaCO_3 + 3C\overline{S}H_2 + AH_3 + 23H_2O \tag{7.8}$$

This reaction leads to the release of water, which leads to further hydration and maintains a high relative humidity inside the solid, which impedes the ingress of CO_2 gas in a certain extent. As confirmed by Chapter 4, the degree of water pore filling affects greatly the gas diffusion: the higher the degree of saturation, the lower the gas diffusion. Nevertheless, the loss of water corresponds to a decrease in the solid volume thus an increase in porosity. Therefore some loss of strength is expected in carbonated samples but we found that for a fully carbonated specimen, the compressive strength remains high (for instance about 70 MPa for F1). The theoretical loss of solid volume may be compensated by the continuing increase of products volume due to further hydration with the released water Eq. (7.2). The formation of AH_3 may also play a role, see the following section.

The kinetic of the carbonation is controlled by the ingress of CO_2 into the porous network and by the nature of the hydration products. For instance, neat Portland F19 and CAC-C$ rich system F6 present similar transport properties but different carbonation rate.

7.3.3 AH_3 role in durability

AH_3 has been identified to be a poorly crystalline phase (almost no gibbsite was detected by XRD) and its massive nature should confer to it cohesion qualities. The specific volume of AH amorphous gel-like phase is higher than that of well crystalline phase, thus the formation of this instead of gibbsite will result in a lower porosity. Recently, Kaiser's work [9] on aluminium hydroxide in crystalline (gibbsite) and amorphous forms tends to support the cohesion role of alumina gel in the cementitious matrix; values of BET specific surface area were given and amorphous AH_3 has an extremely high specific area.

$$S_{gibbsite} = 20m^2/g$$
$$S_{amorphousAH_3} = 285m^2/g$$

Analogies may be drawn with C-S-H which has a surface area quite variable with a conservative value being 200 m^2/g. It is known that C-S-H is the "glue" in the matrix, consequently the cohesion effect of AH_3 gel is relevant.

These properties could explain the good mechanical behaviour of fully carbonated specimen. The high residual strength, figure 7-8 was not expected since carbonation of ettringite would give a solid decrease of about 40%. It seems likely that this could be overcome by further hydration even when assisted by water released by the carbonation reaction. The nature of the observed microstructure containing amorphous alumina gel may be of importance. The AH_3 gel matrix reinforces the packing of hydrates, namely calcite and gypsum. With TEM observations of carbonated CACs specimen, Henry [10] highlighted a very intimate mixture of calcite embedded in a fine-textured alumina gel. Kula's study [11] tends to support the assumption that amorphous alumina gel is an effective cohesive agent but the author suggested that crystallisation of amorphous AH_3 to gibbsite could be a factor in loss of strength. The conversion of amorphous $Al(OH)_3$ to gibbsite required treatment such as 2 hours at 40°C [9] which is not much, but the crystallisation of AH_3 gel will be very likely hindered by absorbed foreign ions (Ca^{2+},SO_4^{2-}, etc…)

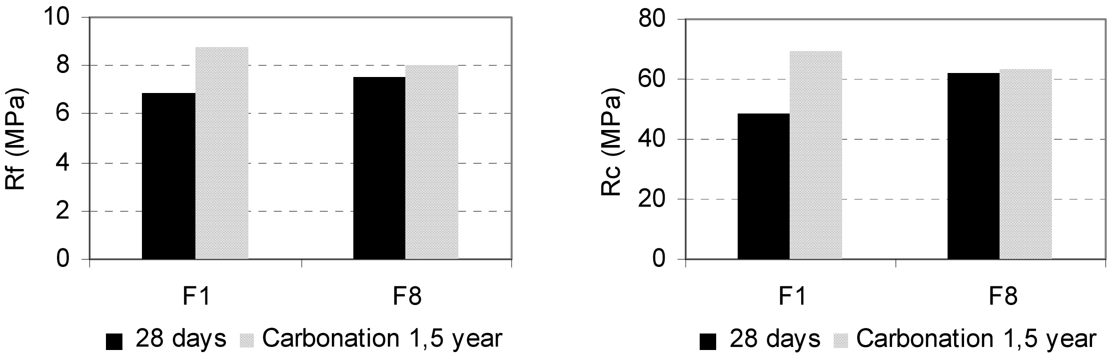

Figure 7- 8: Flexural and compressive strength after curing (28 days) and after 1.5 years in 0.3% CO_2 environment (F1 100% carbonated and F8 80% carbonated).

Otherwise, we have seen that in acidic media, CAC-C$ rich systems better resist than Portland-based binders and this good performance is attributed to AH_3; because of its insolubility at pH>3.5, it seems to act as a protective barrier, greatly slowing down the reaction. As mentioned in section 7.1.4, F2 contains more AH_3 than F6 which in its turn contains more than F8; this explains the best performance of F2, figure 7-9. Higher the AH_3 content, better the protection.

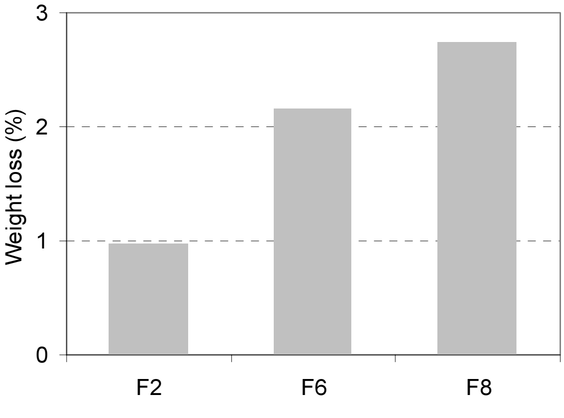

Figure 7- 9: Weight loss during the acid attack

7.3.4 Role of slag

CAC is recognized to perform better than Portland in sulfate-rich environments. Many authors have ascribed the good performance of CAC to the absence of calcium hydroxide but this is too simplistic. Undoubtedly, the calcium aluminate hydrates can react to form ettringite and cracking may result from this reaction. As we have studied in Chapter 5, according to the initial CAC/C$ ratio, systems are more or less resistant.

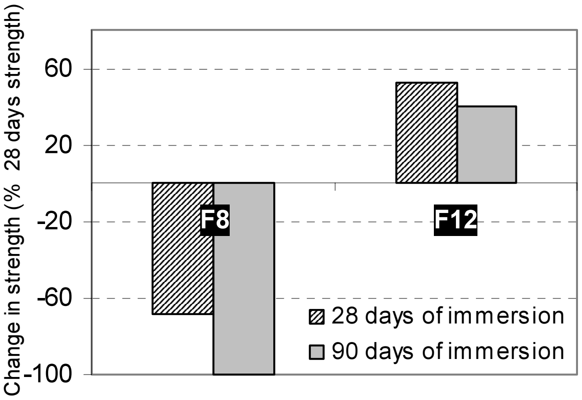

Figure 7- 10: Results of accelerated sulfate test of F8 and F12

Furthermore, on figure 7-10, the benefits of slag in sulfate attack is clear and particularly direct comparison of F8 and F12 which is “F8+slag”. The explanation is probably, at least partially, a reduction of permeability [12] which significantly inhibits the ingress of sulfate and thus the rate of attack is slowed down.

7.4 NATURAL WEATHERING

7.4.1 Mechanical behaviour

As already reported in Chapter 2, the compressive strengths increased between 28 days and 1 year due to further hydration; afterwards, they remain almost constant up to 3 years. The stress due to weathering (moisture, heat) causes concrete to deteriorate over time. During drying, the “dry” concrete at the surface contracts more that the “moist” concrete inside and as a result tensile stress occurs at the outer surface and compressive stress inside. When dry concrete is soaked again, compressive strength appears at the surface and tensile inside. Freezing/thawing cycles could worsen the situation.

Even if the delay of silicates' hydration is reduced over time, compressive strengths of Portland –rich systems F16 and F15 always remain lower than those of plain Portland F19. However, despite a remaining delay of silicates' hydration after 3 years, the Portland-rich system F21 has similar compressive strengths than pure Portland.

7.4.2 Evolution of the microstructure near the exposed surface

The long-term performance is often determined by the rate of ingress of deleterious species (acids, carbon dioxide gas, sulfate…) and as we demonstrated, for an equivalent w/c ratio, Portland and CAC-C$ rich binders present similar transport properties and porosity in the same range, thus the long-term behaviour will be governed by the interactions of the aggressive species and the cementitious matrix. Another parameter has to be taken into account: the degree of filling the pores which affects the transport properties. The more the pores are filled with water, the lower the transport properties. Thus, one well understands the impact of the environment.

7.4.2.1 Aspect of the exposed surface

As observed in section 6.2.1.1, the exposed surfaces have undergone more or less erosion according to the climate and especially the frequency of the rainfalls. Rainfalls wash away cementitious material and sand grains leading to pores opening.

Cracking was also seen visually on certain samples but the impact was not analysed in detail.

We also noticed the importance of w/c ratio by comparing of F5 and F6, figure 6-3. In Chapter 4, we found that the porosity and the transport properties of F5 are very low, this explains the good behaviour of F5. The ingress of various species such as water or CO_2 is limited.

7.4.2.2 Degradation mechanisms

After 3 years under Norwegian climate, all the specimens were affecting by the carbonation and the leaching. The kinetic of carbonation of CAC-C$ blends was higher and gypsum was leached by the rainfalls in the extreme surface creating new pores.

However, one could imagine that competition between different reactions will occur: as the leaching proceeds, the porosity increases, the available path for ingress of deleterious species is higher but the presence of water in the pores will limit the diffusion of CO_2 for example. Moreover, since there remain anhydrous grains in the matrix, the external source of water (rain) could lead to further hydration and thus compensate increase of porosity.

7.5 CONCLUSIONS

The main trends on the performance of the different systems are drawn on the diagram below:

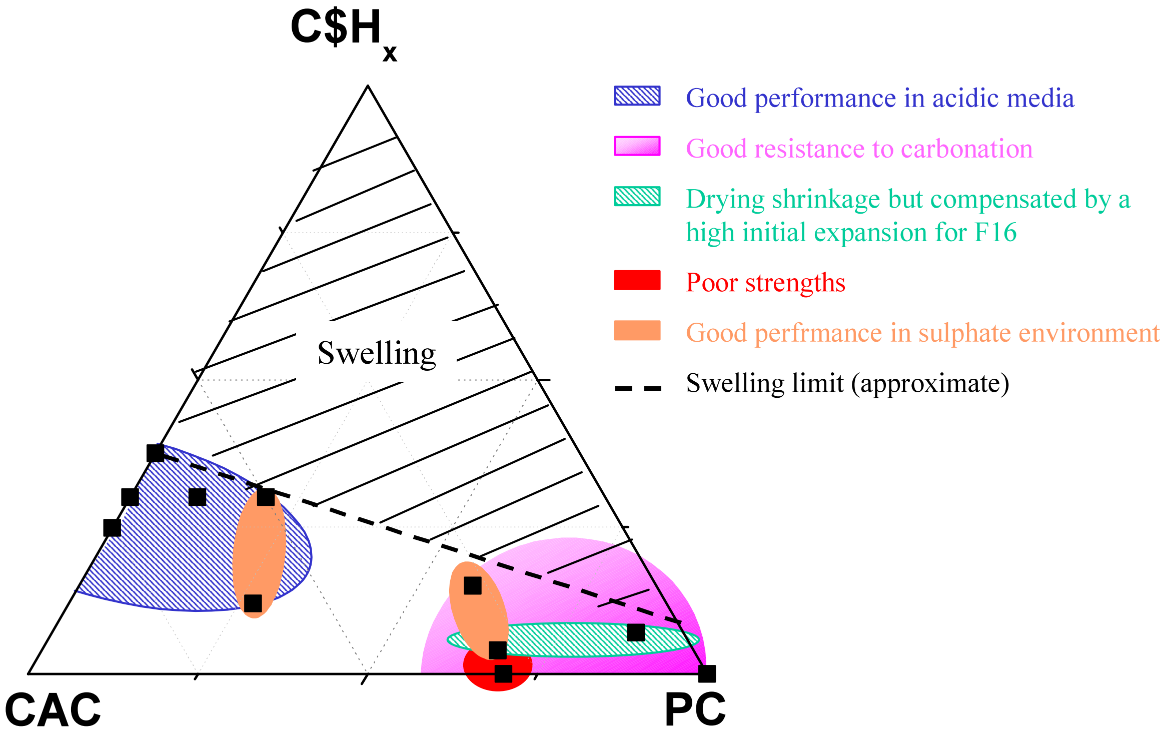

Figure 7- 11: Summary of the performance of the binders

The choice of the ternary binders will be governed by the applications and the service life.

7.6 REFERENCES

1. Cohen, M.D. (1983). Theories of expansion in sulfoaluminate - type expansive cements: Schools of thought. *Cement and Concrete Research* **13**, 809-818.
2. Mehta, P.K. (1973). Mechanism of expansion associated with ettringite formation. *Cement and Concrete Research* **3**, 1-6.
3. Scheler, G.W. (2002). Factors affecting crystallisation pressure. In *Internal Sulafte Attack and Delayed Ettringite Formation* (K.L. Scrivener and J. Skalny, eds.), RILEM: Villars.
4. Scherer, G.W. (1999). Crystallization in pores. *Cement and Concrete Research* **29**, 1347-1358.
5. Scherer, G.W. (2004). Stress from crystallization of salt. *Cement and Concrete Research* **34**, 1613-1624.
6. Deng, M., and Tang, M. (1994). Formation and Expansion of Ettringite Crystals. *Cement and Concrete Research* **24**, 119-126.
7. Famy, C. (1999). Expansion of heat-cured mortars. PhD thesis, Imperial College, London.
8. Taylor, H.F.W., et al. (2001). Delayed ettringite formation. *Cement and Concrete Research* **31**, 683-693.
9. Kaiser, K., and Guggenberger, G. (2003). Mineral surfaces and soil organic matter. *European Journal of Soil Science* **24**, 219-236.
10. Henry, B.M., et al. (1997). The microstructure and strength of carbonated aluminous cements. *Journal of Materials Science* **32**, 6249-6253.
11. Kula, T.M., et al. (1980). Curing temperature and humidity effects on the strength of an aluminous cement. *Cement and Concrete Research* **10**, 491-497.
12. Brown, P., et al. (2004). Microstructural changes in concretes with sulfate exposure. *Cement and Concrete Composites* **26**, 993-999.

Chapter 8. Conclusions and future work

The aims of this thesis were:

- Clarify the hydration pattern of ternary mortars in the long-term
- Identify strengths and weaknesses of the different formulations, as well as important parameters affecting performance

The approach was to understand the hydration mechanisms of different binders regarding the microstructure, porosity and transport properties and to understand how ternary binders evolve in accelerated, laboratory and natural environments.

The microstructural investigations of the cementitious matrix led to several conclusions:

- The Portland-based systems behave very differently from plain Portland and hydration mechanisms depends on the PC/CAC and CAC/C$ ratios. Two of the characteristic feature of these binders are the formation of supplementary ettringite and the delay of the silicates' hydration. However, further studies are necessary to fully understand the origin of these delay of silicates hydration.

- The CAC-C$ rich binders also behave differently from pure calcium aluminate cement and the hydration mechanism is well identified with the formation of ettringite and AH_3.

- The physical aspects of the microstructure were also examined; it was found that at similar porosity, Portland and CAC-C$ rich binder have similar transport properties which evolve in the same way for both systems in regard the pore structure and the environment.

The second part of the work dealing with accelerated and natural ageing allowed to identify some trends of the regions on the PC/CAC/C$ diagram which provide superior resistance to different exposure conditions to be identified:

- It is known that there is a region in which uncontrolled expansion can occur and F4 and F21 seems to belong to this area. All other investigated binders were dimensionally stable under water, in dry conditions and wet-dry cycles.

- Portland-rich systems perform better than CAC-C$ rich ones with regard to carbonation and among Portland-rich systems, those containing Portlandite perform the best.

- CAC-C$ rich blends show the maximum resistance to acid media; this good performance is due to the presence of AH_3 which is believed to act as a diffusion barrier.

- In sulfate bearing environment, the benefits of slag addition in CAC-C$ systems is clear and within the Portland-based binders, those containing no Portlandite perform better.

- Natural weathering samples underwent leaching and carbonation. Similar to the accelerated carbonation, after 3 years, the carbonation of CAC-C$ rich systems is higher than Portland rich binders; the carbonation mechanisms established for the accelerated test are also valid for the natural carbonation, which reveals the relevance of the test. Mechanical strengths remain the same from 1 to 3 years.

All the data collected in this work has been gathered to build a durability “map” for ternary binders (figure 7-11) which has to be completed. In order to optimise the “construction” of this map, a holistic study of CAC/PC/C$ systems has to be done to delimitate some regions:

- As the presence portlandite increases the resistance against carbonation but is also found to be unfavourable for sulfate resistance, the area around pure Portland where CH is formed should be interesting for further studies.

- In the same manner, region where AH_3 is formed is important for acid corrosion.

- The region which is prone to uncontrolled expansion is only known approximately, thus a better definition of the swelling limit should be helpful for the choice of adequate formulation regarding its service life.
- In this work only few forms of degradations were investigated, thus the study can be enlarged to other accelerated tests such as chloride diffusion.

- By a simple decrease of the w/c ratio, we observed an improvement of the resistance to the erosion (figure 6-4). The w/c ratio plays an important in durability because it governs lots of properties, thus it should be interesting to study its influence.

- The various forms of attack can be considered separately but one form of attack renders the concrete more susceptible to damage by another form, so the continuation of the examination of weathering specimens is necessary. The next batch of samples to be studied is due in 2005 (Norwegian and Japanese sites) and 2006 (German and Florida sites). Those samples will be 5 years old, which should be long enough to show differences in the effects of their respective climates. Thus, another parameter (climates) could be added in the durability "map".

Durability is a complex problem because it is the crossroad between chemistry and physics and it exists different scales in cementitious materials. The weathering resistance of materials is not solely related to its mechanical strength. A concrete does not necessarily resist to attack in any environment in which it is placed simply because it has ample strength to fulfil the purpose for which it was designed.

Appendix A. Scanning Electron Microscopy

A.1 BACKSCATTERED ELECTRON

BSE are the incident electrons having undergone a series of elastic atomic collision. The intensity of BSE signal are strongly controlled by the atomic number of the material irradiated. For low atomic number materials, little scattering takes place near the surface and most of the incident are absorbed within the specimen. Materials with a higher atomic number generate more scattering from the surface and consequently a greater proportion of backscattered electrons are produced. The amount of BSE is indicated by the backscattering coefficient η, calculated from the atomic number following the empirical equation [1]:

$$\eta = -0.0254 + 0.016Z - 1.86 * 10^{-4} Z^2 + 8.3 * 10^{-7} Z^3 \tag{A.1}$$

The backscatter coefficient η follows the rule of mixtures based on mass fractions:

$$\eta_{mixture} = \Sigma \eta_i C_i \tag{A.2}$$

where i denotes each constituent, η_i the pure element backscatter coefficient and C_i the mass fraction.

Table A-1 shows the backscatter coefficients for some cementitious components.

Phases	**Z**	η
C_4AF	16.65	0.186
C_3S	15.06	0.171
C_2S	14.56	0.166
C_3A	14.34	0.164
CH	14.30	0.162
CSH ($C_{1.7}SH$)	12.49	0.151
Hydrogarnet	12.27	0.1401
Monosulfate	11.66	0.1328
Sand SiO_2		0.125
Ettringite	10.76	0.123

Table A- 1: BSE coefficients for some cement phases

A.2 ENERGY DISPERSIVE SPECTROSCOPY (EDS)

Interaction of the electron beam with atoms in the sample causes shell transitions which results in the emission of x-rays. EDS is based on the detection of these characteristic x-rays which has an energy characteristic of the parent element.

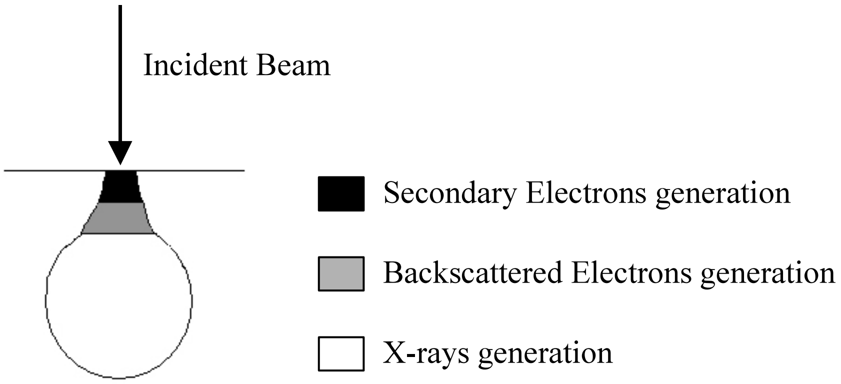

Figure A- 1: Interaction volume

The EDS system has computer software allowing matrix corrections to be made automatically by the ZAF procedure. The microanalysis were standardised by comparison with suitable pure phases. Oxygen was calculated by stoichiometry on the basis of the other elements present.
It is worth pointing out that the volume analysed is larger than the size of many phases, thus chemical analysis may refer to mixtures of phases.

A.3 POLISHED SECTIONS

Polished sections can be prepared to give a representative cross-section of the microstructure. The flat surface required for analysis is obtained through several steps.
The hydration is stopped using isopropanol replacement followed by vacuum drying. The dried slices were then vacuum impregnated with ultra low viscosity epoxy resin (Epotek 301®), lapped to a flat surface with 9 μm diamond paste and polished successively with 3, 1 and ¼ diamond pastes. More details for polished sections preparation may be found in [2-4].
To prevent charging up to the specimen, that results in poor image quality, the polished surface is coated with a thin layer (few microns) of carbon.

A.4 DEGREE OF CEMENT HYDRATION BY BSE IMAGE ANALYSIS

A.4.1 Image analysis

Quantitative analysis by imaging is based on the principles of stereology which deals with the interpretation of three-dimensional structures by means of their two-dimensional sections. In other words, the volume percentage in 3D is equal to the area percentage in a 2D surface.

The image analysis is carried out from the procedure developed in our lab by Dr. E. Gallucci, based on the grey level histogram (256 grey levels from black to white, figure A-2). The challenge in this approach was to correctly discriminate sand, anhydrous and cementitious matrix (outer products + Portlandite) and to measure their area fractions.

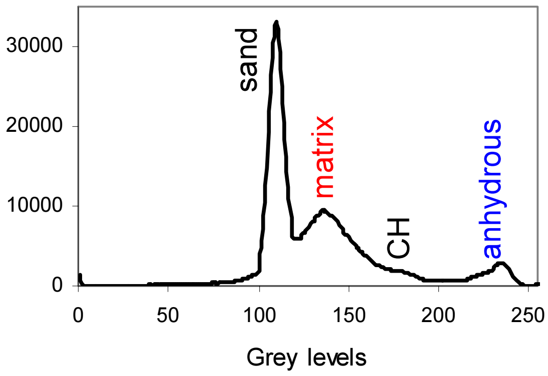

Figure A- 2: Segmentation histogram

Mouret [5] has carried out a study to assess how magnification affects the estimation of the area fraction. ×200 gives enough accurate measurement and in the same time enables to reduce the number of field to be analysed in a given area.

Figure A-3 illustrates the recorded and binary images obtained with the segmentation program.


(a) (b) (c)

Figure A- 3: Segmentation of BSE image. (a) original image, (b) sand segmentation, (c) anhydrous grains segmentation

A.4.2 Hydration degree

By definition, the degree of hydration α is the ratio between the amount of cement that has hydrated at a given time and the original amount of cement $V^0_{anhydrous}$. Using backscattered electron imaging quantification, the fraction area of residual unhydrated cement at a given time can be obtained directly, $V^t_{anhydrous}$ and α is deduced by the formula:

$$\alpha(\%) = \left(\frac{V^0_{anhydrous} - V^t_{anhydrous}}{V^0_{anhydrous}}\right) * 100 \tag{A.3}$$

$V^0_{anhydrous}$ can be obtained as follows: the volume of the paste is the sum of volumes of water, cement and air. The percentage of air present in a paste is usually small and may be ignored in calculations. So the initial volumetric fraction of cement is given by the equation below:

$$V^0_{anhydrous} = \frac{C/\rho_c}{C/\rho_c + W/\rho_w} \tag{A.4}$$

where W is the weight of water, C the weight of cement, ρ_w and ρ_c the density of water and cement respectively.

A.5 REFERENCES

1. Famy, C. (1999). Expansion of heat-cured mortars. PhD thesis, Imperial College, London.
2. Detwiler, R., Powers, LJ. (2001). Preparing specimens for microscopy. *Concrete international* **Nov**, 51-58.
3. Kjellsen, K.O., et al. (2003). Preparation of flat-polished specimens for SEM-backscattered electron imaging and X-ray microanalysis--importance of epoxy impregnation. *Cement and Concrete Research* **33**, 611-616.
4. Stutzman, P.E., and Clifton, J.R. (1999). Specimen preparation for SEM. In *21st Conference on Cement Microscopy*: Las Vegas.
5. Mouret, M., et al. (2001). Image analysis: a tool for the characterisation of hydration of cement in concrete - metrological aspects of magnification on measurement. *Cement and Concrete Composites* **23**, 201-206.

Appendix B. Freezing- Thawing

There are two basic frost durability problems: internal cracking due to freezing and thawing cycles and surface scaling generally due to freezing in presence of de-icer salts. Several theories have been proposed to explain the deterioration of concrete by frost and the most common are referred to as hydraulic pressure, osmotic pressure and ice accretion /capillary effect. However nowadays, the real mechanism is not fully understood.

B.1 TEST PROCEDURES

Two types of resistance to freezing and thawing testing are used at the Lafarge BRAAS laboratory at Horsham, England under the direction of Dr. Steve Sclosa. These tests are the Heat/Freeze/Thaw Test and the “Sekisui” Test (Japanese origin). They can be criticised but are rapid and good experience of correlation with field performance exists. The mortar samples tested in this manner were 5×10×2cm in size and were cured under two different regimes – 28 days at 20°C, 65% RH (cure a) and 28 days at 20°C, 100% RH (cure b). During the freeze/thaw cycles, the samples are laid flat on a plastic tray, half-immersed in water.

B.1.1 Heat/Freeze/Thaw test (HFT)

The samples are exposed repetitively to the following composite cycle until failure or until the testing is stopped after 3 to 4 months:

- 2 days oven heating at 70°C, cooling to room temperature
- 10 cycles of freezing/thawing from –20°C to +20°C (freezing 12 hours and thawing 12 hours).

B.1.2 Sekisui test

The conditions in the environmental chamber are set as follows:

- 5 hours freezing to –20°C
- 3 hours thawing in air at +30°C

In both freeze-thaw tests, the results are based on a direct visual inspection of the samples; the number of cycles to failure, or total cycles of exposure if the samples did not fail, is recorded. Also, if the samples do fail, the different types of damage/mode of failure is noted (swelling/cracking, surface spalling, complete disintegration, etc.).

B.2 RESULTS

Results from HFT and Sekisui frost tests are summarised in graphs below.

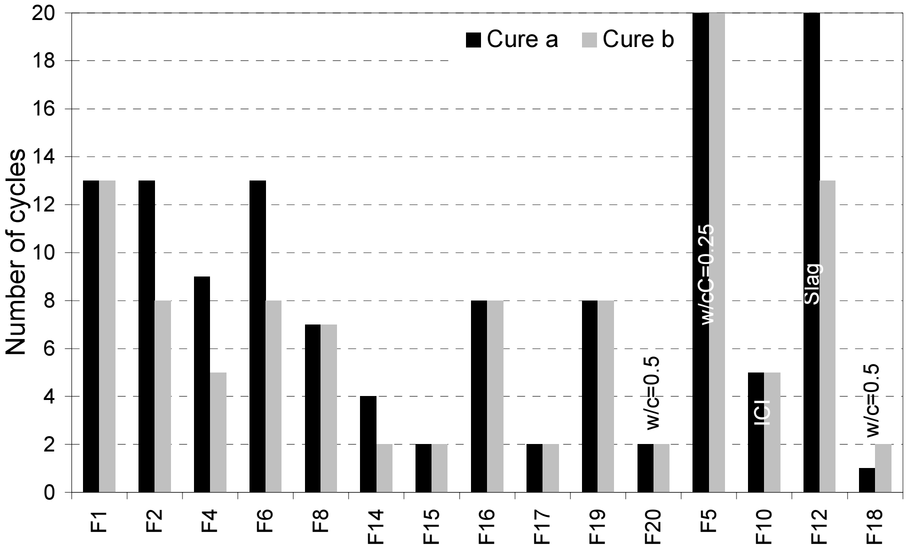

Figure B- 1: Heat/ Freeze/ Thaw results. If not specified, w/c=0.35. Cure a= 28 days, 20°C, 65%RH; cure b=28 days, 20°C, 100%RH

The poor performers were 14, 15, 17, 18 and 20 (all failing in less than 5 cycles). The best binders were F1, 2a, 5, 6a and 12 (all surviving to 13 cycles or more). In most cases (9 out of 15 mixes) it appeared to be no effect of the cure condition and for 4 mixes, the performance appeared to be worse for cure b.

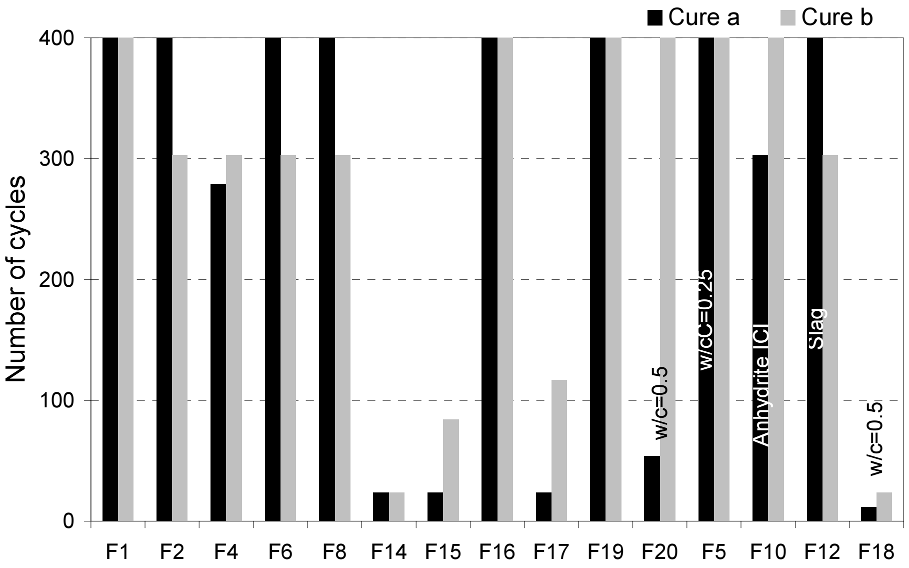

Figure B- 2: Sekisui results. If not specified, w/c=0.35. Cure a= 28 days, 20°C, 65%RH; cure b=28 days, 20°C, 100%RH

The poor performers were F14, 15, 17 and 18 which showed surface scaling, figure B-3.

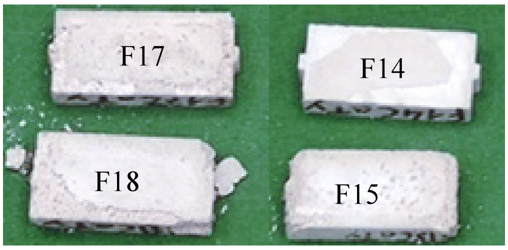

Figure B- 3: Surface scaling of F14, F15, F17 and F18

The best performers were 1, 2, 5, 6, 8, 10, 12, 16, 19 and 20b. Of these binders F5 and F19 were undamaged under both conditions.

Comparing the 2 cure conditions, cure b (100% RH) appeared to improve the frost resistance of the poor performers (mix 15, 17 and 20). For the better performers, cure b gave no difference and appeared to be worse in some cases.

Curriculum Vitae

Séverine LAMBERET

E-mail : slamberet@hotmail.com
Date of birth: 12th November 1975

Nationality: French
Status: Single

EDUCATION

2002-2004	Swiss Federal Institute of Technology- Lausanne, Switzerland PhD Thesis
1999-2000	University Claude Bernard Lyon I, France D.E.A. (Master) Polymer Materials and Composites
1997-1999	University Claude Bernard Lyon I, France Physical chemistry studies

WORK EXPERIENCE

2002-2004	PhD student and research assistant Laboratory of Materials Construction, EPFL Collaboration with Lafarge Aluminates
2001 (4 months)	Research engineer at Lafarge Aluminates, Saint Quentin Fallavier, France
1999-2000	Research assistant Collaboration with Rhodia Silicones, Lyon, France
1999 (3 months)	Research assistant Laboratory Marcel Mérieux, Lyon, France